

PRODUCTION AND CHARACTERIZATION OF CARBON-SILICON
NANOCOMPOSITE ANODE MATERIALS FOR SECONDARY LITHIUM
BATTERIES

A THESIS SUBMITTED TO
THE GRADUATE SCHOOL OF NATURAL AND APPLIED SCIENCES
OF
MIDDLE EAST TECHNICAL UNIVERSITY

BY

BURCU MİSER

IN PARTIAL FULFILLMENT OF THE REQUIREMENTS
FOR
THE DEGREE OF DOCTOR OF PHILOSOPHY
IN
THE DEPARTMENT OF MICRO AND NANOTECHNOLOGY

MARCH 2017

Approval of the thesis:

**PRODUCTION AND CHARACTERIZATION OF CARBON-SILICON
NANOCOMPOSITE ANODE MATERIALS FOR SECONDARY LITHIUM
BATTERIES**

submitted by **BURCU MİSER** in partial fulfillment of the requirements for the degree
of **Doctor of Philosophy in the Micro and Nanotechnology Department, Middle
East Technical University** by,

Prof. Dr. Gülbin Dural Ünver _____
Dean, Graduate School of **Natural and Applied Sciences**

Assoc. Prof. Dr. Burcu Akata Kurç _____
Head of Department, **Micro and Nanotechnology Dept., METU**

Prof. Dr. Mehmet Kadri Aydınol _____
Supervisor, **Metallurgical and Materials Engineering Dept., METU**

Prof. Dr. Mehmet Parlak _____
Co-Supervisor, **Department of Physics., METU**

Examining Committee Members:

Prof. Dr. Caner Durucan _____
Metallurgical and Materials Engineering Dept., METU

Prof. Dr. Mehmet Kadri Aydınol _____
Metallurgical and Materials Engineering Dept., METU

Assoc. Prof. Dr. Z. Göknur Cambaz Büke _____
Materials Science and Nanotechnology Engineering Dept., TOBB - ETU

Assist. Prof. Dr. Mert Efe _____
Metallurgical and Materials Engineering Dept., METU

Assist. Prof. Dr. Metehan ERDOĞAN _____
Materials Engineering Dept., Yıldırım Beyazıt University

Date: 08.03.2017

I hereby declare that all information in this document has been obtained and presented in accordance with academic rules and ethical conduct. I also declare that, as required by these rules and conduct, I have fully cited and referenced all material and results that are not original to this work.

Name, Last name : Burcu Miser

Signature :

ABSTRACT

PRODUCTION AND CHARACTERIZATION OF CARBON-SILICON NANOCOMPOSITE ANODE MATERIALS FOR SECONDARY LITHIUM BATTERIES

Miser, Burcu

Ph.D., Department of Micro and Nanotechnology

Supervisor : Prof. Dr. M. Kadri Aydınol

Co-Supervisor: Prof. Dr. Mehmet Parlak

September 2016, 167 pages

Amongst other anode materials, silicon has the highest capacity (for $\text{Li}_{22}\text{Si}_5$: 4200 mAh.g^{-1}), whereas; the commonly used graphite has only a capacity of 320 mAh.g^{-1} . Although this property of silicon makes it a worthwhile subject, there are technical issues which makes it difficult for commercial use.

In this study, the aim is to investigate methods of producing silicon anode materials from a readily available powder via top down nano-particle forming methods for next generation lithium ion batteries which have higher capacity, longer cycle life, and are safer. These methods are high energy ball milling, metal assisted chemical etching, thermal plasma synthesis and sol-gel methods. Readily available silicon powder was converted into Si/C nanocomposite anode materials by using these methods and their

electrochemical performances were tested. For this purpose, cycle life, impedance and power density of the cells were determined.

According to the obtained results, the produced powders showed high capacity in the first few cycles and then lost their capacity. In particular, metal assisted chemical etching and induction plasma synthesis have yielded promising results to increase the cycle life of the readily available silicon powder. By applying these methods the surface area of silicon powder was increased from $2.4 \text{ m}^2.\text{g}^{-1}$ to around $7 \text{ m}^2.\text{g}^{-1}$. The sol-gel method selected for coating was not homogeneous and can not be obtained uniformly on all surfaces, so that it has not been successful in terms of cycle life increment except for ball-milled powder.

Keywords: Lithium ion batteries, silicon anodes, high energy ball milling, metal assisted chemical etching, induction plasma synthesis, sol-gel coating.

ÖZ

İKİNCİL LİTYUM BATARYALAR İÇİN KARBON/SİLİKON ANOT MALZEMELERİNİN ÜRETİMİ VE KARAKTERİZASYONU

Miser, Burcu

Doktora, Mikro ve Nanoteknoloji Bölümü

Tez Yöneticisi : Prof. Dr. M. Kadri Aydınol

Ortak Tez Yöneticisi: Prof. Dr. Mehmet Parlak

Eylül 2016, 167 sayfa

Diğer anot malzemeleri arasında grafit sadece 320 mAh g⁻¹ kapasiteye sahip iken silikon en yüksek kapasiteye sahiptir (Li₂₂Si₅ için 4200 mAh g⁻¹). Bu özelliği silikonu ilgi çekici kılmaya rağmen silikonun ticari kullanımı için bazı engeller bulunmaktadır.

Bu çalışmayla amaçlanan, yeni nesil lityum iyon bataryalar için; daha yüksek kapasiteli, uzun çevrim ömrüne sahip, güvenli, yukarıdan-asağıya nano-parçacık oluşturma yöntemleri kullanılarak ve hazır bir tozla üretilmiş silikon anot malzemesi üretim metodlarının araştırılmasıdır. Sözü geçen yöntemler; yüksek enerjili bilyeli değirmenle öğütme, metal destekli kimyasal aşındırma, endüksiyon termal plazma sentezi ve sol-jel kaplamadır. Hazır alınan silikon tozu, bu yöntemler kullanılarak Si/C nanokompozit anot malzemesi haline getirilip, elektrokimyasal performansları test

edilmiştir. Bu amaçla, hücrelerin döngüsel ömürleri, empedansları ve güç yoğunlukları belirlenmiştir.

Elde edilen sonuçlara göre üretilen tozlar, ilk çevrimlerde yüksek kapasite göstermişlerdir sonrasında ise kapasite kaybı yaşamışlardır. Özellikle hazır silikon tozunun çevrim ömrünün artırılması için metal destekli kimyasal aşındırma ve endüksiyon plazma sentezi umut vaad eden sonuçlar vermiştir. Bu metodlar uygulanarak silikonun yüzey alanı $2.4 \text{ m}^2.\text{g}^{-1}$ 'dan $7 \text{ m}^2.\text{g}^{-1}$ 'a yükseltilmiştir. Kaplama için seçilen sol-jel metodu ise kaplamanın homojen ve her yüzeyde eşit elde edilememesi sebebiyle bilyeli değirmende öğütülen tozlar dışında çevrim ömrünü artırmak açısından başarılı bir sonuç vermemiştir.

Anahtar Kelimeler: Lityum-iyon batarya, silikon anot, yüksek enerjili bilyeli değirmenle öğütme, metal destekli kimyasal aşındırma, endüksiyon plazma sentezi, sol-jel kaplama.

ACKNOWLEDGMENTS

I would like to express my deepest gratitude to my advisor Prof. Dr. M. Kadri Aydınol for his supervision, knowledge, advice, encouragement and leadership throughout this study. During my studies, his valuable support and guidance helped me tremendously and I will cherish the time I had the honor to work beside him.

Thank are also extended to Prof. Dr. Mehmet Parlak and Prof. Dr. Caner Durucan for providing me many valuable suggestions and helpful discussions on this work and serving on the thesis committee. I also appreciate the help and time spent by the other committee members: Assoc. Prof. Dr. Z. Göknur Cambaz Büke, Assoc. Prof. Dr. Ziya Esen, Assist. Prof. Dr. Mert Efe and Assist. Prof. Dr. Metehan Erdoğan.

Also, the contribution of Prof. Dr. Tayfur Öztürk is deeply appreciated, especially during my induction plasma synthesis studies. His students, Pelin Livan and Cavit Eyövge shared the experience and helped me to understand the process.

I would like to mention and thank my fellow students at the Department of Metallurgical and Materials Engineering, METU, especially; Berke Pişkin, Ayşegül Afal, Burçin Kaygusuz, Burcu Arslan, Cansu Savaş, Özgün Köse, Yedigâr Seymen, Fatih Pişkin and Emre Yılmaz for their friendship and moral support.

The specialists were indispensable in this study, who worked hard and helped me. For SEM and TEM sessions Serkan Yılmaz, for XRD measurements Nilüfer Özel and for particle size measurements Önder Şahin.

My parents and sister for their support, encouragement and trust, I am grateful. They were always beside me. Finally, I am thankful to my husband Ercan Miser for being

such a caring companion. His consistent support and motivation has meant everything to me. I could not imagine to complete this thesis without the supports of my family. I am feeling so lucky to have them.

I would like to acknowledge the Technological Research Council of Turkey (TUBITAK) for the PhD Scholarship (2211-C) they have provided me to conduct my research studies.

TABLE OF CONTENTS

ABSTRACT.....	V
ÖZ	VII
ACKNOWLEDGMENTS.....	IX
TABLE OF CONTENTS	XI
LIST OF TABLES	XIII
LIST OF FIGURES.....	XIV

CHAPTERS

1 INTRODUCTION.....	1
2 LITERATURE REVIEW.....	5
2.1 Introduction	5
2.2 General Information about Lithium-ion Batteries.....	11
2.3 Lithium Ion Battery Electrodes	15
2.3.1 Positive Electrode Materials (Cathode).....	15
2.3.2 Negative Electrode Materials (Anode).....	16
2.3.3 Lithium as Anode Material.....	18
2.3.4 Carbonaceous Anode Materials.....	19
2.3.5 Lithium Alloys as Anode Materials.....	24
3 GENERAL EXPERIMENTAL PROCEDURES	31
3.1 Materials used in the experiments.....	31
3.2 Experimental Methods	33
3.2.1 Ball-milling:.....	33
3.2.2 Metal Assisted Chemical Etching	35
3.2.3 Thermal Plasma Synthesis	35
3.2.4 Sol-Gel Coating	36
3.2.5 Carbon Coating.....	39

3.3	Characterization Techniques.....	40
3.3.1	Structural Characterization Techniques.....	40
3.3.2	Electrochemical Characterizations	41
4	PLANETARY BALL-MILLING	45
4.1	Introduction	45
4.2	Results & discussion of ball-milling studies of silicon powder	48
4.3	Structural characterization of ball-milled powder.....	57
5	METAL ASSISTED CHEMICAL ETCHING	63
5.1	Introduction	63
5.2	Metal assisted chemical etching of silicon powders	66
5.3	Results & discussion of multi-dimensional Si production	68
5.4	Structural Characterization of mSi	82
5.5	Additional studies on metal assisted chemical etching of silicon	89
6	INDUCTION PLASMA SYNTHESIS	95
6.1	Introduction	95
6.2	Structural Characterization of Induction Plasma Synthesized Silicon Powder	98
7	SOL-GEL COATING OF PRODUCED POWDERS	109
7.1	Introduction	109
7.2	Fundamentals of Sol-gel method	109
7.2.1	Pechini Method.....	111
7.3	Coating of High Surface Area Silicon Nanoparticles	111
7.3.1	Properties of selected coating materials in this study	112
7.4	Results & discussion of the coating studies.....	117
8	ELECTROCHEMICAL RESULTS & DISCUSSION	127
8.1	Introduction	127
8.2	Galvanostatic charge-discharge tests	128
8.3	Electrochemical Impedance Spectroscopy	140
8.4	Cyclic voltammetry and Voltage profiles of samples	145
9	CONCLUSIONS.....	155
	REFERENCES.....	157
	CURRICULUM VITAE	167

LIST OF TABLES

TABLES

Table 3.1: The experimental matrix of ball milling trials.	34
Table 3.2 The information about the precursor materials used for sol-gel coatings.	37
Table 3.3 Properties of calcination steps for coating materials.....	39
Table 4.1 The D10, D50, and D90 values based on volume distribution of all ball-milled powders.	55
Table 4.2 The D10, D50, and D90 values based on volume distribution of all ball-milled powders.	57
Table 5.1 Contents and values of each solutions at the etching step.....	69
Table 5.2 Experimental details of Ag deposition step.....	69
Table 5.3 Silver deposition step's obtained best results.....	76
Table 5.4 Experimental details of etching step	77
Table 5.5 Etching step's obtained best results.....	81
Table 6.1 Results of the Rietveld refinement.	100
Table 7.1 Rietveld analysis of the powders.....	125
Table 8.1 Abbreviations of powders	127
Table 8.2 Number of lithium atoms inserted in plain powders at the initial cycle per unit formula per Si.	129
Table 8.3 Number of lithium atoms inserted in the per unit formula of plasma synthesized silicon powders at the initial discharge.	139
Table 8.4 Calculated resistance values of as-received silicon powders	142
Table 8.5 Calculated resistance values of ball-milled silicon powders.....	142
Table 8.6 Calculated resistance values of mSi powders.....	142
Table 8.7 Calculated resistance values of induction plasma synthesized Si powders	144

LIST OF FIGURES

FIGURES

Figure 1.1 Simplified Ragone plot [1].....	2
Figure 2.1 Basic battery components and electrochemical operation of a cell during discharge.....	7
Figure 2.2 Examples of various shapes and combinations in Li-ion battery structure. a) Cylindrical type; b) coin type; c) prismatic; and d) thin and flat cells [5].	7
Figure 2.3 Cell voltage during discharge[6].....	11
Figure 2.4 Reaction mechanism in a rechargeable lithium ion battery during discharge process [7].	13
Figure 2.5 Power need trend of the mobile electronic devices vs the expected increase in battery power [8]	14
Figure 2.6 Crystal structures and electrochemical reactions of various cathodes: (A) layered LiMO_2 , (B) spinel LiM_2O_4 , (C) olivine LiMPO_4 , (D) Li_2MSiO_4 , (E) LiMBO_3 , (F) LiV_3O_8 , (G) V_2O_5 , (H) FeF_3 [10].	16
Figure 2.7 Lithium-ion batteries anode alternative material sources and capacities comparisons [12].	17
Figure 2.8 Voltage and capacity relation of electrode materials currently used and most promising materials studied. The output voltage and capacities of Li batteries are given. [5].	18
Figure 2.9 (a) Li ion battery schematic diagram; (b) Li metal battery schematic diagram; (c) Li dendrite generalized morphology and related main issues (c)[14]. .	19
Figure 2.10 Left-side: The crystal structure of hexagonal graphite showing AB layer stacking order with the unit cell. Right-side: Perpendicular look at the basal plane of the hexagonal graphite layers. The prismatic surfaces may be further divided into armchair and zig-zag faces [15].	21

Figure 2.11 Schematic drawings of the structure of LiC_6 . a) AA layer stacking order and the $\alpha\alpha$ interlayer sequencing of inserted lithium. b) Perpendicular view of the basal plane of LiC_6 [15].	22
Figure 2.12 Constant current charge/discharge curves (1st and 2nd cycle) of the graphite Timrex KS 44 in the electrolyte $\text{LiN}(\text{SO}_2\text{CF}_3)_2$ /ethylene carbonate/dimethyl carbonate (C_{rev} represents the reversible specific charge, C_{irr} represents the specific charge which is irreversible) [15].	22
Figure 2.13 Changes at the anode/electrolyte interface [16].	24
Figure 2.14 Different alloying metals for lithium [18].	25
Figure 2.15 Gravimetric/volumetric capacity graph for some alloying reactions. Capacities are given in comparison with graphite as a reference[20].	26
Figure 2.16 Main degradation mechanisms of Si anodes stemming from the large volume expansion of Si during lithiation process[23].	27
Figure 2.17 Examples of various types of Si-based anode material production strategies; (a) various morphologies of Si-active materials and their composites. (b) reversible lithiation–delithiation process of SiO_x (c) compositing (d) Various binder concepts for Si anodes. SEI, solid electrolyte interphase [23].	28
Figure 3.1 Particle size distribution graph of the as-received silicon powder	31
Figure 3.2 SEM images of the as-received silicon powder, (a) 2500X, (b) 5000X.	32
Figure 3.3 XRD pattern of as-received silicon powder.	33
Figure 3.4 XPS spectrum of the as-received silicon powder.	34
Figure 3.5 Simple schematic of the induction plasma system.	36
Figure 3.6 Schematic illustration of the torch [31]	37
Figure 3.7 Schematic of equivalent circuit model for this study.	43
Figure 4.1 High energy milling types (A) Ball milling, (B) Planetary milling, (C) Vibrational milling, (D) Attritor-stirring milling, (E) Pin milling, (F) Rolling milling [33]	46
Figure 4.2 Motions inside a ball mill: (A).Cascading motion, (B).Falling or cataracting motions, (C).Centrifugal motion [33].	46
Figure 4.3 Directions of the movement of working parts and balls in a planetary mill [33]	47

Figure 4.4 Comparison of effects of rotational speeds on particle size distribution: ball-milled powders with 10 mm balls, weight ratio of balls to powder 15:1 and mill charge 100%.....	49
Figure 4.5 SEM images of ball milled powders with 10 mm balls and rotational speeds of (a) 75 rpm, (b) 150 rpm, (c) 250 rpm, (d) 350 rpm.....	49
Figure 4.6 Comparison of particle size distributions of ball milled powders with the weight ratios of 10:1 and 15:1 with 10 mm balls and mill charge 100%.....	50
Figure 4.7 Comparison of SEM images of ball milled powders with the weight ratios of 10:1 and 15:1 with 10 mm balls and mill charge 100%.	51
Figure 4.8 (a) comparison of particle size distributions of ball-milled powders with mill charges of 60 and 100%, the weight ratios of 15:1, 10 mm balls, 150 rpm (b) Comparison of SEM images of these powders.	52
Figure 4.9 Effect of different milling durations on particle size distribution.....	53
Figure 4.10 Comparison of SEM images of ball-milled powders with milling times of 24, 36 and 48 hours, mill charge was 60%, the weight ratios of 15:1, 10 mm balls, 150 rpm.	53
Figure 4.11 Comparison of particle size distributions of 5 mm ball.....	55
Figure 4.12 SEM images of the samples milled with 5 mm ball size.	56
Figure 4.13 SEM images of powders, (a) before sieving, (b) after sieving.	58
Figure 4.14 XRD data of ball-milled powder.....	59
Figure 4.15 Wide-scan or survey spectrum of ball-milled silicon powder, showing all elements present with atomic percentages.	60
Figure 4.16 High-resolution XPS spectrum of C 1s of ball-milled silicon powder.	60
Figure 4.17 High resolution XPS spectrum of Si 2p of ball-milled silicon powder.	61
Figure 4.18 High resolution XPS spectrum of O 1s of ball-milled silicon powder.	61
Figure 5.1 Schematic illustrations of the formation mechanism of SiNWs arrays: a) at the starting point; (b) during the etching process [39].	65
Figure 5.2 (a) Porous silicon nano-particles preparing procedure. (b) Same weight non-porous and porous Si samples have volumetric contrast[25].....	66
Figure 5.3 An image of the synthetic route of mSi powder. While the Ag deposited Si powder is immersed in an etchant, Ag catalyzes the Si etching, when H ₂ O ₂ is used as an oxidant it improves the etching speed to make the mSi structures [40].....	67

Figure 5.4 (a) A SEM image of mSi. The inset shows Si nano-wires having pores of 15–20 nm; (b) Cross-sectional SEM image of mSi achieved from the focused ion beam (FIB) process [40].....	67
Figure 5.5 SEM images of the samples which show the effect of AgNO ₃ , (a, b) 0,005M, (c, d) 0.02 M, (e, f) 0.04 M, (g, h) 0.08 M at x1000 and x2500 magnifications.	70
Figure 5.6 SEM images of the samples which show the effect of HF, (a, b) 4M, (c, d) 5M, (e, f) 10M, at x1000 and x2500 magnifications.	72
Figure 5.7 SEM images of the samples which show the effect of AgNO ₃ (mol)/Si(mol), (a, b) 0.01, (c, d) 0.1, (e, f) 0.2, at x1000 and x2500 magnifications	73
Figure 5.8 SEM images of the samples which show the effect of deposition duration, (a, b) 1 minute, (c, d) 5 minute, (e, f) 30 minute, at x1000 and x2500 magnifications.	74
Figure 5.9 SEM images of the samples which show the effect of temperature, (a, b) room temperature, (c, d) 50°C, at x1000 and x2500 magnifications	75
Figure 5.10 SEM images of the samples which show the effect of HF, (a, b) 4M, (c, d) 5M, (e, f) 10M at x1000 and x2500 magnifications.	77
Figure 5.11 SEM images of the samples which show the effect of H ₂ O ₂ , (a, b) 0.5ml, (c, d) 1.5ml, (e, f) 2ml, at x1000 and x2500 magnifications.....	78
Figure 5.12 SEM images of the samples which show the effect of time, (a, b) 60 minute, (c, d) 300 minute, at x1000 and x2500 magnifications.....	80
Figure 5.13 SEM images of the samples which show the effect of temperature, (a, b) 50°C, (c, d) room temperature, at x1000 and x2500 magnifications.	81
Figure 5.14 SEM image of produced Silicon particles with porous and columnar surfaces (mSi).....	82
Figure 5.15 Cross sectional SEM images of mSi obtained from the FIB process, (a) 10000x, (b) 30000x, (c) 40000x, (d) 160000x and (e) 15000x – it shows the columnar structure.....	83
Figure 5.16 TEM images showing the wires that were cut off from etched silicon particles.	85

Figure 5.17 Particle size distribution comparison of mSi and as-received Si powders.	86
Figure 5.18 Wide-scan or survey spectrum of multi-dimensional silicon powder, showing all elements present with atomic percentages.....	87
Figure 5.19 High-resolution XPS spectrum of C 1s of mSi powder.....	87
Figure 5.20 High-resolution XPS spectrum of Si 2p of mSi powder.....	88
Figure 5.21 High-resolution XPS spectrum of O 1s spectrum of mSi powder.	88
Figure 5.22 Comparisons of electrochemical electron energy levels of five redox systems in HF solution between Si band edges (E_c and E_v are the conduction and valence band energies, respectively) [42].	89
Figure 5.23 SEM images of the sample produced using one-step etching with $Fe(NO_3)_3$, (a) x1000, (b) x2500 magnifications.....	90
Figure 5.24 SEM images of the sample produced using one-step etching with $Cu(NO_3)_2$, (a) and (b) at x5000 magnifications.....	90
Figure 5.25: SEM images of the etched samples with the solution parameters of 0.135M $Fe(NO_3)_3$ and 5 M HF, solution temperature was 50°C and etching duration was set to 180 minutes.	91
Figure 5.26 SEM of three step etched silicon powder, (a) 2500x, (b) 10000x magnifications.	92
Figure 5.27 SEM images of the sample produced by two-step etching using $AgNO_3$ at metal deposition step and $Fe(NO_3)_3$ at etching step, (a) x1500, (b) x10000 magnifications	93
Figure 6.1 Different types of thermal plasma torches, (a) Transferred DC Plasma Torch, (b) Non-transferred DC Plasma Torch and (c) RF Plasma Torch[45].....	96
Figure 6.2 Phase identification of induction synthesized silicon powder (a) XRD patterns of the powder, (b) Rietveld analysis obtained by MAUD program.	99
Figure 6.3 Raman spectra of induction plasma synthesized powder, (a) typical single spectrum obtained, (b) closer look to D and G bands.	101
Figure 6.4 XPS data of induction plasma synthesized silicon (Full spectrum).....	102
Figure 6.5 XPS spectrum corresponding to Si 2p.	103
Figure 6.6 XPS spectrum corresponding to C 1s.	103

Figure 6.7 SEM micrographs of produced powder, (a) x10000, (b) x50000 and (c) x240000 magnifications.	106
Figure 6.8 TEM micrograph of produced powder, (a) general view of the particles, (b) closer look at the carbon layer, (c) HRTEM of the scene of carbon layer and lattice fringes inside the particle	107
Figure 6.9 Particle size distribution of induction plasma synthesized silicon powder.	108
Figure 7.1 Simplified chart of the sol-gel process	110
Figure 7.2 The crystal structure of γ - Li_3PO_4	112
Figure 7.3 The crystal structure of Li_3VO_4	113
Figure 7.4 The crystal structure of MnWO_4	114
Figure 7.5 The crystal structures of ZrP_2O_7 and ZrV_2O_7	116
Figure 7.6 XRD pattern of Li_3PO_4 calcined at 600°C for 3 hours.....	119
Figure 7.7 SEM images of Li_3PO_4 coated multi-dimensional silicon powder.....	119
Figure 7.8 XRD pattern of Li_3VO_4 calcined at 600°C for 3 hours.	119
Figure 7.9 SEM images of Li_3VO_4 coated multi-dimensional silicon powder.	120
Figure 7.10 XRD pattern of MnWO_4 calcined at 900°C for 2 hours.	120
Figure 7.11 SEM images of MnWO_4 coated multi-dimensional silicon powder...	120
Figure 7.12 XRD pattern of ZrP_2O_7 calcined at 900°C for 2 hours.	121
Figure 7.13 SEM images of ZrP_2O_7 coated multi-dimensional silicon powder.....	121
Figure 7.14 XRD pattern of ZrV_2O_7 at calcined at 600°C for 3 hours.	121
Figure 7.15 SEM images of ZrV_2O_7 coated multi-dimensional silicon powder....	122
Figure 7.16 TEM images of Li_3PO_4 coated multi-dimensional silicon powder.....	122
Figure 7.17 TEM images of induction plasma synthesized silicon powder with Li_3PO_4 coating	123
Figure 8.1 The discharge capacity graph of plain powders.....	128
Figure 8.2 XRD spectrum of electrodes after final discharges.	130
Figure 8.3 The comparison of different coating materials on the cyclic performance of base powder (a) cycles from 1-21, (b) cycles from 11-21 (Lines drawn to facilitate tracking).	132
Figure 8.4 XRD spectrum of coated base powder electrodes after final discharges.	133

Figure 8.5 The comparison of different coating materials on the cyclic performance of ball-milled powder, (a) cycles from 1-21, (b) cycles from 11-21.....	134
Figure 8.6 XRD spectra of coated ball-milled powder electrodes after final discharges.....	135
Figure 8.7 The comparison of different coating materials on the cyclic performance of multi-dimensional powder, (a) cycles from 1-21, (b) cycles from 10-21.....	136
Figure 8.8 XRD spectra of multi-dimensional Si electrodes after final discharge cycles.....	137
Figure 8.9 The comparison of different coating materials on the cyclic performance of induction plasma synthesized powder, (a) cycles from 1-21, (b) cycles from 11-21.....	138
Figure 8.10 XRD spectra of plasma synthesized silicon powder electrodes after final discharge cycles.....	140
Figure 8.11 Impedance spectra comparisons of as-received silicon powders.....	141
Figure 8.12 Impedance spectra comparisons of ball-milled silicon powders	141
Figure 8.13 Impedance spectra comparisons of multi-dimensional silicon powders	143
Figure 8.14 Impedance spectra comparisons of plasma synthesized silicon powders	143
Figure 8.15 Impedance spectra comparisons of uncoated silicon powders	144
Figure 8.16 Cyclic voltammograms of produced silicon powders.....	145
Figure 8.17 The first discharge curves of produced silicon powders.....	146
Figure 8.18 Cyclic voltammetry of LP coated powders.....	147
Figure 8.19 The first discharge curves of LP coated silicon powders.	148
Figure 8.20 Cyclic voltammetry of LV coated powders.	148
Figure 8.21 The first discharge curves of LV coated silicon powders.....	149
Figure 8.22 Cyclic voltammetry of MnW coated powders.	149
Figure 8.23 The first discharge curves of MnW coated silicon powders.....	150
Figure 8.24 Cyclic voltammetry of ZrP coated powders.	151
Figure 8.25 The first discharge curves of ZrP coated silicon powders.	152
Figure 8.26 Cyclic voltammetry of ZrV coated powders.....	153
Figure 8.27 The first discharge curves of ZrV coated silicon powders.	153

Figure 8.28 Cyclic voltammetry of carbon coated powders.	154
Figure 8.29 The first discharge curves of carbon coated silicon powders.	154

CHAPTER 1

INTRODUCTION

The current civilization is getting its lion's share of the energy from fossil fuels. However, global warming primarily the result of extended fossil fuel usage during the last few decades. Also the limited nature of that resource type inflicts both financial and social problems. Therefore, it is essentially unavoidable if we continue to consume energy in that way; energy and environmental issues will become the most important problems of the world in the near future. Therefore, humanity is in need of developing more sustainable systems such as solar cells, fuel cells, and improved batteries. Figure 1.1 shows the simplified Ragone plot (the energy storage spectrum for a variety of systems.) Ragone plot reveals that fuel cells are at the top of the list among the electrochemical energy conversion systems while super-capacitors are deemed as high power systems. On the other hand, batteries are regarded with moderate power and energy ratios. Figure 1.1 also shows that none of the electrochemical energy conversion systems can reach to the characteristics of internal combustion engines (ICE) at today's circumstances. As can be understood from the Ragone plot, batteries are powerful candidates to take the place of ICE [1, 2].

There are many different battery technologies commercially available for different types of applications such as cell phones, cameras, remote controlled devices, flashlights, hearing aids, wireless mouse, fans, lamps (Figure 1.2-a, b). There are even automobiles, which are operated by the electrical energy stored in batteries. For example, many electric vehicles (EV) or plug-in vehicles (Figure 1.1-c) derive at least some of their power from battery packs.

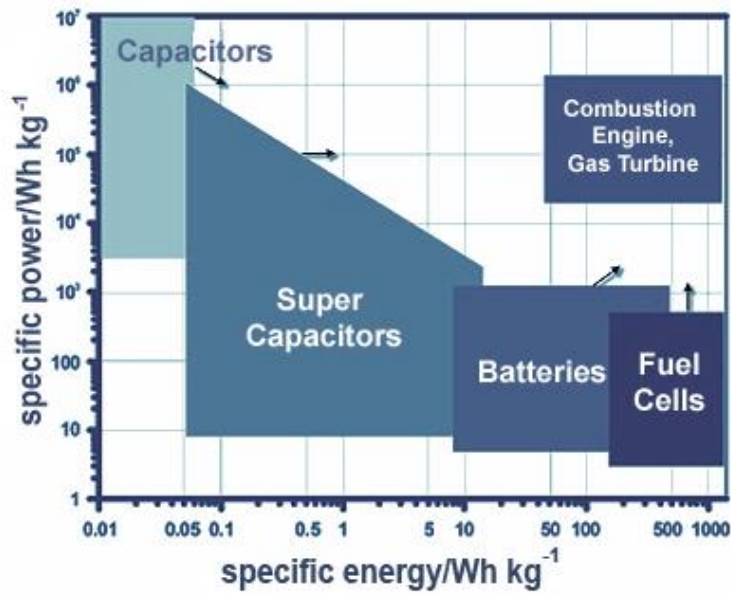


Figure 1.1 Simplified Ragone plot [1].

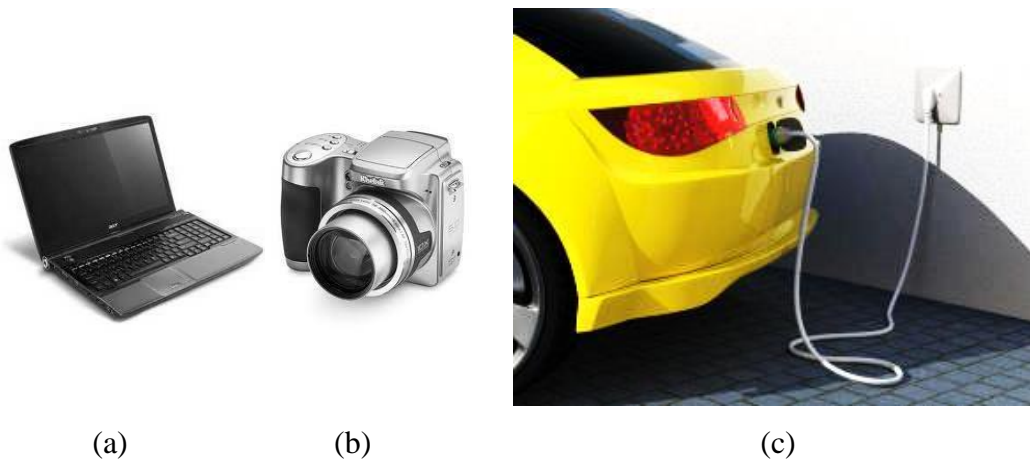


Figure 1.2 Examples of some common devices which use batteries.

Figure 1.3 compares different battery technologies from the point of their energy and power densities. Current Li-ion battery technologies outperform most other commercially manufactured batteries, such as Ni-MH and NiCd based batteries. Their statistics are proof. Their safety, power, cycle life, zonal temperature performances are

indeed superior. However the optimization of the design of electrode makes their usage for portable applications more feasible [2, 3].

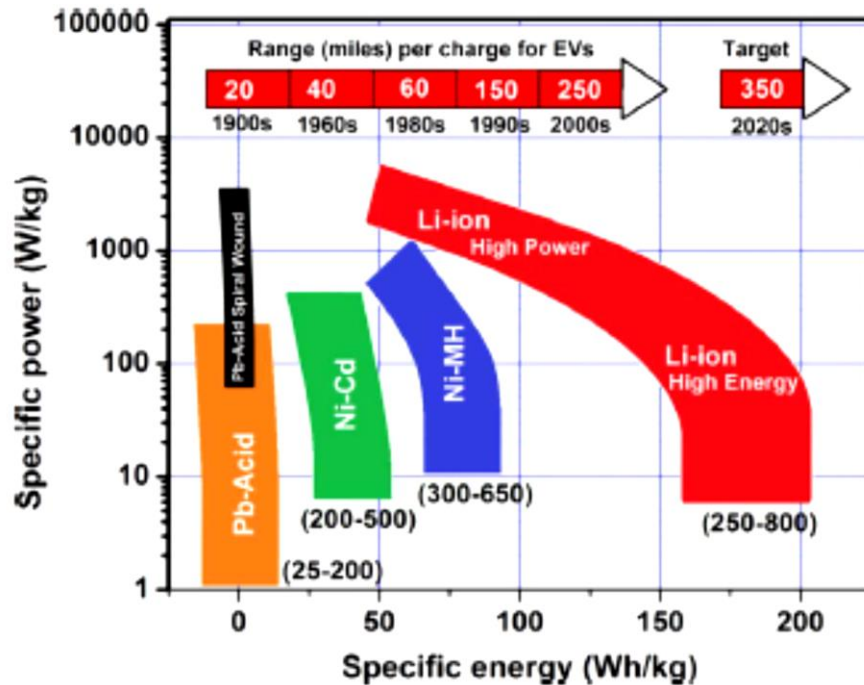


Figure 1.3 Different battery technologies comparison with regard to energy and power densities [3].

As indicated in Figure 1.3 the driving range target for electric vehicles would be 350 miles (~560 km) per charge by 2020 to take on the ICEs [3]. Therefore, the need in the development of lithium ion batteries with better characteristics rises day by day. Although there are many research efforts from the last decade, there is much room for development of lithium-ion batteries for usage in full and hybrid electric vehicles. Particularly, capacity, the power density, energy density, operating voltage, cost of the included materials, cycle life (deep discharge cycles) and safety have to be optimized for the dynamic load profile of an electric vehicle.

The aim of this research project is to find a silicon based nanocomposite anode material for lithium ion batteries from a readily available powder using easy to scale up, top down approaches, which are also cost-effective methods.

To achieve this, strategies (size reduction of silicon and coating with inactive matrix materials) were employed and different methods (metal assisted chemical etching, ball-milling, induction plasma synthesis) were applied to readily available silicon powder. After producing various powders, coating them with inorganic materials (such as Li_3PO_4 , Li_3VO_4 , ZrP_2O_7 , ZrV_2O_7 , MnWO_4) was studied to improve the electrochemical stability using sol-gel techniques. Additionally, carbon coating was applied. After applying these methods, obtained processed powders then were characterized using x-ray diffraction method (XRD), scanning electron microscopy (SEM), Brunauer–Emmett–Teller method (BET), focused ion beam method (FIB), x-ray photoelectron spectroscopy (XPS) and transmission electron microscopy (TEM) structurally and morphologically. Moreover, potentiometric measurements were performed to investigate electrochemical performance of the anodes made from these processed powders in a constructed cell. In addition, cycle life, impedance and cyclic voltammetry of the cells were determined.

CHAPTER 2

LITERATURE REVIEW

2.1 Introduction

A battery can be described as a device that converts electrical energy from chemical redox reactions at its anode and cathode. This occurs through an electric circuit with the transfer of electrons from one electrode to the other. A rechargeable battery has the capability to reverse and repeat these reactions multiple times.

There are three forms of batteries. Primary (single-use or "disposable"), secondary (rechargeable) batteries and reserve batteries.

A battery is called primary when the battery is used up after its discharge and needs to be discarded. In the beginning, they are manufactured in a charged state. Though they are inexpensive, their non-reusable nature exhausts the ecosystem.

Secondary batteries are the batteries which can be charged/discharged repeatedly. They do this by turning into their original state when the current passes in the other direction. Secondary batteries have found widespread usage for the last few decades. Automotive (especially newly developed hybrid and electric cars) and aircraft industry, portable consumer electronics, (UPS) power sources, stationary energy storage (SES) systems for electric utility load leveling, many power tools, and high capacity requiring electrical power applications that would drain the primary batteries too quickly can be listed as their usage areas. Lead-acid, NiCd, Ni-MH, alkaline and Li-ion batteries are the main examples of secondary batteries.

Additionally, reserve batteries are mainly preferred for high energy demanding situations, for a long operational time and/or severe environmental conditions. In this type, one of the main components of the battery is insulated from other components. This insulation restricts the deterioration chemically and self-discharging. Generally, electrolyte is the isolated component. Military applications are their main usage areas that need to meet the expectations of high power and harsh conditions.

A battery consists of cells, which are the units with basic electrochemical properties. Each of these cells consists of four major components:

- i. The negative electrode is anode. During discharge, it emits electrons to the external circuit and is oxidized.
- ii. The positive electrode is cathode. During discharge, it receives electrons from the external circuit.
- iii. The ionic conductor is called the electrolyte. It is the medium in which ions travel from the anode to the cathode. It is usually a liquid solvent like water, in which salts, alkalis and some other soluble is dissolved.
- iv. There is a separator that acts as an electrical insulator. It prevents the contact of the electrodes thus no short circuit happens. There are some types for separators like micro porous plastic films or gelled electrolytes.

Figure 2.1 shows the basic components of a battery and electrochemical operation in discharge.

The cell can be structured in many different geometries and combinations like button batteries, cylindrical batteries, and in various prismatic shapes. The components in batteries are designed in such a way to adjust to the cell shape and volume (Figure 2.2). These cells need to be sealed to prevent leakage and active solvents being exposed to climate [4].

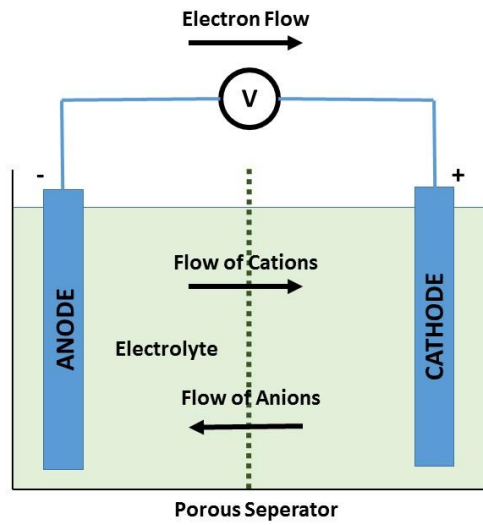


Figure 2.1 Basic battery components and electrochemical operation of a cell at discharge.

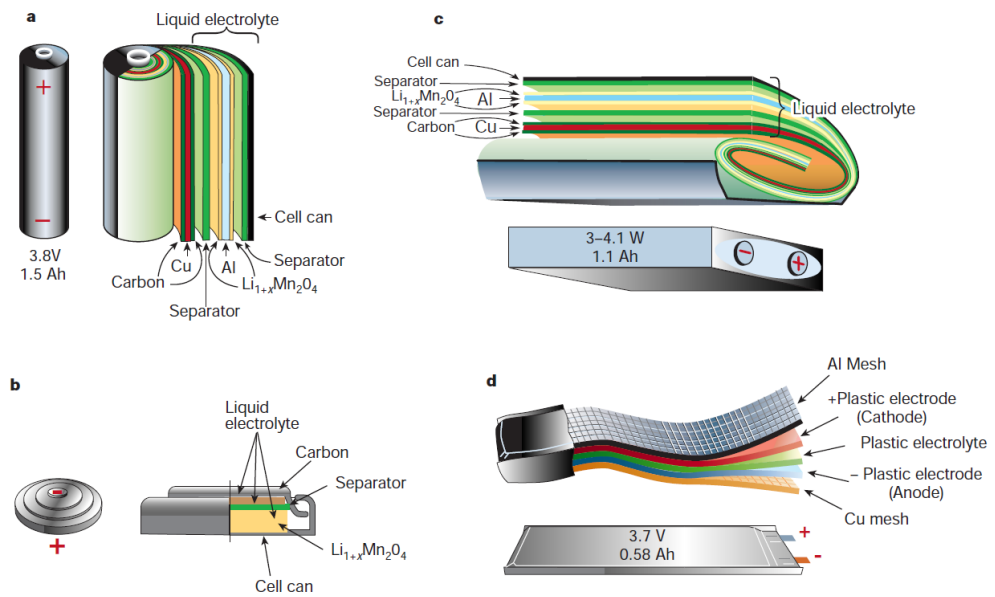


Figure 2.2 Examples of various shapes and combinations in Li-ion battery structure. a) Cylindrical type; b) coin type; c) prismatic; and d) thin and flat cells [5].

In an electrochemical cell, the reactions occur on two poles of the battery. These poles are the electrodes. The reduction reaction can be represented by the following formula:



The reaction on the opposite pole is oxidation, its formula is:



The general formula of the complete battery reaction is:



A rechargeable batteries thermodynamic energy equation is:

$$\Delta G = \Delta H - T\Delta S \quad (4)$$

And

$$\Delta G^{\circ} = \Delta H^{\circ} - T\Delta S^{\circ} \quad (5)$$

Where Gibbs free energy is ΔG , ΔH represents the enthalpy, ΔS is the entropy and T is the absolute temperature of the system. ΔG is the net useful available energy of a given reaction; it can be calculated by the following formulas;

$$\Delta G = -nFE \quad (6)$$

And

$$\Delta G^{\circ} = -nFE^{\circ} \quad (7)$$

ΔG provides electrical energy to an external circuit (the driving force of a cell reaction). “n” is transferred electrons number per mole of reactants. The Faraday constant is represented by F , it is equal to charge of 1 equivalent of electrons. Lastly, E is the voltage of the cell (electromotive force – emf). From these equations, it can be derived that spontaneous reactions have negative free energy and positive emf. This

formula is for the forward direction. The voltage of the cell is unique for each reaction couple.

When conditions differ from the standard conditions, the cell voltage is calculated by Nernst equation:

$$E = E^o - \frac{RT}{nF} \ln \frac{a_C^c a_D^d}{a_A^a a_B^b} \quad (8)$$

a_j gives the activity of relevant species and R is the gas constant ($8.314 \text{ J.K}^{-1} \cdot \text{mol}^{-1}$). Reaction and current flow relationship is determined by Faraday's law:

$$g = \frac{It(MW)}{nF} \quad (9)$$

g is the amount of material reacted (in grams), I is the current (amps), t is the time (seconds or hours), MW is the atomic or molecular weight of the reacted material, and n is the number of electrons in the reaction.

The cell reaction being assumed reversible and with the help of equations 4 and 6, the reversible heat effect can be calculated from:

$$\Delta G = -nFE = \Delta H - T\Delta S = \Delta H - nFT \left(\frac{dE}{dT} \right) \quad (10)$$

While dE/dT is positive, the cells will heat up when charged and cooled during discharge (e.g. NiCd batteries). While dE/dT is negative, the cells will cool down during charge and heat up during discharge (e.g. Lead acid batteries). The total heat released by the cell discharge happens on the surface of the electrodes. For low-rate charge/discharge situations, heat release is not an issue; on the other hand, for high rate applications precautions and provisions for heat dissipation must be taken. Otherwise total failure by heat build up and even more problems caused by the failures might happen [1, 4].

The thermodynamics reflects the feasibility under equilibrium conditions for a given reaction. When current is drawn from the cell during operation, the voltage drops off due to kinetic limitations. This phenomena is known as polarization (η) and given by

$$\eta = E_{ocv} - E_T$$

where E_{ocv} is the open circuit voltage. E_T represents the terminal cell voltage during I current is drawn. In general, there are mainly three types of polarization:

- i. Activation polarization: Related with the redox reactions kinetics on the electrode/electrolyte interfaces of anode and cathode, it follows the Tafel equation:

$$\eta_a = a - b \log\left(\frac{I}{I_0}\right) \quad ; \quad (11)$$

In this equation, a and b are constants, I is current flow of the reaction, and I_0 is the exchange current density.

- ii. Ohmic polarization: It pertains with the resistance of the individual components of the cell and to the resistance due to contact problems between these components. Ohm's law dictates:

$$\eta_o = IR \quad (12)$$

- iii. Concentration polarization: Mass transportation restrictions occurring in the cell during operation generates this type of polarization. It can be calculated by:

$$\eta_c = \left(\frac{RT}{n}\right) \ln\left(\frac{C}{C_0}\right) \quad (13)$$

Here, C denotes the concentration on the surface of the electrode and C_0 is the bulk solution concentration.

Figure 2.3 shows the standard voltage profile of a battery and the effects of polarization [1, 4]

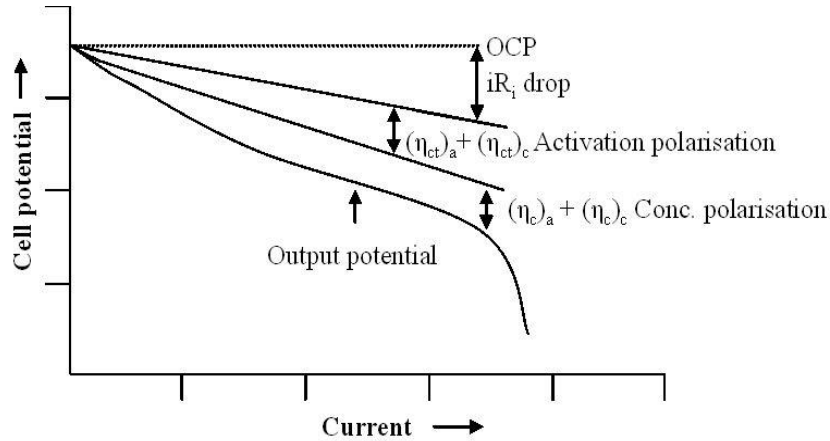


Figure 2.3 Cell voltage during discharge[6].

2.2 General Information about Lithium-ion Batteries

Lithium, is the most electropositive (-3.04V against the hydrogen electrode (SHE)), the lightest ($M_w=6.94\text{ g mol}^{-1}$) and the least dense ($\rho=0.53\text{ g.cm}^{-3}$) metal located in the top corner part of the periodic table. Therefore, lithium batteries deliver highest energy density among all the existing batteries mentioned before [5]. Lithium-ion batteries are belong to secondary battery group and electrodes of the battery comprises lithium intercalation compounds. Rocking chair batteries are also called to this type of batteries. Because during charge-discharge processes lithium ion rock back and forward between the two electrodes, while chemical energy is released or replenish inside the cell [5].

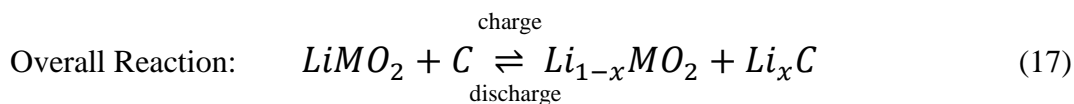
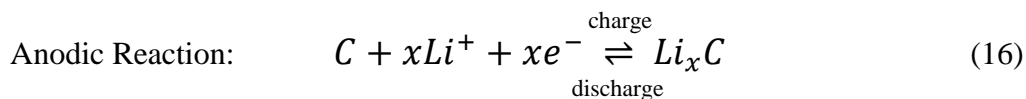
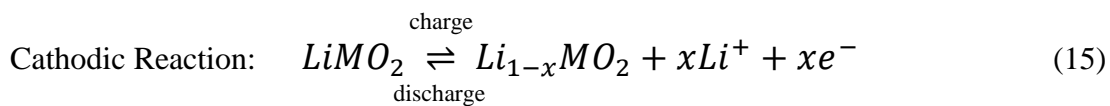
Compared with other battery systems, lithium ion batteries show distinct advantages that can be listed as:

- Maintenance is not required
- High specific energy and energy density

- Broad operation temperature range
- Extended shelf life
- Low rate of self-discharge
- Quick charging capability
- High rate and powerful discharge
- High columbic efficiency
- No memory effect
- Design flexibility
- Long cycle life [4].

A commercial lithium ion battery system generally consists of LiCoO₂ as cathode, graphite as anode and an electrolyte. The electrolyte can be liquid, a gel or a solid polymer Dimethyl Carbonate (DMC), Ethylene Carbonate.(EC), Diethyl Carbonate (DEC), and Propylene Carbonate containing a lithium salt, such as LiPF₆, LiClO₄, LiBF₄, LiBC₄O₈ are the most commonly used electrolytes.

Figure 2.4 represents the reaction mechanism of lithium ion batteries. During discharge, Li ions move from anode (graphite) to the cathode (LiCoO₂) via the electrolyte, which contains lithium ions, while electrons spontaneously go through the external circuit, giving up the energy stored. During the charge process, energy is supplied through the external circuit to the system and Li ions go back to the anode (graphite) and the electrical energy is stored as chemical energy. Reaction mechanisms during charge are shown as follows [4]:



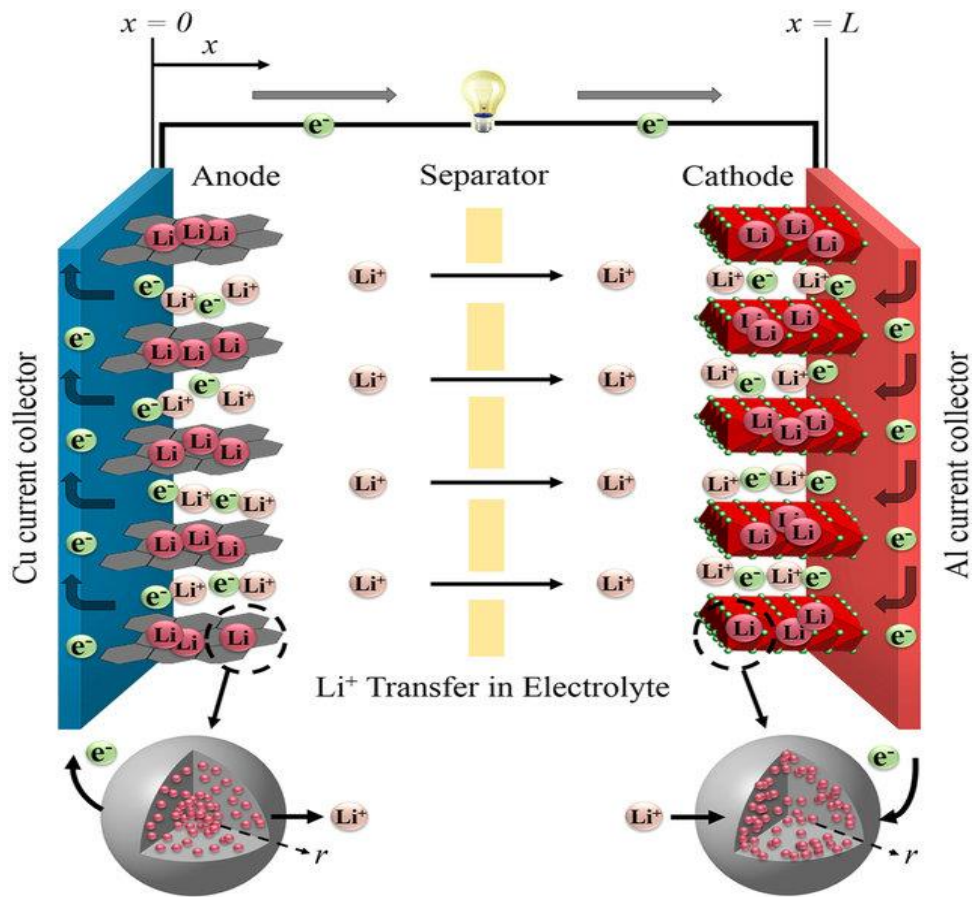


Figure 2.4 Reaction mechanism in a rechargeable lithium ion battery during discharge process [7].

Nowadays lithium-ion batteries are widely used in every area. Besides, with the revolution in portable devices and with the hit of micro-hybrid, hybrid, plug-in electric and all-electric vehicles to the market, expectations for high energy and power density batteries with longer lasting and safety are needed. However, despite there is a huge interest on the studies for the development of high-performance rechargeable lithium-ion batteries, the advancement is not as fast as expected by the market. As shown in Figure 2.5, the electrical output required to supply power to mobile devices is expected to increase around 20% yearly, whereas the improvement in the energy density of Li-ion batteries is predicted to be 10% annually. The main challenges and areas that need improvement can be listed as:

- Stability problems related to mechanical and chemical issues, which stem from electrochemical reactions of the electrolyte, changes in phase, deterioration of materials.
- Moderate energy and power density
- Cycle life (capacity loss with cycling)
- Operation temperature range
- Need for protective circuitry (battery management system is crucial for LIBs for operation)
- Safety issues related to overcharging and crushing
- Moderate initial cost (it needs to be decreased for especially automobile applications) [4, 8, 9]

If we generalize, the demand for next-generation lithium-ion batteries are to increase energy density and power density, increase safety, enhance cycle life, reduce cost, and achieve sustainable and greener Li-ion batteries. As the electrode materials play the key role in a battery, in order to increase the electrochemical performance and reduce the cost, designing better electrode materials is the main task.

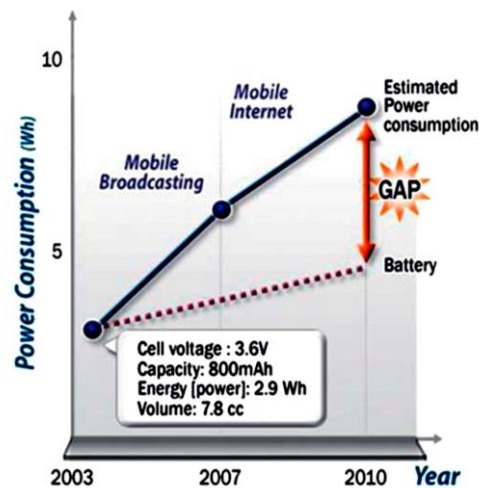


Figure 2.5 Power need trend of the mobile electronic devices vs the expected increase in battery power [8]

2.3 Lithium Ion Battery Electrodes

2.3.1 Positive Electrode Materials (Cathode)

Lithium-ion cells work by a chemical reaction mechanism called “intercalation” wherein lithium ions penetrate to the molecular structure of the electrode. Lithium-ion positive electrode materials are metal oxides or phosphate compounds. Cathode materials are prepared and built into cells in their discharged states. Commercialized batteries contain graphite as anode and positive electrodes are synthesized containing lithium. General requirements for Li-ion positive electrodes can be listed as:

- High Gibbs free energy (higher voltage than lithium metal potential)
- High lithium incorporation capability
- Lithium ions can travel without too much mechanical damage
- High diffusivity of lithium ions
- High conductivity
- Insoluble
- Low cost synthesis, manufactured from cheap sources[4].

According to the above requirement list, there are many cathode materials that have unique and varied crystal structures (Figure 2.6), some of them are listed as:

- LiCoO_2 (layered structure) – (cathode of most commercial batteries)
- Li mixed metal oxides ($\text{LiNi}_{0.8}\text{Co}_{0.2}\text{O}_2$, $\text{LiNi}_{0.8}\text{Co}_{0.15}\text{Al}_{0.5}\text{O}_2$, $\text{LiNi}_{0.33}\text{Co}_{0.33}\text{Mn}_{0.33}\text{O}_2$)
- LiMn_2O_4 (spinel structure)
- LiFePO_4 (olivine structure) [4]

As improvement of cathode materials is not a concern of this study, detailed information will not be given on cathode materials. Literature review will focus on anode materials.

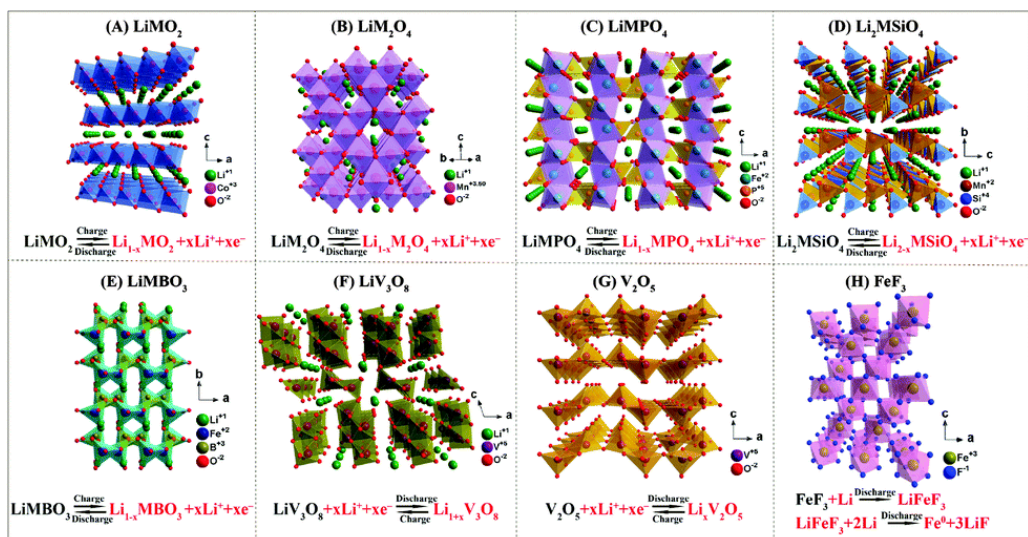


Figure 2.6 Crystal structures and electrochemical reactions of various cathodes: (A) layered LiMO_2 , (B) spinel LiM_2O_4 , (C) olivine LiMPO_4 , (D) Li_2MSiO_4 , (E) LiMBO_3 , (F) LiV_3O_8 , (G) V_2O_5 , (H) FeF_3 [10].

2.3.2 Negative Electrode Materials (Anode)

As mentioned earlier, anode is the reducing electrode and is the oxidation source. The electrons are released from anodes into the external circuit during discharging process. It means that during discharge anode is the negative pole.

The first stages of research studies on lithium-ion batteries focused on lithium metal as anode material. Those batteries were outstanding in terms of their high specific capacity. However, lithium plating problem caused safety issues and lithium metal gave up its place to graphite anodes in 1990s with the invention that made by Sony. Although graphite is a good lithium intercalation material because of its low cost, low operation voltage and safety issues compared to the lithium ion itself its capacity (372 mAh.g^{-1}) is not sufficient for next-generation applications' requirements [4, 11]. Desired properties of a good anode electrode can be listed as; easily transferring lithium ions, high capacity, conductivity, chemical potential and sound stability that withstands mechanical damage due to changes in volume after cycling. Figure 2.7 shows the theoretical capacities of various anode materials. Group IV elements have

the highest capacity values, and metal oxides have the most diversity. These have been studied thoroughly as anode materials over the past decade [12].

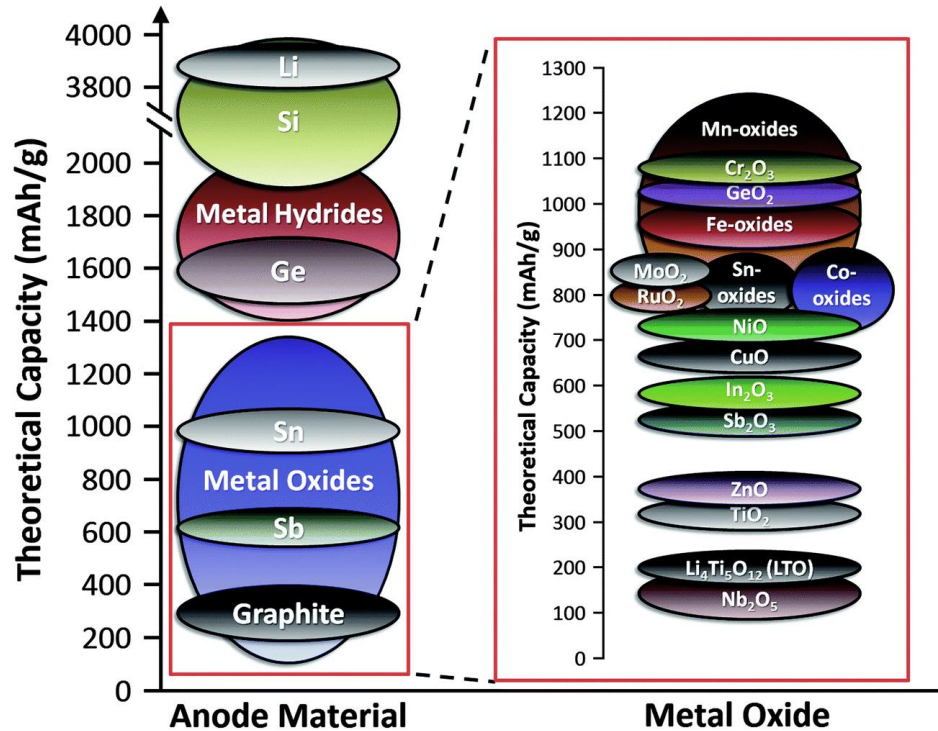


Figure 2.7 Lithium-ion batteries anode alternative material sources and capacities comparisons [12].

Any of the positive active material described in section 2.3.1 could be combined with either of the negative materials to form a discrete electrochemical system. Figure 2.8 shows some of more common combinations and their operating voltages for around the middle of discharge. Every combination has its own advantages and disadvantages. For example, LiFePO_4 - $\text{Li}_4\text{Ti}_5\text{O}_{12}$ couple is one of the safest combinations with their lower cell voltage, however this results to lower energy and power density. On the other hand, carbonaceous anodes have a voltage closest to the lithium metal but, on the first charge intercalated lithium ions react with the solvent of the electrolyte and a permanent layer (SEI) is formed on the negative electrode surface [5, 13]. Below sections, indicate details about various anode materials.

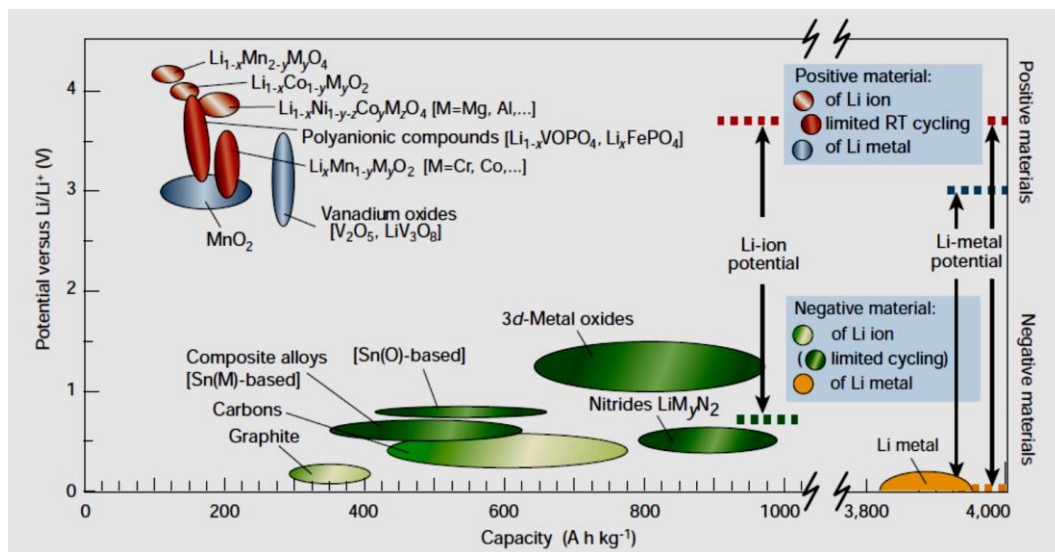


Figure 2.8 Voltage and capacity relation of electrode materials currently used and most promising materials studied. The output voltage and capacities of Li batteries are given. [5].

2.3.3 Lithium as Anode Material

One of the essential factors to develop a battery with high energy density is that the usage of electrode materials with high capacity. Being the most electro-positive alkali metal in the group as well as being light weight makes it primary. It has a density of 0.534 g.cm^{-3} , which means having a 3.86 Ah.g^{-1} specific capacity, and energy density (1470 Wh.kg^{-1}), which stands exceptional.

The anode reaction of metallic lithium:



In spite of remarkable properties of lithium metal, there are vital problems on the commercial usage of lithium metal at lithium-ion batteries. Two main barriers can be mentioned. The enlargement of Li dendrites during cycling processes, and the other

issue is their low Coulombic efficiency (CE). First problem raises safety issues because it can cause short circuits internally and create higher surface area, also it may lead to a short cycle life. At the early stages, there were efforts to compensate low Coulombic efficiency by putting an excess amount of Li to the batteries, the rise of Li-ion batteries has postponed after the safety problems occurred. Figure 2.9 (a) and (b) respectively illustrate typical Li ion battery and a Li metal battery diagrams.

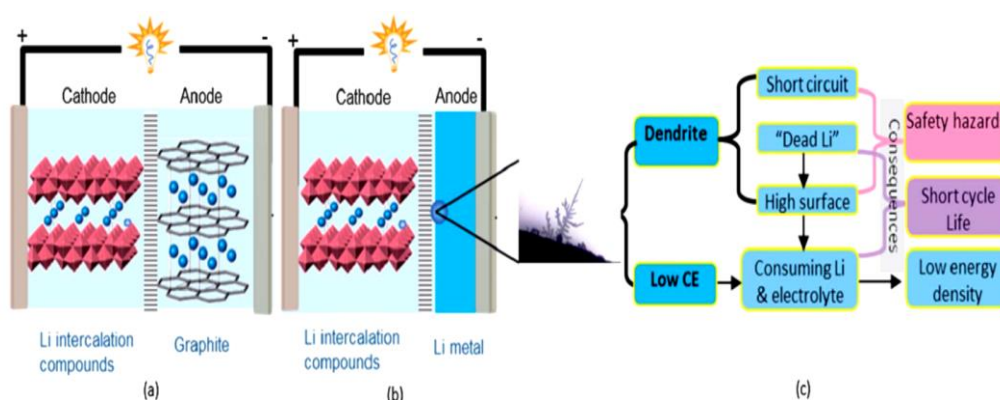


Figure 2.9 (a) Li ion battery schematic diagram; (b) Li metal battery schematic diagram; (c) Li dendrite generalized morphology and related main issues (c)[14].

2.3.4 Carbonaceous Anode Materials

Carbonaceous materials allows the intercalation of Li within its layers reversibly, which lead to commercial usage of them in every existed battery system. Carbon has good capacity, moderate conductivity and electrochemical potential. It also advantageous in terms of cost and availability. Its specific capacity is 372mAh g^{-1} . The maximum number of lithium atoms that can be intercalated within the graphite structure is 1 per 6 carbon atoms (LiC_6). Another advantage is that there is no significant swelling after cycling and therefore little pressure is generated by the carbon based electrodes even after numerous cycles and this allows Li-ion cells to be constructed in many shapes and sizes with thin-walled cases such as button, prismatic

cells or in many other configurations [11]. The intercalation of lithium within carbon in discharging process is given as:



During intercalation process, the lithium reception and the state it will be stored depends mainly on its crystallinity, the microstructure of the compound, and also the morphology of the carbonaceous materials in micro scale. The graphite term is used only for carbons having a lattice layered structural shape with a perfectly stacked order among graphene layers, either the prevalent AB (hexagonal graphite, Figure 2.10) or the less common ABC (rhombohedral graphite). The small transformation energy of AB into ABC stacking (and vice versa), means perfectly ordered graphite crystals are not readily available. Therefore, the term “graphite” is often used regardless of stacking order. There are mainly two types of carbons which can accommodate reversible lithium intercalation, graphitic and non-graphitic (disordered). Graphitic carbons have a layered carbonaceous structure but also come with structural distortions and defections.

The intercalation reaction occurs only at prismatic surfaces (arm-chair and zig-zag faces). Through the basal planes, intercalations are said to be possible only at defected zones. In intercalation process, the order of stacking of the carbon layers (named graphene layers) shifts towards AA form. Therefore, the adjacent graphene layers inside LiC_6 are directly faced to each other (Figure 2.11-a). The distance between the graphene layers are increased to some extent due to lithium intercalation (10.3% in LiC_6). $\alpha\alpha$ is the order of stacking of the lithium inter-layers (a chain of Li-C₆-Li- C₆-Li alongside the c-axis). In the LiC_6 the lithium is scattered in such a way that it avoids the occupation of the adjacent sites (Figure 2.11-b).

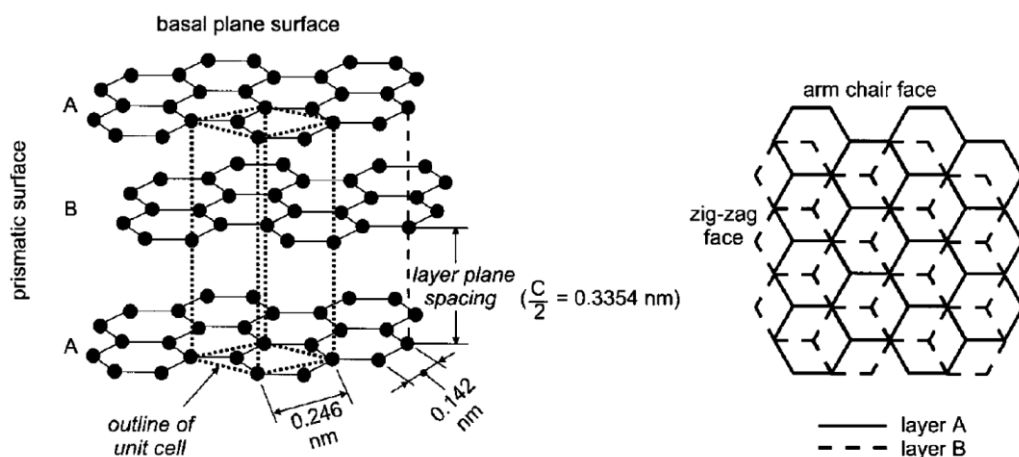


Figure 2.10 Left-side: The crystal structure of hexagonal graphite showing AB layer stacking order with the unit cell. Right-side: Perpendicular look at the basal plane of the hexagonal graphite layers. The prismatic surfaces may be further divided into armchair and zig-zag faces [15].

Theoretically, Li^+ intercalations are fully reversible into carbon. However, in practice the charge consumed in the first cycle significantly exceeds the theoretically stated specific charge of the first stage LiC_6 of 372 mAh g^{-1} compared to the mass of carbon (Figure 2.12). The subsequent deintercalation of Li^+ recovers only about 80-95% of this mentioned charge. During the second and subsequently following cycles, however, charge consumed because of Li^+ intercalations are lowered and recovery of the charge gets closer to fully charged state.

One of the main problems of carbon anodes is ageing. It might happen during shelving (e.g., impedance build-up, self-discharging) and could reduce the useful cycle life of these batteries, in addition to the defects and deteriorations which happen during active use (e.g., mechanically occurring degradations, plating of lithium metal). The ageing of batteries through time and usage causes changes (i) in the electrodes/on the electrolyte interfaces/the electrolytes, (ii) the active materials, and also (iii) in the compound electrodes (current collector, active materials, conductive additives, binder, porosity, etc.) [16].

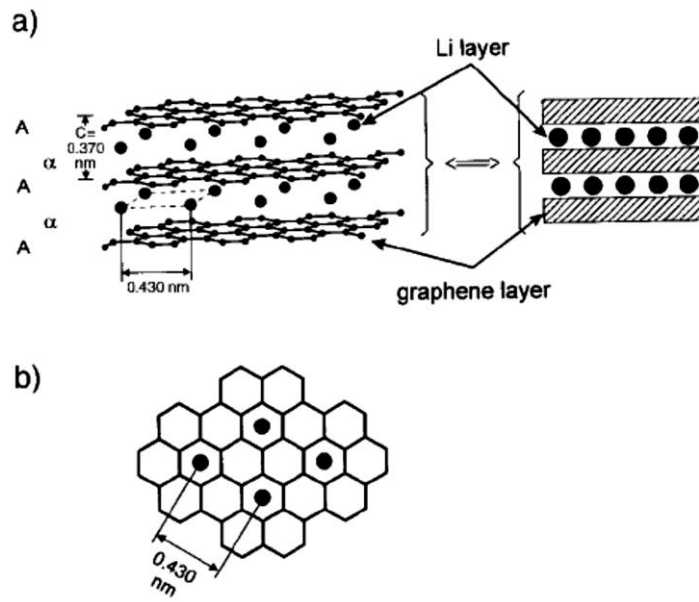


Figure 2.11 Schematic drawings of the structure of LiC₆. a) AA layer stacking order and the $\alpha\alpha$ interlayer sequencing of inserted lithium. b) Perpendicular view of the basal plane of LiC₆ [15].

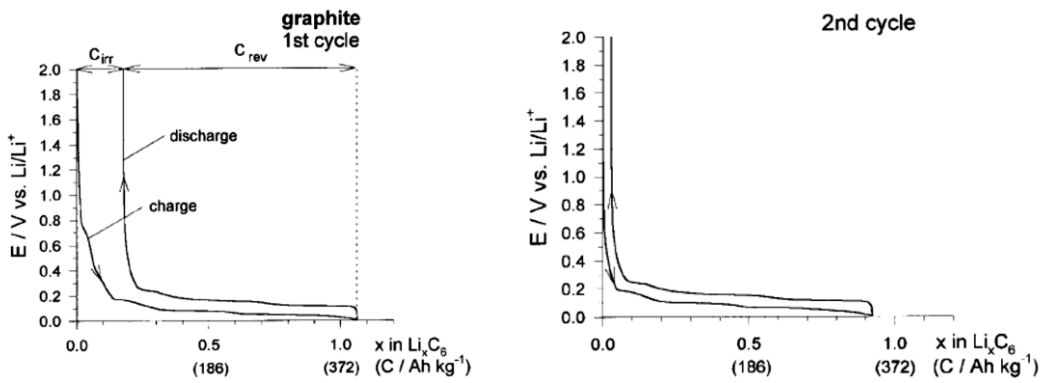


Figure 2.12 Constant current charge/discharge curves (1st and 2nd cycle) of the graphite Timrex KS 44 in the electrolyte LiN(SO₂CF₃)₂/ethylene carbonate/dimethyl carbonate (C_{rev} represents the reversible specific charge, C_{irr} represents the specific charge which is irreversible) [15].

The alterations of the electrodes and electrolyte interfaces due to reactions of anode with the electrolyte are shown in Figure 2.13. These reactions are the main source of aging of/at anode. The anodes of Lithium-ion batteries function at electrical potentials exceeding the electrochemically stable zones of their electrolyte components. Therefore, irreversible consumption of lithium ions occurs with the reductive electrolyte decomposition at the interface of the electrolytes while the electrode is polarized to low potentials in the charged state. The byproducts accumulate and form “protective layers” that insulate the electrode’s surface. This phenomenon significantly takes place in the first cycle, but also during the initial cycling phase. Here, these protective layers have to behave in such a manner that it is called "solid electrolyte inter-phase", SEI, which is permeable to lithium cations but highly impermeable to different components of the electrolyte and electrons. Significantly decreases (i) further reduction of the electrolyte compounds and also(ii) the corrosion of charged electrodes. [16].

Film formation takes place on metallic Li upon contact with the electrolyte on Li_xC_6 surfaces as a charge-consuming reaction in the first few Li^+ intercalation/deintercalation cycles. This reaction happens mostly during the first cycle as mentioned before. Even after the formation of these films, the self-discharge rates in Li_xC_6 electrodes are considerably high because of the reactivity of Li_xC_6 with the organic electrolyte.

The solvated intercalation of lithium into carbon electrodes is a serious problem. Particularly in the initial cycles, before the formation of these protective films on Li_xC_6 are finished, there is a high tendency for solvent co-intercalation. Moreover, owing to the self-discharge of Li_xC_6 , the SEI film on the carbon electrode grows, thus increasing the internal resistance of the cell. Therefore, the power density of lithium ion cells with carbonaceous negative electrodes gradually decreases with the number of cycles.

Various researchers have focused on the development of these "protective films" and the tried to suppress solvent co-intercalation. This was tested either choosing potentially proper electrolyte components or by pre-conditioning the carbon

electrodes. Significant improvements have been achieved by adding inorganic components to the base electrolyte, for example CO_2 , N_2O , SO_2 , and S_x^{2-} . The additives promoted more compact and probably thinned inorganic films, which allow the selective penetration of unsolvated Li^+ cations. Films formed from organic decomposition compounds were supposedly easily penetrated by the organic solvent molecules.[15, 16].

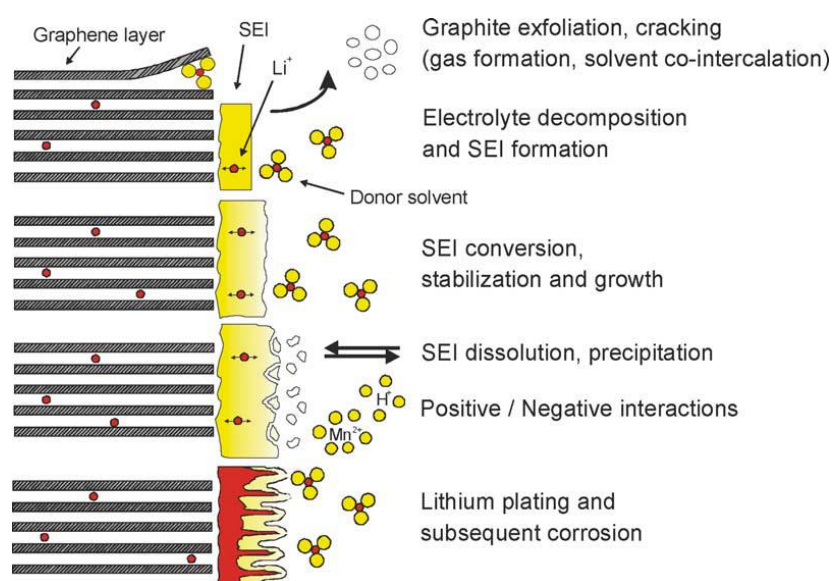


Figure 2.13 Changes at the anode/electrolyte interface [16].

2.3.5 Lithium Alloys as Anode Materials

Because there is a high demand for safe Li-ion batteries with high power capacities, high output, and high rate capabilities are improved daily, researchers worldwide have investigated various electrode materials in order to develop better materials. Li has the ability to alloy and de-alloy with other metals electrochemically even at room temperatures in an organic electrolyte. For the past few decades, Li-alloying reactions with metallic or semi-metallic elements (e.g., Sn, Sb, Al, Si, Ge, Pb, P, As, Bi, Au, In, Ga, Zn, Cd, Ag, Mg and their alloys) and various compounds have been investigated (Figure 2.16). Even though these alloying materials can provide a better specific

capacity than graphite (except some transition metal oxides, see Figure 2.7), they usually lack in irreversible capacity at the first cycle and unimpressive cycling life because of significant damages stemming from huge volume changes during cycling. That is why materials to manufacture anode alloys with high capacities (with respect to graphite) are still studied. But many have been unsuccessful to create commercially feasible products due to failed capacity retention after cycling or due to phase transformations and/or huge volume expansion related electrode cracking and pulverization problems after repeated Li alloying–dealloying. In other words, the more the host anode material accommodates Li, the worse the mechanical degradation issues and hence, the larger the volume expansion and with perpetual cycling [17, 18].

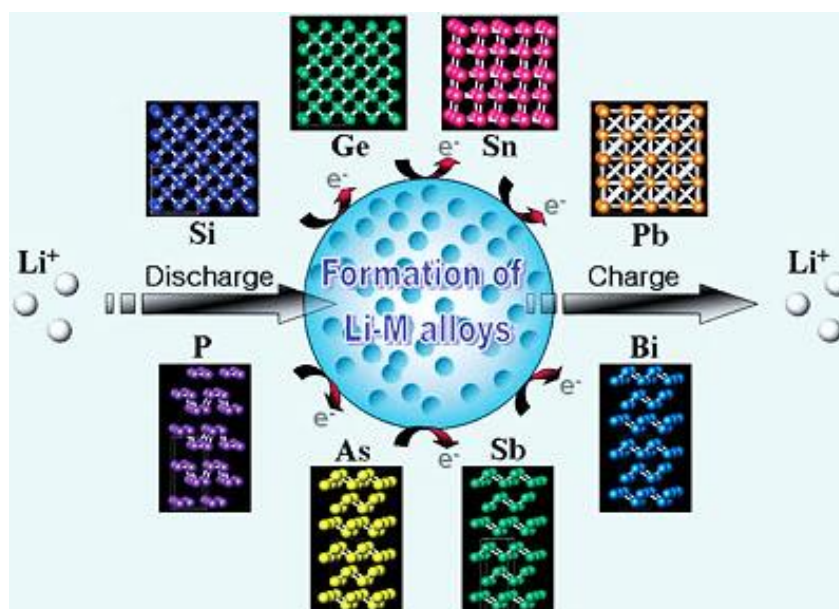


Figure 2.14 Different alloying metals for lithium [18].

Amongst other metals, Sn and Si seem to be the most promising anode materials as alternatives to graphite thanks to their high specific capacities (993 mAh g^{-1} for $\text{Li}_{4.4}\text{Sn}$ and 4200 mAh g^{-1} for $\text{Li}_{4.4}\text{Si}$) and decent operating electrochemical potentials (Sn: 0.5-0.6 V and Si: 0.3 V vs. Li^+/Li) [19].

In this study work, the aim was to produce new generation silicon anode materials, thus a detailed literature review on silicon anodes will be given in the below section.

2.3.5.1 Silicon Anodes

Silicon is a strong anode material alternative to graphite in terms of its high energy and power capacity. It has other properties like being cheap, abundant and environmentally safe; this makes it unique for research studies.

Silicon anodes have received lots of interest because of the fact that a single atom of silicon can accommodate 4.4 lithium atoms, forming $\text{Li}_{22}\text{Si}_5$. As a result, silicon has the highest theoretical capacity (4200 mAh.g^{-1}) of any alloying element and attractive operating voltage ($\sim 0.3\text{V}$ vs versus Li/Li^+) (Figure 2.15). This means that silicon anodes could possibly have over ten times the gravimetric capacity with respect to graphite based anodes.

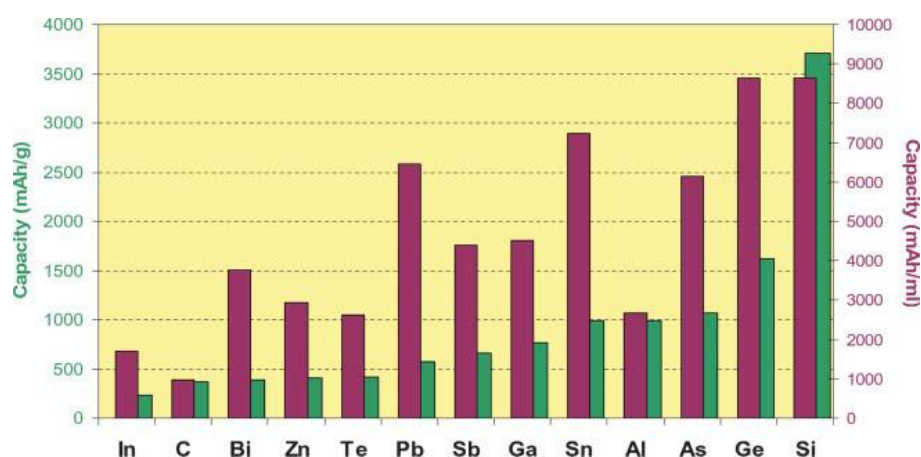


Figure 2.15 Gravimetric/volumetric capacity graph for some alloying reactions. Capacities are given in comparison with graphite as a reference[20]

On the other hand, the insertion of 4.4 lithium atoms per silicon atom has some cons. The full lithiation of silicon results in a 400 % increase in volume from cubic silicon

(20.0 \AA^3 per silicon atom) to cubic $\text{Li}_{22}\text{Si}_5$ (82.4 \AA^3 per silicon atom) [21]. This drastic volume change causes diffusion-induced stress, which may lead to fragmentation, disintegration due to fractures and bonding problems of the current collectors with active materials. It also damages the solid-electrolyte interface (SEI) which protects electrodes from further deterioration. The degradation and loss of electrical conductivity lead to significant losses in capacity and hence, poor cycle performance (Figure 2.16) [22]. Many approaches have been proposed to overcome these problems of silicon based anode materials.

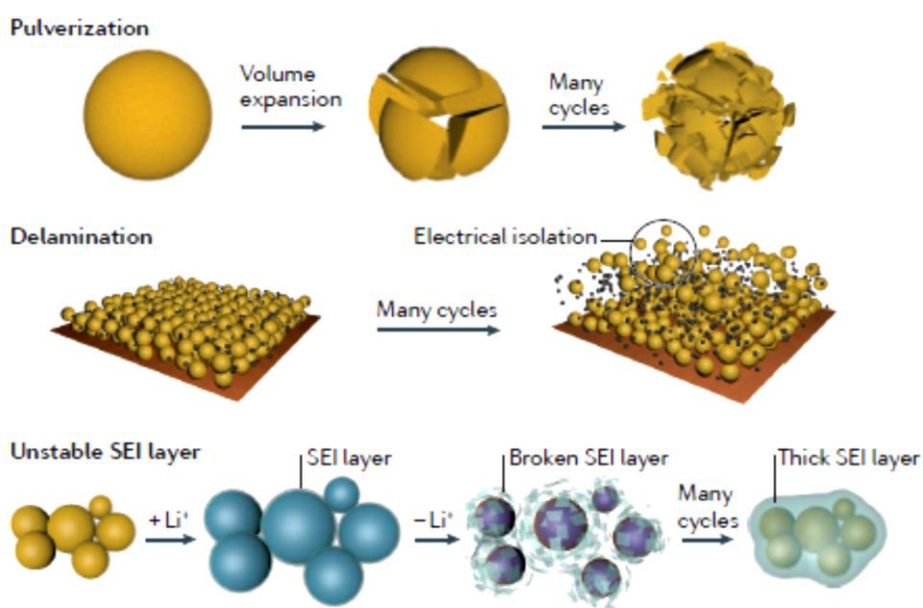


Figure 2.16 Main degradation mechanisms of Si anodes stemming from the large volume expansion of Si during lithiation process[23].

The general strategies of creating silicon-based anode materials with good cycle performance can be categorized as follows: (i) controlling the structure and morphology (e.g. minimization of particle size or creating a hollow nanostructure which has a small volume to limit the volumetric expansion) (Figure 2.17-a), (ii) active or inactive matrix compositing (also prevents aggregation) (Figure 2.17 b-c), (iii)

blending with various binders (e.g. elastomeric binders which expands during lithiation and shrinks during delithiation process) (Figure 2.17-d), (iv) controlling of the cycling voltage window, (v) use of different salts such as LiFSI and introduction of electrolyte additives, such as vinylene carbonate (VC) to form a more stable SEI [23, 24].

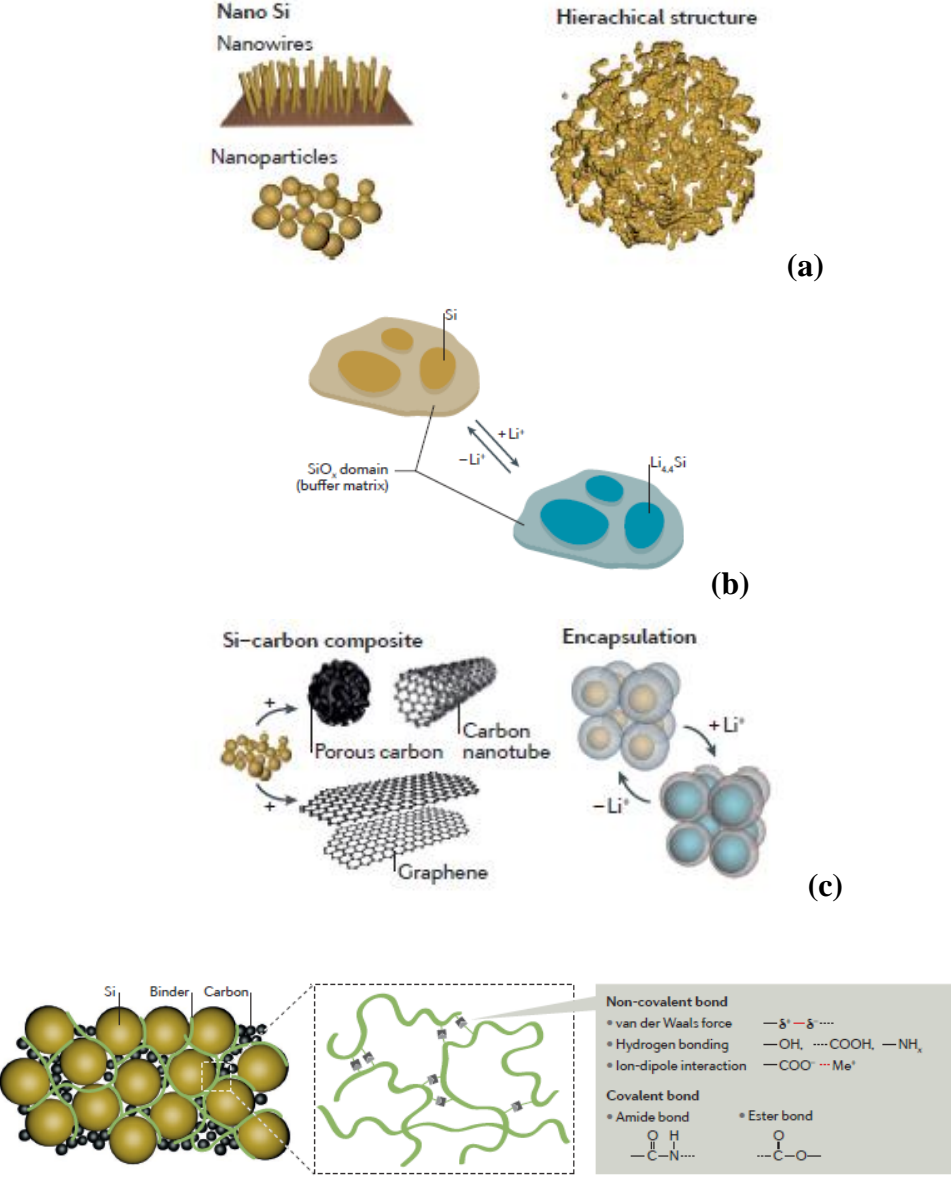


Figure 2.17 Examples of various types of Si-based anode material production strategies; (a) various morphologies of Si-active materials and their composites. (b) reversible lithiation–delithiation process of SiOx (c) compositing (d) Various binder concepts for Si anodes. SEI, solid electrolyte interphase [23].

Some researchers have been able to attain specific capacity of 1400 and 1000 mAh g⁻¹ at 1/4 C and 1/2 C after 200 cycles [25]. Through the use of silicon nanoparticles, gravimetric capacities close to the theoretical limit have been acquired. For example, Kim *et al.* claimed a capacity of 3380 mAh.g⁻¹ with a coulombic efficiency of 80% through the use of silicon nanoparticles with the size of <10 nm [26].

Huang *et al.* worked on the effect of elastic binders. They compared binders of LA132 (whose major co-polymerization chain is polyacrylonitrile-polyacrylic acid (PAN-PAA)) and polyacrylic acid (PAA) with a commercial PVDF binder. SiO_x powder was used as anode active material. The electrochemical tests showed that SiO_x-PAA delivered 1090 mAh.g⁻¹ discharge capacity after 50 cycles, whereas, PVDF could not lessen rapid capacity decay in the first ten cycles. The degree of crystallization of the binder improved the adhesion and strength of polymer. The low adhesion property of PVDF could not support large volume expansion of SiO_x due to its high crystallinity. Compared with SiO_x-PVDF, the capacity of SiO_x-LA132 decayed with twenty cycles and subsequently the decay gradually slowed down with more cycling tests [27].

Another research of interest is amorphous silicon usage, instead of crystalline silicon as the active anode material. Bourderau *et al.* worked on cycling behavior of amorphous silicon thin films (1.2 μm thick) depositing on the substrates of porous nickel by low pressure chemical vapor deposition using silane as the precursor gas. In the first three cycles they measured 1000 mAh.g⁻¹ discharge capacity, however, the films had insufficient results after 20 cycles which was due to mechanical damages on the electrodes. This was because of the severe active material loss during the electrochemical cycling, porous current collector was not capable to prevent these losses [28]. At another study, capacity decay of amorphous silicon thin films were overcome and the mechanical stability was preserved for more than 400 cycles by lowering the limit of the voltage window from 0 to 0.2 V. In this state their discharge capacity was about 400 mAh.g⁻¹ [29]

To summarize, the progress in advanced nanoscience and nanotechnology contributed to the improvement in cycle performance of silicon anodes. Yet, there is plenty room for improvement.

CHAPTER 3

GENERAL EXPERIMENTAL PROCEDURES

3.1 Materials used in the experiments

As-received silicon powder (Beijing Haoyun Industry Co. Ltd, -325 mesh, 99.99% purity) was used as the starting material at all the processes. Figure 3.1 shows particle size measurement of the powder.

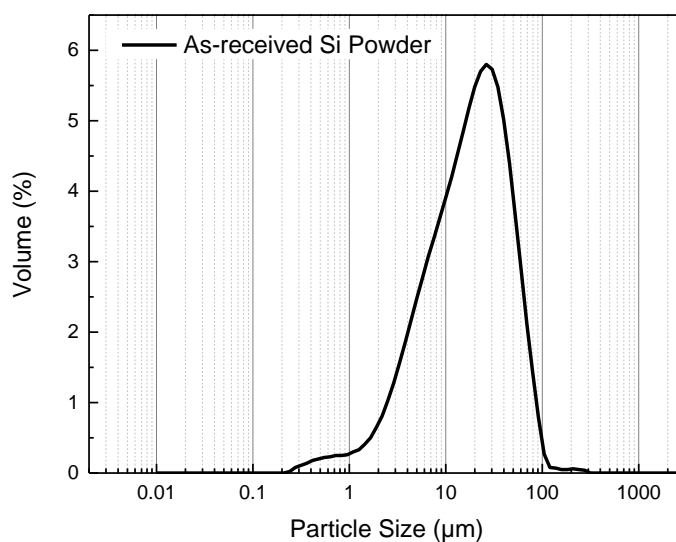


Figure 3.1 Particle size distribution graph of the as-received silicon powder

The surface area of the as-received powder was measured via Brunauer–Emmett–Teller (BET) technique. $2 \text{ m}^2 \cdot \text{g}^{-1}$ was the result of the measurement.

The above measurement shows that the average particle size of the powder is around 17 μm and ninety percent of the powders are smaller than 50 micrometer. In addition, SEM micrographs were taken. Figure 3.2 shows SEM images of the powder.

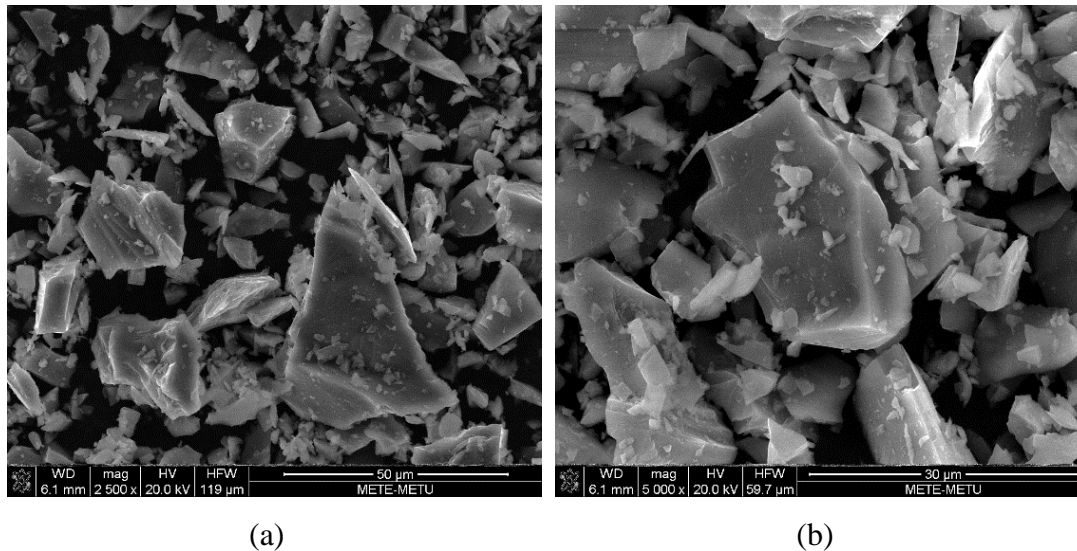


Figure 3.2 SEM images of the as-received silicon powder, (a) 2500X, (b) 5000X

To verify the purity of the purchased silicon powder XRD data was taken. Figure 3.3 shows the pattern. It is seen that all the peaks are belong to silicon element which has a diamond cubic crystal structure with a lattice spacing of 0.5435 nm (calculated with MAUD program). Its space group is Fd-3m (227).

Final investigation was X-ray photoelectron spectroscopy (XPS) (further explanation on XPS study is provided in section 3.3.1). The aim was to understand the surface properties of the as-received powder. Firstly, full spectrum (survey spectrum) test was done to see all the surface elements. It was observed that peaks for oxygen, silicon and carbon existed at the atomic ratios of 61.2, 30.3 8.4, respectively. After that, a high resolution scan was applied to the silicon spectrum to understand binding states. Figure 3.4 shows the XPS spectrum of the as-received silicon powder. Before beginning the process of peak identification, the peak shifting due to specimen charging was

corrected by taking reference of C 1s peak as 285 eV. Two distinct peaks appeared at the Si 2p spectrum. One is at the 98.85 eV and other one is at the 103.4 eV. At the XPS data, Si-Si bonds is located at around 99.4 eV however, overlapping of Si 2p_{3/2} and 2p_{1/2} components, possible existing impurities, environmental effects during test conditions could have caused this shift. Second peak is due to +4 oxidation state and this shows that there is SiO₂ structure existent. Surface native oxide is a necessary film layer for the passivation of silicon from further oxidizing. During preparation for some cases, to eliminate this oxide layer, the sample was washed with hydrofluoric acid.

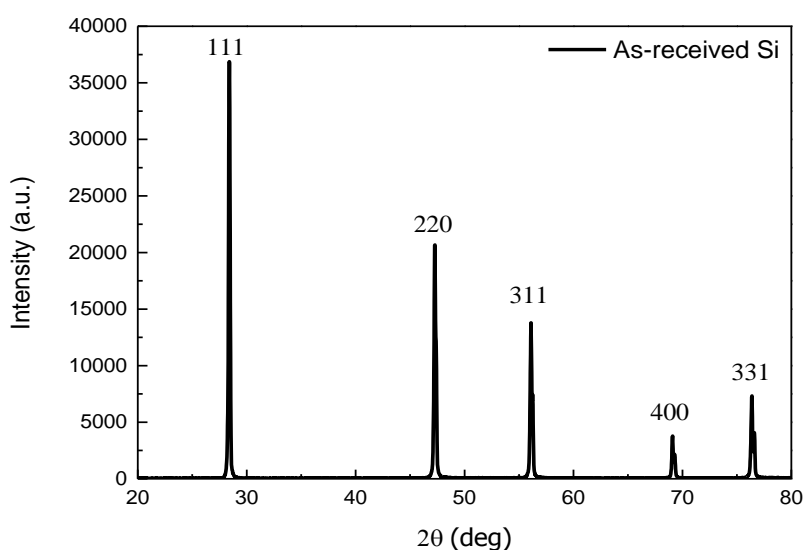


Figure 3.3 XRD pattern of as-received silicon powder.

3.2 Experimental Methods

3.2.1 Ball-milling:

In this study, planetary ball-milling system (PM 400, RETSCH Retsch GmbH, Germany) was chosen to reduce particle size of the as-received silicon powder. As grinding media, tungsten carbide was used in order to decrease contamination from walls and balls. Volume of the jar was 250 ml. Milling medium was ethanol and its volume was set to a certain value, because, it was shown that increasing the volume of

the medium changes the ball milling effect. Such that, viscosity of the slurry and temperature control is dependent on it [30]. So, a standard amount of medium (50 ml per charge) for 250 ml jar was used during ball milling experiments. 10 and 5 mm ball sizes were used for the experiments. After that point, an experimental matrix was derived in such a way that effects of weight ratio of balls to powder, rotational speed, milling time and mill charge on average particle size were tabulated. Table 3.1 shows the experimental matrix of ball milling trials. The effect of a single parameters' variance on the particle size reduction was studied in each experiment.

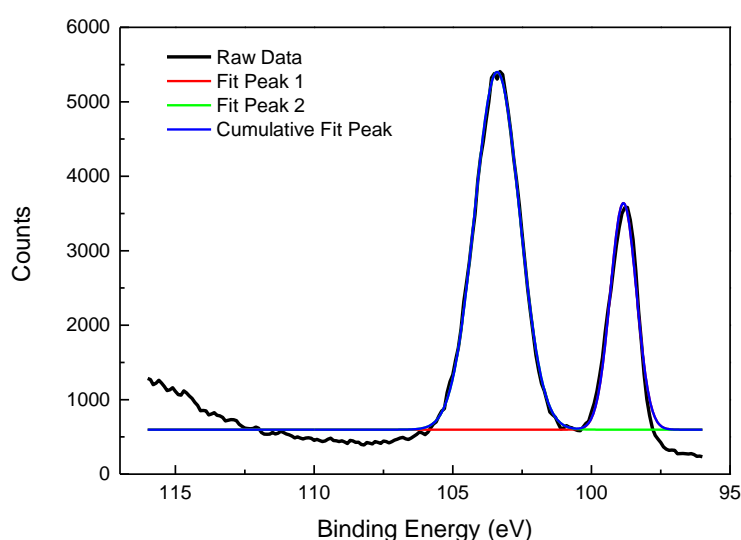


Figure 3.4 XPS spectrum of the as-received silicon powder.

Table 3.1: The experimental matrix of ball milling trials.

Balls size (mm)	Weight ratio of Balls to Powder	Rotational Speed (rpm)	Milling Time (Hours)	Mill Charge (vol%)
10	10:1	75	24	100
5	15:1	150	36	60
	27:1	250	48	30
		350		

3.2.2 Metal Assisted Chemical Etching

To produce multi-dimensional silicon powder, two-step metal assisted chemical etching method was applied. Names and properties of the used materials are as follows: Silver nitrate (AgNO_3 , 99+%, Alfa Aesar, Germany), hydrofluoric acid (HF, 38-40%, extra pure, Merck KGaA., Germany), hydrogen peroxide (H_2O_2 , 30% stabilized, Merck KGaA., Germany), nitric acid (HNO_3 , 65%, Merck KGaA., USA).

Before the etching, silicon powder is always washed with 10% hydrofluoric acid for ten minutes to remove silicon oxide from the surface of the powder. Then, Si powder was immersed in an AgNO_3 and HF containing solution for a controlled time to deposit Ag nanoparticles onto the Si surfaces. Subsequently, powder is washed with deionized (DI) water to remove silver salts. Silver deposited Si powder, then, was immersed into the etching solution, which contains HF and H_2O_2 as oxidizing agents. After etching Ag was removed in concentrated nitric acid. After removal of Ag, powder is washed with DI water and dried at 70 °C. By controlling the amounts of AgNO_3 , HF, oxidizing agents, dwelling time and temperatures, different types of structures were obtained during experimental studies. Details of the experiments and obtained results will be given in Section 5.3.

3.2.3 Thermal Plasma Synthesis

The solid state method was chosen for nano-sized silicon powder production. Starting material was as-received silicon and methane gas (CH_4) was used for carbon encapsulation. The Tekna Plasma Systems Inc PL-35 Plasma Torch system was used. Induction plasma system was operated at 25 kW under 0.97 bar pressure and typical duration of the production runs lasted 10–15 minutes. The silicon powder-feeding rate was 2-3 g/min, it was not possible to feed more precisely because of the irregularities in the shape of the precursor powders and with a methane flow rate of 1 l.min⁻¹.

Prior to the ignition of plasma, the reactor system was evacuated with argon gas at 60 slpm. After the ignition process, the flow of hydrogen was gradually increased to 6 slpm. In addition, nitrogen gas was used for quenching with flow rate of 150 slpm. The synthesized Si powder was collected from powder collector at the end of the test (Figure 3.5). Figure 3.6 was given to show illustration of the torch in detail.

3.2.4 Sol-Gel Coating

Table 3.2 provides the used sources, the information from where they were taken, the chemical formulas and abbreviations that are used to make ease to tell experimental method which were given in.

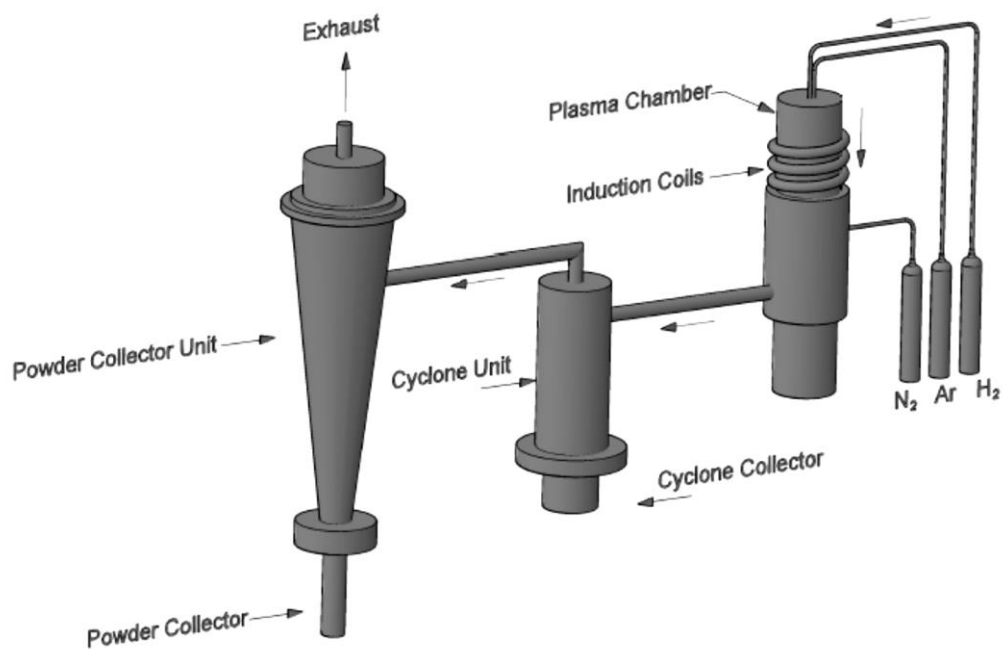


Figure 3.5 Simple schematic of the induction plasma system.

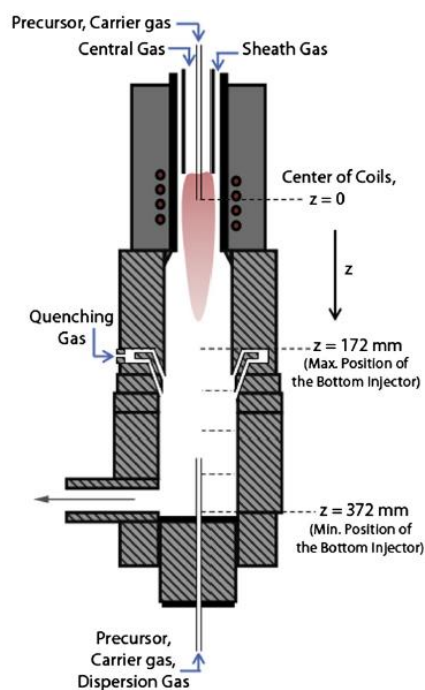


Figure 3.6 Schematic illustration of the torch [31]

Table 3.2 The information about the precursor materials used for sol-gel coatings.

Source	Chemical Formula	Abbreviation	Company	Formula Weight (g/mol)
Li source	LiNO_3	LiN	Merck	68.95
PO₄ source (for Li₃PO₄)	H_3PO_4 (85%)	HP	Merck	97.99
V source	NH_4VO_3 (99% min)	AmV	Alfa Aesar	116.98
W source	$(\text{NH}_4)_6\text{W}_{12}\text{O}_{39} \cdot x\text{H}_2\text{O}$	AmW	Alfa Aesar	2938.41
Mn source	$\text{MnN}_2\text{O}_6 \cdot 4\text{H}_2\text{O}$	MnN	Alfa Aesar	251.01
Zr source	$\text{Zr}(\text{SO}_4)_2 \cdot 4\text{H}_2\text{O}$ (98+%)	ZrS	Alfa Aesar	355.41
PO₄ source (for ZrP₂O₇)	$(\text{NH}_4)\text{H}_2\text{PO}_4$	AmP	Merck	115.02

Sol-gel coating was done in two steps. Firstly, gels were produced and after then powders were coated with appropriate amount of gel. After coating, calcination was conducted to obtain desired coating materials. XRD measurement and Rietveld analysis were done to understand obtained phases and quantitative ratios. At the sol preparation stage, the concentration of precursors was taken according to their molar ratios of the elements in the alloy. For example, to produce Lithium phosphate (Li_3PO_4) precursors of LP and HP were mixed in the molar ratio of 3:1. In addition to precursors, citric acid (citric acid monohydrate, $\text{C}_6\text{H}_8\text{O}_7 \cdot \text{H}_2\text{O}$, Sigma Aldrich, Co. LLC). and ethylene glycol (EG) (spectrophotometric grade, 99+%, Alfa Aesar, Germany) were used as complexing agents. Citric acid and metal source was used at the same molar ratio with 1:1 mol ratio. Ethylene glycol (EG) amount was taken constant for all batches and 3 ml was used every time. Experimental steps of sol-gel coating were as follows:

- i. 50 ml hot water was poured and citric acid was added to the water and stirred until completely dissolved.
- ii. First precursor material was added into the water and stirred until completely dissolved.
- iii. After clear solution was obtained, second precursor was added to the solution and stirred until complete dissolution.
- iv. Then EG was added to the solution and stirred at 130°C to evaporate water. This step was continued until 30 wt% of the beginning solution was remained. This solution was used to coat silicon powders. Before coating process, desired solution amount was calculated according to the remaining solution.
- v. To coat silicon powders, 1 g of silicon and calculated amount of solution was taken to mortar. They mixed with each other and a toothpaste like viscosity was aimed. Additional water was poured in to get the desired viscosity.
- vi. The paste was dried at 120°C over night and then taken into the oven for calcination.
- vii. Before calcination, dried mixture was first pre-calcined at 300°C . Calcination temperatures were adjusted to obtain pure phases. Many trials were done on sol-gel products before coating. After determining the required

temperatures, coating and calcinations were made. Table 3.3 gives the calcination temperatures, times and atmospheric conditions of coating materials.

Table 3.3 Properties of calcination steps for coating materials.

Coating Material	Calcination Temperature (°C)	Calcination Times (min)	Calcination Atmosphere
Li₃PO₄	600	180	Air
Li₃VO₄			
ZrV₂O₇			
MnWO₄	900	120	
ZrP₂O₇			

3.2.5 Carbon Coating

In addition to sol-gel coating of silicon powders, carbon coating; which has been studied widely in the literature, was also tried as part of this study. In the coating process, sucrose (C₁₂H₂₂O₁₁, 99%, Alfa Aeser, Germany) was used as carbon source. The reason for this is that sucrose is a cheap and readily found material whose coating process is also easy and quick.

In pyrolysis process, sucrose was dissolved in water and then powders were added to the medium and well stirred to obtain homogeneous coating. Subsequently, the solution was dried and the remainder was pyrolyzed at 650°C under Argon atmosphere. The only powder that was not coated with this method was the thermal plasma synthesized one. Because, base powder was already covered with carbon during the process for passivation of silicon powder.

Carbon contents' of the samples were measured by ELTRA CS 800 carbon sulfur determinator.

3.3 Characterization Techniques

3.3.1 Structural Characterization Techniques

To clearly understand the morphology of each produced silicon powder, observation using a field emission type scanning electron microscope (FE-SEM, Nova NanoSEM 430, FEI, Eindhoven, Netherlands) was made. To understand the morphology of etched and thermal plasma synthesized powders deeply, characterization by Transmission Electron microscopy (Jeol JEM-2100F UHR/HRP Transmission Electron Microscope (200 kV)) were done. For multidimensional silicon powders, Focused Ion Beam (UNAM, Bilkent) technique were also used to see porosity and columnar structures. Brunauer–Emmett–Teller (BET, MERLAB, METU) method was used to identify the surface area of all the powders. Particle size assessments were done on ball-milled powders. They were sonicated in ethanol as dispersant before the measurement. These measurements were done with the use of the laser diffraction particle size analyzer (Mastersizer 2000). To make these measurements, the particles were passed through a focused laser beam. These particles were said to be scattering coming light at an angle that is inversely proportional to their size. The angular intensities of these scattered lights are then measured by utilizing a series of photosensitive detectors. The provided map of this scattered intensity versus angle is the main informational source used to assess the particle sizes. X-Ray diffraction patterns were obtained by Bruker D8 Advance Diffractometer (Bruker Corporation, Billerica, USA) instrument with Cu_K α radiation. The method of Rietveld was applied to analyze the X-Ray datasets and to classify structures of their phases. Quantitative phase analysis and structural refinements (lattice parameters, atomic positions and occupancy) were achieved by running the MAUD program. The Raman spectrum of thermal plasma synthesized silicon was taken using the Renishaw inVia Raman spectrometer (MERLAB, METU) with 532 nm laser.

A detailed investigation on surface chemistry of the produced powders was done using X-ray photoelectron spectroscopy (XPS/ESCA) technique. XPS spectra are obtained by beaming a solid surface with a radiation of X-rays, simultaneously measuring the

kinetic energy of electrons that are emitted from the top 1-10 nm of the surface material. The analysis begins with producing a survey spectrum to see the existing surface elements. The energies and their intensities in the photoelectron peaks are used in identifying and counting of the existing surface elements of the sample material (except hydrogen). The photoelectron spectrum is registered via counting the ejected electrons through different electron kinetic energies. The peaks are then shown in the spectrum. The chemical states from an XPS spectrum is later assessed with a higher resolution scan.

In this study, the peak fit, for high resolution scans, was done with software to identify the different peaks which show different oxidation states of the studied element. Multiple peak fitting method was applied to fit multiple peaks into the original single peak which is assumed to be contributing to a shift or distortion in the peak. The values of the center of the peak and full width at half maximum (FWHM) were compared with NIST XPS library to find a resemblance.

3.3.2 Electrochemical Characterizations

Cyclic Voltammetry (CV), Galvanostatic tests and Electrochemical Impedance Spectroscopy (EIS) were done to the cells, which have the produced powders as anode materials. As anode, lithium foil was used for all the cells. For cathode preparation, powders were mixed with LA132 (Chengdu Indigo power sources CO., Ltd. Chengdu, Sichuan) aqueous binder, which is a new alternative to commercial binders like PVDF, CMC and SBR. The reason for choosing LA 132 as binder is because it is aqueous and does not need addition of thickeners like CMC and organic solvents such as NMP, besides; production process is simple, safe, and environmentally friendly. Besides, less binder is required during this process. Additionally, some recent studies showed that NCM cathode with LA132 binder exhibited a much higher specific capacity than cathodes made up with PVDF and CMC [32]. Silicon, binder and carbon black with the ratio of 75:20:5 was mixed. The slurries were stirred vigorously at the mixer mill (Retsch MM 400) in order to get uniform distribution of the active materials. Anode

slurry was coated on copper foil by using Doctor Blade technique. Thickness of the coating was adjusted to 200 μm . The coated sheets were dried at 80°C for a few hours and then pressed under 0.02MPa pressure. The discs with a diameter of 18 mm were cut from the previously produced electrodes were further dried in vacuum at 80°C for overnight. Then, the bunch were kept in a glove box (having 0.1 ppm O₂ and 0.1 ppm H₂O) and waited there assembly time. During the assembly process, as separator a glass microfiber filter (GE Healthcare Life Sciences) was utilized. The used electrolyte was 1 M of LiPF₆ in a 50:50 EC:DEC solution. Airtight cells were utilized and assembly was done in the glove box.

Solartron 1470 potentiostat was used for both galvanostatic tests and cyclic voltammetry. On the other hand, to measure electrochemical impedance spectroscopy Versastat III was used.

3.3.2.1 Cyclic Voltammetry (CV)

From high potential to low potential, in cathodic direction, the first scan was done. At the first scan, CV was applied at a rate of 0.01 mV.s⁻¹ between 0.01 and 1.2 V. The CV tests were started at the charged state.

3.3.2.2 Galvanostatic (Charge-Discharge) Tests

During charge-discharge cycles, a rate of 0.2 mA.cm⁻² were used. The cells were then cycled 20 times to see the cyclic performance of anodes. The charge-discharge tests were conducted between 0.05 to 1.2 V. For all samples, following the CV tests, precycling was performed with four cycles where the batteries were discharged successively for 5, 10, 15 hours and charged up to 1.2 V. After the last charging, cell was fully discharged. Before going back to the cycle tests EIS was applied to the cells.

3.3.2.3 Electrochemical Impedance Spectroscopy (EIS)

Between the 10 mHz and 100 kHz frequency ranges, at the open circuit potential (OCV) of the cells Potentiostatic EIS was applied. The AC amplitude was $\pm 5 \text{ mV.s}^{-1}$. EIS was applied at the discharged state at the end of activation procedure. The main purpose was to understand the effect of production methods on resistivity of different silicon anodes. Equivalent circuit of an electrode was consisted from surface layer (film) resistance (R_{sf}), charge transfer resistance (R_{ct}), electrolyte resistance (R_{el}), constant phase element for surface layer (Φ_{sei} or Φ_s) and double layer (Φ_{dl}) and resistance due to the diffusion of Li through the Si (R_{diff}). Electrical circuit models used in this study are:

1. LR(QR)(Q(RW)) (Figure 3.7)
2. R(QR)(QR)(QR)W

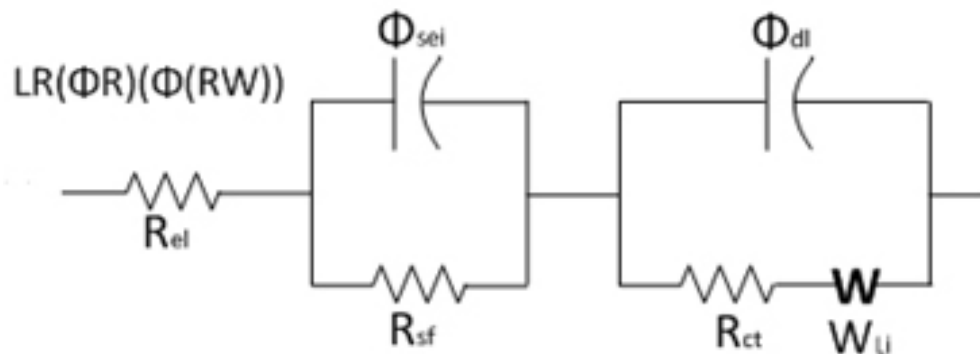


Figure 3.7 Schematic of equivalent circuit model for this study.

CHAPTER 4

PLANETARY BALL-MILLING

4.1 Introduction

Ball-milling is a cheap and efficient top-down method for sub-micron or nano-structured particle production [30]. The process can be described as the mechanical wear and break off larger particles into smaller particles by milling. This process provides particles of certain size and shapes without actually changing their state of aggregation. There are several types of mills utilizing balls as milling media with varying motion and rotation patterns. Figure 4.1 shows some of the different types of mills and Figure 4.2 shows the motion types in a ball mill [33].

The name of the planetary ball mill comes from its movement of vials. The centrifugal forces act in alternating like and opposite directions while the vials and the supporting disc rotate in the opposite directions. This runs down the milling balls towards the inside wall of the vial, creating friction effects, causing the material being milled against the inner walls and milling balls wandering randomly inside the milling chamber of the vial and pushing the material against the walls. Planetary mills make use of the centrifugal acceleration forces instead of gravitational acceleration. The improvement in milling action comes from the fact that the combined action of two centrifugal fields is utilized on the balls in contrast to the conventional ball milling. The mill charge is a combined effect of two motions, first a rotary motion around the mill axis and second a planetary motion around the vial axis. (Fig. 4.3). The advantage of planetary mills is their high energy density, which is 100-1000 times higher than

the conventional mills. This makes possible to obtain sub-micron structures with reduced times [33, 34].

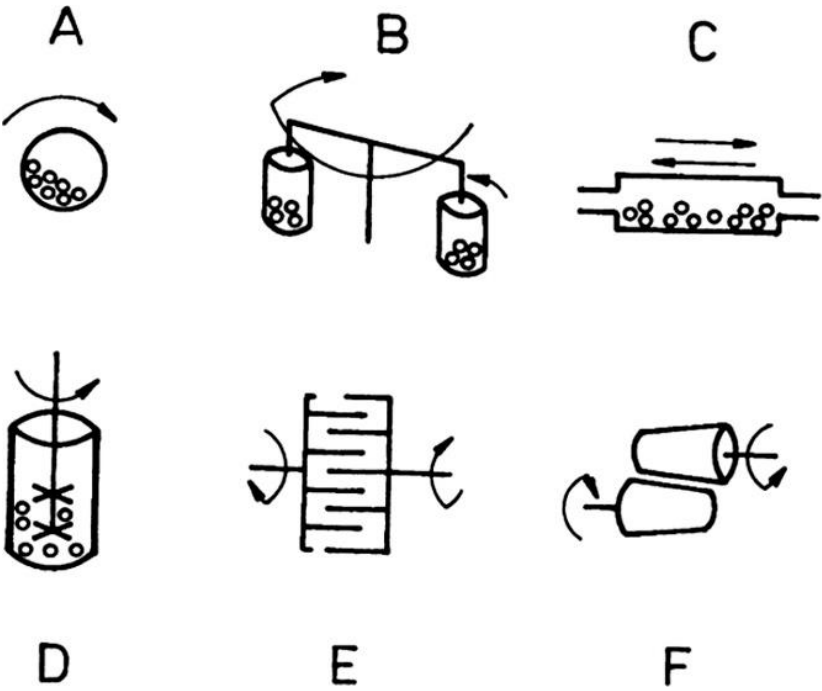


Figure 4.1 High energy milling types (A) Ball milling, (B) Planetary milling, (C) Vibrational milling, (D) Attritor-stirring milling, (E) Pin milling, (F) Rolling milling [33]

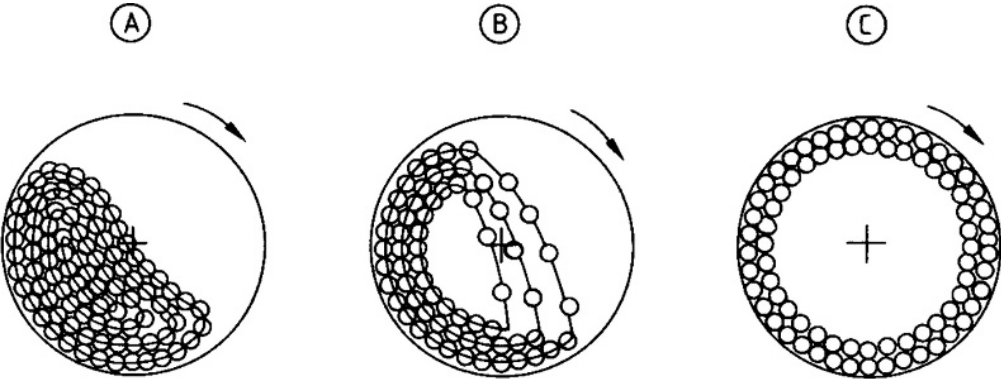


Figure 4.2 Motions inside a ball mill: (A) Cascading motion, (B) Falling or cataracting motions, (C) Centrifugal motion [33]

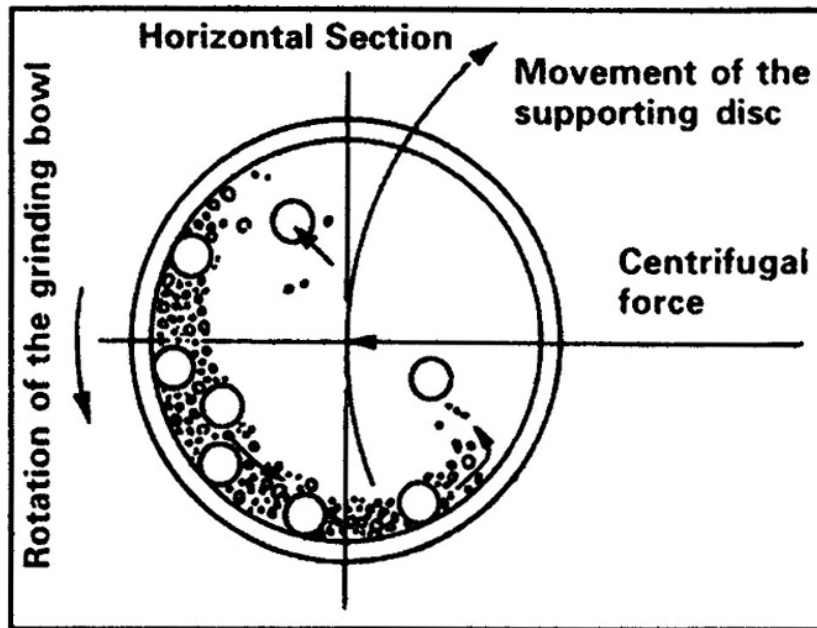


Figure 4.3 Directions of the movement of working parts and balls in a planetary mill [33]

Although the milling process has benefits, it also has some weaknesses. Such as, contamination from the balls and milling chamber, amorphization, agglomeration and aggregation due to surface, highly polydisperse size distribution of as-prepared powders. Therefore, to obtain high surface area silicon particles, careful selection of milling parameters is important. The variables that influence the milling process most are the material of milling media, weight ratio of balls to powder, balls size, types of milling medium, rotational speed and milling time [30, 35].

Yim, Chae-Ho et al. used high-energy ball-milling technique to decrease the particle sizes of their as-purchased powder (325 mesh). When they applied 200 hours milling, final particle size were reached to $0.73 \mu\text{m}$ and surface area became $18.3 \text{ m}^2.\text{g}^{-1}$. Their XRD results showed that crystal structure of the powder turned to amorphous which is kinetically and structurally more favorable than crystalline Si. By using only 5 wt% silicon powder in addition to graphite, they reached to the capacity of 524 mAh.g^{-1} after 350 cycles at C/12 rate with the binder of polyetherimide (PEI). This capacity is 1.6 times higher than the commercial graphite anode [36].

4.2 Results & discussion of ball-milling studies of silicon powder

Before the production of the powders, an experimental matrix was first generated as given in section 3.2.1. Findings of the 10 mm experiments were compared with the results of 5 mm balls. After making the decision of the best milling parameters, it is then switched to the production of sub-micron structured powder for lithium ion battery anode production. To build the best parameters for ball-milled powder, particle size measurements and SEM micrographs were used (the sample was examined with the use of a microscope; it was a critical step to verify the results from the particle size analysis).

After finalizing the milling parameters; in order to understand the whole characteristics of ball-milled powder, XRD, BET and XPS techniques were also applied before coating of powders. Results of these analyses will be given at the Section 4.3.

Particle size and SEM micrograph of as-received powder were given at Figure 3.1 and 3.2 at Chapter 3. Particle size reduction studies first begin with rotational speed trials. Four different speeds were tried for 24 hours time. Figure 4.4 shows the effect of rotational speed on particle size. Weight ratio of balls to powder was set to 15:1. Mill charge was 100%.

According to the particle size measurement results, there is no correlation with rotational speed and particle size. The particle size distribution of 75 rpm is more diverse than other speeds, meaning, larger particles still exist in the structure (over micron-range particles). Another issue is that further increase of rotational speed beyond 150 rpm does not lead to a decrease in particle size. Size distribution becomes more segregated with speed increments. It is probably due to agglomeration problems. Increasing rotational speed could also increase the temperature and this causes diminishing of milling medium (ethanol) with time and increases the viscosity of the slurry. As mentioned in literature [30], media loss effects particle size reduction adversely. Comparing the rotational speeds for 10 mm balls showed that 150 rpm gave

the best median result. Fifty percent of the particles were less than 400 nm (See also Table 4.1). This phenomenon is also approved by SEM images. (Figure 4.5)

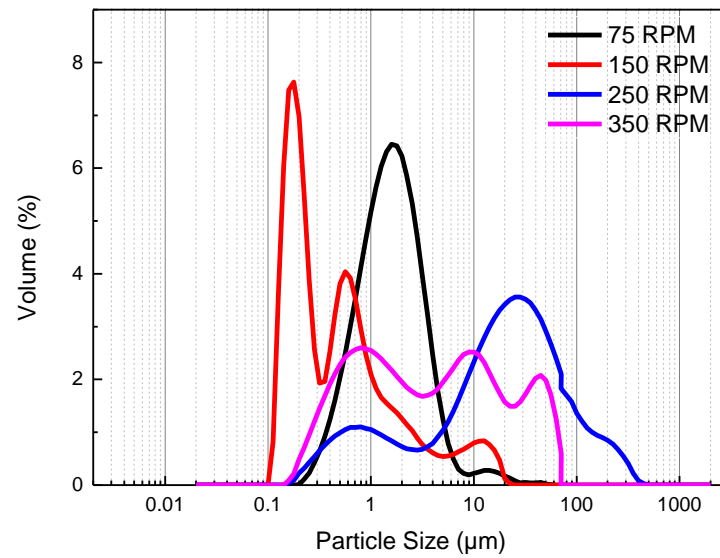
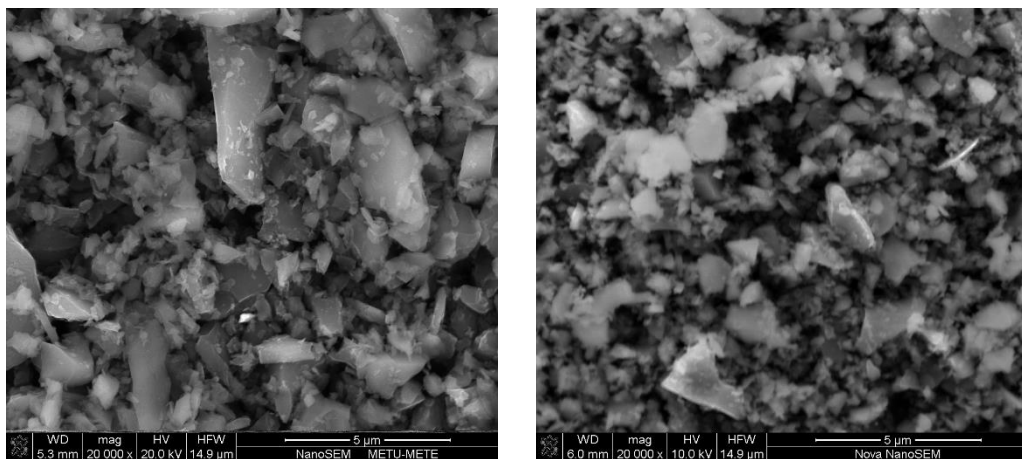


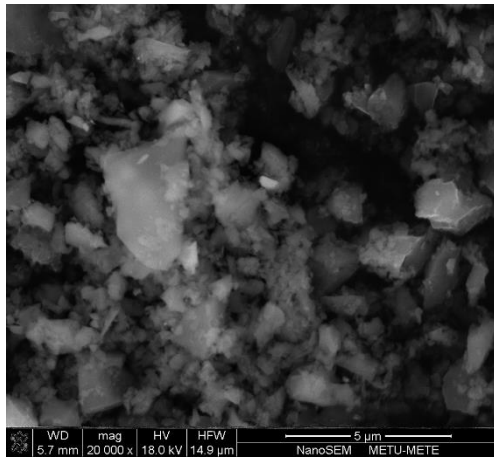
Figure 4.4 Comparison of effects of rotational speeds on particle size distribution: ball-milled powders with 10 mm balls, weight ratio of balls to powder 15:1 and mill charge 100%.



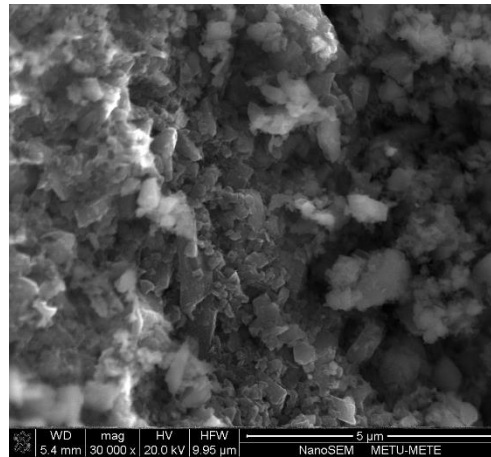
(a) 75 rpm

(b) 150 rpm

Figure 4.5 SEM images of ball milled powders with 10 mm balls and rotational speeds of (a) 75 rpm, (b) 150 rpm, (c) 250 rpm, (d) 350 rpm.



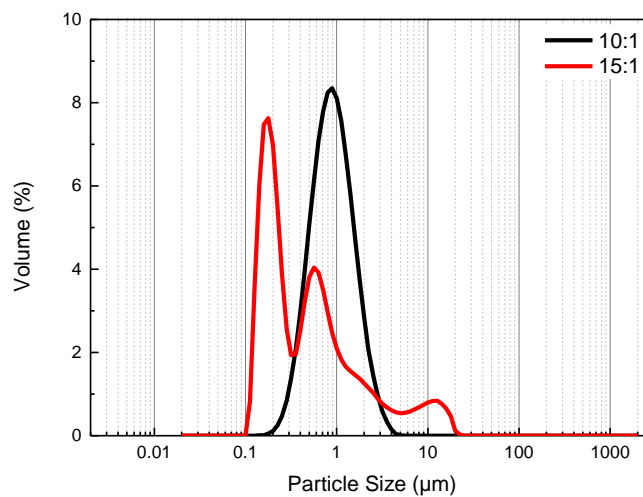
(c) 250 rpm



(d) 350 rpm

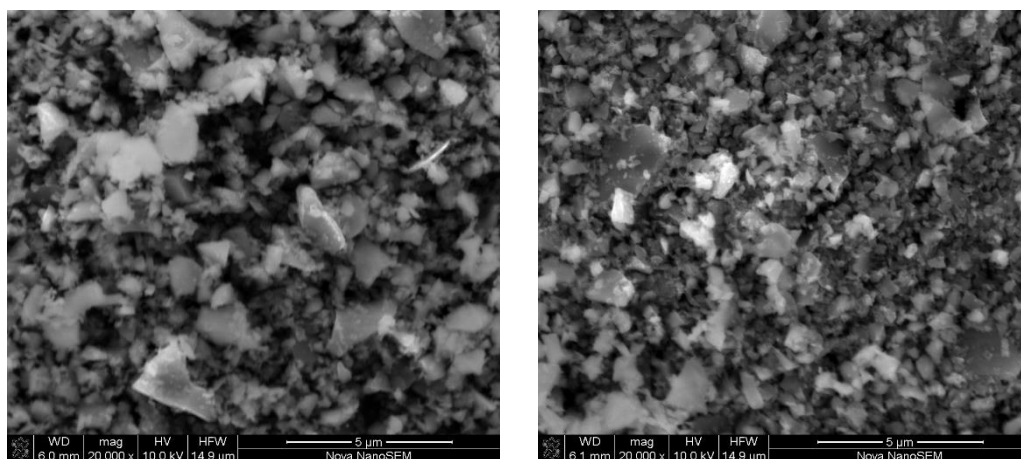
Figure 4.5 Cont'd.

Besides rotational speeds, effect of weight ratio of balls to powder was investigated. Rotational speed was fixed at 150 rpm and other parameters were kept constant for both batches. Figure 4.6 shows particle size distributions and Figure 4.7 gives the SEM images of these two powders, respectively.



(a)

Figure 4.6 Comparison of particle size distributions of ball milled powders with the weight ratios of 10:1 and 15:1 with 10 mm balls and mill charge 100%.



(c) 10:1

(d) 15:1

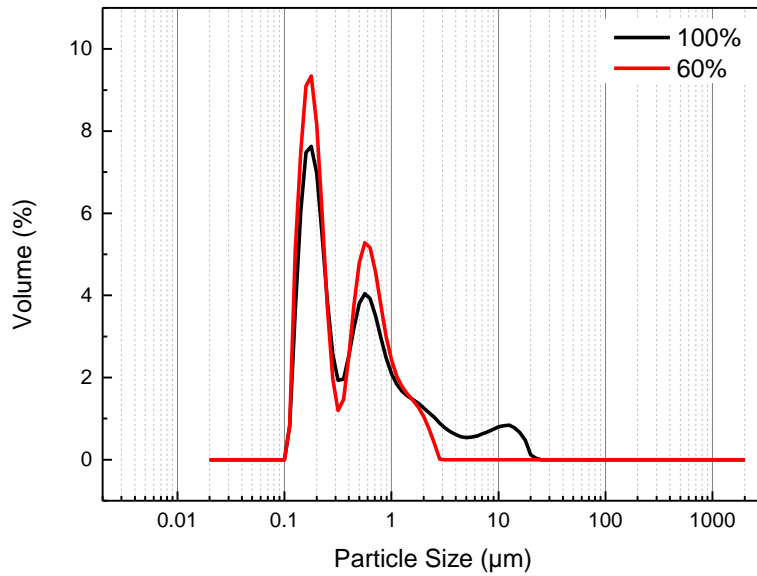
Figure 4.7 Comparison of SEM images of ball milled powders with the weight ratios of 10:1 and 15:1 with 10 mm balls and mill charge 100%.

Analysis showed that 15:1 weight ratio of ball to powder provides broader particle size distribution, on the other hand 10:1 had a homogeneous distribution and there was a shoulder over 10 micron for 15:1 ratio. Furthermore, fifty percent of the total particles were under 400 micron however for 10:1 ratio average particle size was bigger (0.836 vs 0.384 μm). So, after this point, experiments continued with 150 rpm rotational speed and 15:1 ball to powder weight ratio.

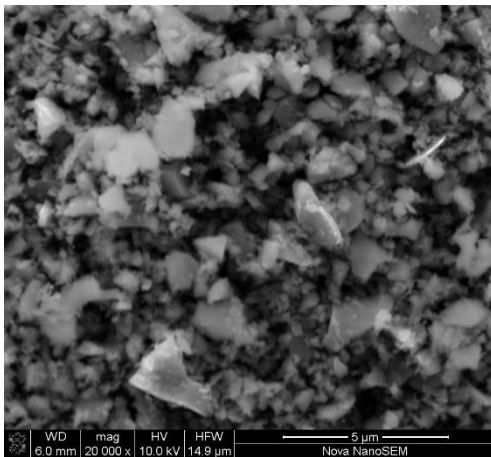
Mill charge was the next parameter to be considered for a) 60% charges and b) full charges. Comparison of particle size distribution clearly showed that lesser charge resulted in smaller median diameters; hence, 60% charges are significantly preferable. That is why; further experiments were continued with 60% charging. Figure 4.8 a, b, and c show particle size distributions and SEM images of these two powders respectively.

Next, three different milling durations were investigated (24, 36 and 48 hours). Figure 4.9 shows particle size distributions and Figure 4.10 shows the SEM images of these three powders. Analysis showed that milling times should be set carefully. The distribution graph shows that increasing the duration did not yield the expected result.

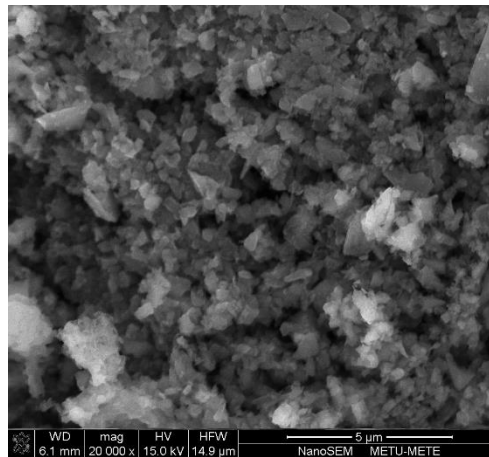
First reason was that ethanol evaporates when ball-milling temperature increases as time passes. This in return results in increased viscosity of the slurry. Another reason is the agglomeration problem. After reaching a critical size, due to high energy, particles start to stick back together.



(a)



(b) 100%



(c) 60%

Figure 4.8 (a) comparison of particle size distributions of ball-milled powders with mill charges of 60 and 100%, the weight ratios of 15:1, 10 mm balls, 150 rpm (b) Comparison of SEM images of these powders.

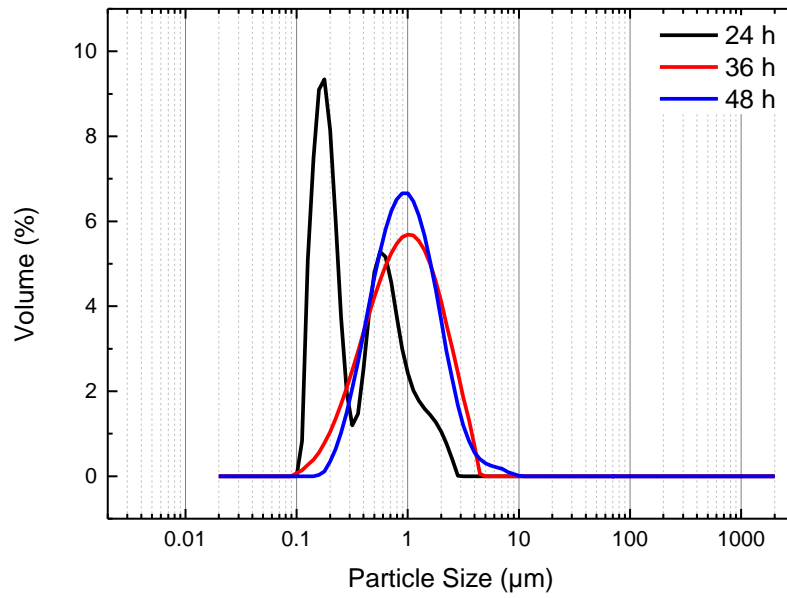
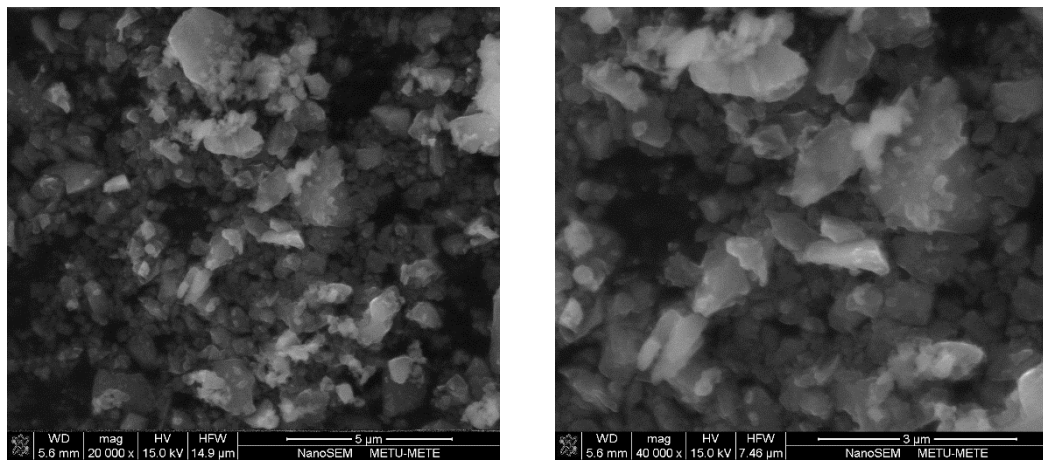
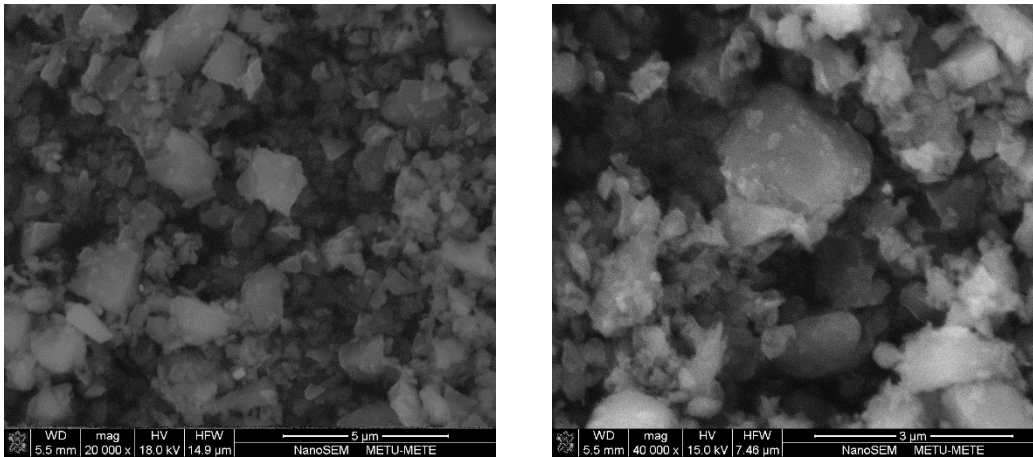


Figure 4.9 Effect of different milling durations on particle size distribution.

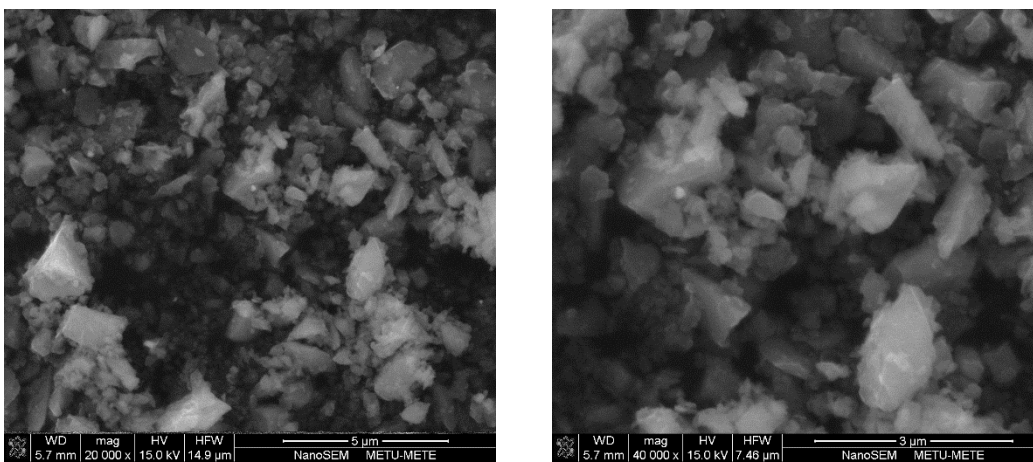


(b) 24 hours

Figure 4.10 Comparison of SEM images of ball-milled powders with milling times of 24, 36 and 48 hours, mill charge was 60%, the weight ratios of 15:1, 10 mm balls, 150 rpm.



(c) 36 hours



(d) 48 hours

Figure 4.10 Cont'd.

Table 4.1 reports the D10, D50, and D90 values based on volume distribution. After comparing average particle sizes and distribution characteristics it can be said that best results were obtained with 150 rpm, 15:1 weight ratio of balls to powder, sixty percent mill charge and minimum 24 hours time.

After studying ball-milling process and the effects of the parameters previously mentioned, a few more experiments were conducted for 5 mm ball diameter. Particle size distribution comparison graph was shown at Figure 4.11 and SEM images was shown at Figure 4.12 a-c, for 5 mm ball size. During these experiments, rotational speed and durations were increased to enhance the milling effect. Different mill

charges and weight ratio of ball to powder were also tried. Optimal rpm for these tests turned out to be 200 rpm as 36 hours duration gave the best results.

Table 4.1 The D10, D50, and D90 values based on volume distribution of all ball-milled powders.

Modified Process parameters	d(0,1)	d(0,5)	d(0,9)
75 rpm, 15:1, 100%, 24 h	0.570	1.461	3.502
150 rpm, 15:1, 100%, 24 h	0.141	0.384	3.214
250 rpm, 15:1, 100%, 24 h	0.783	18.466	89.984
350 rpm, 15:1, 100%, 24 h	0.429	3.468	34.811
150 rpm, 10:1, 100%, 24 h	0.422	0,836	1,693
150 rpm, 15:1, 60%, 24 h	0.135	0.254	1.020
150 rpm, 15:1, 60%, 36 h	0.305	0.873	2.196
150 rpm, 15:1, 60%, 48 h	0.377	0.878	2.070

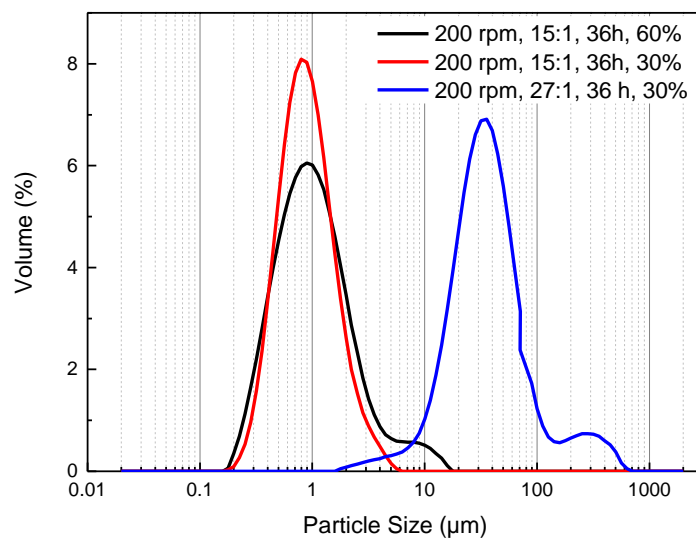
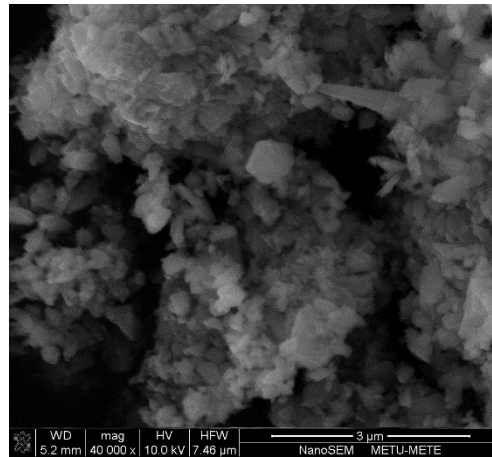
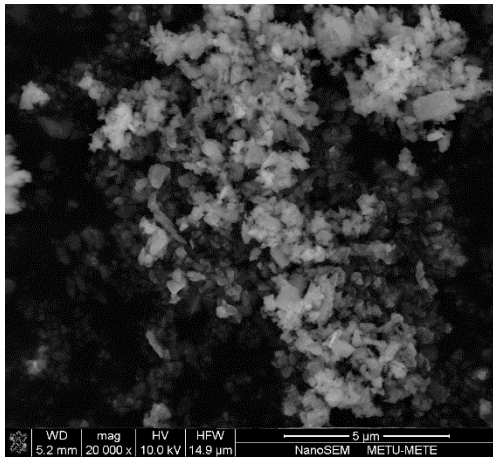
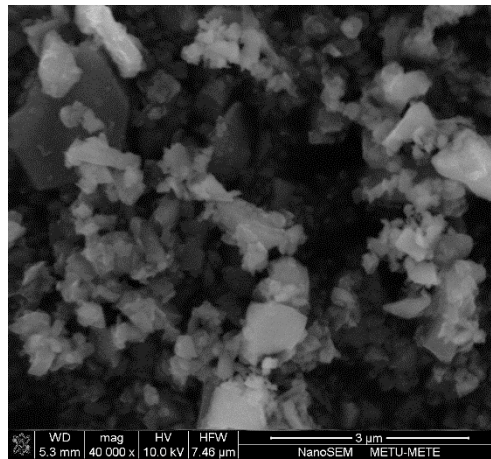
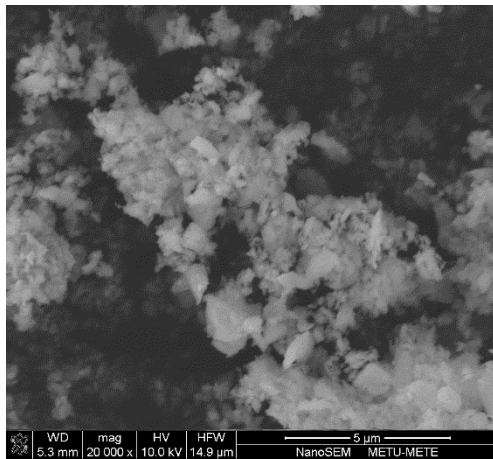


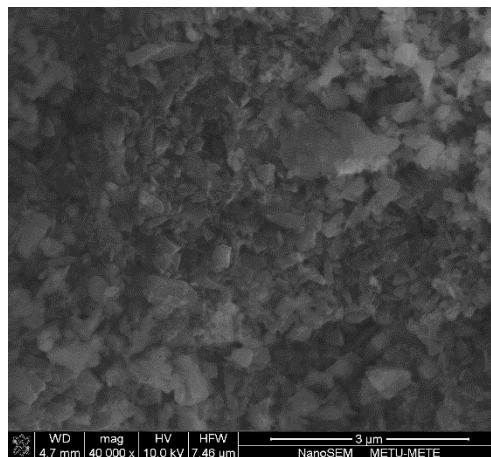
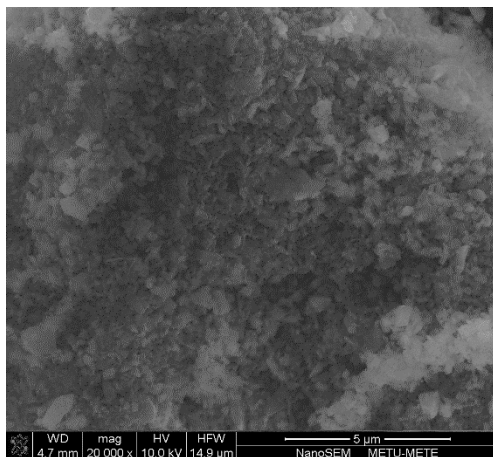
Figure 4.11 Comparison of particle size distributions of 5 mm ball.



(a) 200 rpm, 15:1, 36 h, 60%



(b) 200 rpm, 15:1, 36 h, 30%



(c) 200 rpm, 27:1, 36 h, 30%

Figure 4.12 SEM images of the samples milled with 5 mm ball size.

SEM images of 27:1 weight ratios of ball to powder clearly indicate an agglomeration problem. The other two did not propagate difference in particle size distribution. Table 4.2 gives the D10, D50 and D90 values of these three trials.

Table 4.2 The D10, D50, and D90 values based on volume distribution of all ball-milled powders.			
Modified Process parameters	d(0,1)	d(0,5)	d(0,9)
200 rpm, 15:1, 60%, 36 h	0.370	0.909	2.696
200 rpm, 15:1, 30%, 36 h	0.368	0.930	3.725
200 rpm, 27:1, 30%, 36 h	13.494	32.733	93.083

Having all the results from the conducted tests, it is found that 10 mm ball size, 15:1 weight ratios of ball to powder, 60% mill charge and 24 hours milling duration yielded the best results. Sufficient amount of ball-milled powder was produced by applying these parameters to the as-received powder and an in depth analysis was made before coating and further electrochemical experiments.

4.3 Structural characterization of ball-milled powder

All the particle size measurements were made from wet samples, which were taken immediately after milling process so that the effect of agglomeration is minimized. After the drying process, visual inspection showed that color of the powder turned from grey to dark brown and big and rigid aggregates were formed. The color change suggests formation of smaller particles. Similar observations were encountered in the literature [36]. Attained powders were sieved using U.S standard sieve series before coating procedure. Sieves were used in this manner; ball-milled powder was put into the first sieve with the largest screen hole diameter. Sieves beneath had smaller openings consecutive to each other, so that the one above had slightly bigger screen

openings. At the bottom lies the receiver, a pan instead of a screen. The largest sieve mesh was 300 μm and the lowest was 25 μm . Then, the setup was placed in a mechanical shaker. After the shaking was completed, there were no particles in the bottom collector. So, the material accumulated on the smallest sieve was used (particles over 32 μm in this case). Characterization studies were done with this powder.

Surface area measurement is the first step to understand how successful the ball-milling was. Unfortunately, BET surface area measurements showed that it only increased from 2.4 $\text{m}^2\cdot\text{g}^{-1}$ to 3.6 $\text{m}^2\cdot\text{g}^{-1}$. Although ball-milling is a powerful method in terms of particle size reduction, flocculation problem is unavoidable. This effected the surface area increase. Figure 4.13 shows the agglomerates before and after sieving.

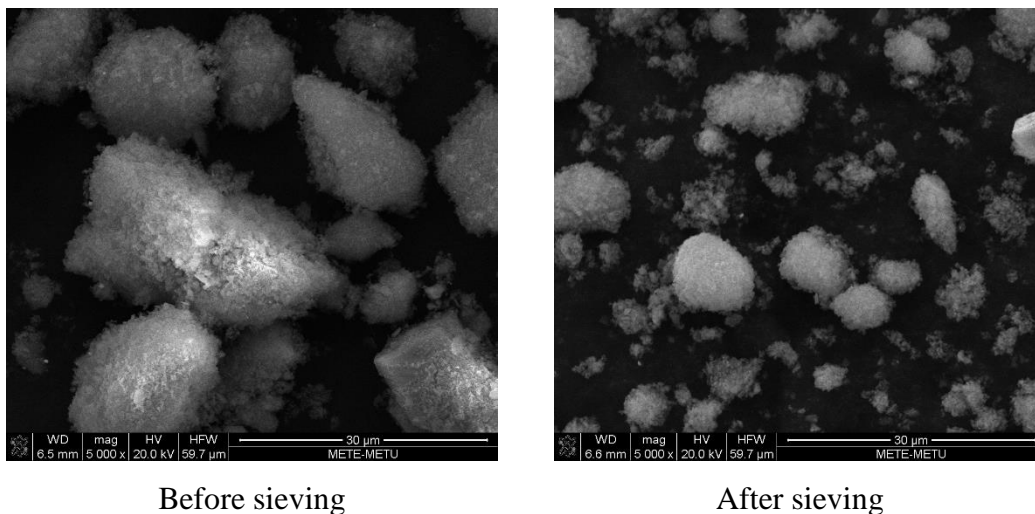


Figure 4.13 SEM images of powders, (a) before sieving, (b) after sieving.

Contamination was another risk of ball-milling, especially for increased milling durations. To see whether the produced powder was contaminated or not, XRD was used (Figure 4.14). As seen from the figure, there is four observable broad peaks at 31.4, 35.5, 48.1 and 72.8, which belong to tungsten carbide, and coming from the walls

and balls of the mill. Trace amount of inactive tungsten carbide phase can be negligible (its amount was calculated ~ 0.4 wt% from Rietveld analysis).

To understand the surface properties clearly, XPS analysis was carried. Figure 4.15 shows the XPS graph and fitted peaks. Survey spectrum was taken and Si, O, C and F peaks were observed (with atomic percentages of 49.1, 36.6, 12.5, 1.8, respectively, Figure 4.15). F in the spectrum is present because of the HF, which was used for washing the oxide from the surface of the milled powder. After having the results from the survey spectrum, high resolution spectrum of C1s and Si 2p were obtained. C 1s spectrum is given in Figure 4.16. Two peaks were fitted to C1s spectrum that shows carbon contamination components (C-C and C-O-C). Carbon contamination is also used as a charge reference for Si 2p spectrum. Three peaks were fitted to the Si 2p spectrum. The peaks at the 103.3 and 101.3 point out the presence of an oxide layer at the surface of the ball-milled silicon powder (Figure 4.17). Additionally, O 1s spectrum was examined and the peak appeared at the 532.9 eV belonging to binding energy of SiO₂ (Figure 4.18).

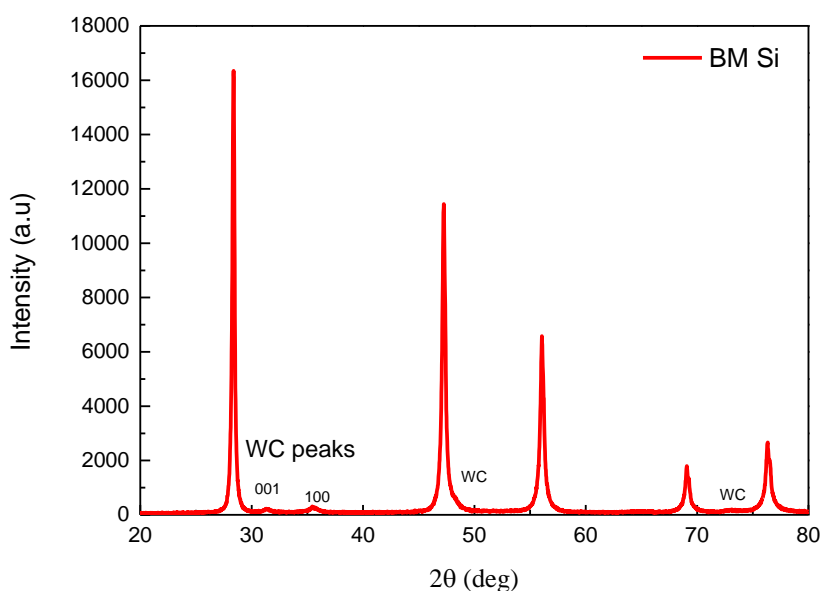


Figure 4.14 XRD data of ball-milled powder.

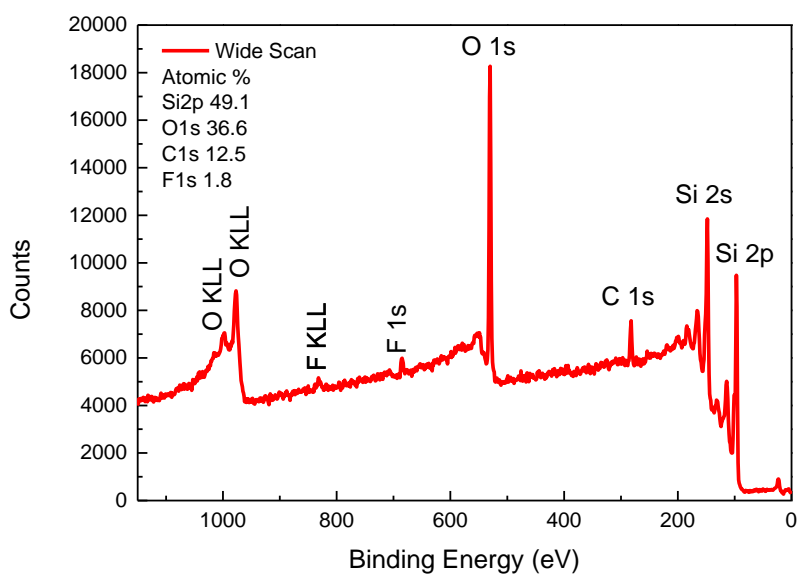


Figure 4.15 Wide-scan or survey spectrum of ball-milled silicon powder, showing all elements present with atomic percentages.

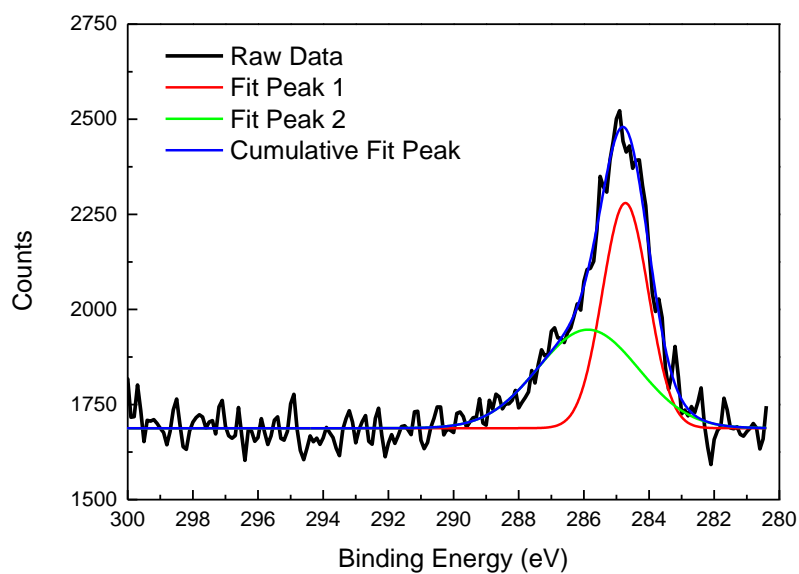


Figure 4.16 High-resolution XPS spectrum of C 1s of ball-milled silicon powder.

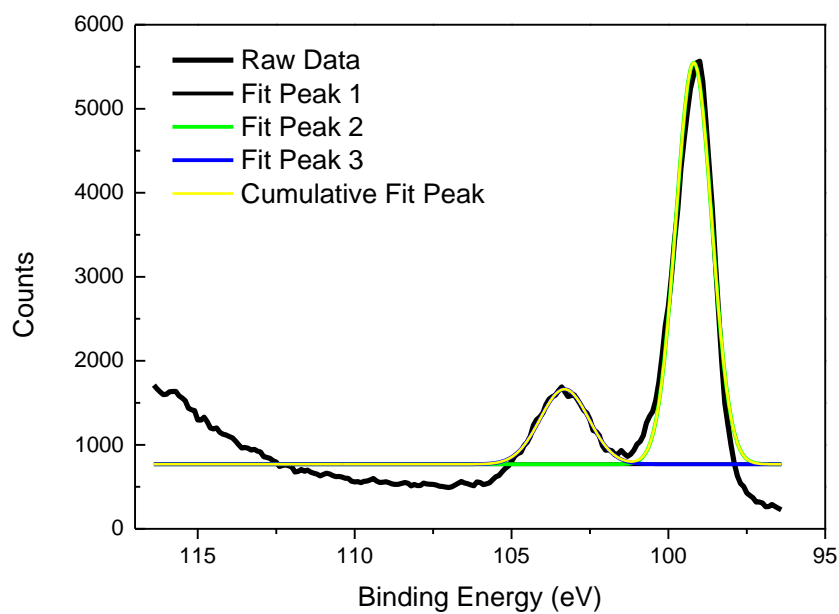


Figure 4.17 High resolution XPS spectrum of Si 2p of ball-milled silicon powder.

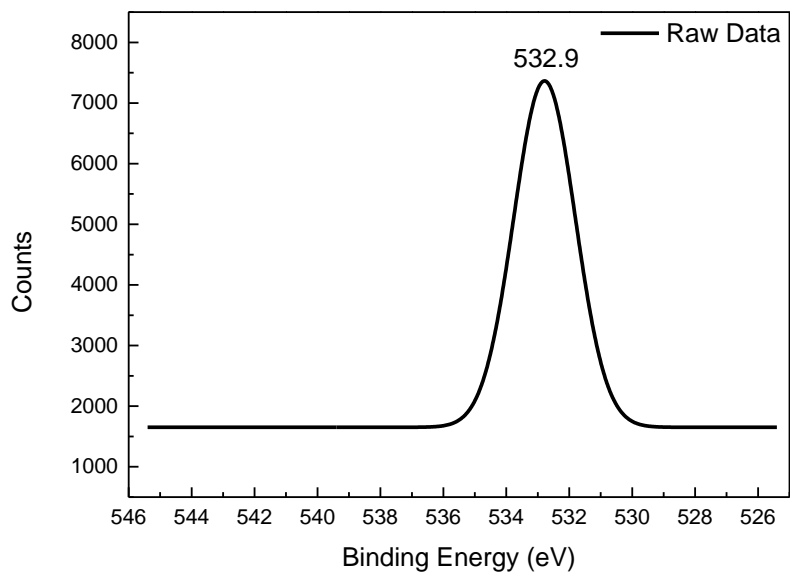


Figure 4.18 High resolution XPS spectrum of O 1s of ball-milled silicon powder.

CHAPTER 5

METAL ASSISTED CHEMICAL ETCHING

5.1 Introduction

Metal assisted chemical etching method has become a popular method for producing high surface area structures (e.g. nanowires, nanotubes, nanoparticles, porous structuring). It is an easy to apply, cheap, and powerful semiconductor etching technique with relatively precise control of orientation the nano-wire creation (vertical vs slanted), size (nano vs microscale), shape and density [37]. Metal assisted etching involves three fundamental agents: (1) a dissolving oxidant for silicon, (2) a proper complexing agent that removes native silicon oxide surface and dissolves ionic silicon, and (3) a transition metal that locally enhances silicon dissolution in the vicinity of the metal. In fact, any oxidant can be used with a reduction potential higher than silicon. A number of oxidants have been tried, including: $\text{Cr}_2\text{O}_7^{2-}$, MnO_4^- , HNO_3 , $\text{S}_2\text{O}_8^{2-}$, Fe^{3+} , Pt^{3+} , Au^{3+} , Ag^+ , and H_2O_2 . Among these oxidants, generally HF is preferred as the complexing agent. HF clears the silicon of insulating surface oxides, additionally it combines with silicon and produces soluble fluorosilicates, SiF_6^{2-} . [38].

Ag, Au, Pt, Pd, Cu, etc. have been claimed to be effective catalysts as noble metals. To formulate high aspect ratio semiconductor array based structures, the catalyst patterns might be defined by using lithography from evaporated or sputtered continuous metal films. It can also generate itself chemically by plating from metal salt solution. As an example, dendrite-like Ag metal network can be self-generated from AgNO_3 solution, NO_3^- in this case acts as the oxidizing agent. Obviously, solution based patterning is easier and cheaper since no evaporation/sputtering and no

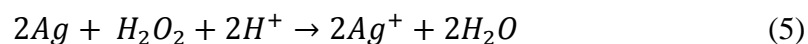
lithography are involved. Still, there is lack of proper control on the manufactured features such as shape, size, etc. Because the etching conditions, such as the concentration of oxidant in etchant, etching temperature, and time, alter the morphology [37]. Nanowire can be produced by using either the “one step” mechanism or the “two step” mechanism at wafer surfaces. However, as this study is focused on etching of powder materials with two-step etching, here after, the literature review on the two-step etching will be mentioned.

Two-step process implies using two different solutions. First solution causes the deposition of silver particles on the surface of silicon. This solution contains AgNO_3 and HF. Ag nanoparticles are deposited on the silicon surface prior to nanowire formation. This process forces the reaction to occur locally within the nanowires, and prevents direct oxidation of silicon by solution oxidant, Ag^+ or H_2O_2 .

The second solution contains H_2O_2 and HF. Peroxide directly reacts with Ag nanoparticles forming again Ag^+ locally around the nano-particles. Half reactions for two step method are given below:



The etching of silicon includes two main reactions:



The net etching reaction is:

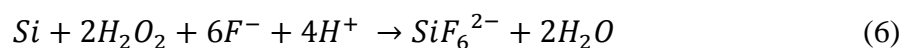


Figure 5.1 shows the two step etching process in detail. In Figure 5.1-a, Ag nanoparticles (AgNPs) are coated on the surface of Si wafer by reaction 4. After the removal of Ag^+ ion, the wafer is put into an etchant containing HF and H_2O_2 . The Ag is immediately oxidized and partially dissolved in the solution to form Ag^+ ions in accordance with the reactions 2 and 5. Then, the Ag^+ ions rapidly react with the Si on the interfaces between the wafer and the Ag nano-particles as in reaction 4, so the etching is localized in the regions covered by Ag and the AgNPs gradually decrease. Therefore, SiNWs arrays are formed by the residual Si. The net etching reaction 6 is shown in Figure 5.1-b, in which the H_2O_2 and HF diffuse into the pores and the SiF_6^{2-} and H_2O come out. With the continuous etching reaction, the AgNPs go deeper. Meanwhile, some Ag^+ ions formed by reaction 5 diffuse out. So the AgNPs become smaller, which will lead to the formation of gradient and rough pore walls. In addition, when the concentration of the diffused out Ag^+ ions reaches a certain degree, it will etch the sidewalls of Si again. Because of the accumulation effect at the tips, the concentration gradient of Ag^+ ions occurs and decreases toward bottom. Consequently, more Si dissolves at the top of the pore and leads to the cone-like tips of SiNWs. This etching process also result in roughened surfaces in SiNWs [39],

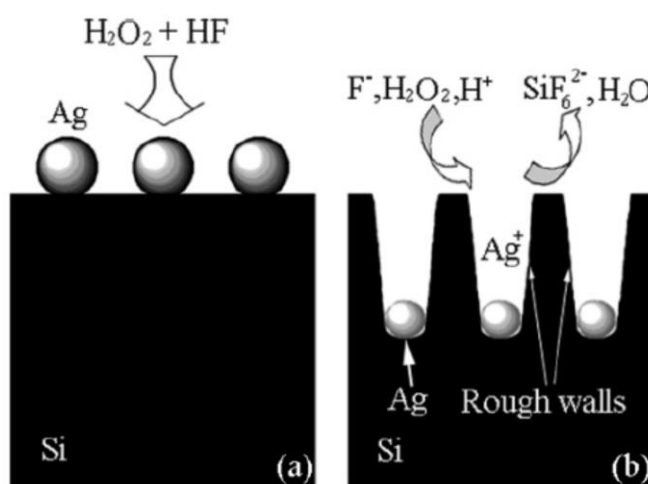


Figure 5.1 Schematic illustrations of the formation mechanism of SiNWs arrays: a) at the starting point; (b) during the etching process [39].

5.2 Metal assisted chemical etching of silicon powders

Etching of silicon powders follows the same production route as etching of silicon wafers. Similarly, one or two-step methods can be used. Silicon powder can be both un-doped or p- or n- type doped. Ge et al. produced porous silicon nanoparticles using a two-step approach, combining controlled boron doping and metal assisted chemical etching. They assigned porous silicon nanoparticles as lithium-ion battery anode material, with capacities around 1400 mAh.g^{-1} . This was done at a discharge current rate of 1 A.g^{-1} , and 1000 mAh.g^{-1} capacity was measured at 2 A.g^{-1} discharge current, and a stable operation up to 200 cycle was achieved. Figure 5.2 shows the illustration of their porous silicon nanoparticle manufacturing process [25].

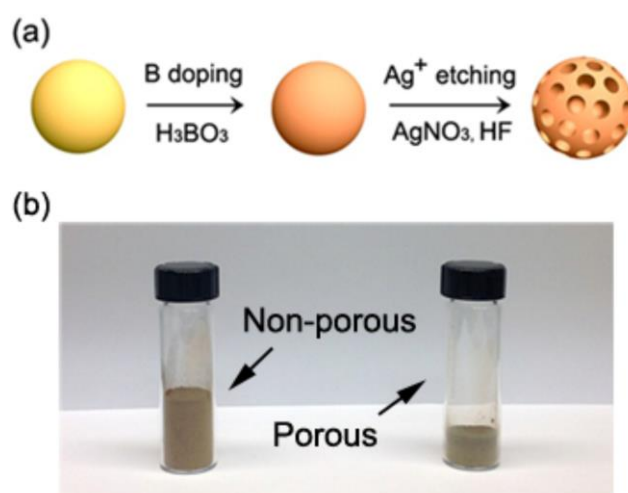


Figure 5.2 (a) Porous silicon nano-particles preparing procedure. (b) Same weight non-porous and porous Si samples have volumetric contrast[25].

Bang et al. also worked on a similar experimental method. They employed a bulk silicon powder, which was commercially available at a low-cost, to produce a multi-dimensional silicon structure composed of porous nano-wires and micro-sized cores. This could be used as anode material in lithium-ion batteries, with two step metal-assisted chemical etching process (Figure 5.3 and 5.4). These anodes showed a high

reversible charge capacity of 2400 mAh.g^{-1} with an initial coulombic efficiency of 91% and stable cycling performance [40].

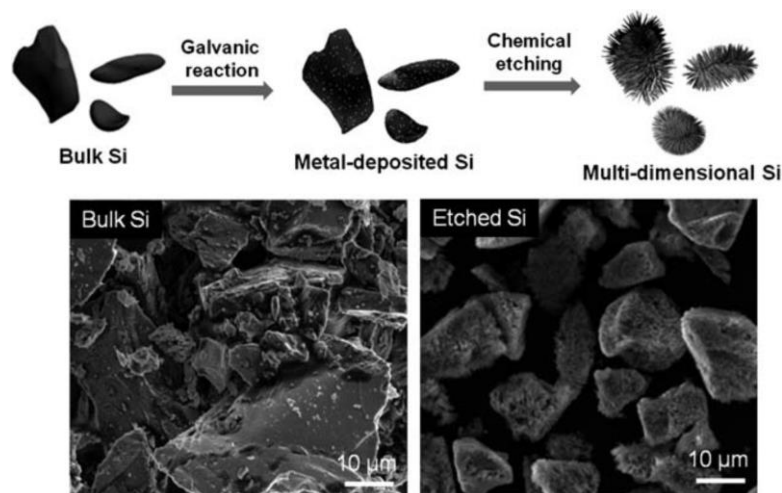


Figure 5.3 An image of the synthetic route of mSi powder. While the Ag deposited Si powder is immersed in an etchant, Ag catalyzes the Si etching, when H_2O_2 is used as an oxidant it improves the etching speed to make the mSi structures [40].

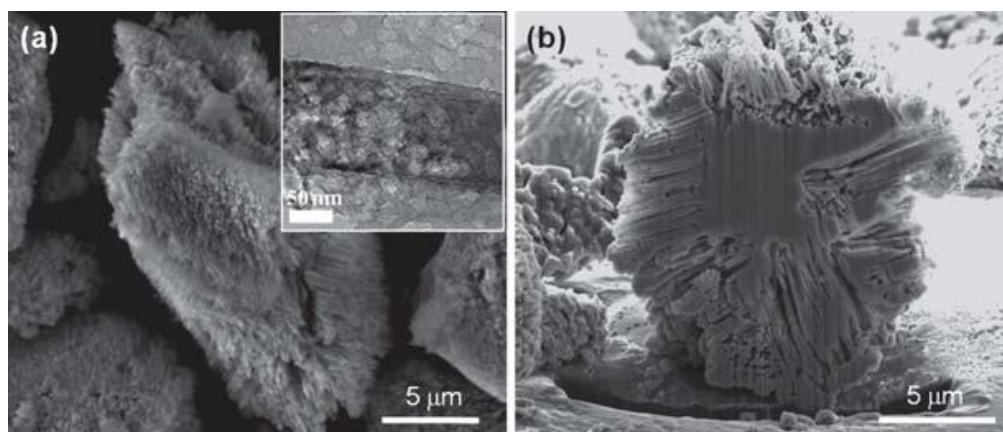


Figure 5.4 (a) A SEM image of mSi. The inset shows Si nano-wires having pores of 15–20 nm; (b) Cross-sectional SEM image of mSi achieved from the focused ion beam (FIB) process [40].

Same research group used SiO₂ coating to accommodate volume expansion of their multi-dimensional Si anode materials. They formed an oxide layer on the nanowire surfaces, by using thermal annealing under O₂ stream, with different thicknesses such as 2, 7, 10, 15 nm. The cells with 7 nm coating thickness demonstrated the best performance and yielded 2000 mAh.g⁻¹ capacity. Capacity retention after 50 cycles was 83%. They claimed that this result was the consequence of Li₂Si₂O₅ phase surrounded by carbon layers, which was participated in the charge/discharge process. However, increasing its thickness increased the charge transfer resistance and decreased the rate capability [41].

5.3 Results & discussion of multi-dimensional Si production

The main purpose of this chapter is to determine the proper experimental parameters of two-step metal assisted chemical etching. In the beginning, each step's conditions were specified and given in Table 5.1. The aim was to create an experimental matrix.

Experiments began with the silver deposition step. Table 5.2 shows the conditions of silver deposition step and details of the experiments to investigate the optimal values of these variables. At each experiment, only one variable was changed. Other parameters were kept constant for all solutions. Values, which were used as standard, were written with bold / bigger font in the table. A standardized etching solution was used for all experiments.

To understand the effect of these variables on the microstructure of the silicon powder SEM micrographs were taken from each sample. AgNO₃ amount was the first investigated variable and Figure 5.5 shows the SEM images of the samples with Ag contents of 0,005 M, 0.02 M, 0.04 M, 0.08 M.

SEM images showed that the AgNO₃ amount in the solution is important. 0.05 M was insufficient, as the images of wires and porous were absent in the structure. Columnar structure was weak in case of 0.08M. The reason could be the dendritic growth of

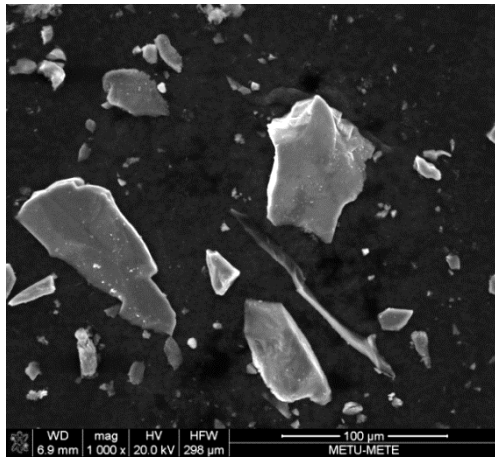
silver particles despite homogeneous deposition on silicon. Dendritic silver particles could be seen in the solution visually. There was not much difference between 0.02 and 0.04 M. Thus, 0.02 was preferred, since; silver is an expensive, corrosive and hazardous substance.



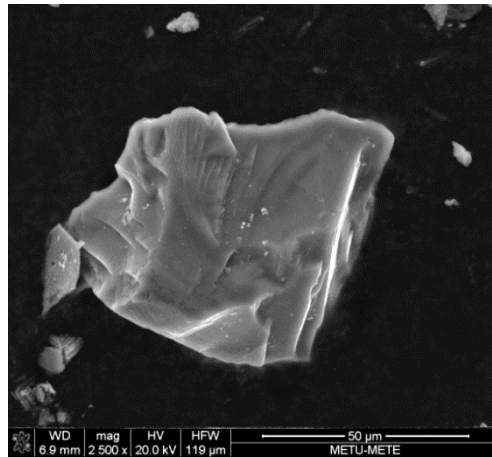
Table 5.1 Contents and values of each solutions at the etching step.

Metal Deposition Solution	Etching Solution
<p>The contents of metal deposition solution can be listed as:</p> <ul style="list-style-type: none"> • HF • AgNO₃ • Water <p>Critical variables of deposition step:</p> <ul style="list-style-type: none"> • AgNO₃(mol)/Si(mol) ratio • Temperature • Time • Type of metal 	<p>The contents of etching solution can be listed as:</p> <ul style="list-style-type: none"> • HF • H₂O₂ • Water <p>Other critical variables of etching step:</p> <ul style="list-style-type: none"> • Temperature • Time • Type of oxidizing agent

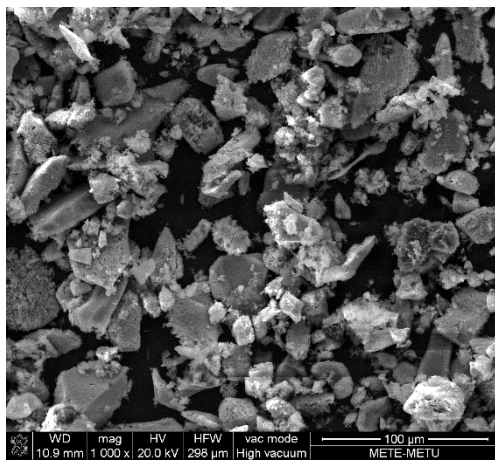
Table 5.2 Experimental details of Ag deposition step	
Conditions of Ag deposition step:	Values:
AgNO ₃ (M)	0.005, 0.02 , 0.04, 0.08
HF (M)	4, 5 , 10
AgNO ₃ (mol)/ Si(mol)	0.01, 0.1 , 0.2, 1
Temperature (°C)	Room temperature , 50°C
Time (minute)	1, 5 , 30



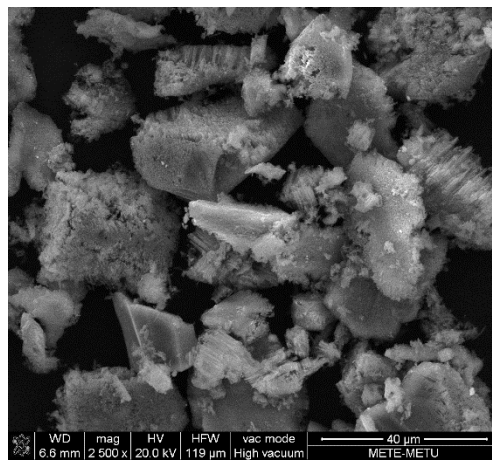
(a)



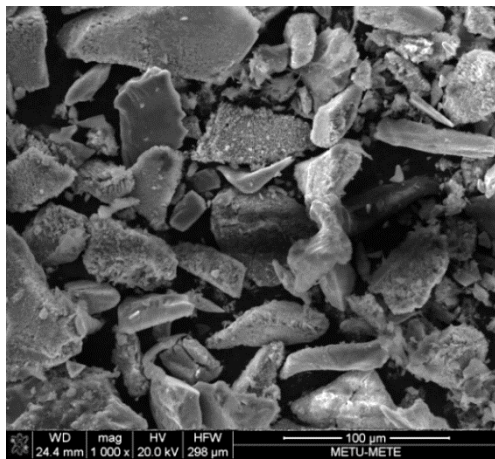
(b)



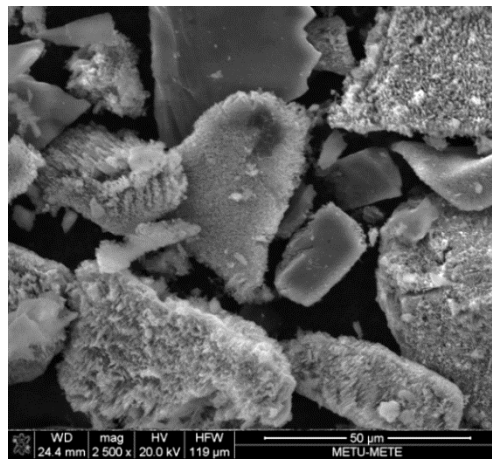
(c)



(d)



(e)



(f)

Figure 5.5 SEM images of the samples which show the effect of AgNO_3 , (a, b) 0,005M, (c, d) 0.02 M, (e, f) 0.04 M, (g, h) 0.08 M at x1000 and x2500 magnifications.

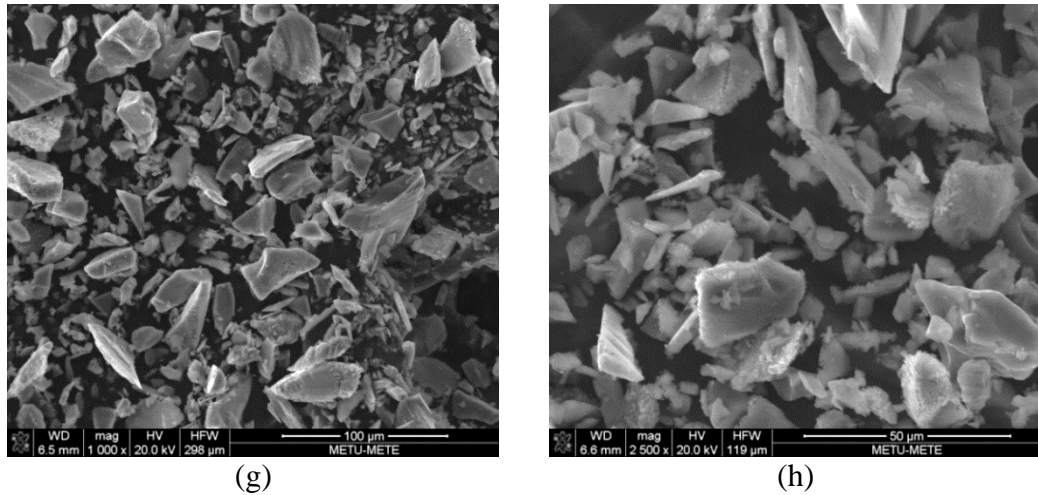
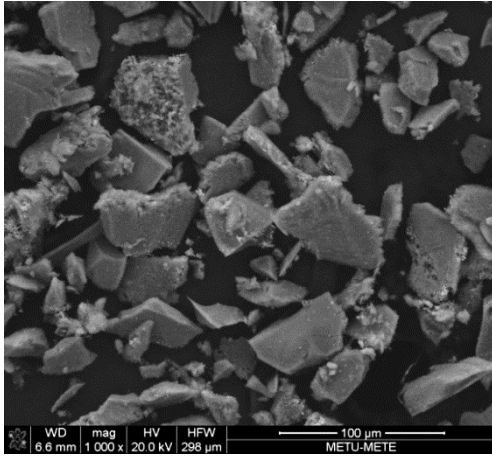


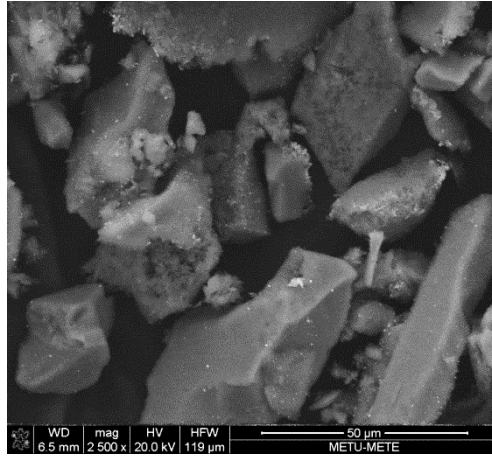
Figure 5.5 Cont'd.

After determining AgNO_3 concentration, experiments were focused on the investigation of molarity of HF. Figure 5.6 shows the SEM images of the samples. Concentration of HF was set as 4, 5 and 10 M. When HF concentration is set as 4 M, some particle surfaces were etched. Obtained wires were shorter when compared to the other two concentration setups. On the other hand, 5 M and 10 M HF concentrations resulted in different architectural structures. These structures have very different pore sizes as seen from SEM (Figure 5.6-c-f). Also, when 5 M solution was used, more wires were found than that of 10 M. More importantly, 10 M solution concentration proved to be too abrasive for the smaller sized surface particles such that only larger particles remained at that concentration level. Only a small amount of usable silicon powder remained due to this abrasion. According to these results obtained from HF concentration tests, 5 M was selected as the optimal value in terms of wired/porous structure formations and usable material.

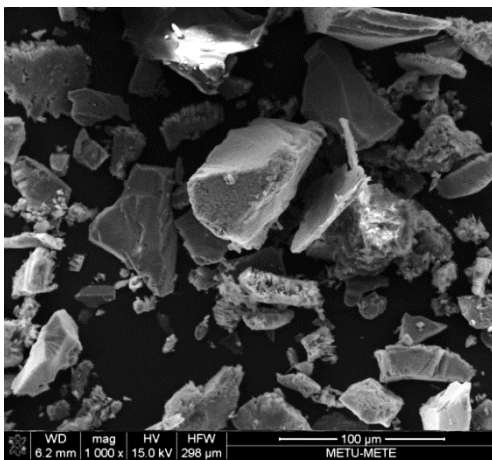
The effect of $\text{AgNO}_3(\text{mol})/\text{Si}(\text{mol})$ ratio was investigated. Three different ratio were studied, 0.01, 0.1 and 0.2. Figure 5.7 shows the SEM images of these samples. Etching could not be obtained on all the particles when ratio was as low as 0.01. When ratio is increased to 0.2, homogeneity of porous structure on particles disappeared, probably due to the dendritic growth of Ag particles on each other instead of Si. The best results in terms of porosity and wire generation were obtained with 0.1 mol ratio. However, there were too much abrasion loss which counter balanced surface increase.



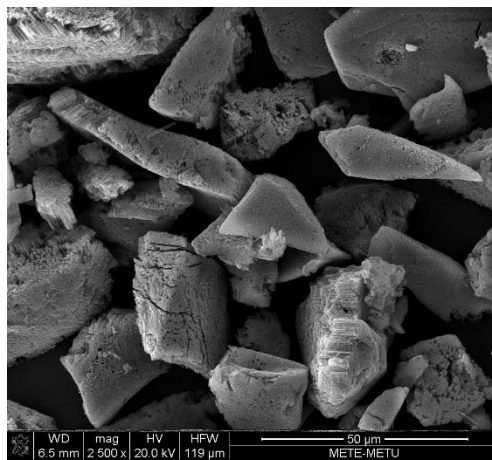
(a)



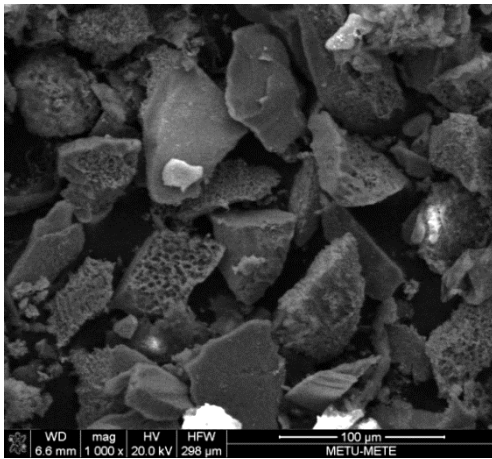
(b)



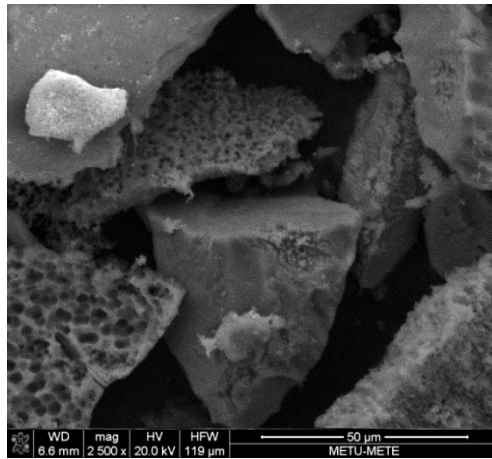
(c)



(d)

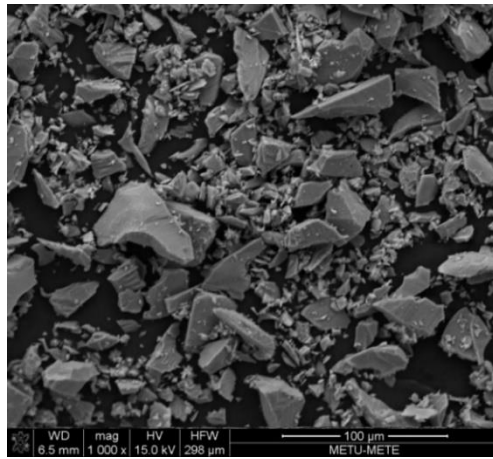


(e)

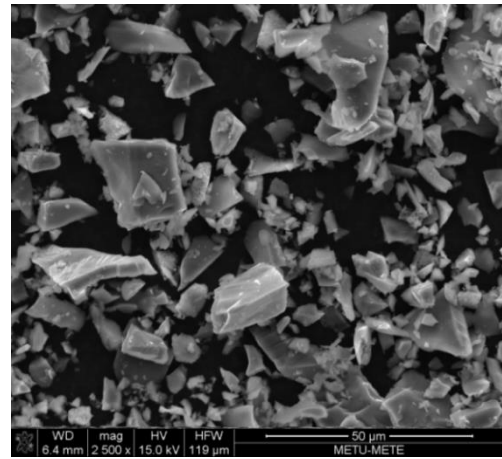


(f)

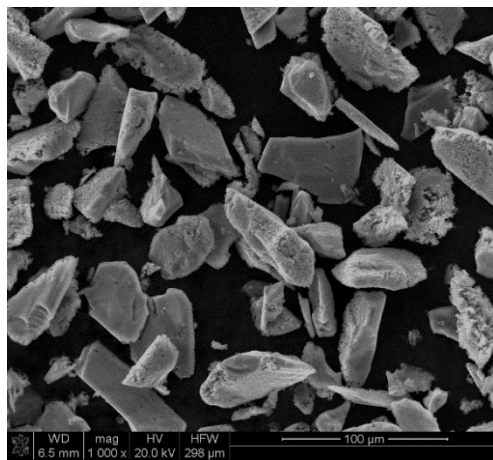
Figure 5.6 SEM images of the samples which show the effect of HF, (a, b) 4M, (c, d) 5M, (e, f) 10M, at x1000 and x2500 magnifications.



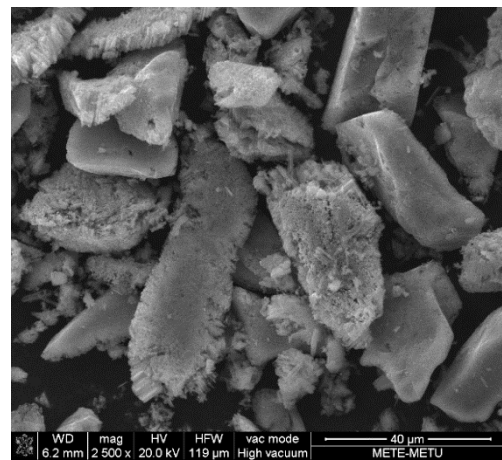
(a)



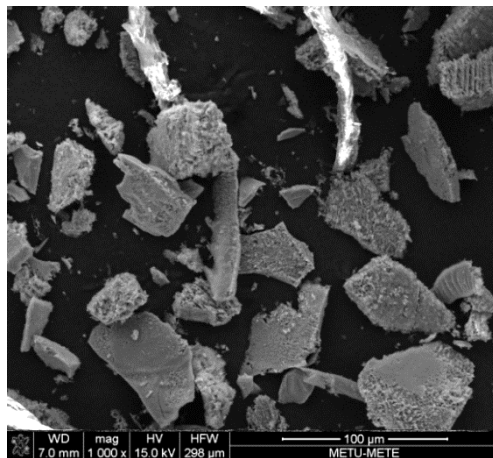
(b)



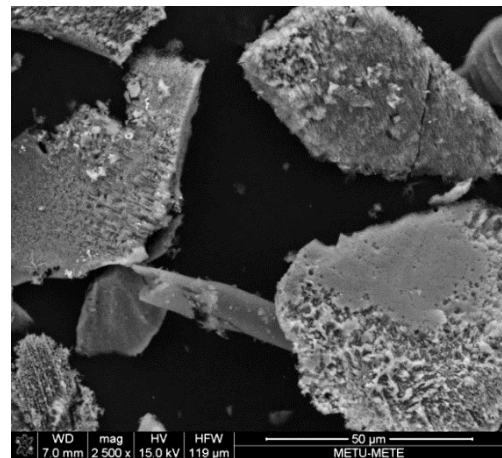
(c)



(d)



(e)



(f)

Figure 5.7 SEM images of the samples which show the effect of $\text{AgNO}_3(\text{mol})/\text{Si}(\text{mol})$, (a, b) 0.01, (c, d) 0.1, (e, f) 0.2, at x1000 and x2500 magnifications

Then, trials to determine the effect of deposition duration were conducted (Figure 5.8). SEM images showed that 1 minute is not enough to deposit Ag particles homogeneously. On the other hand, there was not a significant difference between 5 and 30 minutes deposition duration. Some porous structure is produced as can be seen in the Figure 5.8 c-f. As a result, 5 min is chosen to conduct as standard.

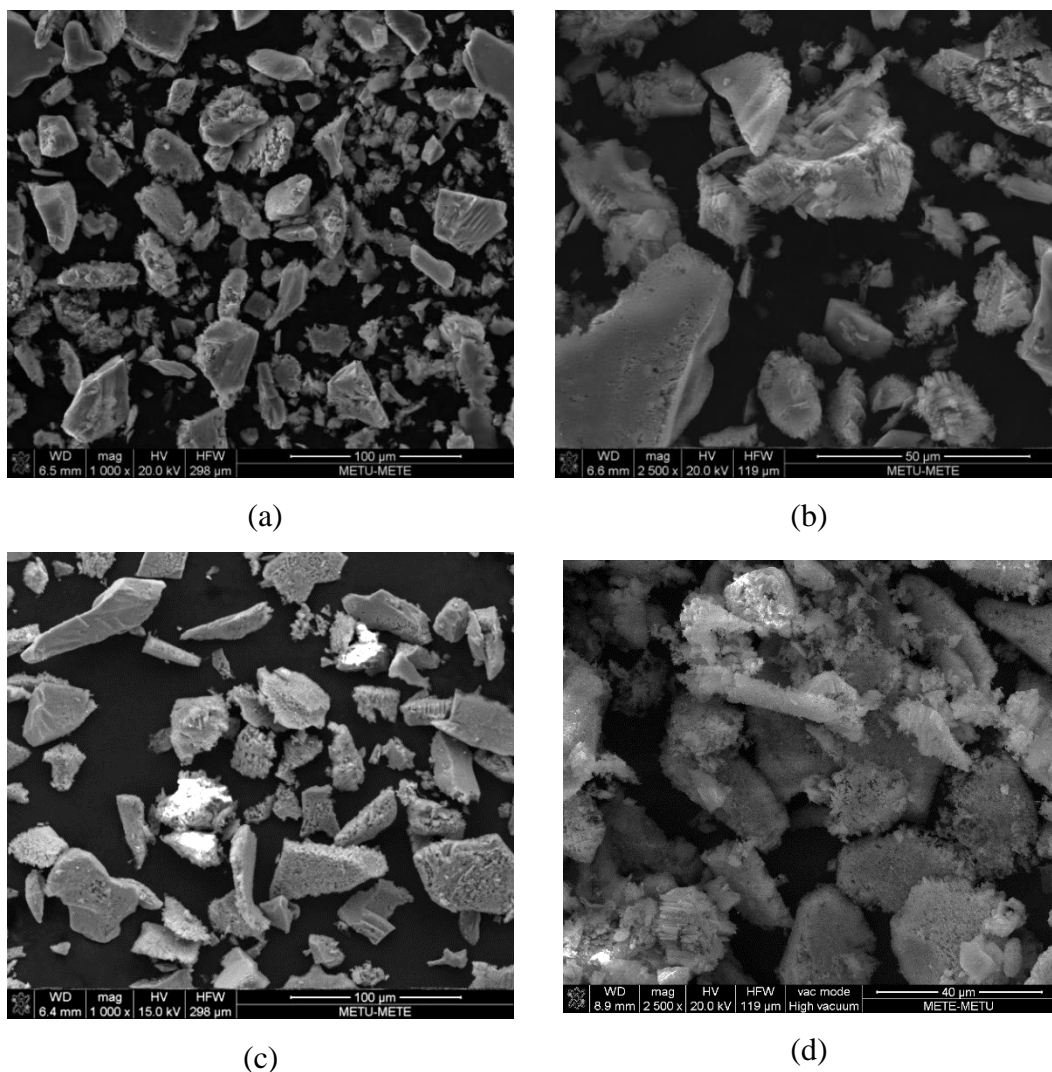
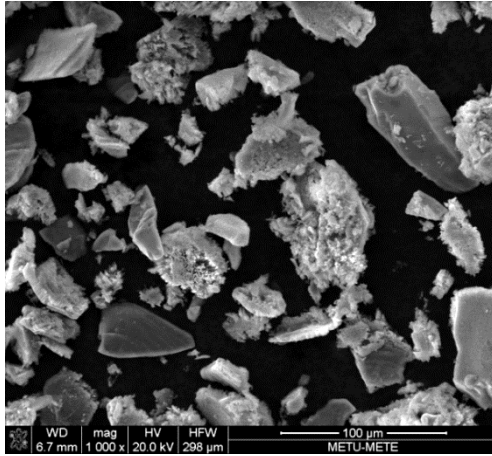
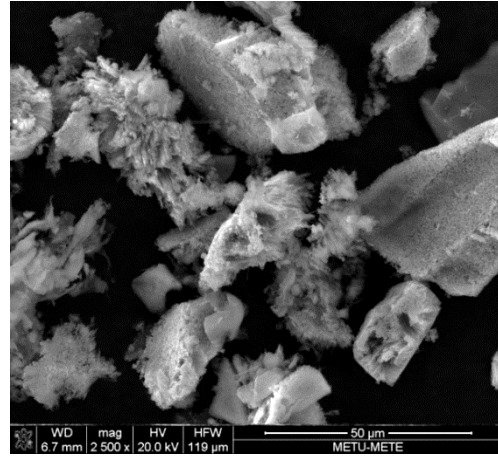


Figure 5.8 SEM images of the samples which show the effect of deposition duration, (a, b) 1 minute, (c, d) 5 minute, (e, f) 30 minute, at x1000 and x2500 magnifications.



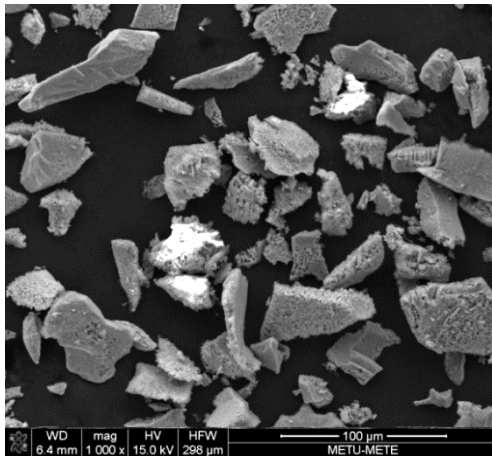
(e)



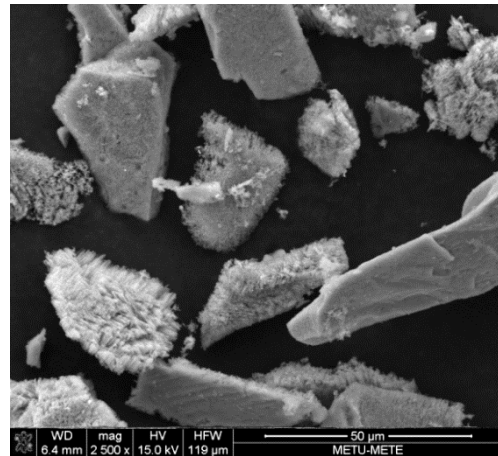
(f)

Figure 5.8 Cont'd

Finally, the effect of the test temperature was explored. It is found that there was not a big difference in terms of silver deposition between RT and 50°C. Deposition could be conducted at room temperature without any difficulty, so, it is decided not to increase the testing temperatures any further (Figure 5.9).

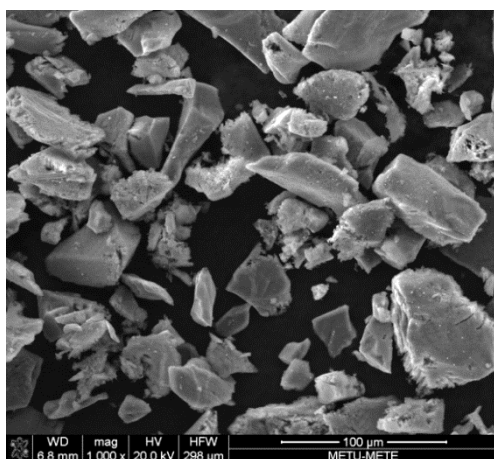


(a)

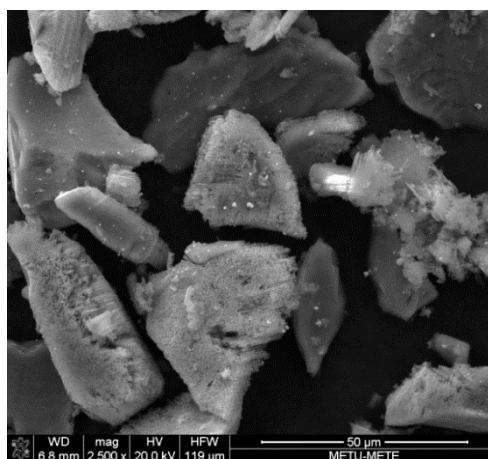


(b)

Figure 5.9 SEM images of the samples which show the effect of temperature, (a, b) room temperature, (c, d) 50°C, at x1000 and x2500 magnifications



(c)



(d)

Figure 5.9 Cont'd

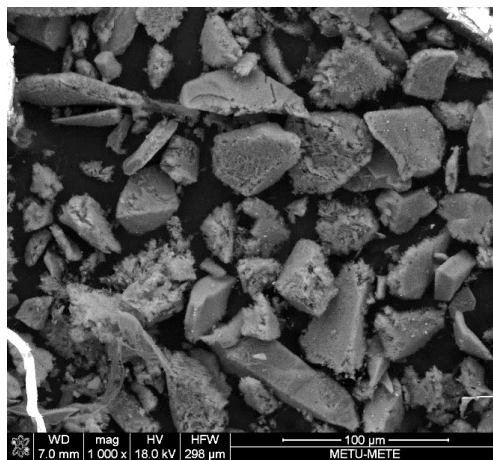
According to these results, selected parameters of Ag deposition step are summarized in Table 5.3.

Table 5.3 Silver deposition step's obtained best results	
Name of the variable	Selected Values
AgNO₃ (M)	0.02
HF (M)	5
AgNO₃(mol)/Si(mol)	0.1
Time (min)	5
Temperature (°C)	Room temperature

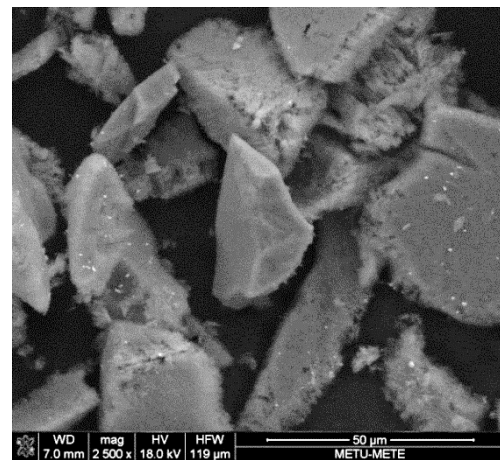
After determining the optimal test parameters and values, experiments were continued with etching step. Table 5.4 shows the variables of etching step. Values, which were used as constant, are pointed out in bold and bigger.

Experiments started with the molarity of HF and H₂O₂ since this is a top-down approach involving redox reactions. At Figure 5.10, the SEM images of the samples are shown. Increasing HF concentration seemed to have a positive effect. However, increasing HF concentration is problematic due to sudden increases in temperature, which can reduce the amount of produced powder.

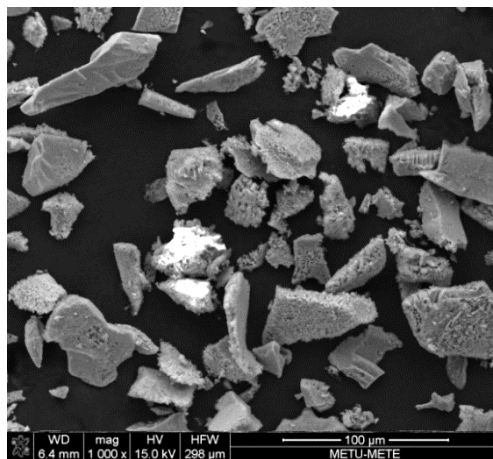
Table 5.4 Experimental details of etching step	
Variables of etching step:	Test Values:
H ₂ O ₂ (ml)	0.5, 1.5 , 2, 5
HF (M)	4, 5 , 10
Temperature (°C)	Room temperature, 50°C
Time (minute)	60 , 300



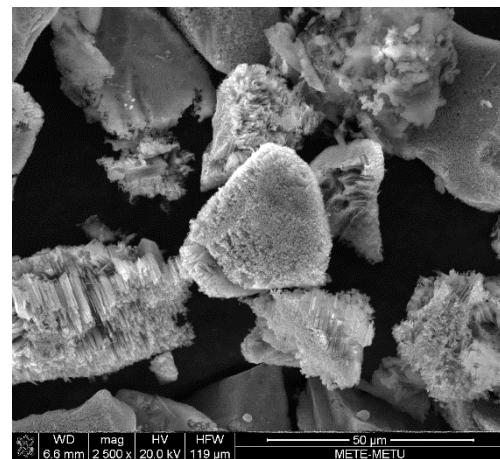
(a)



(b)

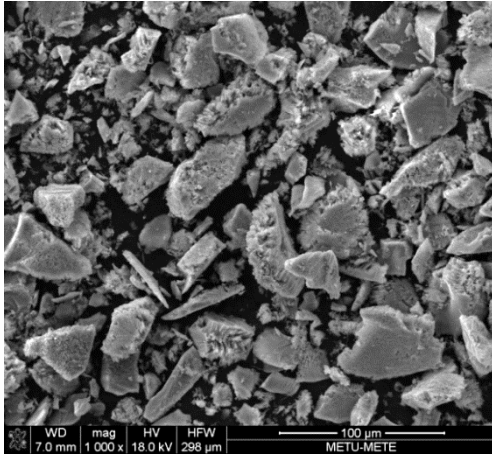


(c)

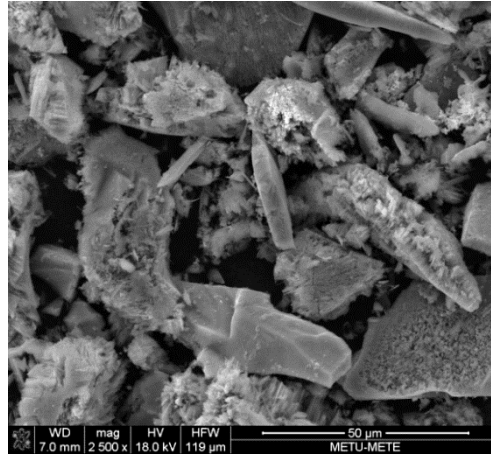


(d)

Figure 5.10 SEM images of the samples which show the effect of HF, (a, b) 4M, (c, d) 5M, (e, f) 10M at x1000 and x2500 magnifications.



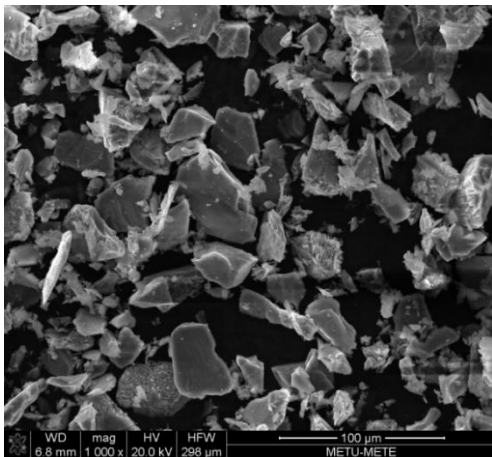
(e)



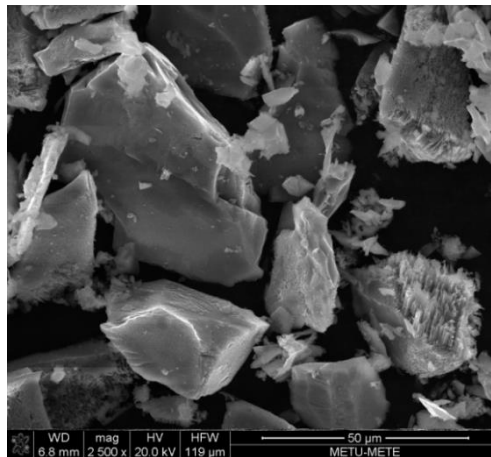
(f)

Figure 5.10 Cont'd

Second investigated parameter was H_2O_2 concentration. 0.5 ml was not enough to generate a porous structure. On the other hand, 5 ml H_2O_2 did not improve the sample. At 5 ml with 10 minutes etching, all of the powder vanished. When the 1.5 and 2 ml volume were tested, the porosity of the silicon became obvious and an improved structure was formed around silicon particles. In the case of 1.5 ml, wires with the length of 3-5 μm were clearly seen in the SEM. 2 ml case also produced a porous structure, but, with larger pore sizes. Because, increasing the H_2O_2 volume can lead to high rate etching. Figure 5.11 a-f shows the SEM images of these experiments.

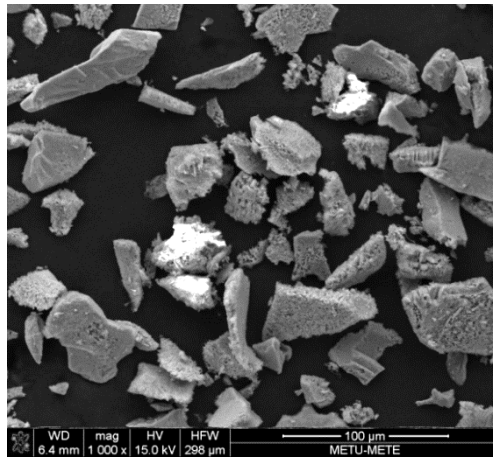


(a)

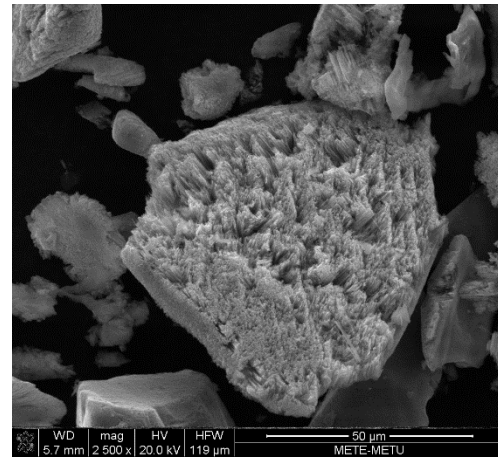


(b)

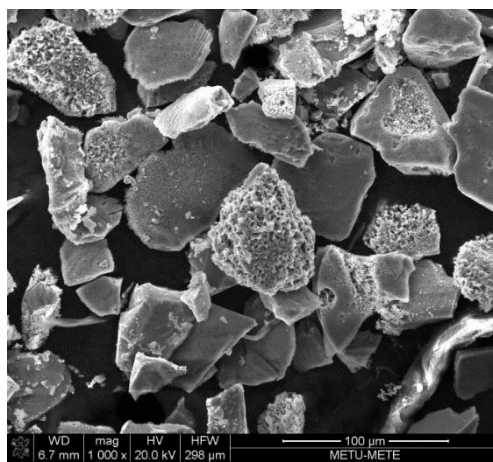
Figure 5.11 SEM images of the samples which show the effect of H_2O_2 , (a, b) 0.5ml, (c, d) 1.5ml, (e, f) 2ml, at x1000 and x2500 magnifications.



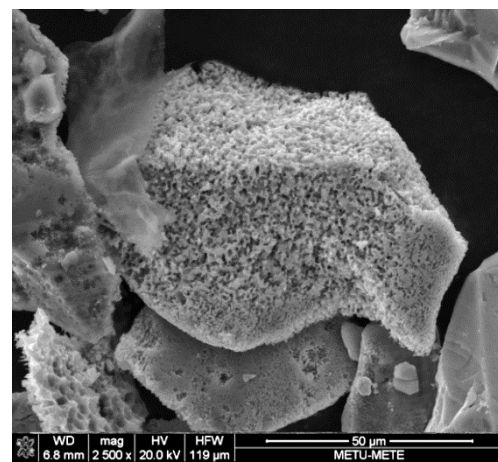
(c)



(d)



(e)



(f)

Figure 5.11 Cont'd

The next focused parameter was duration. Figure 5.12 shows the SEM images of the samples. Prolonging etching duration improves the surface properties, but also decreases the amount of usable powder dramatically.

Another factor having a direct influence on the structure is the temperature of the etching solution. It has an impact on the kinetics of the reduction–oxidation reactions. In the 0–50°C range, the effect of the temperature was observed and the length of the wires were proportionally linked with the temperature of the solution (Figure 5.13). Temperatures that exceed of 50°C were avoided for safety concerns and to regulate a stable solution concentration. From SEM images, it seems that increasing etching

temperature did not create a dramatic difference on etching. Further experiments showed that controlling of temperature yields a homogeneous structure.

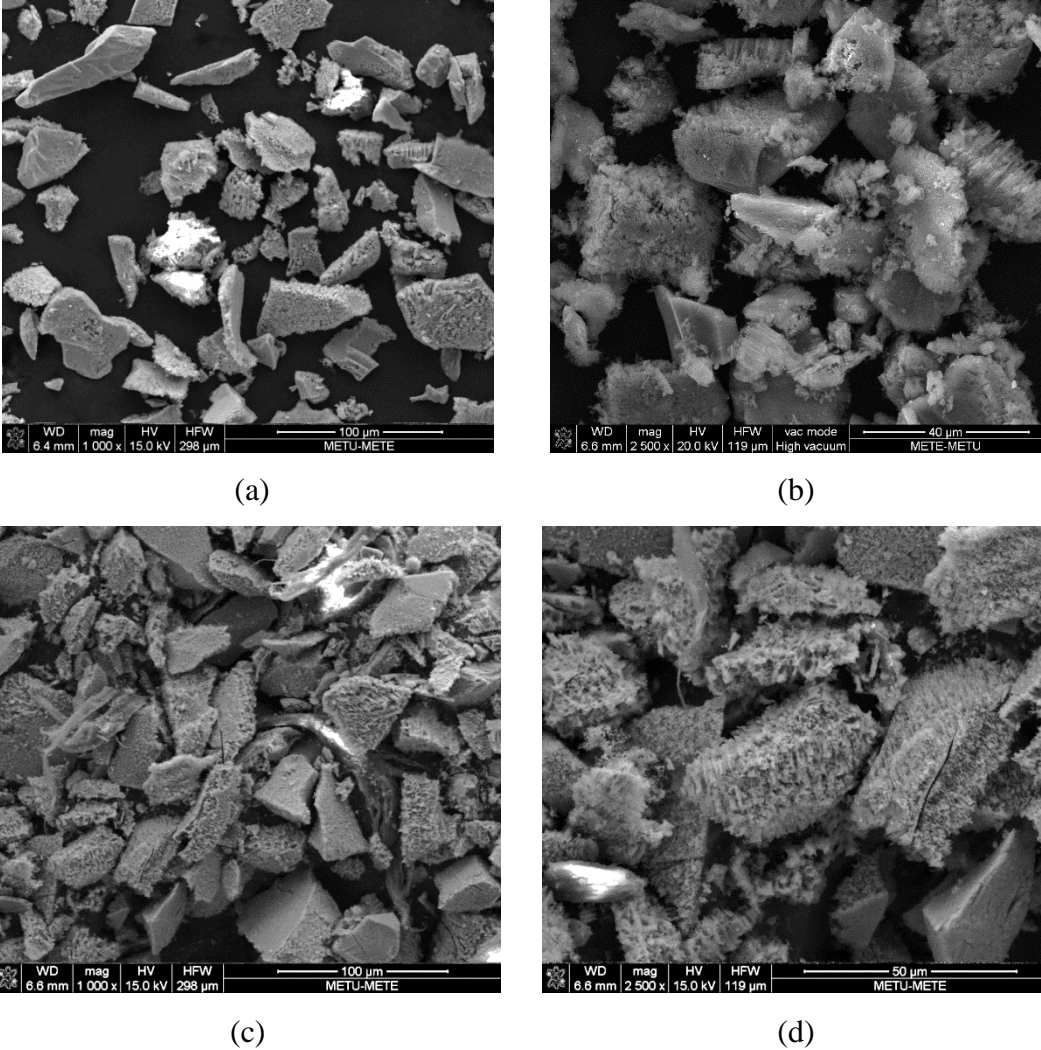
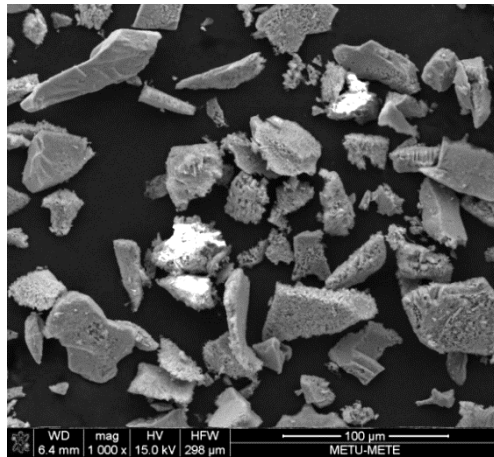
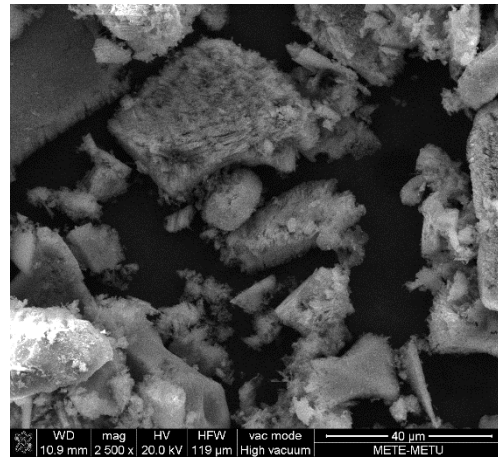


Figure 5.12 SEM images of the samples which show the effect of time, (a, b) 60 minute, (c, d) 300 minute, at x1000 and x2500 magnifications.

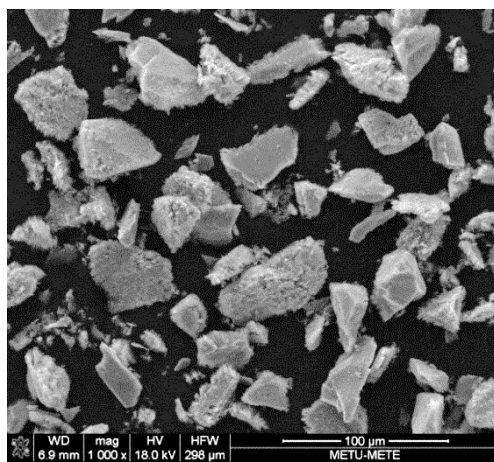
According to these SEM images, results of etching step on the production of mSi were summarized in Table 5.5.



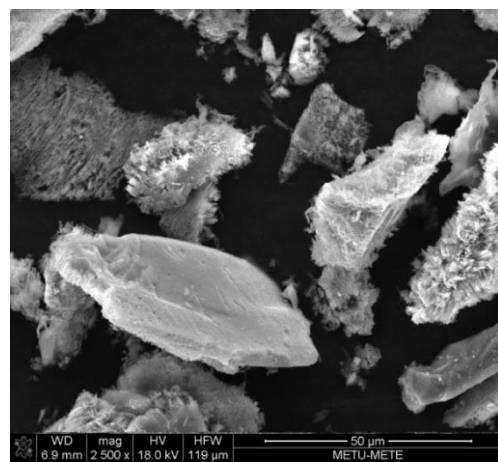
(a)



(b)



(c)



(d)

Figure 5.13 SEM images of the samples which show the effect of temperature, (a, b) 50°C, (c, d) room temperature, at x1000 and x2500 magnifications.

Table 5.5 Etching step's obtained best results	
Name of the variable	Selected Values
H₂O₂ (M)	0.02
HF (M)	5
Time (min)	60
Temperature (°C)	50

5.4 Structural Characterization of mSi

Before electrochemical tests, detailed SEM images of produced powder under different magnifications are given in Figure 5.14 in order to understand the structure. SEM images shows that porous/columnar structures could not be obtained on all of the particles. Some of them seem to have porous structure and others seem non-etched.

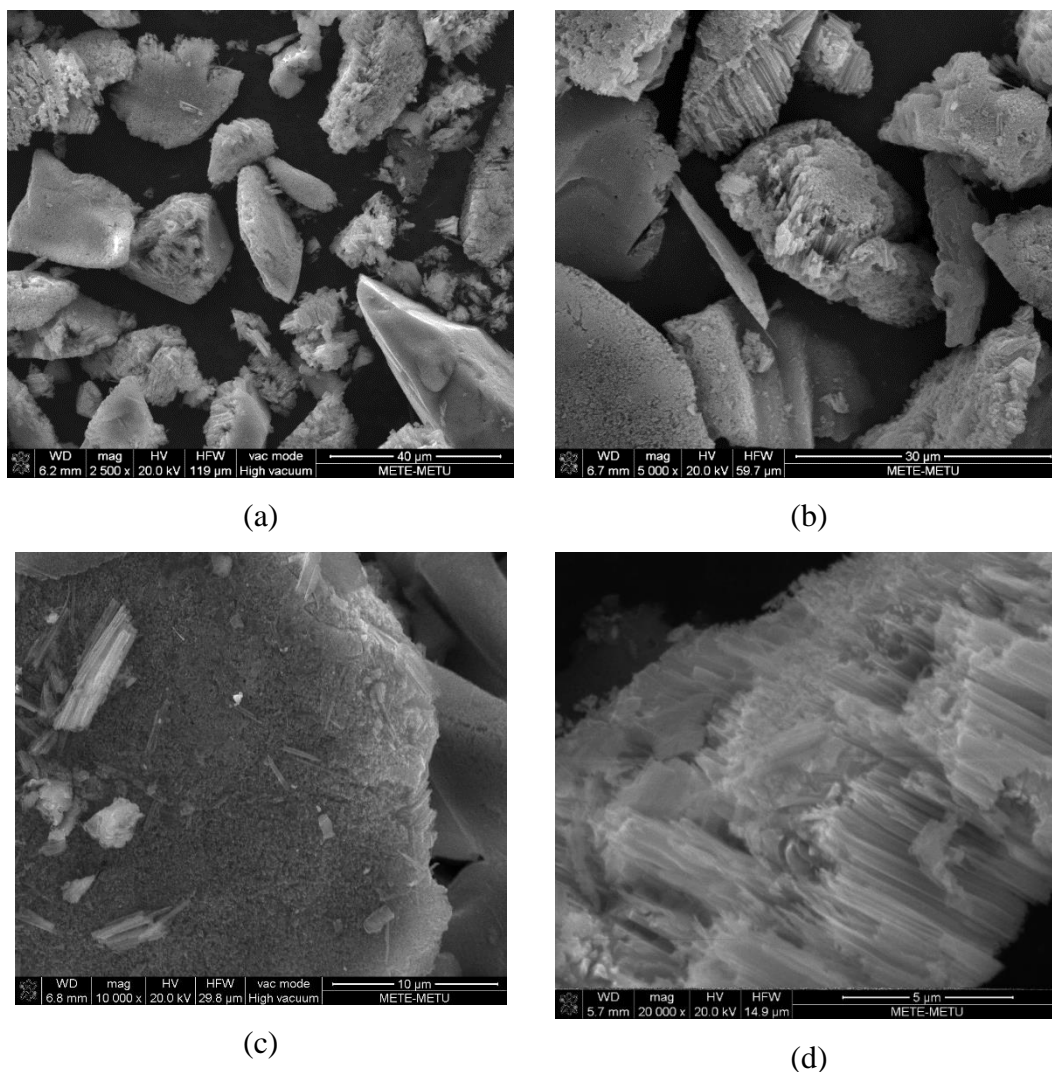


Figure 5.14 SEM image of produced Silicon particles with porous and columnar surfaces (mSi).

The most important aspect of anode material production for this study is to increase the surface area of the as-received silicon powder. Surface area of mSi was measured

as $7.135 \text{ m}^2 \cdot \text{g}^{-1}$ which is three times larger than that of as-received powder (mentioned in chapter 3.1). Surface area of this processed powder was not as high as expected. This implies that the particles were not sufficiently etched. To see the formation of pores, focused ion beam (FIB) technique was used and cross-sectional SEM images of the particles were taken (Figure 5.15). Cross-sectional observations verified the findings. Porous structures are not homogeneous throughout the structure and the open pores are up to $3\text{-}4 \text{ }\mu\text{m}$ deep. This is also consistent with other SEM images. Also, not all the surfaces of the particles seem to be etched. At image (e), inner wire formations are visible.

To investigate the existence of columnar structure, etched powder were dispersed in ethanol and ultra-sonication was applied for 10 minutes. After that, the suspension was rested for a couple of minutes and then a drop of the suspension was transferred onto a copper grid. The images of the detached wires are in Figure 5.16. EDS analysis were done on all the wires to make sure that they were silicon. Images show that the average diameter of the wires is smaller than 100 nm and their lengths vary. The longest tube height measured is $3 \text{ }\mu\text{m}$.

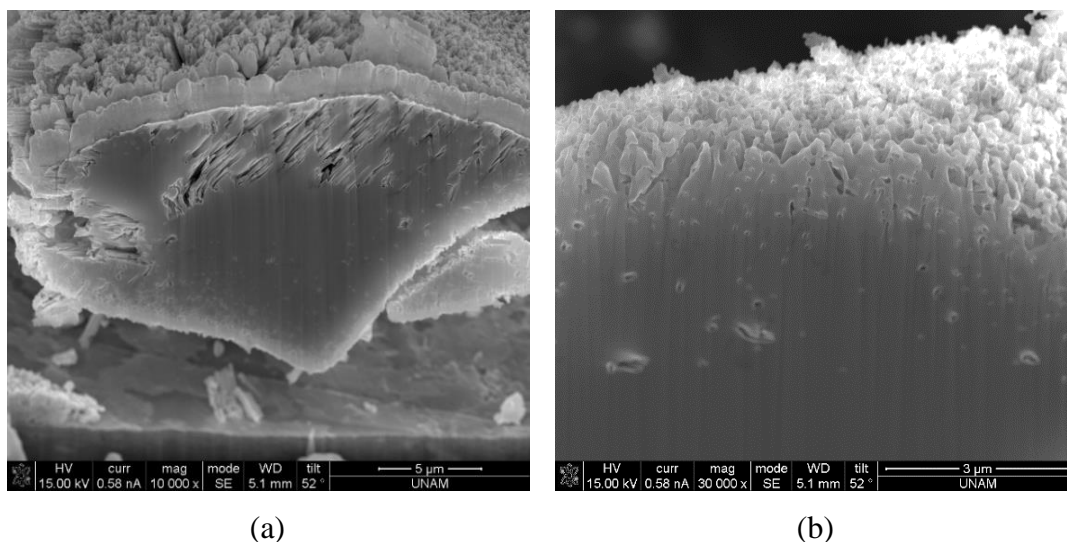
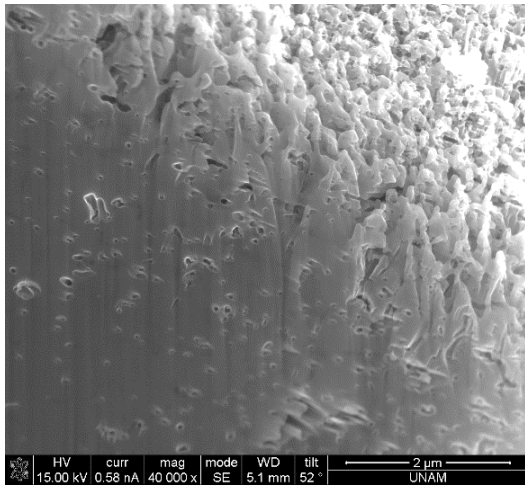
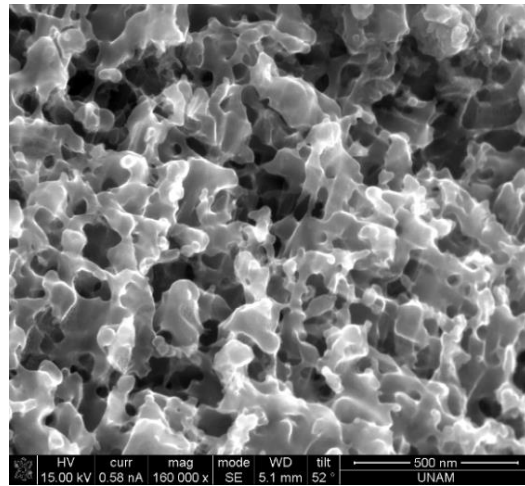


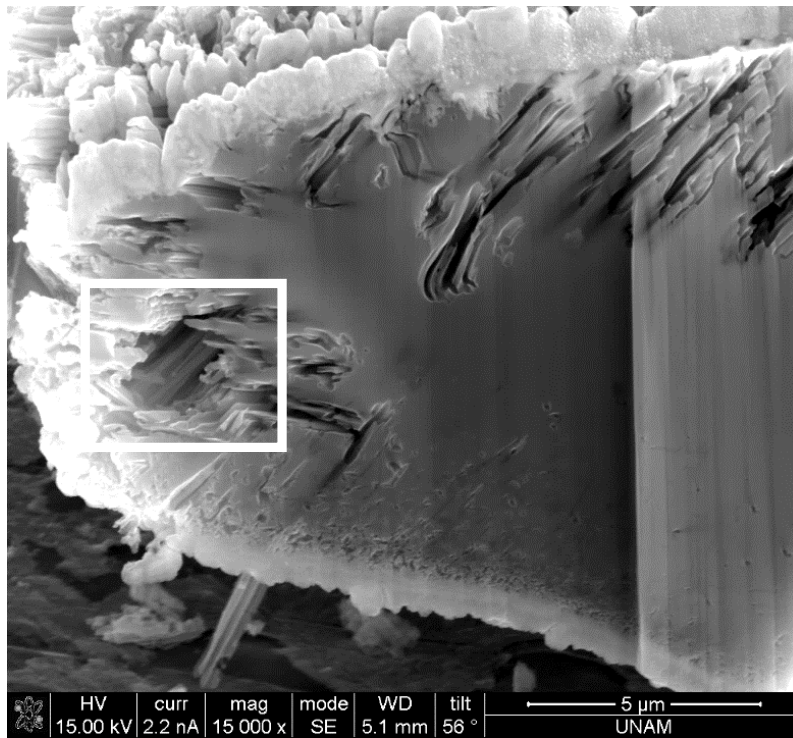
Figure 5.15 Cross sectional SEM images of mSi obtained from the FIB process, (a) $10000\times$, (b) $30000\times$, (c) $40000\times$, (d) $160000\times$ and (e) $15000\times$ – it shows the columnar structure.



(c)



(d)



(e)

Figure 5.15 Cont'd.

Particle size distribution analysis was done to these samples, because an important factor of lowered surface area could be due to the abrasion of smaller sized particles after etching (all SEM images). Particle size distribution verified that during etching most of the particles under 10-micron range vanished and average particle size

increased up to 26 μm . Figure 5.17 gives the comparison of particle size distribution graph of mSi with the as-received powder.

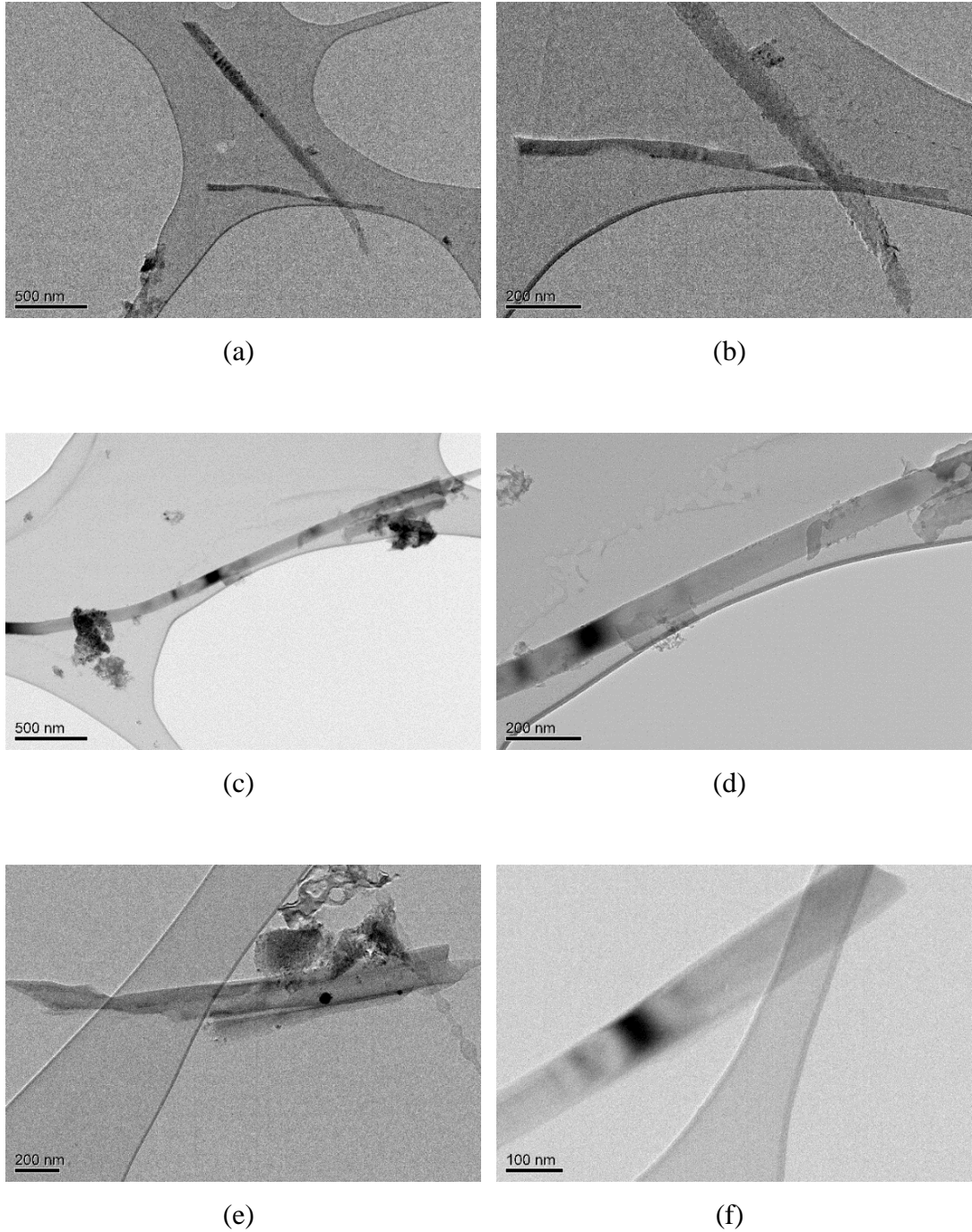


Figure 5.16 TEM images showing the wires that were cut off from etched silicon particles.

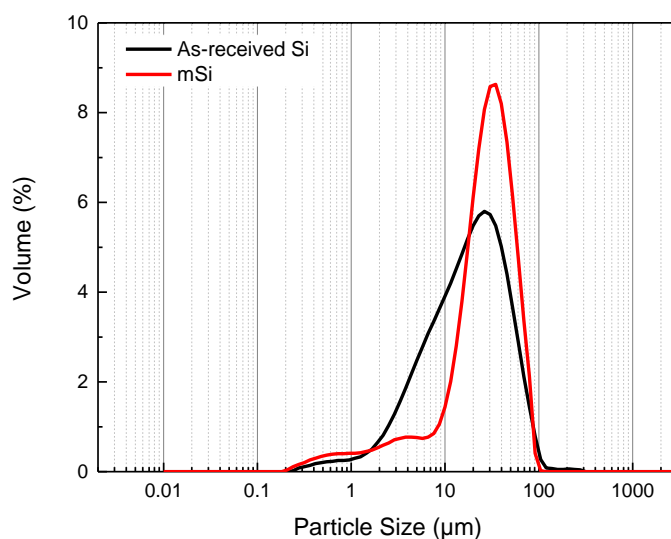


Figure 5.17 Particle size distribution comparison of mSi and as-received Si powders.

At the end of etching, surface of the powder becomes oxide free, however, its surface oxidized again under exposure to oxygen and humidity at the atmospheric conditions. As mentioned in section 5.2, thickness of silicon dioxide (SiO_2) is critical because this native silicon dioxide is an electrical insulator and causes high charge transfer resistance in the Si electrode and causes low rate capability. XPS was conducted to see the existence of SiO_2 and/or SiO_x phases on the surface.

First; survey spectrum (Figure 5.18) was taken and Si, O, C and F peaks were observed with atomic percentages of 39.0, 47.1, 10.1, 3.8, respectively. F in the spectrum is present because of the HF. After having the results from the survey spectrum, high resolution spectrum of C1s and Si 2p were obtained. C 1s spectrum is given in Figure 5.19. Two peaks were fitted to C1s spectrum that shows carbon contamination components (C-C and C-O-C). Carbon contamination is also used as a charge reference for Si 2p spectrum. Two peaks were fitted to the Si 2p spectrum. The peak at the 103.2 points out the presence of an oxide layer at the surface of the etched silicon powder and the peak at 99.5 eV match with elemental Si 2p peak. (Figure 5.20). Additionally, O 1s spectrum was examined and the peak appeared at the 532.9 eV

belongs to binding energy of SiO_2 (Figure 5.21). Effect of the oxide layer on the electrochemical performance will be discussed in Chapter 8.

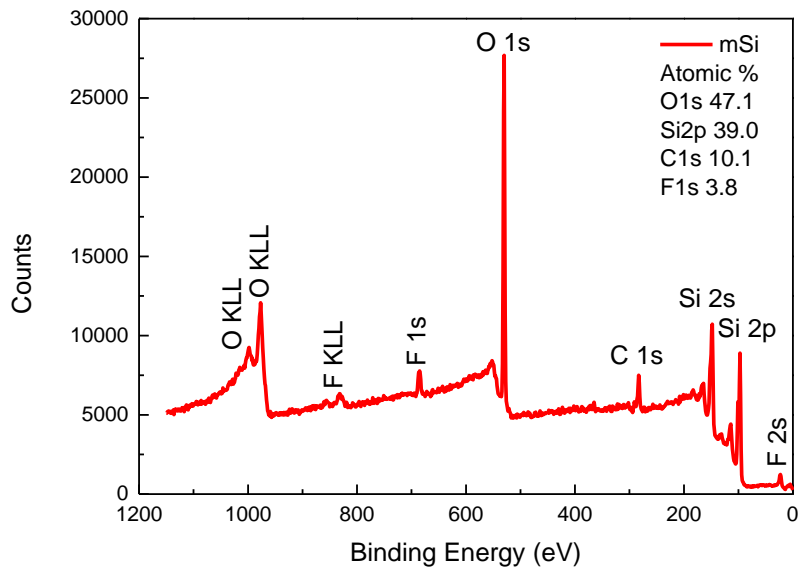


Figure 5.18 Wide-scan or survey spectrum of multi-dimensional silicon powder, showing all elements present with atomic percentages.

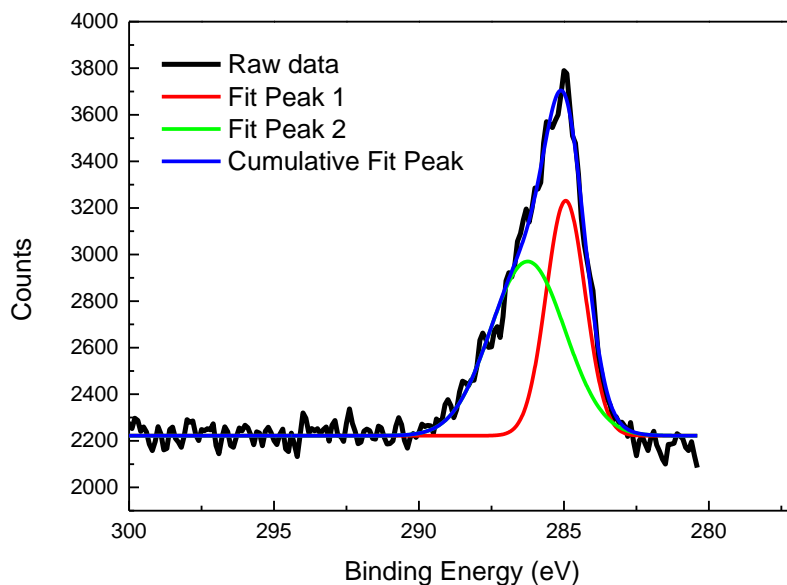


Figure 5.19 High-resolution XPS spectrum of C 1s of mSi powder.

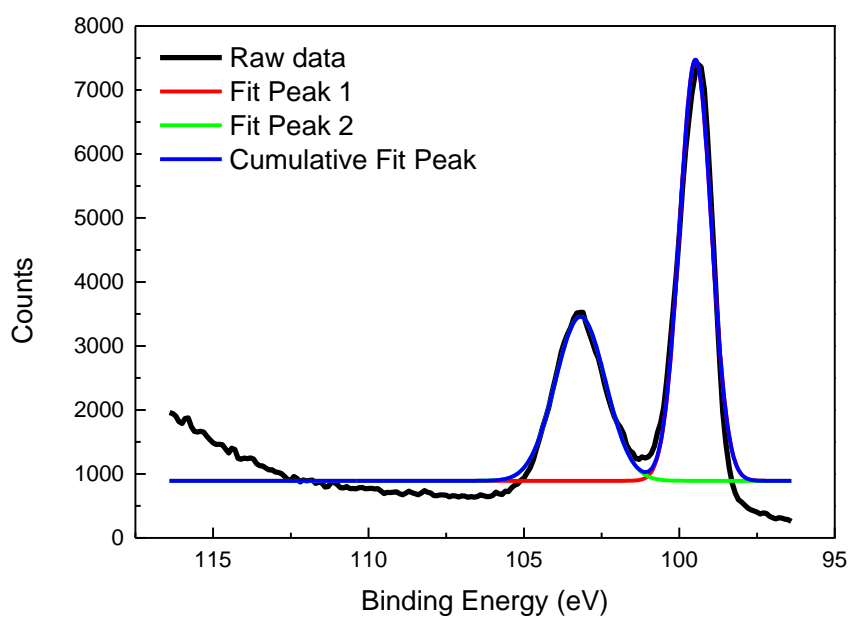


Figure 5.20 High-resolution XPS spectrum of Si 2p of mSi powder.

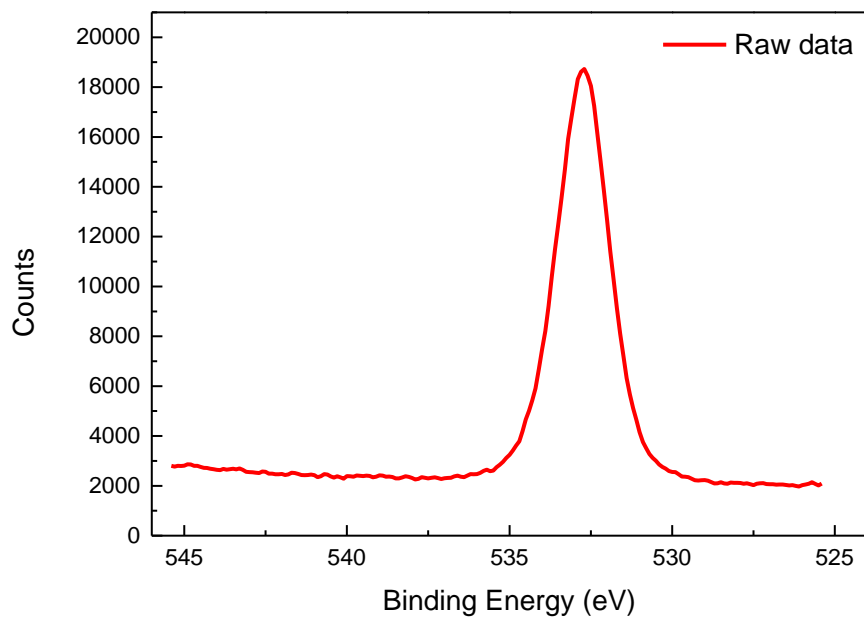


Figure 5.21 High-resolution XPS spectrum of O 1s spectrum of mSi powder.

5.5 Additional studies on metal assisted chemical etching of silicon

In order to increase the surface area of silicon with MACE technique, additional studies were carried out with different metals and oxidizing agents other than AgNO_3 and H_2O_2 . Alternative metals and oxidizing agents as well as surfactant materials were also investigated.

If the electronegativity of a metal nanoparticle is higher than silicon it can attract electrons from Si to become negatively charged [42]. As shown in the Figure 5.22, Ag has a superior etching performance over other elements (Au, Pt, Cu, or Fe), on the other hand it is an expensive and environmentally unfriendly material compared to its alternatives.

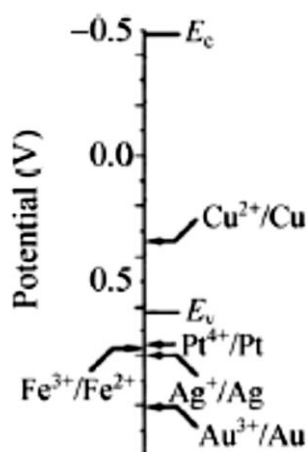


Figure 5.22 Comparisons of electrochemical electron energy levels of five redox systems in HF solution between Si band edges (E_c and E_v are the conduction and valence band energies, respectively) [42].

[Cu (Copper(II) nitrate hemi(pentahydrate) ($\text{Cu}(\text{NO}_3)_2$) and Fe (iron (III) nitrate ($\text{Fe}(\text{NO}_3)_3 \cdot 9\text{H}_2\text{O}$) ingredients were used as the metal content for the first solution. However, they did not deposit on the surface of the silicon powder that is why two-step etching was not successful. Best deposition metal was silver.

Cu and Fe were also used for one step etching. Porous structure was obtained using $\text{Fe}(\text{NO}_3)_3$ as oxidizing agent with the solution parameters of 0.135M $\text{Fe}(\text{NO}_3)_3$ and 5M HF, solution temperature was 50°C and etching duration was set to 60 minutes. Figure 5.23 shows the images of the etched powders with different oxidizing agents. Bigger pores were obtained by using Fe source. There was some scratches on the particles (Figure 5.23-a and b). However, copper did not successfully generate a porous structure (Figure 5.24 – a and b).

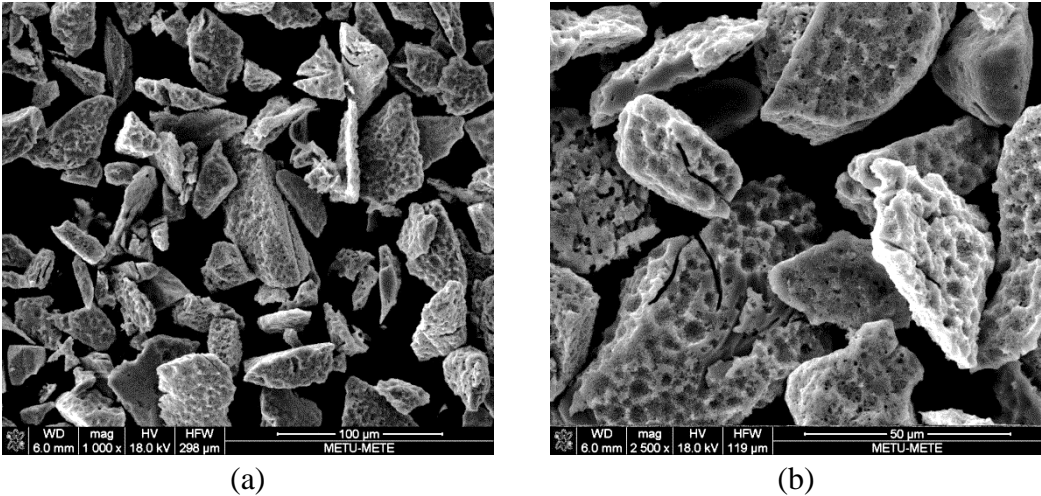


Figure 5.23 SEM images of the sample produced using one-step etching with $\text{Fe}(\text{NO}_3)_3$, (a) x1000, (b) x2500 magnifications.

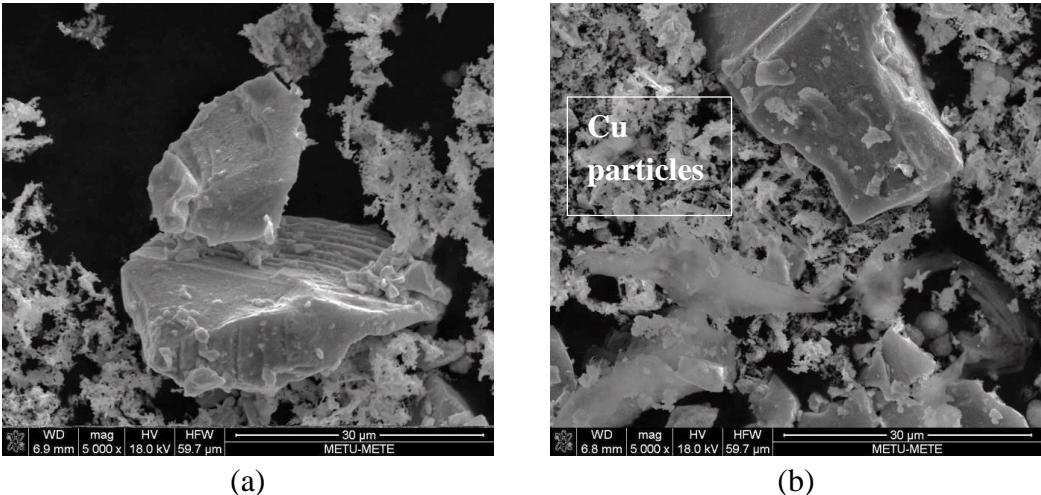


Figure 5.24 SEM images of the sample produced using one-step etching with $\text{Cu}(\text{NO}_3)_2$, (a) and (b) at x5000 magnifications.

After obtaining remarkable porous structure with $\text{Fe}(\text{NO}_3)_3$, etching duration was studied and the structure like in Figure 5.25 was achieved after three hours of etching. Surface area was measured as $7.8 \text{ m}^2 \cdot \text{g}^{-1}$ after etching which is close to the two-step etched powder.

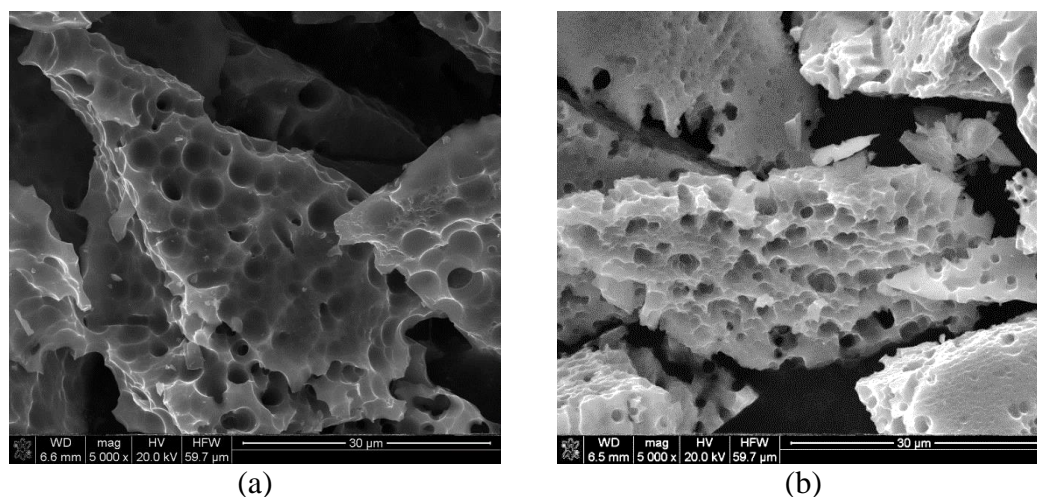


Figure 5.25: SEM images of the etched samples with the solution parameters of 0.135M $\text{Fe}(\text{NO}_3)_3$ and 5 M HF, solution temperature was 50°C and etching duration was set to 180 minutes.

This powder was tried as the base powder for multi-dimensional silicon etching. Standardized etching was applied, Figure 5.26 shows the images of processed particles. Surface area of this powder was $11.4 \text{ m}^2 \cdot \text{g}^{-1}$. The difference between standard mSi production and three step etching was unsubstantial when the etching time is taken into consideration. As a result, two-step etching was preferred over three-step etching.

Inhomogeneous structure of the etched particles were showed by FIB method in Section 5.4. To increase homogeneity, anionic surfactants were used as additives. At both silver deposition steps and etching steps, Cetrimonium bromide (CTAB), 90% 2-amino-2-methyl-1-propanol solution (AMP-90, ANGUS Chemical Company), Disperbyk-180 (BYK-Chemie Gmb, Germany), Sodium dodecyl sulfata (SDS) and

Benzotriazole (BTA) were tried as agents. Results were not promising to change the experimental method. So, etching operation continued without surfactants.

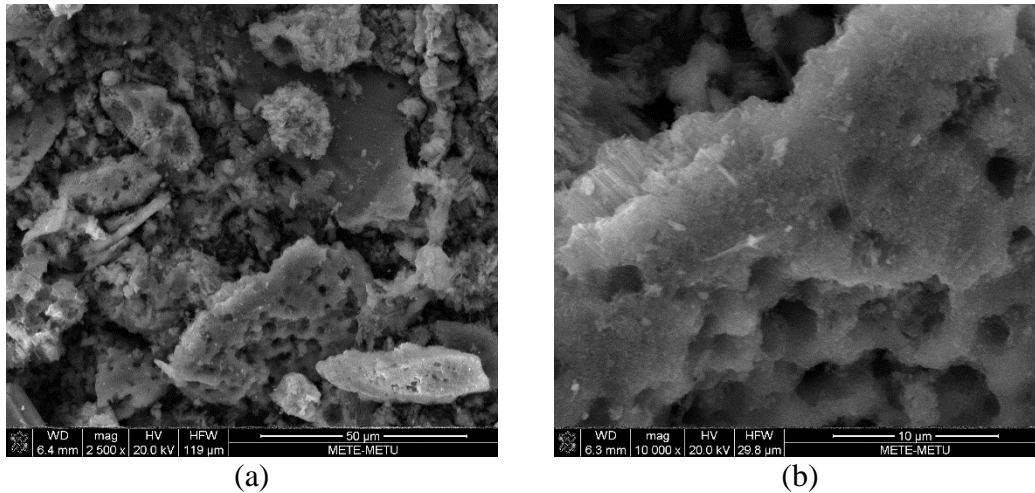
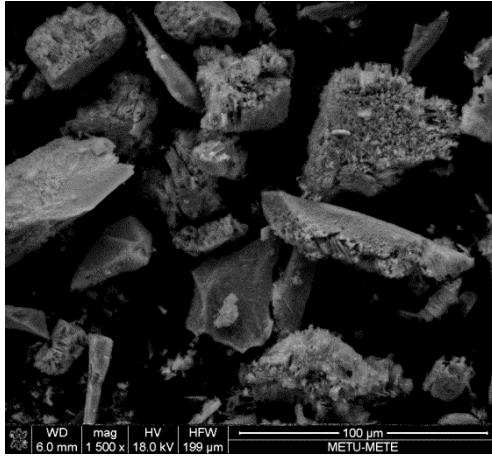


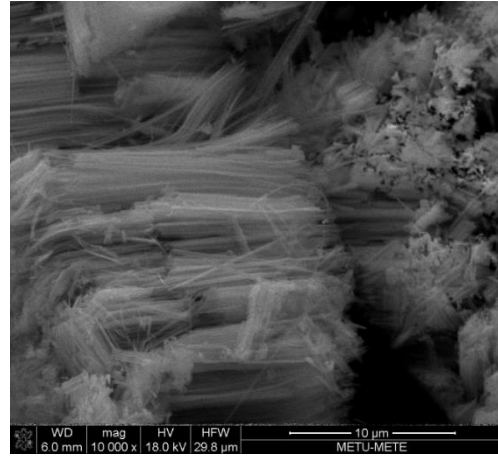
Figure 5.26 SEM of three step etched silicon powder, (a) 2500x, (b) 10000x magnifications.

Lastly, other oxidizing agents with the etching solutions were tried, such as $\text{H}_2\text{O}_2/\text{K}_2\text{S}_2\text{O}_8/\text{KClO}_4/\text{K}_2\text{Cr}_2\text{O}_7/\text{Fe}(\text{NO}_3)_3$. Experimental procedure for these oxidants were the same with the standardized etching solution. Among these oxidants, only the results of $\text{Fe}(\text{NO}_3)_3$ were decent enough. . Figure 5.27 shows the images of this sample. In Figure 5.27 – b columnar structure is obvious. Other oxidants did not produce any substantial oxidizing effect.

After these trials, it was concluded that $\text{Fe}(\text{NO}_3)_3$ can be used both at the metal deposition solution to create bigger pores and at the etching solution for oxidation of silicon powder. Despite of this; because 3-step etching was dismissed and hydrogen peroxide was preferred due to being more economical, etching studies were continued with conventional two-step etching method.



(a)



(b)

Figure 5.27 SEM images of the sample produced by two-step etching using AgNO_3 at metal deposition step and $\text{Fe}(\text{NO}_3)_3$ at etching step, (a) x1500, (b) x10000 magnifications

CHAPTER 6

INDUCTION PLASMA SYNTHESIS

6.1 Introduction

Most of the matter is in plasma state in the universe. A plasma consists of ionized particles interacting with each other. Plasmas are widely used in the fields of astrophysics, laser-matter interaction, technology, fusion, and so on [43].

With the development in nanomaterials, the use of plasma torches triggered an evolution in the field of nano-powder production. Among all the alternative processes, thermal plasma technology has the most potential for low-cost and large-scale production. Another benefit that promotes thermal plasma method is its ability to synthesize materials using both gas, liquid and solid precursors and to allow size reduction of a solid precursor (metal or non-metal powders). For example, Aktekin et al. did produce Mg_2Ni nanoparticles around 100 nm in size with thermal plasma. As starting materials, they used micron sized Mg (300 mesh) and Ni (325 mesh) powders [31].

Typical examples of thermal plasma torches are (1) transferred DC plasma torch, (2) non-transferred DC plasma torch and (3) RF plasma torch. Figure 6.1 shows the diagrams of these torches.

Transferred DC plasma torches use target metals as electrodes. Target metal (anode electrode) evaporates by the transferred arc plasma during the process. The main characteristic of this method is that the rate of generated nano-sized metal particles is

strongly dependent on physical properties (such as heat of vaporization and melting point) of target metals. The system is usually non-continuous due to the nature of the anode electrodes being consumable.

Non-transferred DC plasma torch emerged as an alternative to the transferred DC plasma system. At this type, precursor materials are injected to the torch flame. Electrodes are used only for plasma torch formation. The disadvantage of this system is to provide full evaporation of precursor materials during their flight in plasma flame.

Shortcomings of both transferred and non-transferred plasma torches were solved by RF plasma systems. In this method, precursors are preheated before injecting along the centerline of the torch. There is no need for electrodes at this system which is advantageous in terms of high purity nano-particle production. Besides, axial feeding of precursors increases the residence time and decreases the required torch lengths. This feature allows many micron-sized metal and ceramic powders with high melting points to be heated up and brought to the evaporation point by the RF plasma torch system. Any kind of gas can be used in RF plasma systems to generate the plasma, regardless of its oxidative, reductive, or reactive properties. The applied power and consequently the reaction temperature can be independently controlled from the gas composition and flow rate. Heating process of the injected precursors is dependent on various operation parameters like plasma input power, feeding rate and size of the precursor material [44, 45].

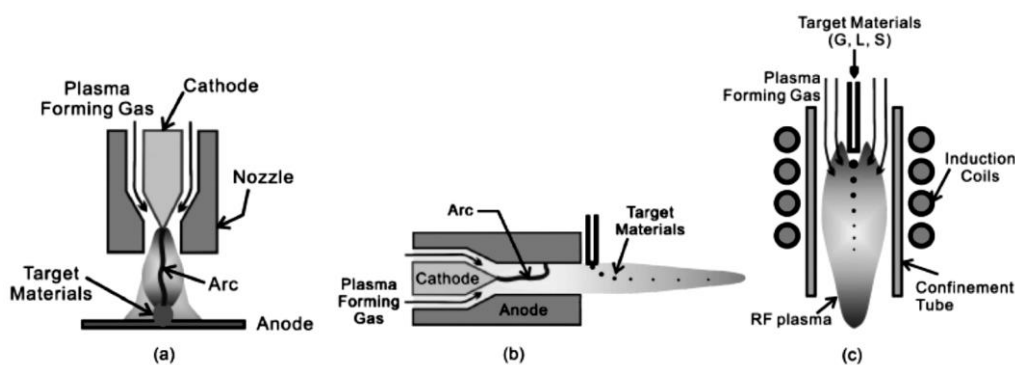


Figure 6.1 Different types of thermal plasma torches, (a) Transferred DC Plasma Torch, (b) Non-transferred DC Plasma Torch and (c) RF Plasma Torch[45]

Production of metal nano-powders has difficulty in terms of handling. They should be passivated before exposure to atmosphere. Core-shell structured nano-materials, such as nano-metal particles encapsulated by carbon cage, could be easily produced by thermal plasma systems [46-48]. However, silicon was not successfully processed by this system because of its strong tendency of carbide formation. Lee, Chang-Hyun et al. synthesized Si/SiC nano-powder via non-transferred arc thermal method with Si/C mol ratios of 1/1 and 1/1.5. They obtained 20-60 nm sized Si/SiC nano-composites in both specimens. In the XRD data, both α and β SiC peaks existed [49]. Another study was done to produce SiC powder from elemental silicon and methane by using induction plasma technique. This reaction route involves evaporation of the injected pure silicon powder and carburization of silicon vapor using methane. Their silicon feed rate was $4 \text{ g}\cdot\text{min}^{-1}$ and Si/C molar ratio was 0.7. Mean particle diameter of silicon powder was $100 \mu\text{m}$ and final composition of the product was 49.2 wt% Si and 50.8 wt% SiC. They increased the SiC content by using smaller particle sized silicon powder ($45 \mu\text{m}$) up to 98 wt%. Particle size of these processed powders were between 40-80 nm. XRD results showed that the obtained powders contain metallic silicon, free carbon (graphite) and SiC (α and β polymorphous) [50].

Zhong, L. et al. produced an anode material that contains thermal plasma synthesized silicon quantum dots, PVP and carbon nanotubes. Their anodes maintained $1000 \text{ mAh}\cdot\text{g}^{-1}$ capacity for 200 cycles. To produce silicon, silane was used as base material. Final silicon quantum dots had a particle size of 10 nm. They said that plasma process yields $14\text{-}52 \text{ mg}\cdot\text{h}^{-1}$ nano-silicon particles and is easily scalable through parallelizing. In this case, PVP had an important role, which was annealed at 500°C and restructured the anode material. Without PVP addition, anodes showed smaller capacity and fast decay in the performance. After 200 cycles the capacity fell to $200 \text{ mAh}\cdot\text{g}^{-1}$. Annealing of PVP acted as a carbon source for the formation of an amorphous carbon matrix, which surrounds the silicon nano-particles, and at the same time creating a bond with the carbon nanotube. PVP also improved the carbon nano-tube dispersion in the non-polar solvent of choice, and had been claimed to be very successful regarding improving the cycle lives. The only problem about the produced anode was the presence of amorphous silicon carbide. The formation of silicon carbide is claimed to

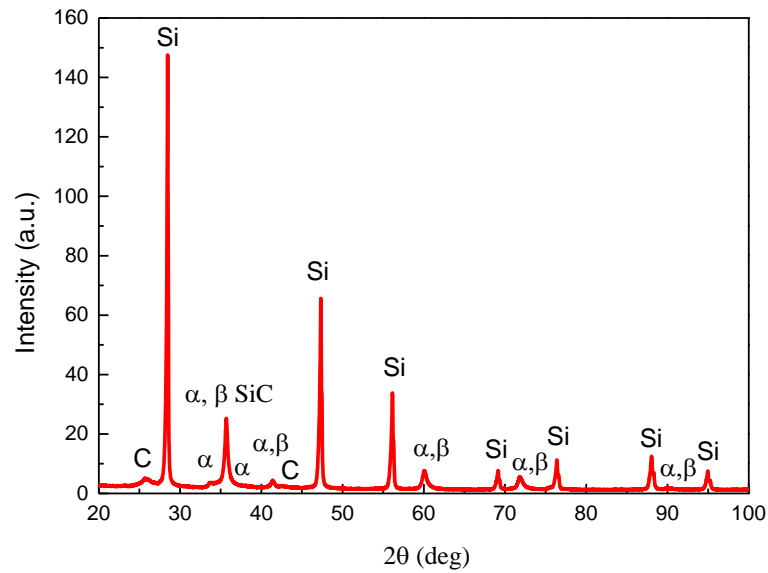
lower initial cycle capacity of the structure ($\sim 1600 \text{ mAh.g}^{-1}$) because; silicon carbide is rendered inactive during the lithiation process. [51, 52]

6.2 Structural Characterization of Induction Plasma Synthesized Silicon Powder

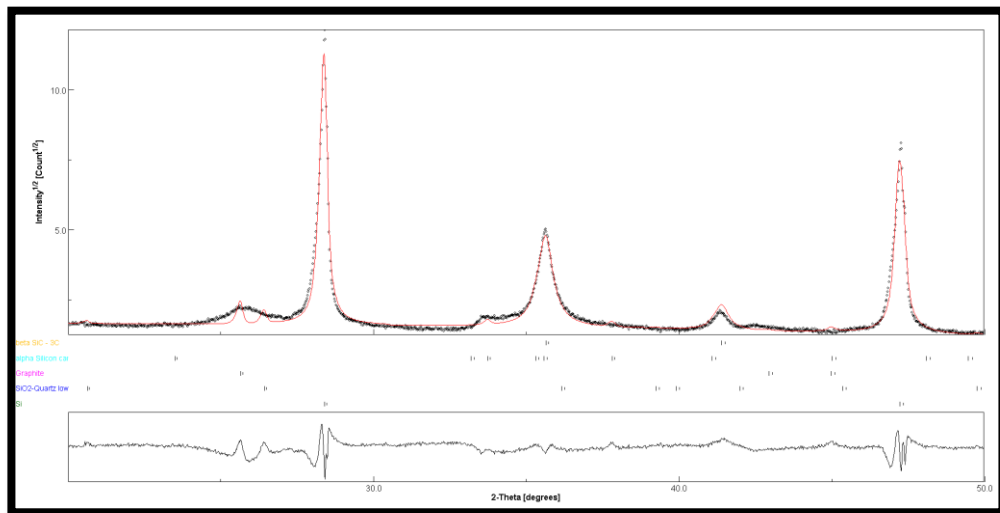
In Section 3.2.3 synthesis route was described in detail. Only one experiment was conducted with induction plasma method and characterization was made for the obtained powder by using XRD, SEM, TEM, XPS, BET, Raman, carbon determination and particle size measurement techniques. After characterization, powder was coated by sol-gel method and electrochemical performances were measured. Thermal plasma method was applied to the as-received silicon powder in order to reduce the particle size below the micron range. Carbon coating was preferred for passivation although, methane gas is known to cause silicon carbide formation during the process [50]. Since the SiC is chemically stable and electrochemically inert it could help to restrict the volume expansion of silicon as shown in literature [53]. Besides, as explained in section 2.2.5.1, the inactive carbon matrixes function for either buffering the strain produced during electrochemical cycling or a uniform distribution of Si particles, which is desirable to accommodate isotropic volume expansion. To lower the SiC amount molar ratio of C/Si was set to 0.5, which is much smaller than the usual [50].

First characterization was done to understand the chemical composition of produced powder via XRD technique. Peaks were determined by Match program and after that quantitative analysis were done by Maud. Figure 6.2-a gives the peak identities and b gives graph after obtaining the Rietveld analysis. Table 6.1 summarizes the results. It showed that approximately 63 wt% of the total powder is made from silicon phase and 33 wt% is β and α SiC. Silicon dioxide amount was found ~ 0.9 wt% and the remaining is carbon/graphite (Note that to understand the bond structure of the carbon phase in detail, Raman spectroscopy was also used). Carbon content was less than 3 wt%. However, the peak of carbon is very broad and close to the oxide peak, therefore

successful refinement was not possible. Carbon content was measured with carbon-sulphur-determinator. The carbon was at 6 wt%. However, it calculates all the carbon content, including graphitized or disordered carbons and carbides.



(a)

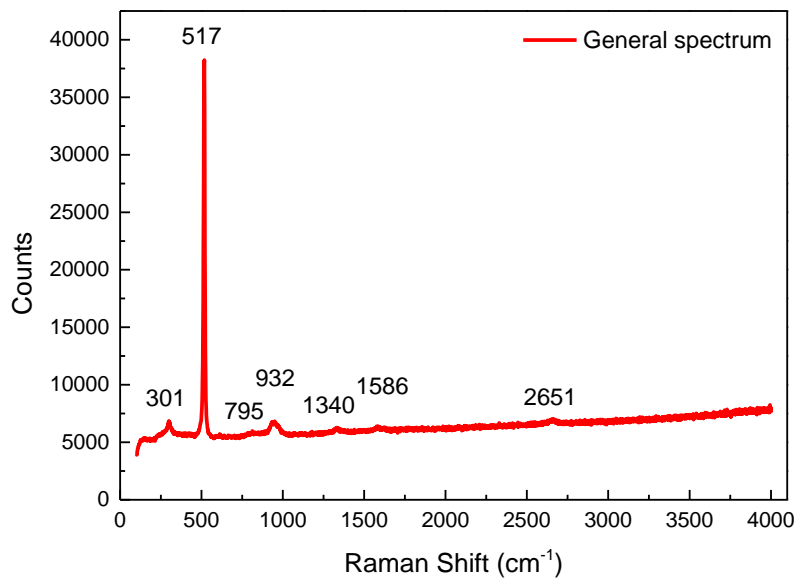


(b)

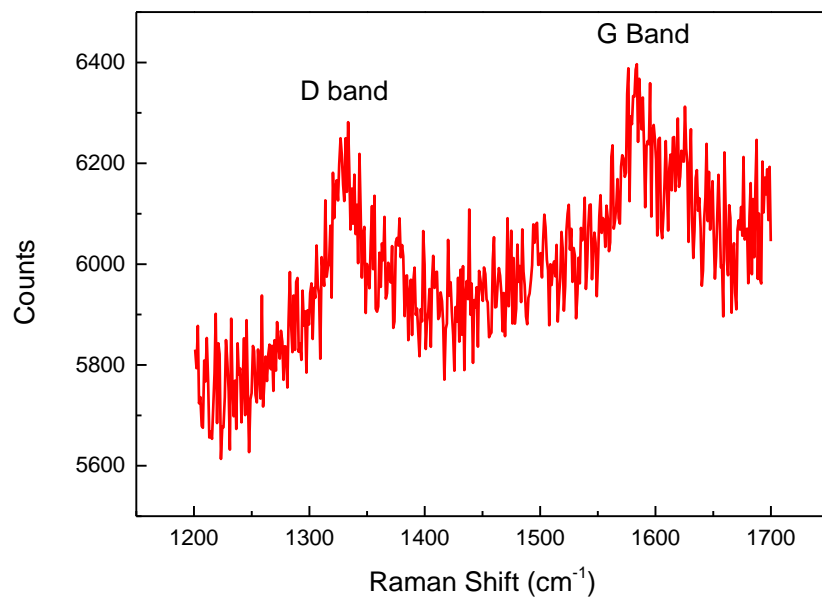
Figure 6.2 Phase identification of induction synthesized silicon powder (a) XRD patterns of the powder, (b) Rietveld analysis obtained by MAUD program.

Table 6.1 Results of the Rietveld refinement.					
Rwp value (%)			14.84		
Existing Phase	Amount (wt%)	Symmetry	Space Group	Unit cell dimensions	
				a (Å)	c (Å)
Si	62.99	cubic	Fd-3m	5.4403	
SiO₂ (Quartz low)	0.88	trigonal	P3121	4.965	5.424
β - SiC (3C)	31.17	cubic	F-43m	4.3595	
α - SiC (6H)	2.02	hexagonal	P63mc	3.1136	15.1248
Graphite	2.94	hexagonal	P63/mmc	2.43	6.94

A typical Raman spectrum taken from the sample is shown in Figure 6.3-a, b. The peaks at 301, 517 and 932 belong to crystalline silicon. The main peak for bulk silicon is normally located at 521 cm^{-1} and the shift to 517 cm^{-1} is related with the reduced crystallite size. This is consistent with the literature [54, 55]. The peaks at 1340 cm^{-1} are labeled as the D-band, and this band is associated with the vibrations of carbon atoms with dangling bonds for the in-plane terminations of disordered graphite. The peak at 1586 cm^{-1} (G-band) is closely related to the vibrations in all sp^2 bonded carbon atoms in a 2-dimensional hexagonal lattice, as in a graphite layer. Generally, a ratio of $I(\text{D})/I(\text{G})$ reflects relative disorder and high graphitic crystallinity. The intensity ratio of the D to G band is 0.92, reflecting high graphitic crystallinity of carbon layer. The peaks around 795 and 970 cm^{-1} correspond to the TO and LO phonons of 3C-SiC, respectively, as explained by Xi, G. et al. [56]. The last peak of the spectrum is at 2651 cm^{-1} , in the G^{I} band which is also labeled 2D band. Both the D and G^{I} bands are results from second-order Raman scattering processes in which the D band consists of one-elastic and one-inelastic scatterings, while the G^{I} band consists of two inelastic scatterings. Ordered peaks are probably belongs to carbons coated around silicon particles and disordered peaks are probably belongs to the free carbon that were produced during non-continuous feeding of silicon powder.



(a)



(b)

Figure 6.3 Raman spectra of induction plasma synthesized powder, (a) typical single spectrum obtained, (b) closer look to D and G bands.

Survey spectrum was taken and Si, O, and C peaks were observed with atomic percentages of 30.3, 61.2, and 8.4, respectively (Figure 6.4). After having the results from the survey spectrum, high-resolution spectrum of C1s and Si 2p were obtained. Si 2p spectrum is given in Figure 6.5. The XPS data presented here are in good agreement with the results obtained by XRD analysis. The Si 2p spectrum displays a first Si 2p peak (composed of 2p_{3/2} and 2p_{1/2} due to spin-orbit coupling) assigned to bulk silicon (98.5 eV in red) and another one assigned to surface oxide SiO₂ (103.4 eV in green). Some other Si oxides are also present (peak at the binding energies of around 102 eV). Peak 5, located around 101.6 may belong to silicon carbide. When C 1s spectrum was investigated, similar results with both XRD and XPS Si 2p data were seen. The first peak belongs to SiC (282.97 eV in red) and second peak belongs to C-C bond, which proves the existence of carbon phase (Figure 6.6).

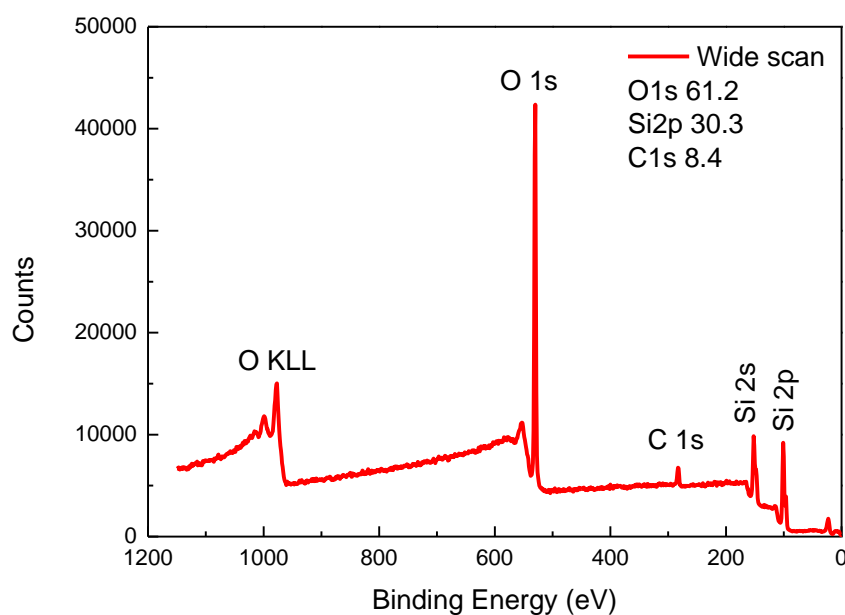


Figure 6.4 XPS data of induction plasma synthesized silicon (Full spectrum).

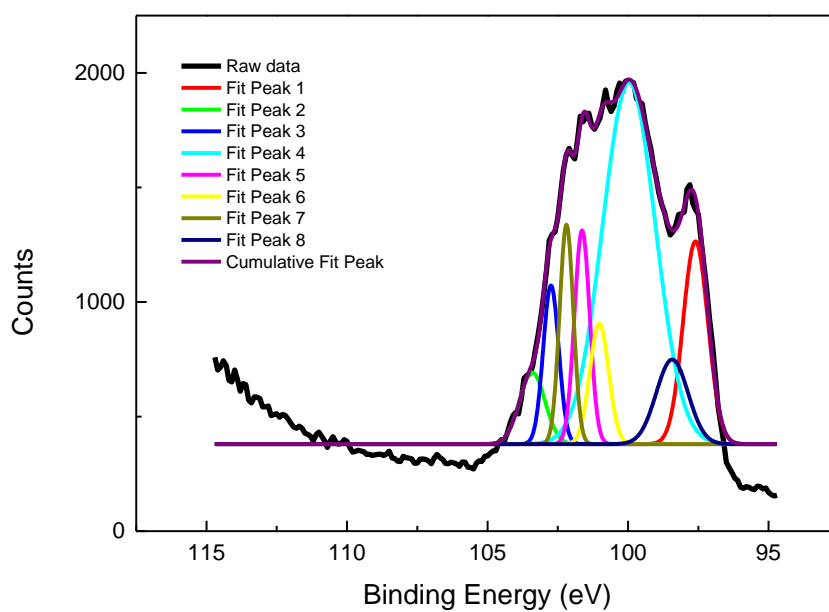


Figure 6.5 XPS spectrum corresponding to Si 2p.

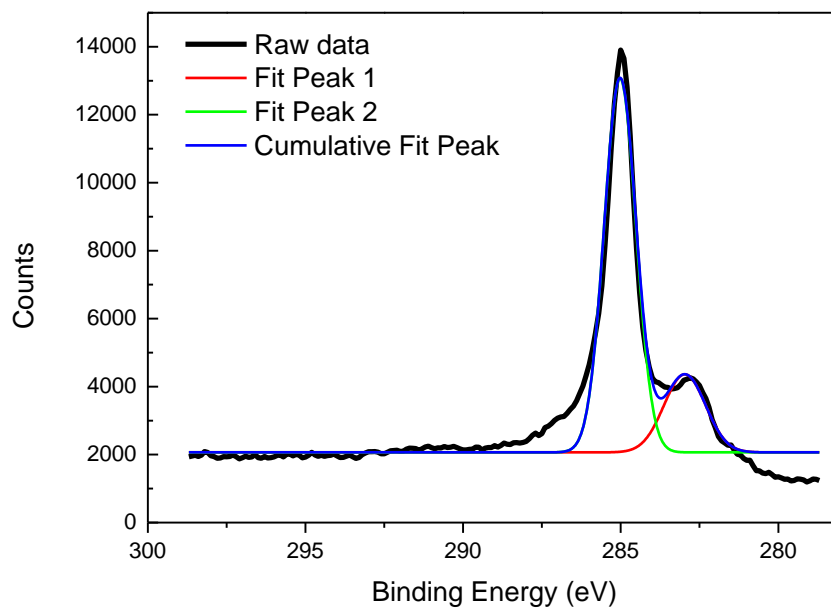
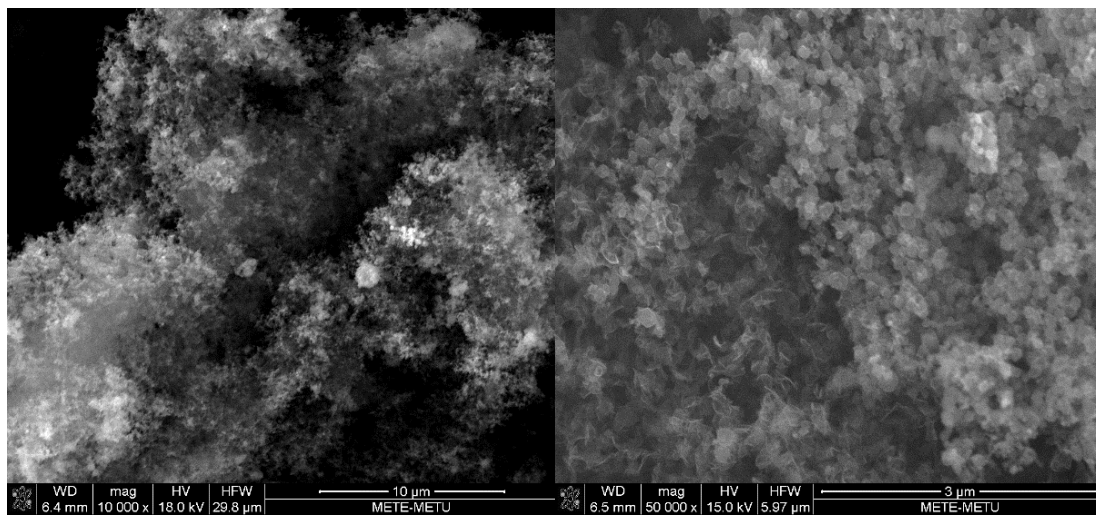


Figure 6.6 XPS spectrum corresponding to C 1s.

After phase determination, morphological properties of the produced powder needed to be investigated with SEM and TEM. Figure 6.7 and 6.8 shows the images, respectively. SEM micrographs show that small particles within the range of 100 – 200 nm diameter exist in the form of agglomerates (Figure 6.7 – a, b, c). They are spherical which is expected in this technique. When TEM images are checked, individual particles can be spotted, also a carbon layer around the particle has been found using HRTEM mode. Lattice fringes inside the particle are shown in Figure 6.8-c.

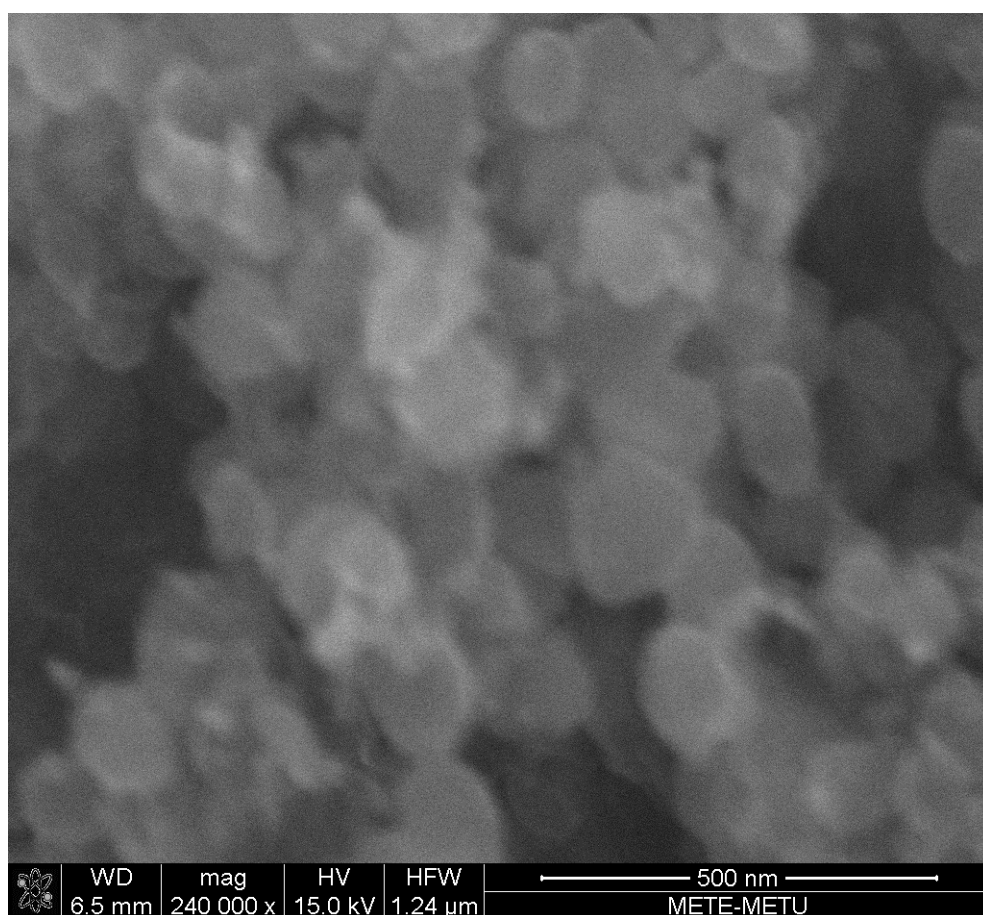
Finally, the particle sizes were measured (Figure 6.9). The average particle size after plasma synthesis process became 2.3 μm which is due to small particles agglomerating. 90 % of the particles were smaller than 5 μm . Surface area of the powder was also found as 7.72 $\text{m}^2.\text{g}^{-1}$. It is three times larger than that of the as-received silicon, and similar to the multi-dimensional silicon powder.

As can be seen from this chapter, induction plasma synthesis is a powerful technique in terms of particle size reduction. The average particle size decreased from 17 micron to 2 μm and the surface area increased from 2.4 to 7.7 $\text{m}^2.\text{g}^{-1}$. Carbon encapsulation was successful, however 33 wt% of existed silicon turned into SiC phase which is electrochemically inert and this means that some of the silicon became inactive which in return lowers the energy density of the anode.



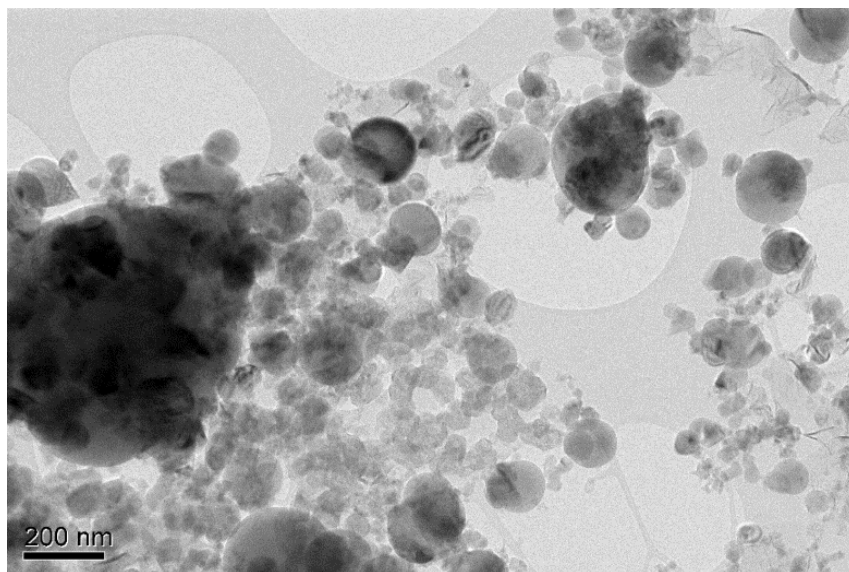
(a)

(b)

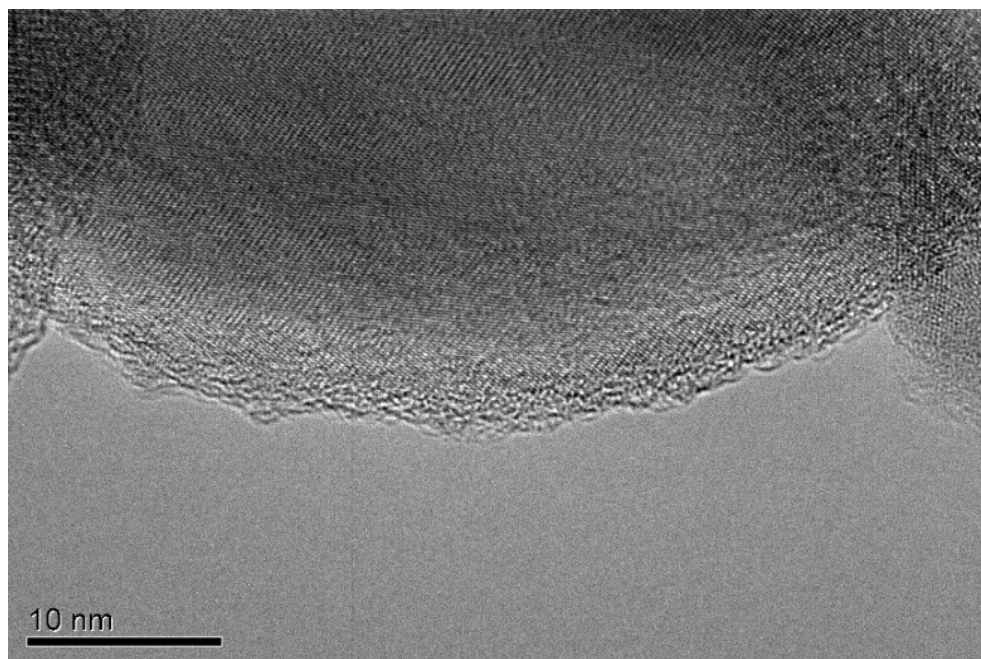


(c)

Figure 6.7 SEM micrographs of produced powder, (a) x10000, (b) x50000 and (c) x240000 magnifications.

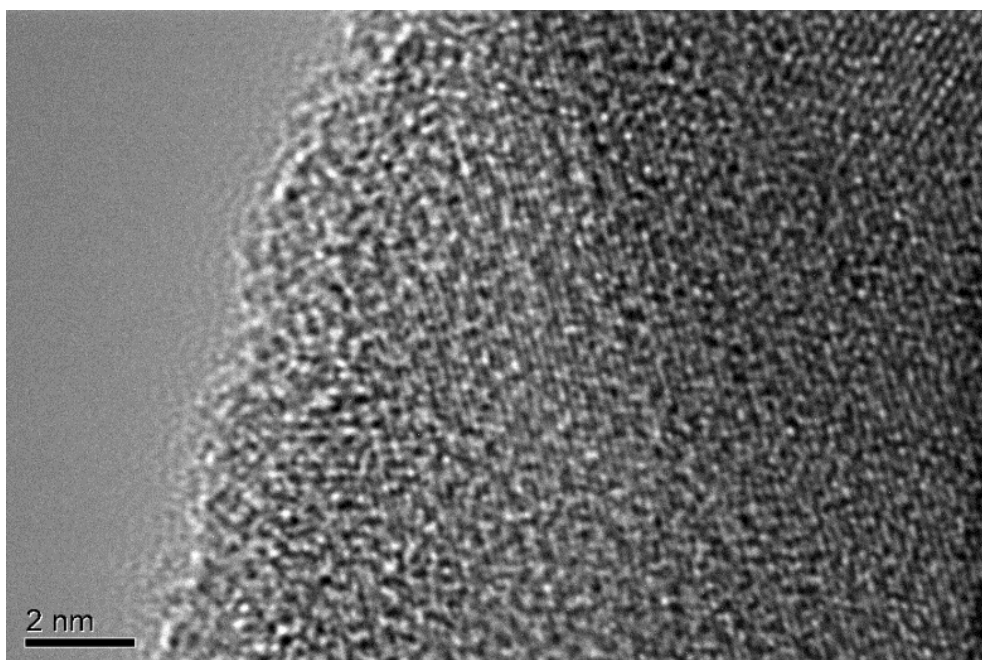


(a)



(b)

Figure 6.8 TEM micrograph of produced powder, (a) general view of the particles, (b) closer look at the carbon layer, (c) HRTEM of the scene of carbon layer and lattice fringes inside the particle



(c)

Figure 6.8 Cont'd.

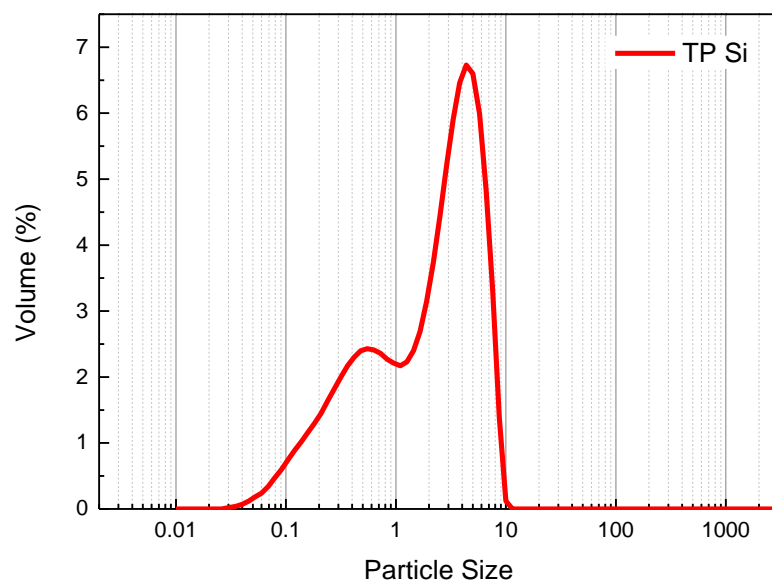


Figure 6.9 Particle size distribution of induction plasma synthesized silicon powder.

CHAPTER 7

SOL-GEL COATING OF PRODUCED POWDERS

7.1 Introduction

Six different types of coating materials were produced by sol-gel method to improve the cycle performance of silicon powders. Steps and details of the sol-gel method were mentioned in the experimental chapter. Selected materials were Li_3PO_4 , Li_3VO_4 , MnWO_4 , ZrP_2O_7 and ZrV_2O_7 . This chapter contains information about sol-gel method and detailed results of each coating materials, especially Pechini Method.

7.2 Fundamentals of Sol-gel method

Simple definition of sol-gel processing starts with the generation of colloidal suspensions (sols) which then are subsequently converted to viscous gels and eventually to solid materials. Powders, fibers, coatings and thin films can be easily produced by using sol-gel method. Figure 7.1 gives a simplified chart of sol-gel process. The main advantages of the sol-gel process are listed below:

- Required temperatures for all stages are low (apart from densification for bulk ceramics). Hence, thermal negative effects of both the coating itself and coated material is reduced, and high purity and stoichiometry can be achieved,
- High purity products can be produced by choosing precursors carefully,
- Doping the product using many soluble organometallic precursors is achievable,
- Highly porous and nano-crystalline materials can be prepared,

- By adjusting chemical modification porosity, pore size and pore wall chemistry of the final product are controlled,
- Use of liquid precursors makes it possible to cast ceramic materials into various shapes without machining or melting,
- The temperature of sol-gel process is usually under the crystallization temperatures of the oxide materials, which enable the production of amorphous materials.

Despite outstanding advantages of the sol-gel process, there are some limitations and disadvantages, such as:

- Expensive precursor materials increase the total cost,
- Careful ageing and drying required, the process becomes time-consuming,
- Dimensional changes upon densification, shrinkage and cracking due to stress during drying process require attention.[57]

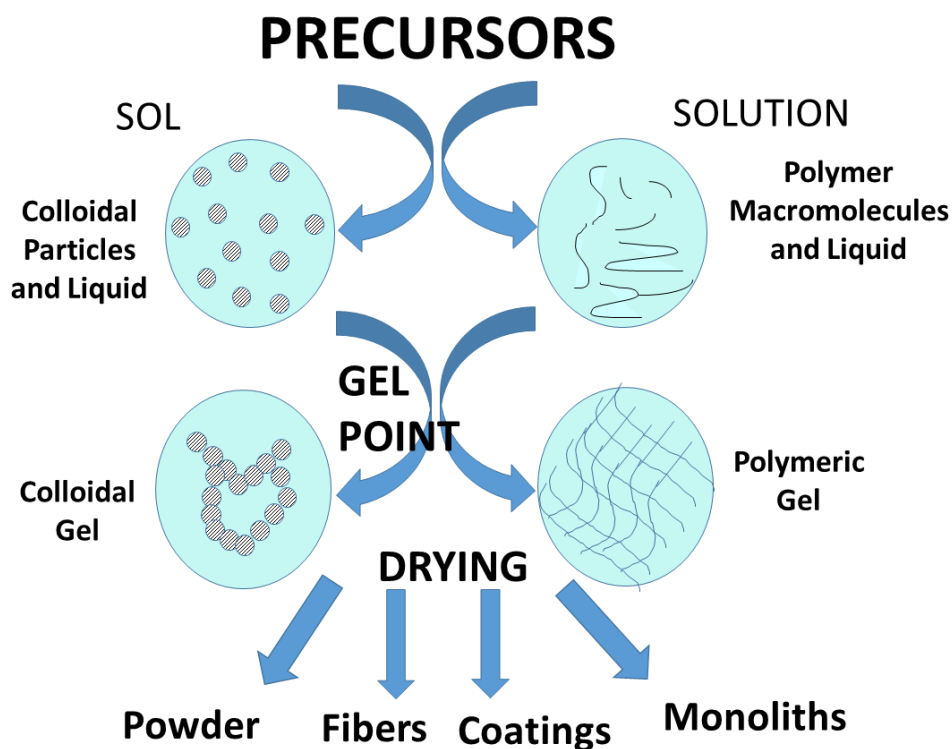


Figure 7.1 Simplified chart of the sol-gel process

7.2.1 Pechini Method

Pechini method is used widely for the production of many complex oxide compositions. Precursors consisting of metal ions (such as metal nitrates, carbonates, sulphates and alkoxides) are complexed in an aqueous solution with a stoichiometric amount of α -carboxylic acid like citric acid. The resulting solution is stirred and then poured on a hot plate, at that time ethylene glycol is added at a mass ratio of 40:60 with respect to citric acid. The temperature needs to be maintained at a constant to allow the resin formation. The resin is then heated to decompose the organic constituents, then ground and calcined to produce the required powder up to several hours at various temperatures. This method enables to manufacture homogeneous and low crystalline products at relatively low temperatures. Yet they usually call for complicated synthesis procedures and/or expensive initial compounds. The resin obtained could be applied on a substrate as a film or as a powder for coating to obtain homogeneous oxide powder [58, 59]

7.3 Coating of High Surface Area Silicon Nanoparticles

Electrochemical degradation is the main hindrance of silicon anodes becoming commercial. Different from the situation with graphite anodes, there is no self-passivating in the natural solid electrolyte interphase (SEI) films generated from carbonate electrolytes. This leads to decomposition of electrolytes and loss of Li ions [60]. To improve the electrochemical stability of silicon, many coating materials are being tried by researchers. A wide variety of methods are being used for coating which can be listed as sol-gel, pyrolysis, mechanical milling, vapor deposition methods, spray pyrolysis, hydro-thermal methods, electro-plating, etc. Some of the most important and widely used coating materials for silicon anodes can be listed as:

- Carbonaceous coatings (e.g. soft and hard carbons) [61-64]
- Inorganic materials (such as Al_2O_3 [65], TiO_2 [66, 67], SiO and SiO_2 [68, 69], ZrO_2 [70], etc.)

- Composites (such as Mg/Mg₂Si [71], Si/Sn-Ni/C [72], Si/C/B₂O₃ [73], Si-C-O glass-like compounds [74])

7.3.1 Properties of selected coating materials in this study

7.3.1.1 Lithium Phosphate (Li₃PO₄)

Lithium phosphate is a fast, solid lithium ion conductor which is often used as a coating for cathodes of lithium-ion batteries. It has two different crystal forms: β and γ-Li₃PO₄. γ-Li₃PO₄ form is more common with its orthorhombic structure and the space group is Pmnb. The lattice parameters are $a = 6.1147 \text{ \AA}$, $b = 10.475 \text{ \AA}$, $c = 4.9228 \text{ \AA}$. Figure 7.2 shows the crystal structure of γ-Li₃PO₄.

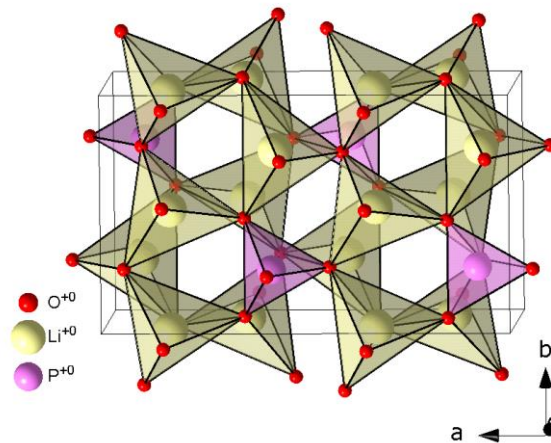


Figure 7.2 The crystal structure of γ-Li₃PO₄.

In the literature, Li₃PO₄ has attracted attention as a coating, which possess good capacity retention in a wide range voltage window. Song et al. enhanced discharge capacity, rate capability and cyclic performance of their Li(Ni_{0.4}Co_{0.3}Mn_{0.3})O₂ cathodes in the voltage range of 3.0-4.8 V [75]. Li et al. also achieved a similar result with Li₃PO₄ coating for LiMn₂O₄ cathodes. They showed that Li₃PO₄ coating reduced

the charge transfer resistance between cathode and electrolyte and resulted in the suppression of Mn dissolution during cycling due to the protection effect. The capacity retention was 85% after 100 cycles, higher than 66% of their pristine cathode material [76].

7.3.1.2 Lithium vanadate (Li_3VO_4)

Li_3VO_4 is also a good Li ion conductor. The crystal structure is orthorhombic and space group is the $P12/c1$ and the lattice parameters are $a = 6.3259\text{\AA}$, $b = 5.4460\text{\AA}$, $c = 4.9469\text{\AA}$. The structure is isotypic with that $\beta\text{-Li}_3\text{PO}_4$ (Figure 7.3).

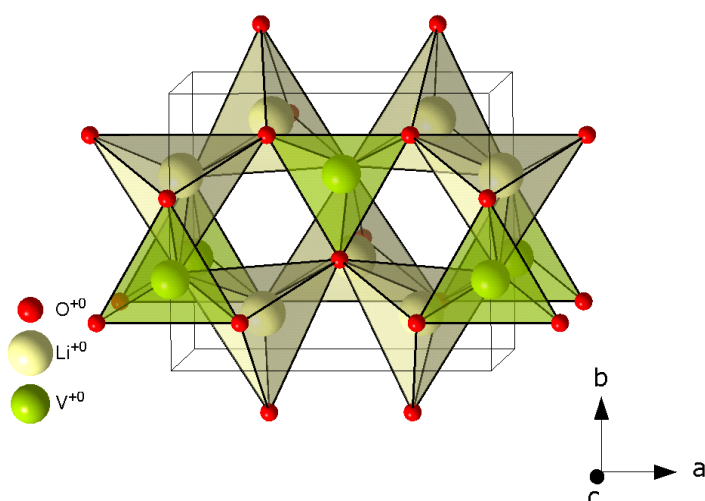


Figure 7.3 The crystal structure of Li_3VO_4 .

In the past, Li_3VO_4 have been studied for the solid electrolyte, nonlinear optical materials, synthesis, and crystal chemistry. Recently, the intercalation properties of lithium vanadates start to attract interest. In literature, it is both used as anode material and for surface modification of cathode materials. For example, Pu and Yu coated Li_3VO_4 to the surface of LiCoO_2 cathode material and improved the performance. With 5.5 wt% coating, 85% of the first discharge capacity was preserved for 100 cycles,

whereas it was only 67% for the bare cathode. Coating also enhanced the high-rate capability [77].

Another study showed that pure phase of Li_3VO_4 might be worthy as an insertion anode material for lithium ion batteries with a considerable reversible specific capacity ($\sim 323 \text{ mAh.g}^{-1}$) and a low and safe discharge voltage ($\sim 0.75 \text{ V vs. Li/Li}^+$). It could retain its structural integrity even after repeated charge/discharge and exhibited promising stability for several tens of cycles [78].

7.3.1.3 Manganese tungstate (MnWO_4)

Manganese tungstate (MnWO_4 , also known as the mineral huebnerite) is a wolframite type tungstate. It is a multi-ferroic material which combines magnetism and ferroelectricity.

The crystal structure is monoclinic and space group is the paramagnetic phase $P2/c$. The lattice parameters are $a = 4.8237 \text{ \AA}$, $b = 5.7552 \text{ \AA}$, $c = 5.0019 \text{ \AA}$ and $\beta = 91.0838^\circ$. It consists of edge-sharing oxygen octahedrals that make zig-zag chains along the c axis, with the Mn atoms located inside the distorted octahedra and the W atoms located between the chains [79, 80] Figure 7.4 shows the crystal structure of MnWO_4 .

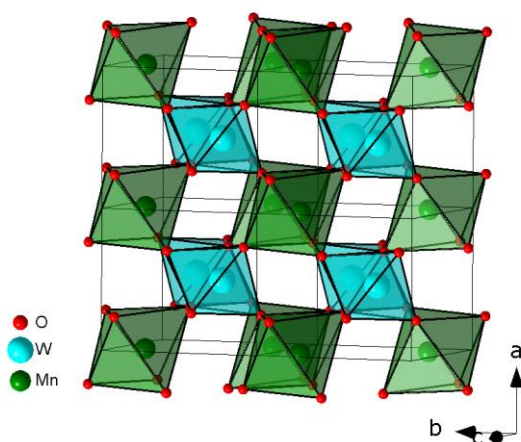


Figure 7.4 The crystal structure of MnWO_4 .

The lithium insertion characteristics of MnWO_4 has been studied previously and found that the compound accommodated only 1 lithium atom while discharging to 0.3V vs Li^+/Li also this reactional phase was not reversible [81].

In a previous work done in our laboratory, MnWO_4 was tested as anode material for lithium ion batteries. MnWO_4 was first synthesized and used in the battery without utilizing lithium. Manganese tungstate had 1000 mAh.g^{-1} initial discharge capacity and inserted lithium atoms numbers were 8 for the first discharge. After that, lithium atoms gradually decreased to 4 and then to 2 at the following five cycles carried at room temperature. This can be interpreted that inserted lithium atoms do not return from the structure. Consequently, the capacity dropped dramatically to 350 mAh.g^{-1} at the end of the sixth cycle. Almost complete amorphization was observed at the end of the cycling procedure [82].

7.3.1.4 ZrP_2O_7 and ZrV_2O_7

The Pa3 space group is typical of many MeX_2O_7 compounds, such as the ZrP_2O_7 and ZrV_2O_7 structure. The ZrP_2O_7 structure consists of a NaCl-like distribution of Zr^{4+} and $\text{P}_2\text{O}_7^{4-}$ ions. Each Zr^{4+} ion is surrounded by six O^{2-} ions. The crystals belong to the cubic crystal system, space group Pa3 (No. 205) with values of 8.2928, 8.8969 Å ZrP_2O_7 and ZrV_2O_7 structures, respectively [83, 84]. Figure 7.5 shows the crystal structure of both materials.

In literature, this structure is studied mostly for its thermal expansion properties. There are few attempts on ZrP_2O_7 for battery applications. Sacks et al. used it as solid electrolyte for the diffusion of Na^+ , K^+ , Ag^+ and Li^+ ions [85].

As mentioned before, a broad range of ceramic materials are used to improve cyclic performance of cathode materials. Wu et al. used ZrP_2O_7 and ZrO_2 with the amount of 1wt%. Their ZrP_2O_7 coating was amorphous. At 25°C , both coated and non-coated samples proved to have decent cycle stability without major capacity fade even after

50 cycles. When temperature is increased to 55°C the pristine and ZrP_2O_7 coated cathodes experienced capacity fading after 150 cycles. ZrP_2O_7 modification did not give the expected effect because at the surface of the high voltage cathode, particles aggregated and scattered. This produced limited cover against surface reactivity especially at elevated temperatures [86]

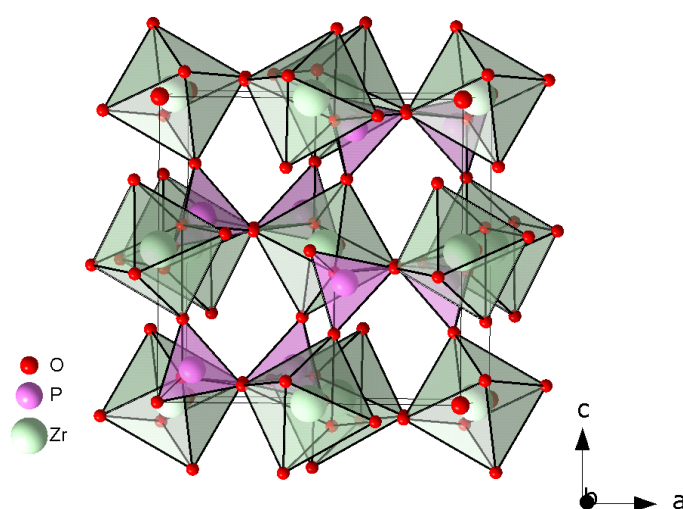


Figure 7.5 The crystal structures of ZrP_2O_7 and ZrV_2O_7 .

7.3.1.5 Carbon

Silicon/carbon composite anode materials have had considerable attention. Carbon is an attractive candidate matrix material because of its superior features. It provides high conductivity, prevents agglomeration of silicon particles, has little volume expansion, and its elastic structure helps to improve cycle life. Another one of its major advantages is that coating it is relatively easy. Numerous methods can be used such as chemical vapor deposition, spray pyrolysis, chemical reaction of gels, combining ball-milling with pyrolysis of a pitch, citric acid or sugar [87]. Below are some examples.

Zuo et al. have reported that the composite of equal amounts of silicon and graphite coated with thermally decomposed pitch exhibit a first discharge capacity of 485 mAh.g⁻¹ with a coulombic efficiency of 70% [88].

Si et al. proclaim a discharge capacity of 1335 mAh.g⁻¹ and charge capacity of 923 mAh.g⁻¹ could be obtained for a carbon-nano-Si (average size 50 nm) composite with 48 wt% carbon during first cycle, giving 69.2% coulombic efficiency. Amorphous carbon coating was done by pyrolysis of polyvinyl chloride (PVC) with chlorinated polyethylene (CPE) at 900°C for 2h. The degradation rate upon cycling was 0.24% per cycle. Their anode could retain 880 mAh.g⁻¹ discharge capacity after 40 cycle [89].

Gu et al. produced Si/C anode material via pyrolysis of citric acid as the carbon source. They used high energy ball-milling method for particle size reduction of their silicon powder and suppressing the aggregation of fine silicon particles. Anodes had 13-15 wt% carbon ratio after thermal treatment and their anode retained 626.7 mAh.g⁻¹ discharge capacity after 30 cycles with their 5h ball-milled sample [87].

Yang et al. prepared silicon/carbon composites at room temperature by dehydration of a mixture of sucrose and silicon powders using concentrated H₂SO₄ with the particle size of silicon less than 100 nm. The composite demonstrated a high initial coulombic efficiency of 82% and a large charge capacity above 560 mAh g⁻¹ after over 75 cycles. The improved electrochemical characteristics are attributed to the uniform distribution of silicon particles in an amorphous carbon matrix, which could buffer the volume change during cycling [90].

7.4 Results & discussion of the coating studies

In this chapter, Rietveld analysis of the coated samples and some SEM images of them will be provided in addition to detailed information about the coated powders.

Four individually processed silicon powders were each coated with six different coating materials. The experimental procedure was described in Section 3.2.4. Coating of different powders was considered successful only if the crystalline phase was present in the X-ray pattern.

Multi-dimensional silicon powders are selected to give detailed information. For other powders, results of the Rietveld analysis are only tabulated to compare the existing phases.

The first coating test was done with Li_3PO_4 gel. Figure 7.6 shows the refinement graph and results are given as inset. The aimed Li_3PO_4 ratio was 3 wt%, but it turned out to be 9.22 wt%. This may have been due to the complications experienced during the coating process. In addition, there was a small amount (0.7 wt%) quartz phase (oxidation of silicon). Figure 7.7 shows the SEM micrographs of coated sample and no change was observed in the structure. The existence of coating material on the Si surface was verified by EDS analysis during SEM session.

The similar experimental procedure was applied to coat Li_3VO_4 . Figure 7.8 shows the refinement graph and results. Rietveld analysis showed that Li_3VO_4 ratio was 5.54 wt% and the amount of quartz phase was higher than the Li_3PO_4 coating. Figure 7.9 demonstrates the SEM micrographs of the coated sample and according to these results there was no change in the structure.

MnWO_4 ratio is 5.18 wt% which is similar to the Li_3VO_4 test results. There was no oxide formation (Figure 7.10). SEM image in Figure 7.11. MnWO_4 peaks are broad which indicates that crystallinity is low.

Hardships of the production process affected the final coating amounts, even though all the calculations of gel coatings were made to obtain 3 wt% ratio. In the case of ZrP_2O_7 and ZrV_2O_7 coating, ratios are 0.99 and 1.84. Oxidation of silicon did not occur even at 900 degrees which means the silicon powder was fully insulated and there was no contact with the atmosphere.

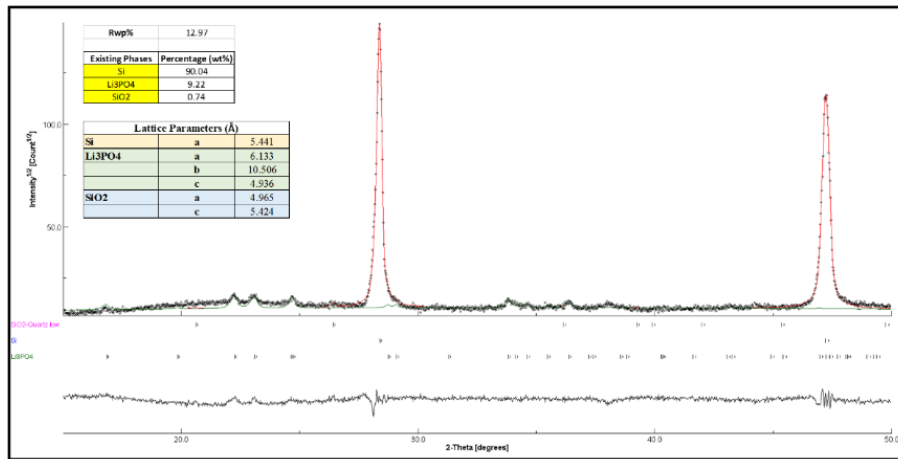


Figure 7.6 XRD pattern of Li_3PO_4 calcined at 600°C for 3 hours.

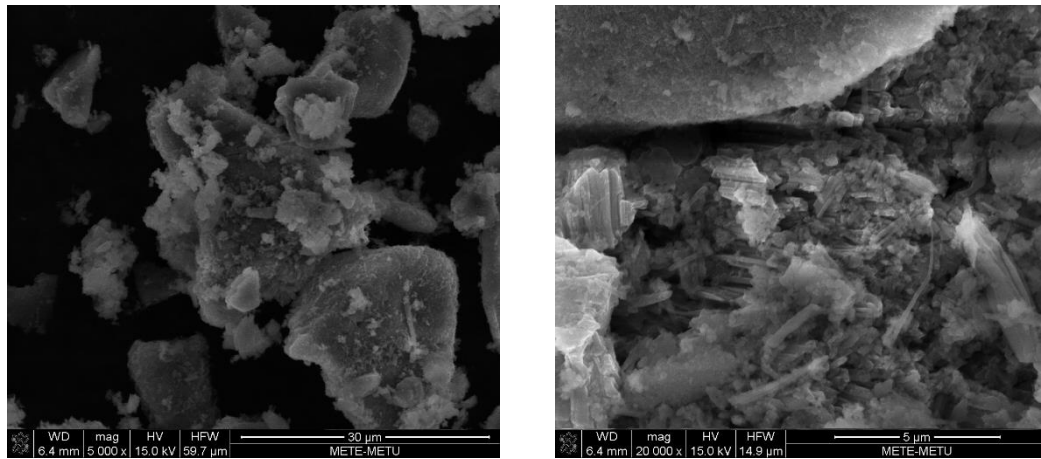


Figure 7.7 SEM images of Li_3PO_4 coated multi-dimensional silicon powder.

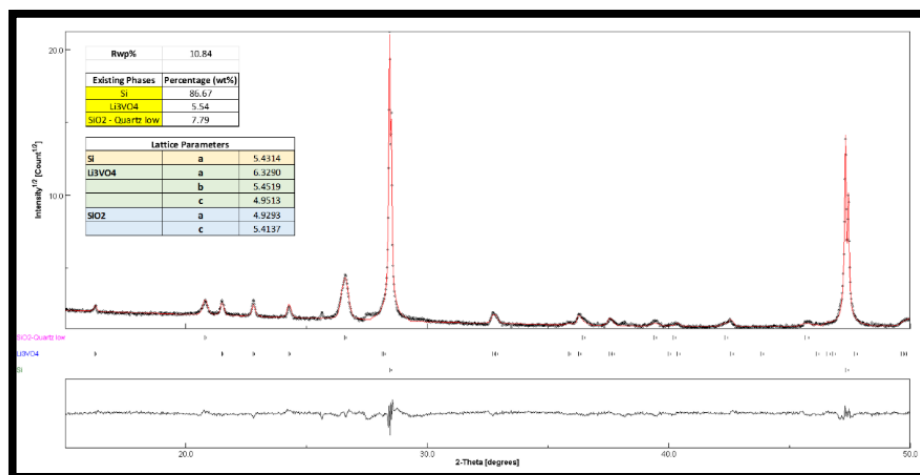


Figure 7.8 XRD pattern of Li_3VO_4 calcined at 600°C for 3 hours.

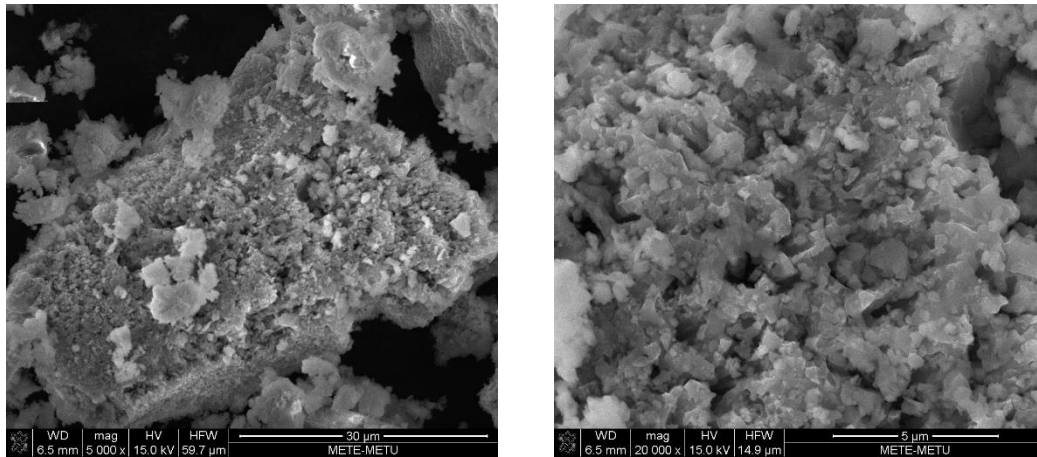


Figure 7.9 SEM images of Li_3VO_4 coated multi-dimensional silicon powder.

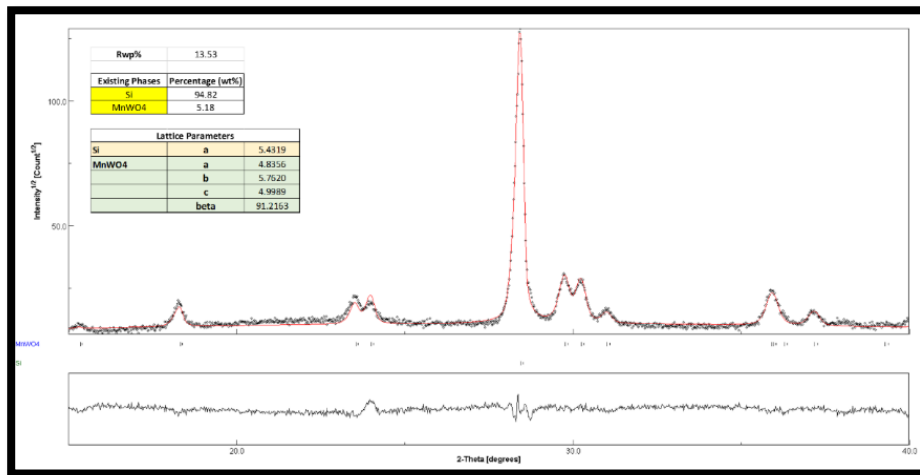


Figure 7.10 XRD pattern of MnWO_4 calcined at 900°C for 2 hours.

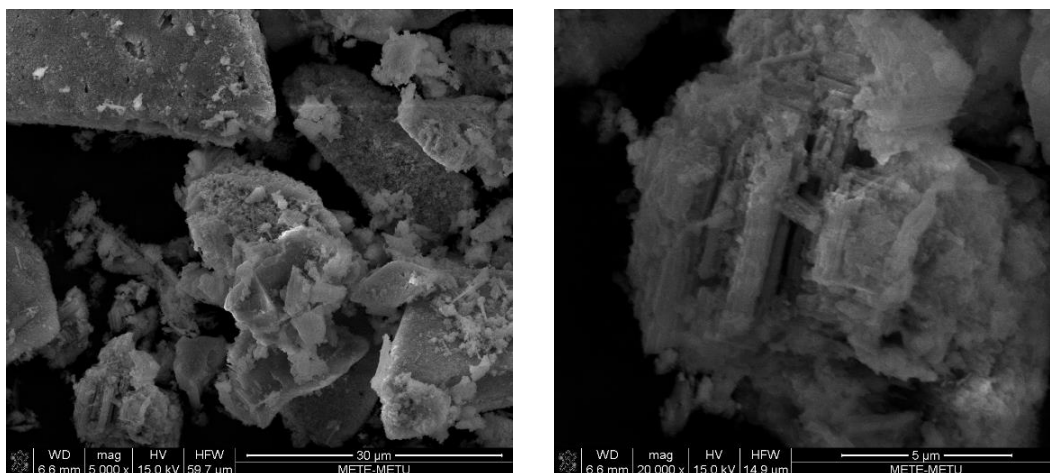


Figure 7.11 SEM images of MnWO_4 coated multi-dimensional silicon powder.

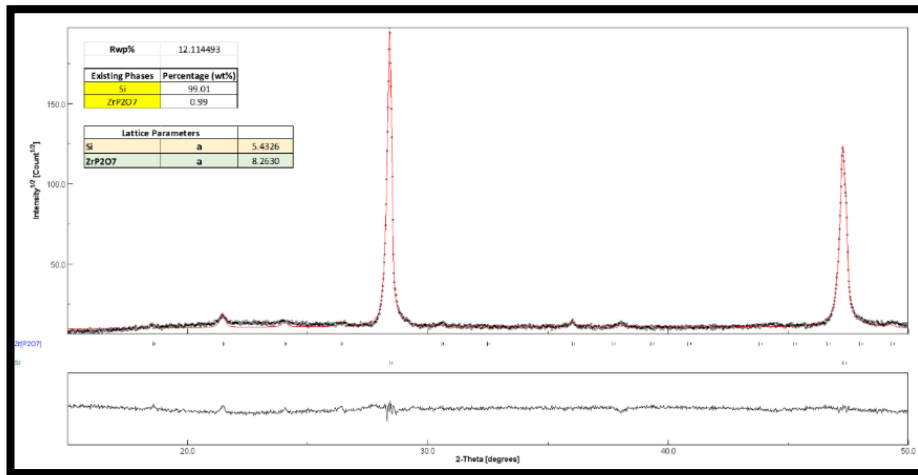


Figure 7.12 XRD pattern of ZrP_2O_7 calcined at 900°C for 2 hours.

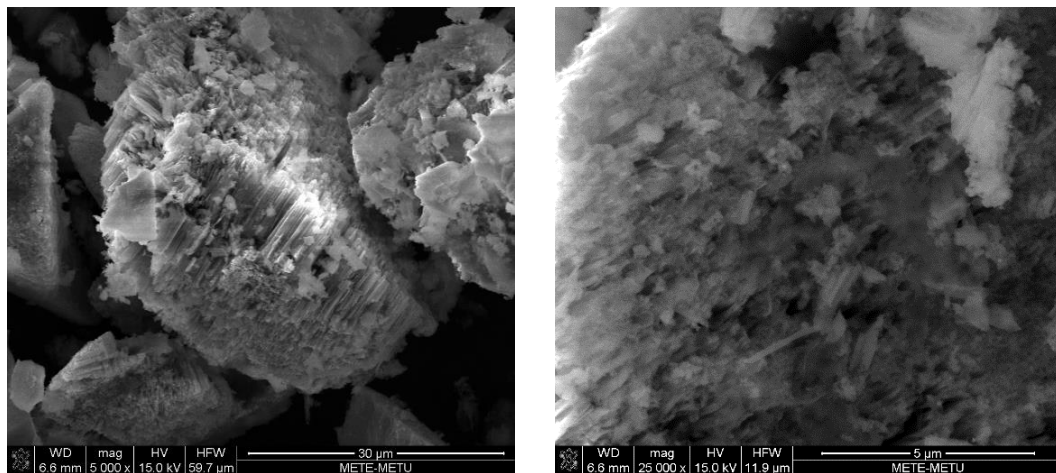


Figure 7.13 SEM images of ZrP_2O_7 coated multi-dimensional silicon powder.

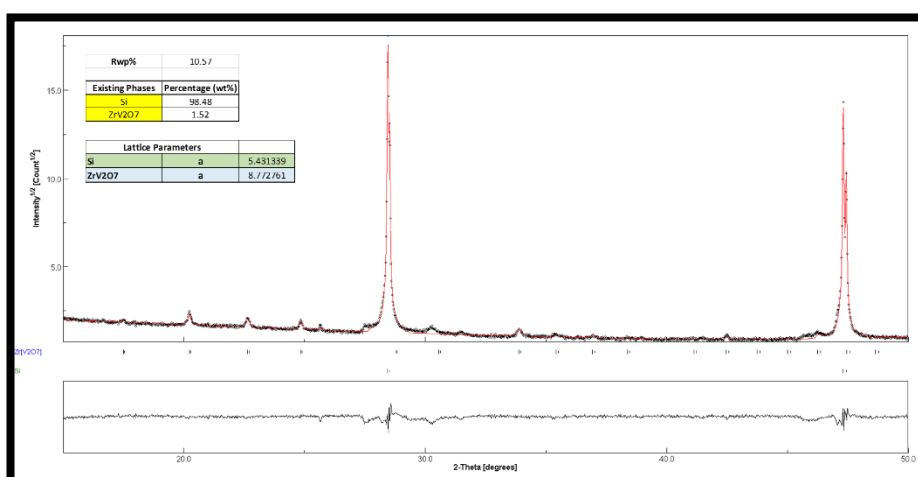


Figure 7.14 XRD pattern of ZrV_2O_7 at calcined at 600°C for 3 hours.

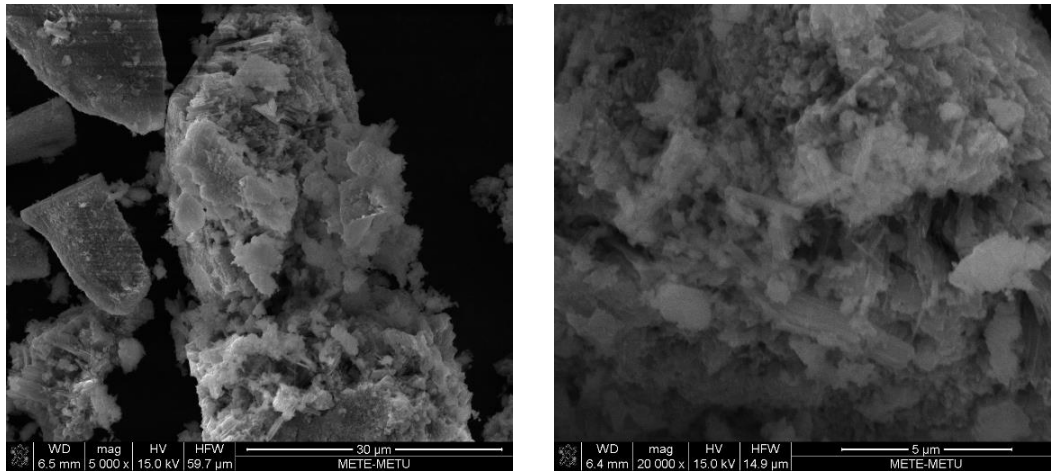


Figure 7.15 SEM images of ZrV_2O_7 coated multi-dimensional silicon powder.

Transmission electron microscope was used to investigate the morphology of the Li_3PO_4 coated multi-dimensional silicon powder in detail. Ultrasonication was used to pull the columnar structure off. Figure 7.16 shows the images. EDS analysis were made to make sure that the structures belonged to the coated silicon before the images were taken. Figure 7.16-a and b gives a general look. The coating is clear at Figure 7.16-c and its thickness was around 10 to 15 nm. A smooth coating layer was created.

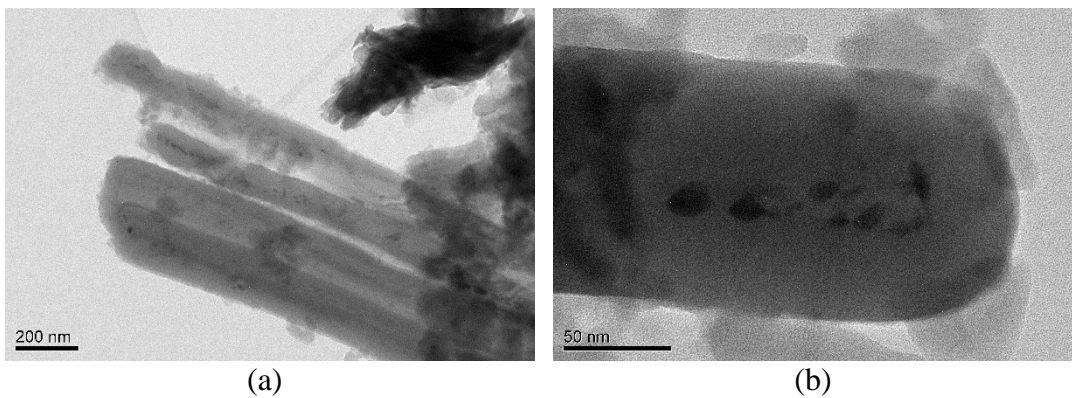
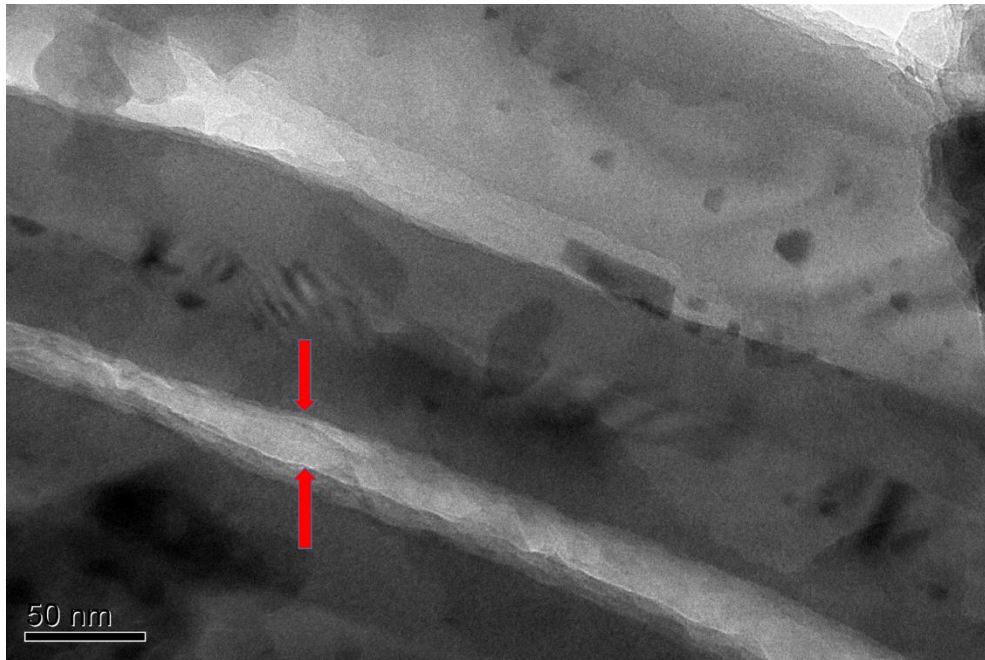


Figure 7.16 TEM images of Li_3PO_4 coated multi-dimensional silicon powder.



(c)

Figure 7.16 Cont'd.

Another TEM image of the Li_3PO_4 coating layer was taken of the induction plasma synthesized powder (Figure 7.17).

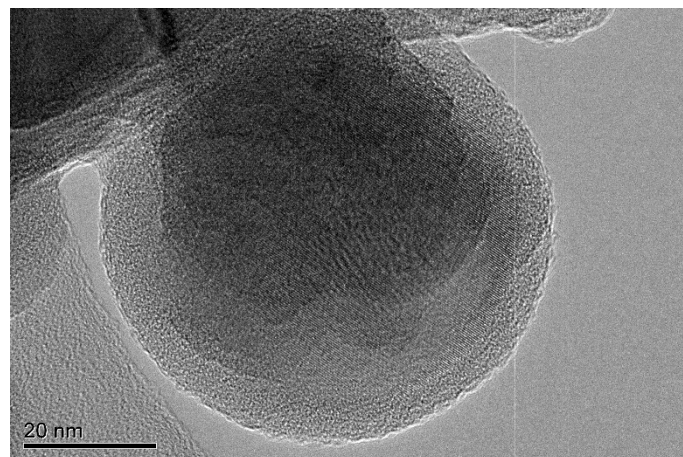


Figure 7.17 TEM images of induction plasma synthesized silicon powder with Li_3PO_4 coating

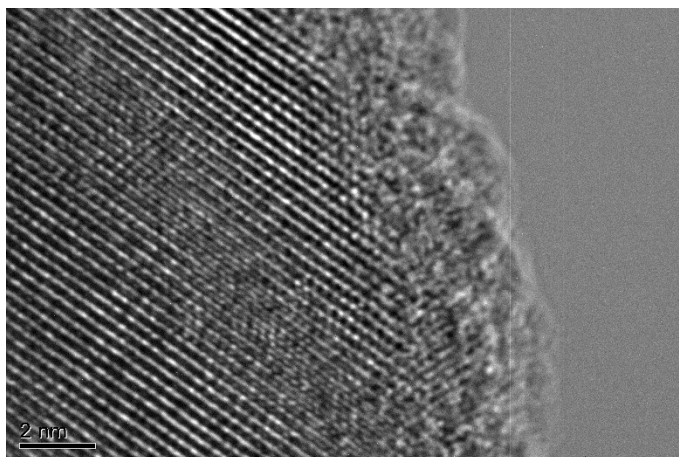


Figure 7.17 Cont'd.

TEM images indicate that the thickness of the coating layer increased compared with the bare induction plasma synthesized powder. According to the XRD results the Li_3PO_4 coating is in the crystalline form. At the HRTEM images, there seems to be epitaxial growth at the interface region. It is difficult to determine whether lattice fringes belong to the coating material or carbon/oxide/SiC. An amorphous layer is seen at the outer shell. Previously, a similar structure was found to be present at the bare powder. At that time, this structure was interpreted as carbon layer. Maybe the fringes inside belong to carbides and Li_3PO_4 is at the outer shell, and its lattice fringes cannot be seen. This is so because coating layer is thin (a few nanometers) which makes it difficult to see.

Same procedures on the base and other processed powders were also followed with similar results. Here, the ratios of existing phases are listed in Table 7.1. The important revelation was; even though the production procedure and used gels were the same, the coating weight ratio changed each time. This is an important finding in terms of the electrochemical performance of anodes. It is important, because all the coating thicknesses will differ and their electrical conductivities will be lower. Hence, the charge transfer resistance of the anode material will be increased. A more detailed discussion will be held at Section 8.

Another important outcome of XRD results was; when mSi/ ball-milled silicon were coated with Li_3VO_4 and when MnWO_4 was used to coat induction plasma synthesized silicon powders, high oxidation has occurred. Especially, induction plasma synthesized silicon powder with MnWO_4 coating was affected from this. Furthermore, all the SiC and half of the Si transformed to cristobalite phase. Also, the MnWO_4 ratio was lower than expected (0.59 wt%). The increase in temperature was the main reason of the oxidation of Si during calcination. Argon and nitrogen atmospheres were also tested to overcome this issue. However, no phase formation was occurred under these conditions, because; for calcination, available oxygen was needed.

Table 7.1 Rietveld analysis of the powders

	Li_3PO_4					
	Rwp%	LP	Si	SiO_2	$\beta\text{-SiC}$	$\alpha\text{-SiC}$
Base Si	13.90	2.97	97.03	-	-	-
mSi	12.97	9.22	90.04	0.74	-	-
B.M. Si	13.06	98.86	0.85	0.19	-	-
TP Si	24.64	7.02	65.72	0.34	26.56	0.36

	Li_3VO_4					
	Rwp%	LV	Si	SiO_2	$\beta\text{-SiC}$	$\alpha\text{-SiC}$
Base Si	17.23	4.73	95.27	-	-	-
mSi	10.84	5.54	86.67	7.79	-	-
B.M. Si	12.07	2.07	55.44	42.49	-	-
TP Si	13.90	4.71	69.14	2.55	21.36	2.24

	ZrP_2O_7					
	Rwp%	ZrP	Si	SiO_2	$\beta\text{-SiC}$	$\alpha\text{-SiC}$
Base Si	14.65	1.08	98.72	0.20	-	-
mSi	12.11	0.99	99.01	-	-	-
B.M. Si	13.79	4.03	95.53	0.44	-	-
TP Si	14.06	2.93	67.37	-	29.26	0.44

	ZrV_2O_7					
	Rwp%	ZrV	Si	$\beta\text{-SiC}$	$\alpha\text{-SiC}$	SiO_2
Base Si	15.92	4.38	95.62	-	-	-
mSi	10.57	1.52	98.48	-	-	-
B.M. Si	16.02	1.60	98.21	-	-	0.19
TP Si	13.72	1.55	72.57	23.54	2.34	

	MnWO_4					
	Rwp%	MnW	Si	$\beta\text{-SiC}$	Cristobalite - High	Coesite
Base Si	12.95	5.77	94.23	-	-	-
mSi	13.53	5.18	94.82	-	-	-
B.M. Si	12.30	9.20	86.02	-	2.30	2.48
TP Si	14.39	0.59	29.67	1.84	67.40	0.50

	Carbon	
	C	Si
Base Si	1.63	98.37
mSi	1.99	98.01
B.M. Si	2.91	97.09
TP Si	2.90	97.10

CHAPTER 8

ELECTROCHEMICAL RESULTS & DISCUSSION

8.1 Introduction

Following the production of active materials, all the anode materials were tested electrochemically to see their performance improvement. Cycle life, cyclic voltammetry and impedance measurements were performed.

In this section, abbreviations in table 8.1 are used to facilitate narration.

Table 8.1 Abbreviations of powders	
As-received silicon	A.R. Si
Ball-milled silicon powder	B.M. Si
Metal assisted chemically etched silicon powder (multi-dimensional silicon)	mSi
Induction plasma synthesized silicon powder	P. Si
Li_3PO_4	LP
Li_3VO_4	LV
MnWO_4	MnW
ZrP_2O_7	ZrP
ZrV_2O_7	ZrV
Carbon	C

8.2 Galvanostatic charge-discharge tests

As the aim of this study is to improve the cyclic performance of a readily available powder, tests began with cycle tests. To gauge the change in the performance, as-received powder was also tested with a rate of 0.2 mA.cm^{-2} during cycling. The cells were cycled for 20 times. Charge-discharge tests were conducted between 0.05 to 1.2 V. To calculate the capacity, only the weight of silicon powder was considered as active material.

The results of the first test is shown in Figure 8.1. It compares the cyclic performances of plain silicon powders. Even though there is a carbon coating layer outside of the induction plasma synthesized powder, it is included in this comparison. Another one will be held with carbon coated powders. The value at the end of pre-cycling is taken as the first discharge capacity. Then, 20 consecutive cycles were carried out.

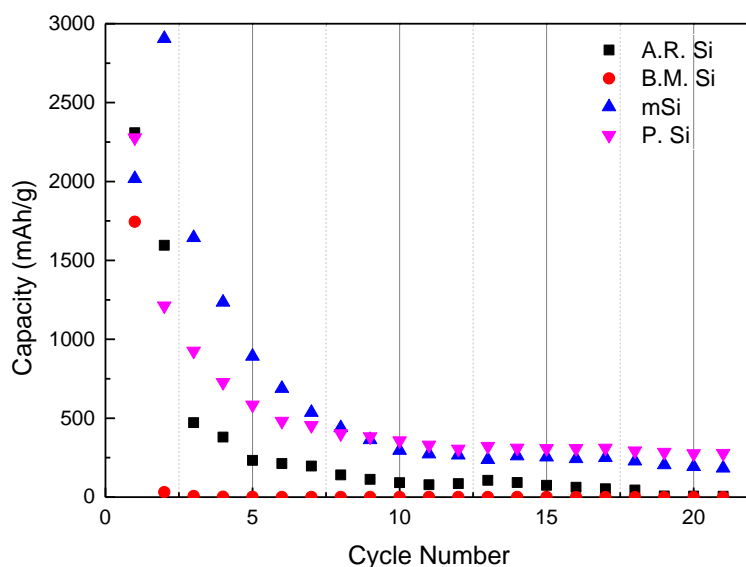


Figure 8.1 The discharge capacity graph of plain powders.

The capacity graph shows that the highest capacity was achieved with mSi powder (2900 mAh.g^{-1}). In the above graph, the first capacity of mSi is lower than the second, although in reality, time was insufficient to fully discharge the material at the end of

the pre-cycling procedure. First capacities of P. Si and A.R. Si were very close ($\sim 1300 \text{ mAh.g}^{-1}$). Although initial capacities of these three powder were in an acceptable range, there was a sharp decrease in their capacity after cycling. The capacity of mSi fell under 1000 mAh.g^{-1} after 5 cycles, whereas it was 3 cycles for A.R. Si and P. Si. After 8 cycles, mSi and P. Si reached to similar capacity values and capacity retention increased after that; especially for P. Si powder. Carbon coating layer helps P. Si to keep cycling. At the end of the 21st cycle, it still had a capacity of 280 mAh.g^{-1} . On the other hand, the capacity of the as-received silicon dropped under 100 mAh.g^{-1} after 10 cycles, which means the battery was failed. As the particle size of A.R. Si was the biggest while its surface area was the smallest, this failure was expected. What is remarkable in here is that the success of the etching method. Without any coating layer, it resulted in the highest capacity and continued to so till the end of the test.

Although, two of the three top-down approaches were successful in terms of increasing cyclic behavior, ball-milling did not provide the expected improvement. Even at the first cycle, it had the lowest capacity and battery failed at the second cycle. This is attributed to huge agglomerates of the powder. At the first discharge, Li ions are assumed to seep into the aggregates and caused fragmentation, disintegration fractures and debonding between the current collectors and the active materials.

At the first cycle, the number of lithium atoms inserted in the per unit formula of silicon were evaluated according to Faradays law (see equation 9) and tabulated in Table 8.2 assuming that all silicon powders are involved in the lithiation reaction.

Table 8.2 Number of lithium atoms inserted in plain powders at the initial cycle per unit formula per Si.	
	1st cycle
A.R. Si	2.4
mSi	3.04
B.M. Si	1.83
P. Si	2.4

The calculated theoretical capacity of silicon is 4200 mAh.g^{-1} according to $\text{Li}_{4.4}\text{Si}$ compound. However, at room temperature, maximum lithium amount that one silicon atom can accept is reported to be present at $\text{Li}_{15}\text{Si}_4$ phase (3.75 lithium atoms per silicon at around 3600 mAh.g^{-1} capacity). Only mSi sample with the capacity of 2900 mAh.g^{-1} came close to full lithiation. On the other hand, the reversibility of the lithium insertion reaction is either very limited since most of the lithium atoms cannot be extracted during charge or shedding of particles has occurred.

Therefore, in order to find out what structural changes took place after 21 cycles, all cells were disassembled after the final discharge and the active materials were analyzed implementing XRD. The XRD patterns of the electrodes were given in Figure 8.2.

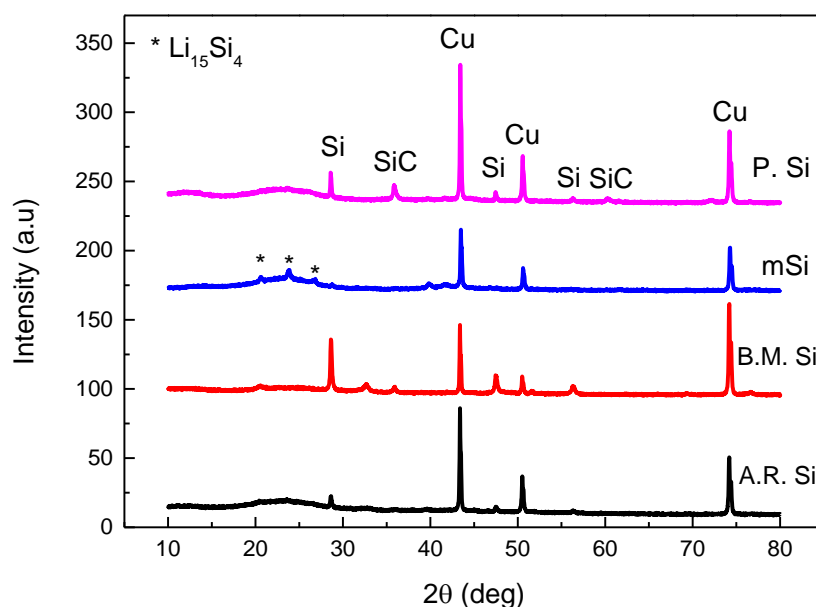


Figure 8.2 XRD spectrum of electrodes after final discharges.

XRD results proved the existence of both crystalline Li-Si phases (especially for mSi) and amorphous structure after galvanostatic cycling. At a previously carried study, Beaulieu et al. claimed that inhomogeneous expansion occurs in the crystalline materials due to the presence of coexisting phases with different Li concentrations; on

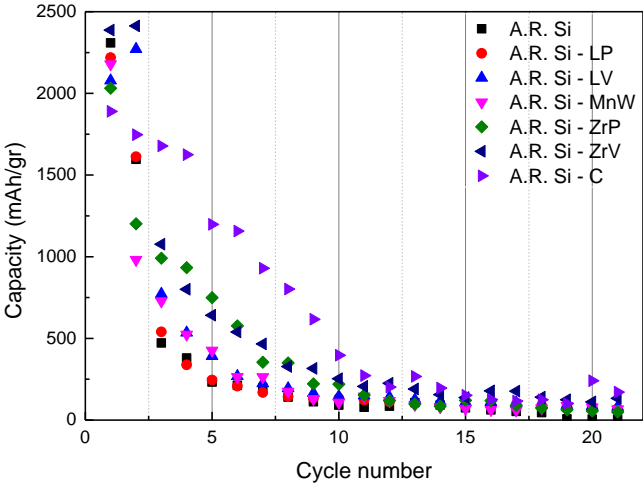
the other hand, the amorphous phases undergo reversible shape and volume changes. They attributed this difference to the homogeneous expansion and contraction that happens within the amorphous structure [91]. With that knowledge, XRD results indicates a big gap in the intensity of amorphous regions of the powders. Amorphous regions of mSi and P.Si are wider than the other two, which could be the reason of their better cyclic performance.

In addition, there is silicon peaks at B.M. Si, A.R. Si and P. Si electrodes, which means some of the active material did not undergo electrochemical reaction. For B.M. Si electrodes, this could be due to lack of the insertion of lithium ions through the big aggregates. For A.R. Si, the reason was similar to B.M. Si. Existence of particles in the micron range aggravated fully lithiation. For P.Si, there was electrochemically inactive SiC phase, which inhibited the diffusion of lithium ions through some inner silicon regions.

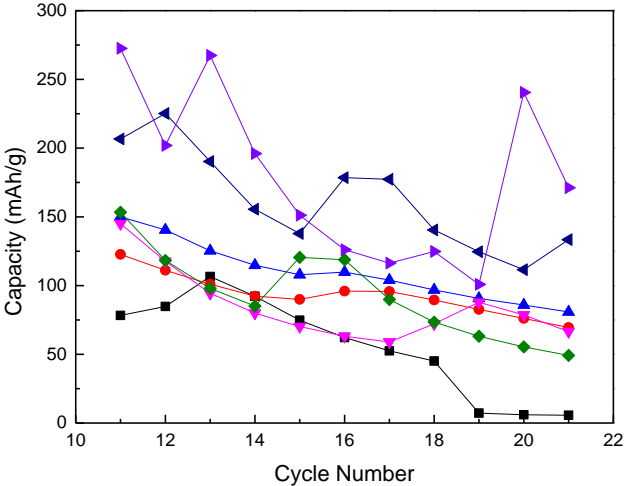
As mentioned earlier, the production of high surface area powder without any coating layer would not be sufficient to restrict the volume expansion problem. Therefore, further study on the effect of each coating material on cyclic performance for all the processed powders was investigated in detail.

Figure 8.3-a shows the comparison of different coating materials on the cyclic performance of the as-received powder. At the first discharge cycle, capacities are 2309 mAh.g⁻¹ for A.R. Si, 2219 mAh.g⁻¹ for A.R. Si-LP, 2078 mAh.g⁻¹ for A.R. Si-LV, 2178 mAh.g⁻¹ for A.R. Si-MnW, 2031 mAh.g⁻¹ for A.R. Si-ZrP, 2387 mAh.g⁻¹ for A.R. Si-ZrV, 1889 mAh.g⁻¹ for A.R. Si-C. These values were close to each other, which means 2.5 lithium was bonded with each silicon atom. However, there was a tendency towards a decrease in capacity with all the powders. The lowest value belonged to carbon coated powder which could stem from SEI layer. This layer increased the impedance of the battery during the first discharge, which will be mentioned at section 8.3. On the other hand, the best capacity retention performance also came from carbon coated anodes. Advantages of carbon coatings were mentioned in Section 7.3.1.5. Figure 8.3-b shows the capacities after 10th cycle. It was noted that

all coating materials had a positive effect on the capacity. Without any treatment after nineteenth cycle, A.R. Si electrode was dead while the worst result of the coated bunch was 50 mAh.g⁻¹ (ZrP coated powder). The highest capacity achieved with coating, at the final cycle was 171 mAh.g⁻¹ (carbon coating). Surrounding carbon/inorganic coating layers preserved the integrity of the structure and enhanced the cyclic performance of the cell.



(a)



(b)

Figure 8.3 The comparison of different coating materials on the cyclic performance of base powder (a) cycles from 1-21, (b) cycles from 11-21 (Lines drawn to facilitate tracking).

After discharge tests, XRD data was taken from all the electrodes. Figure 8.4 shows the spectrum of each electrode.

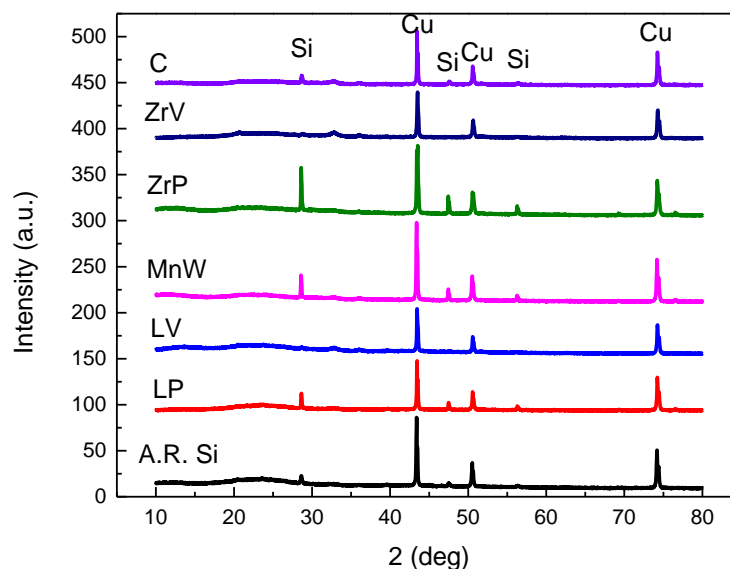
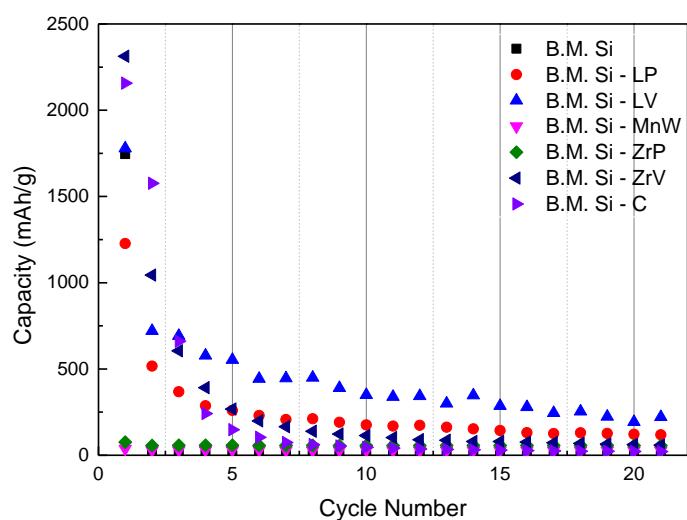


Figure 8.4 XRD spectrum of coated base powder electrodes after final discharges.

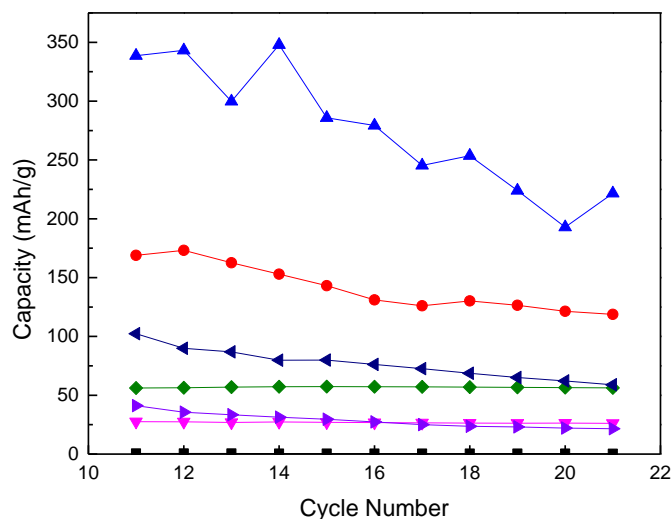
Although plain ball-milled powder did not yield any promising capacity, electrochemical performances of coated materials were also compared, in order to see whether any improvement could be achieved. Figure 8.5 gives the discharge capacity comparison of processed powders.

In terms of cyclic performances, best results were obtained with LV coating among ball-milled powders. MnW and ZrP coated powders had no capacity, their thick coating insulated them increasing their impedances. (MnW and ZrP ratios were 9.20 and 4.03 wt%, respectively). Other first discharge capacities for coated materials were 1745 mAh.g⁻¹ for B.M. Si, 1228 mAh.g⁻¹ for B.M. Si – LP, 1779 mAh.g⁻¹ for B.M. Si - LV, 2313 mAh.g⁻¹ for B.M. Si - ZrV and 2157 mAh.g⁻¹ for B.M. Si-C. Carbon and ZrV coatings improved the first discharge capacity; the reason might be low resistances of the electrodes providing constant voltage profiles and longer discharge time.

Coating of the powder inhibited the failure of battery after the first cycle. Although for all the coatings, second capacities suddenly dropped, yet they could still continue cycling. In Figure 8.5-b, the anode material with LV coating has still a capacity over 200 mAh.g⁻¹. This may be due to the safe discharge voltage of LV which is around 0.75 V vs. Li/Li⁺ [78].



(a)



(b)

Figure 8.5 The comparison of different coating materials on the cyclic performance of ball-milled powder, (a) cycles from 1-21, (b) cycles from 11-21 (Lines drawn to facilitate tracking).

After discharge tests, XRD data was taken from all the ball-milled electrodes. Figure 8.8 shows the spectrum of the ball-milled electrodes. Except LV coating, all spectra are identical. LV coated sample has SiO₂ peak. This silicon dioxide phase occurred during coating process and detailed XRD results were given at Section 7.4. In literature, it was mentioned that silicon dioxide can accept lithium ions and contribute to the capacity. However, XRD study showed that SiO₂ phase remained unchanged after 20 cycles. Also, contaminated inactive tungsten carbide (WC) phase can be clearly observed. For the MnW, ZrP and LP coated samples; there are distinct silicon peaks which prove lithium did not react with the silicon entirely. This explains their low discharge capacities. Neither the peaks of coating phases nor their lithiated structures' peaks can not be identified in the spectra. There is an amorphous region. From here, it is difficult to interpret whether they contribute to the reaction, as their specific peaks were not observed on the amorphous region. They may have been covered by the background noise of the XRD, rendering them unidentifiable. On the other hand, except carbon and ZrV coated silicon powders, there was considerable unreacted silicon phase. Intensity comparison of Si (111) peaks show a reverse relation with the discharge capacities of the electrodes. The lower the capacity, the higher the unreacted silicon phase.

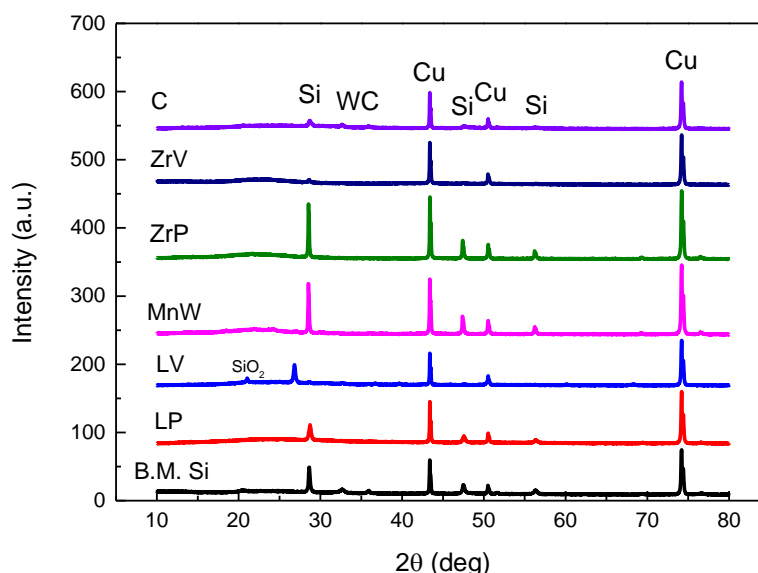
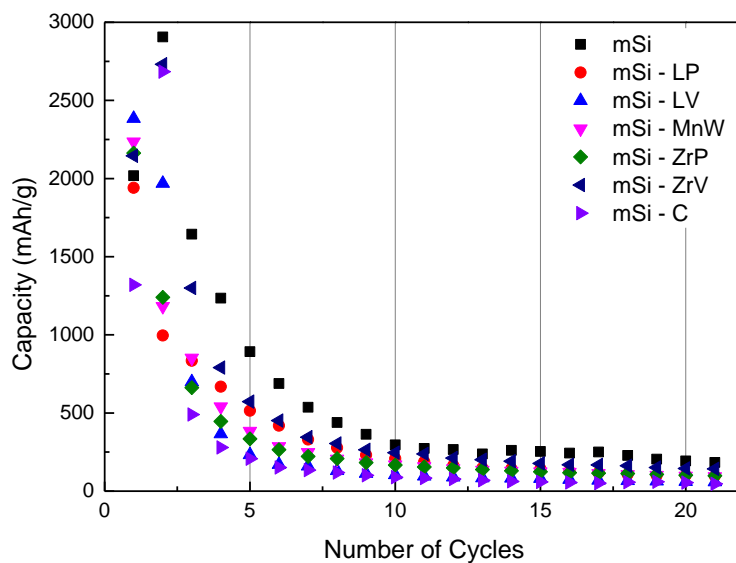
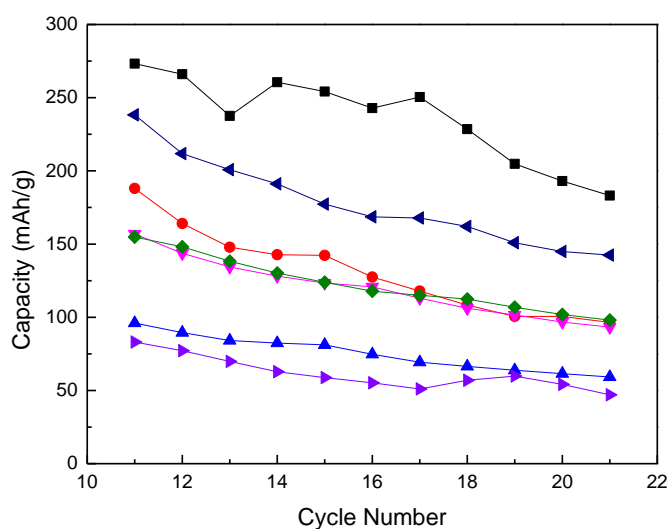


Figure 8.6 XRD spectra of coated ball-milled powder electrodes after final discharges.

Figure 8.6 shows the discharge capacity comparison of mSi powders. The highest capacities belonged respectively to mSi, mSi-ZrV and mSi-C with the numbers of 2906 mAh.g⁻¹, 2735 mAh.g⁻¹ and 2683 mAh.g⁻¹. However, after the first two discharges, capacities dropped dramatically and after the fifth cycle, all capacities were under 1000 mAh.g⁻¹.



(a)



(b)

Figure 8.7 The comparison of different coating materials on the cyclic performance of multi-dimensional powder, (a) cycles from 1-21, (b) cycles from 10-21.

XRD study was also done for mSi electrodes. The peaks located at the spectrum belong to $\text{Li}_{15}\text{Si}_4$, copper and silicon phases, but there were no peaks from the coating materials. Besides the crystalline Li-Si phase there is an amorphous region. The amorphous state provides the reversible capacity, since the diffusion of lithium ions inside the structure becomes easier. However, from XRD data, the presence of crystalline $\text{Li}_{15}\text{Si}_4$ indicates that lithium ions were trapped in this form at the beginning of cycling and became unavailable for extraction. This could be the reason of capacity loss during cycling.

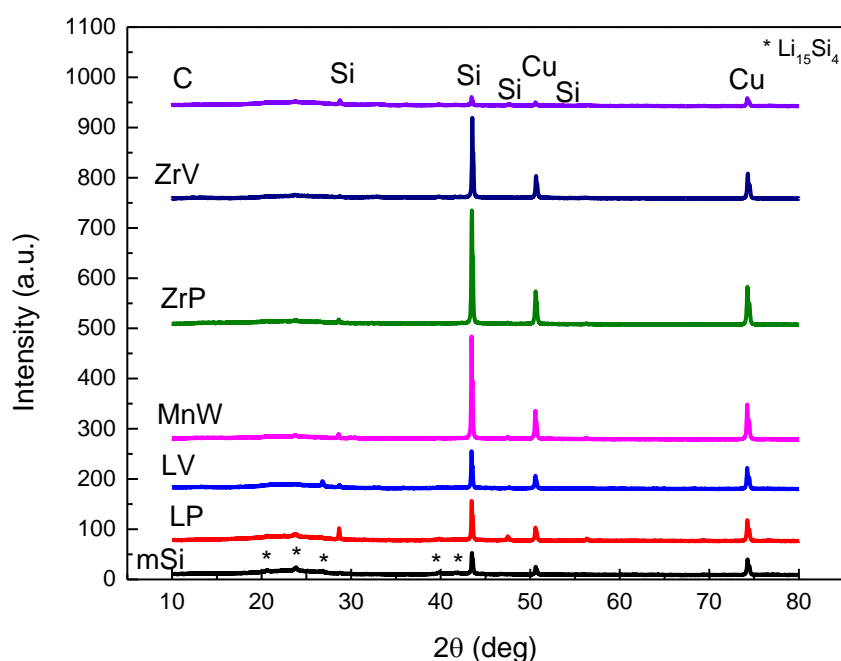
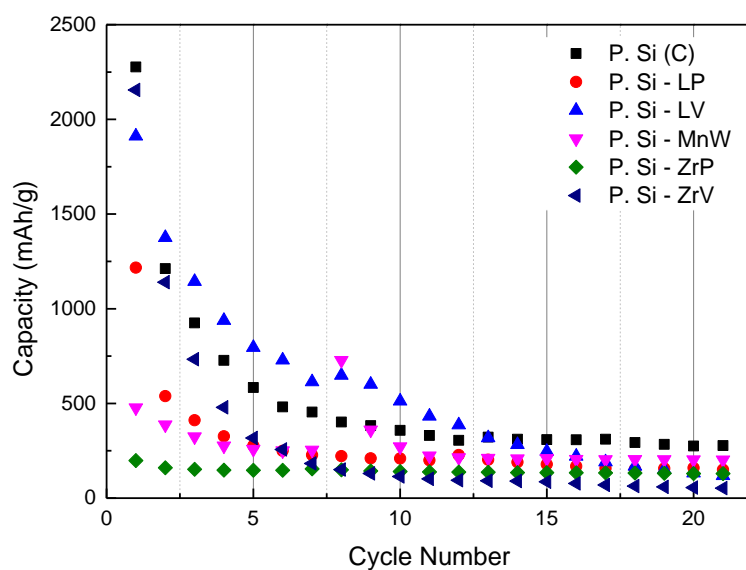
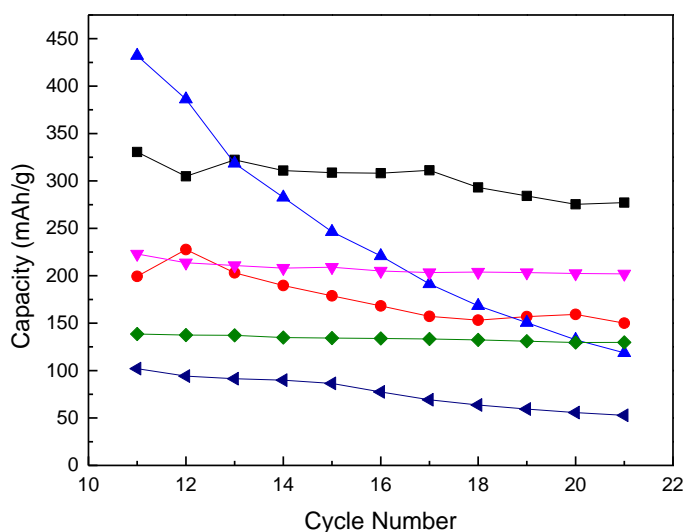


Figure 8.8 XRD spectra of multi-dimensional Si electrodes after final discharge cycles.

Last tested powder was induction plasma synthesized silicon powder. Plain powders' first discharge capacity was same as mSi and A.R. Si powders, however; its capacity retention was better. Figure 8.7 shows the comparison of all the coated P. Si electrodes. After the first discharge cycle, capacities were 2277 mAh.g^{-1} for P. Si (coated with carbon, C), 1217 mAh.g^{-1} for P. Si-LP, 1911 mAh.g^{-1} for P. Si-LV, 477 mAh.g^{-1} for P. Si-MnW, 198 mAh.g^{-1} for P. Si-ZrP, 2156 mAh.g^{-1} for P.Si-ZrV.



(a)



(b)

Figure 8.9 The comparison of different coating materials on the cyclic performance of induction plasma synthesized powder, (a) cycles from 1-21, (b) cycles from 11-21 (Lines drawn to facilitate tracking).

Similar to previously achieved test results, there was a decline in the capacities due to shedding of the particles. The plain powder (carbon coating) had the best performance. The plasma synthesized powder capacities were low, especially after 10th cycle all

dropped under 300 mAh.g⁻¹. The number of lithium atoms inserted in the per unit formula of silicon at the first cycle are tabulated in Table 8.3 which shows that outside coating layer restrained the lithium ion diffusion and lowers lithium intake which decreases the discharge capacity of the electrode.

Table 8.3 Number of lithium atoms inserted in the per unit formula of plasma synthesized silicon powders at the initial discharge.	
	1st cycle
P. Si (C)	2.39
P. Si - LP	1.28
P. Si - LV	2.00
P. Si - MnW	0.50
P. Si - ZrP	0.21
P. Si - ZrV	2.26

XRD data taken after cycling is given in Figure 8.10. No crystalline peak of Li-Si alloy were observed for any of the electrodes. Amorphization of silicon with alloying occurred. However, for all the seven electrodes there were unreacted silicon peaks observed. Cristobalite phase for MnW coated silicon remained unreacted after cycling, this means that SiO₂ did not contribute to electrochemical reactions. Besides, it increased impedance of the cell and obstructed the lithium ion insertion in to silicon.

To understand the cyclic behavior of the electrodes, detailed investigation was needed. For this purpose, impedance spectroscopy and cyclic voltammetry techniques were used. Section 8.3 & 8.4 give the results of these tests.

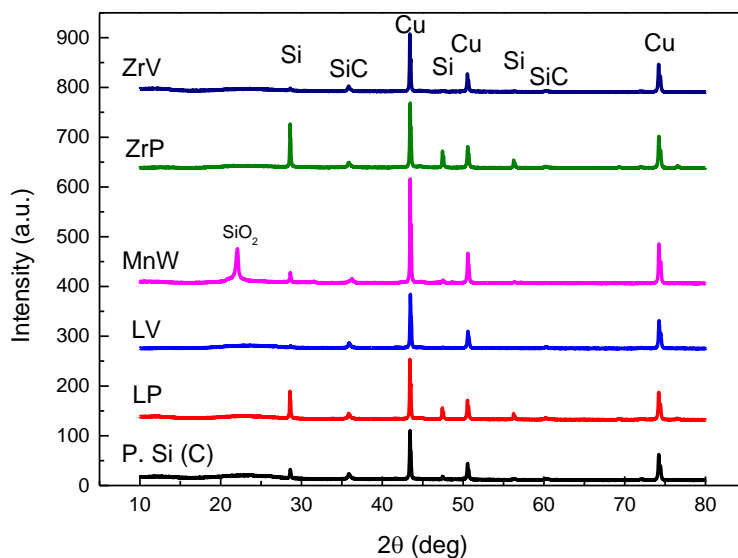


Figure 8.10 XRD spectra of plasma synthesized silicon powder electrodes after final discharge cycles.

8.3 Electrochemical Impedance Spectroscopy

The effect of coating materials on impedances were studied for silicon based powders. First; pre-cycling was applied, then the impedances were measured (between 100 kHz-10 mHz) at a scan rate of ± 5 mV/s.

In the beginning, the impedances of the as-received silicon and its coatings were measured and compared. According to this study, the highest impedance value got measured on carbon coating, while lithium phosphate had the lowest value. The high impedance in the carbon stems from the hindrance of charge transfer due to the SEI film layer. Table 8.4 & 8.5 gives the calculated resistance values of as-received and ball-milled powders, respectively.

When the impedances of the ball-milled powders were checked, as-received powder had better impedances than processed powder. This means ball-milling worsened the powders potential (Figure 8.11 & 8.12).

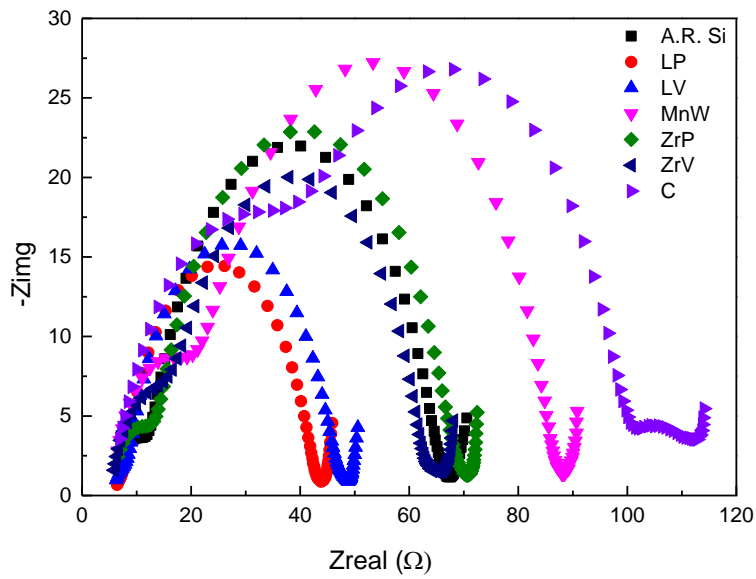


Figure 8.11 Impedance spectra comparisons of as-received silicon powders

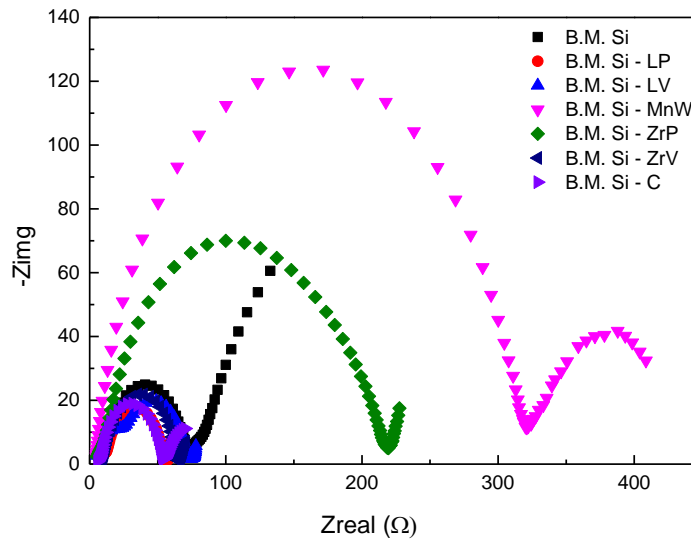


Figure 8.12 Impedance spectra comparisons of ball-milled silicon powders

Multi-dimensional Silicon powder tests revealed slightly lower impedances with respect to as-received and ball-milled powders. Similar to mSi, carbon coating had the best results. SEI formation on the electrodes were observed (Figure 8.13). Table 8.6 gives the calculated impedance values of mSi powders.

Table 8.4 Calculated resistance values of as-received silicon powders				
	R_f	R_{ct}	R_{diff}	χ²
A.R. Si	6.17	54.15		7.613e-05
A.R. Si - LP	10.71	33.38		1.073e-04
A.R. Si - LV	15.95	33.63		1.134e-04
A.R. Si - MnW	14.83	66.32		3.939e-05
A.R. Si - ZrP	8.68	53.93	2.31	3.463e-05
A.R. Si - ZrV	11.61	45.43	2.78	1.765e-05
A.R. Si - C	30.63	68.79		6.199e-04

Table 8.5 Calculated resistance values of ball-milled silicon powders				
	R_f	R_{ct}	R_{diff}	χ²
B.M. Si	6.73	61.02		2.957e-04
B.M. Si - LP	9.00	41,52	1.74	7.142e-05
B.M. Si - LV	20.68	45.61	3.73	2.522e-05
B.M. Si - MnW	309,4	144,2		2.673e-04
B.M. Si - ZrP	6.70	46.90	158,2	2.769e-05
B.M. Si - ZrV	0.47	50,59	13,03	1.159e-05
B.M. Si - C	9.44	44.91	27,78	1.368e-04

Table 8.6 Calculated resistance values of mSi powders			
	R_f	R_{ct}	R_{diff}
mSi. Si	17.59	20.09	8.11
mSi - LP	30.09	32.27	
mSi - LV	7.25	31.51	4.12
mSi - MnW	26.30	3.45	
mSi - ZrP	25,3	3.75	
mSi - ZrV	20,48		
mSi - C	25,97	3.35	

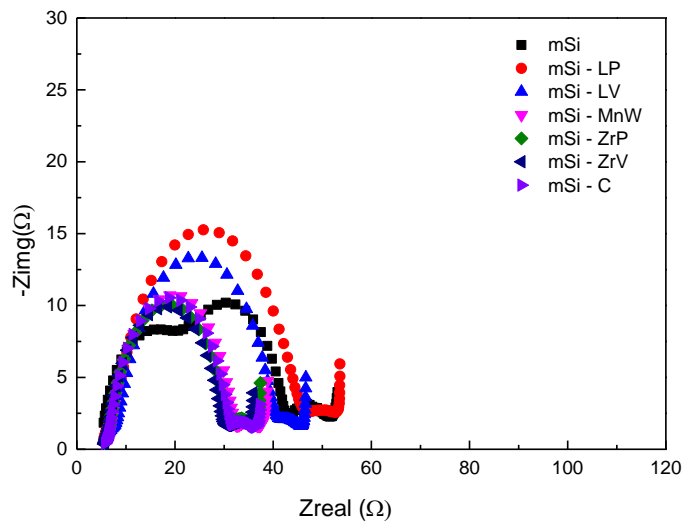


Figure 8.13 Impedance spectra comparisons of multi-dimensional silicon powders

Lastly, powders produced by induction plasma method were studied. Uncoated silicon, LV and ZrV had similar behaviors/values, but none were sufficient. The worst case was that of MnW, because of its high cristobalite phase (highly insulative). Below, Figure 8.14 shows the comparison of impedance graphs of the cells and Table 8.7 gives the calculated resistance values.

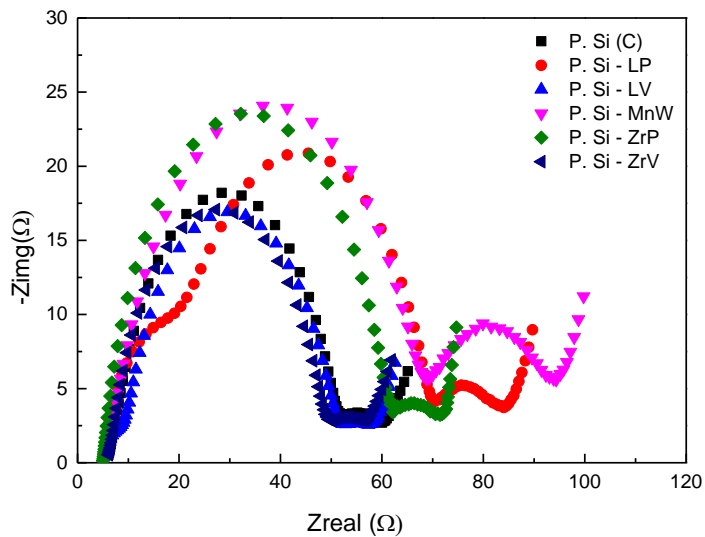


Figure 8.14 Impedance spectra comparisons of plasma synthesized silicon powders

Table 8.7 Calculated resistance values of induction plasma synthesized Si powders				
	R_f	R_{ct}	R_{diff}	χ²
P. Si (C)	43.33	6.20		9.206e-05
P. Si - LP	16.43	47.65	12.95	9.120e-06
P. Si - LV	4.94	40.59	6.83	8.940e-06
P. Si - MnW	2.44	61.28	22.94	1.574e-05
P. Si - ZrP	7.10	56.72		8.786e-05
P. Si - ZrV	6.94	41.85	3.54	4.889e-06

The research on the impedance results of different powders/methods revealed that only mSi had an improvement whereas the rest either had similar (negligible) or even worse values. Another revelation was that on carbon coated samples SEI formation occurred.

Figure 8.15 shows the impedance spectra of plain powders. So, the only notable improvement was with mSi due to three phenomena. In the high frequency zone the half-semi circle results from film resistance (SEI). In the mid-range, the semi circle was formed by charge transfer resistance. In the low frequency zone between 40 and 55 ohms in real axis, resistance mainly resulted from the diffusion of lithium ions that pass through Si.

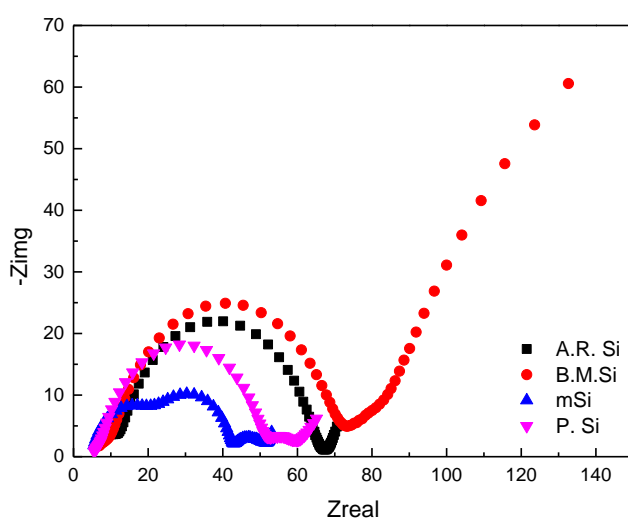


Figure 8.15 Impedance spectra comparisons of uncoated silicon powders

8.4 Cyclic voltammetry and Voltage profiles of samples

Alloying (lithiation) and dealloying (delithiation) are the main electrochemical mechanisms of the silicon based anode materials. As stated before, CV was tested at a scan rate of 0.01 mV/s between 0.01 and 1.2 V and applied towards the cathodic direction from higher to lower potential. CV response for the anodes was checked at the beginning of the tests. First comparison was made between plain powders. CV graphs are given in Figure 8.16.

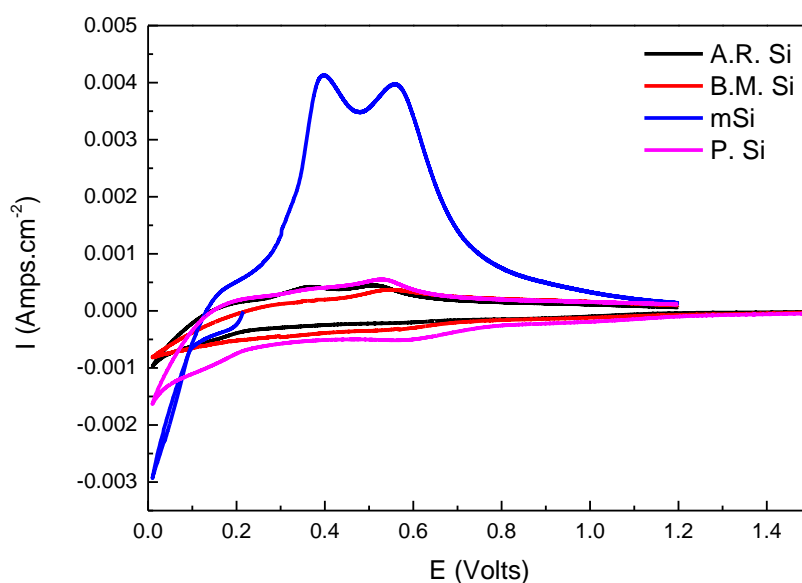


Figure 8.16 Cyclic voltammograms of produced silicon powders.

At the cathodic scan, no clear peaks were observed except plasma synthesized powder. At this stage, only crystalline silicon phase existed and lithiation of silicon takes place. On the other hand, for the plasma synthesized silicon powder, there is a carbon layer outside of the powder. So, there is a broad peak at around 0.5 to 0.7 V. this peak is generally attributed to the formation of SEI layer for carbon coated silicon powders. [92]. The other peak at $\sim 0.25\text{V}$ corresponds to the lithiation of crystalline silicon to form amorphous Li-Si alloys. In literature, anodic peaks are usually observed at around

0.35 and 0.5 for delithiation [90, 93, 94]. These two peaks are clearly observable for mSi, because it had the lowest impedance value among the four powders. The discharge curves of these four powders are also given in Figure 8.17. As seen from the figure, during the initial discharge there are several voltage plateaus at certain values. As mentioned earlier, there are different crystalline Li-Si intermetallic phases (LiSi , $\text{Li}_{12}\text{Si}_7$, $\text{Li}_{15}\text{Si}_4$, $\text{Li}_{22}\text{Si}_5$). The plateaus can be attributed to two phase equilibrium regions. XRD studies showed that beside the crystalline $\text{Li}_{15}\text{Si}_4$ phase there are also amorphous Li_xSi alloys. Each of these different plateaus could be representing these reduction voltages.

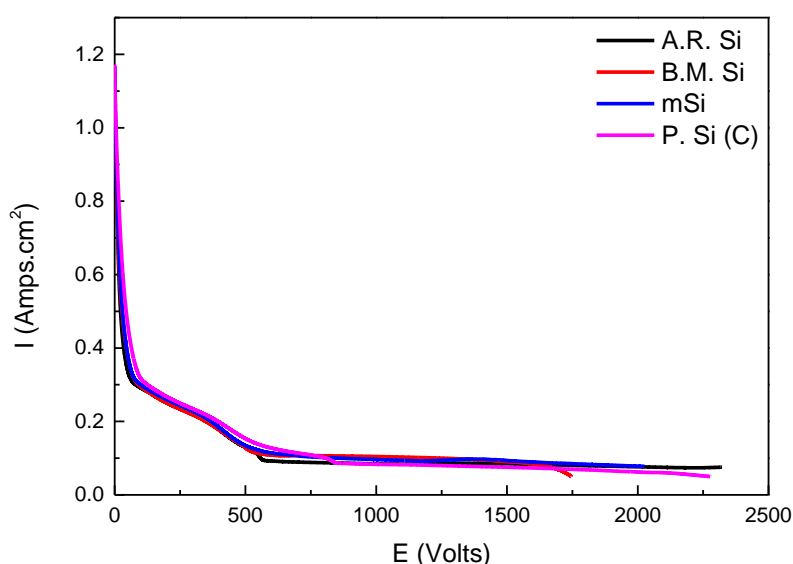


Figure 8.17 The first discharge curves of produced silicon powders.

To understand whether coating materials contribute to the lithiation/delithiation process or not, CV were applied to each specimen. Figure 8.18 gives the CV of LP coated powders. Anodic side of the voltammograms are similar with the previous graphs of cycling voltammetry. There was only a slight shift at the anodic peaks for different types of powders that can be explained with Ohm's law (varying impedances results different voltages and current values). However, at the cathodic side there are three peaks at the values of 1V, 0.6 V and 0.25 V. first two is generally attributed with the decomposition of electrolyte and formation of SEI layer and last one shows the

alloying of silicon. All four graph have the exact peaks. There is not an obvious peak for the reduction of LP phase. However, XRD data does not contain any LP peaks after cycling. There is only amorph phase. Either LP may be contributing to the lithium intercalation, or its structure turns into amorph due to diffusion of lithium ions inside, despite of not having involved in insertion reactions.

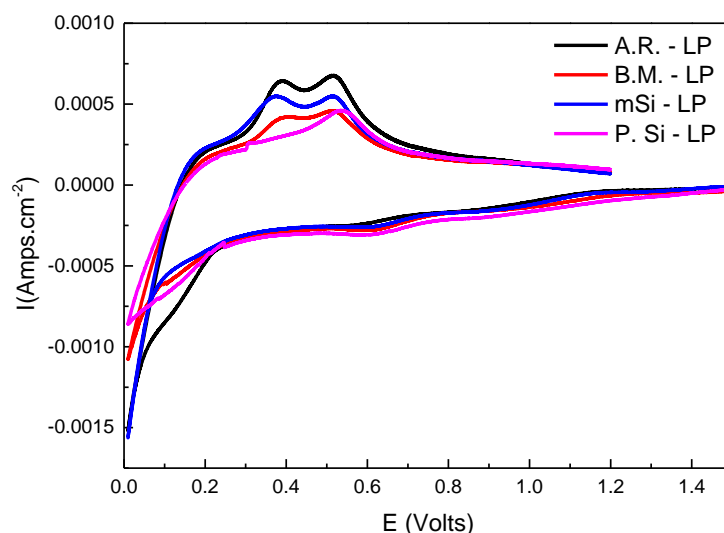


Figure 8.18 Cyclic voltammetry of LP coated powders.

The discharge curves of LP coated powders are given in Figure 8.19. As-received powder had the highest capacity and plasma synthesized had the lowest. However in terms of capacity retention, the situation is reversed.

Figure 8.20 shows the CV curves of LV coated samples. The voltammogram is very similar to the LP coated powders. Peaks belong to SEI formation and lithiation/delithiation of silicon. Different from the LP coating, LV coated silicon powders had SiO_2 phase after calcination. However, there is not a peak that shows the oxidation or reduction of oxide phase. There is not any reduction peak at the voltammogram, although silicon dioxide is an electrochemically active material. SiO_2 peaks still existed at the end of the cycling at the XRD spectrum. The discharge curves

of LV coated samples are given in Figure 8.21. The best capacity was observed for mSi powder and the worst is ball-milled silicon.

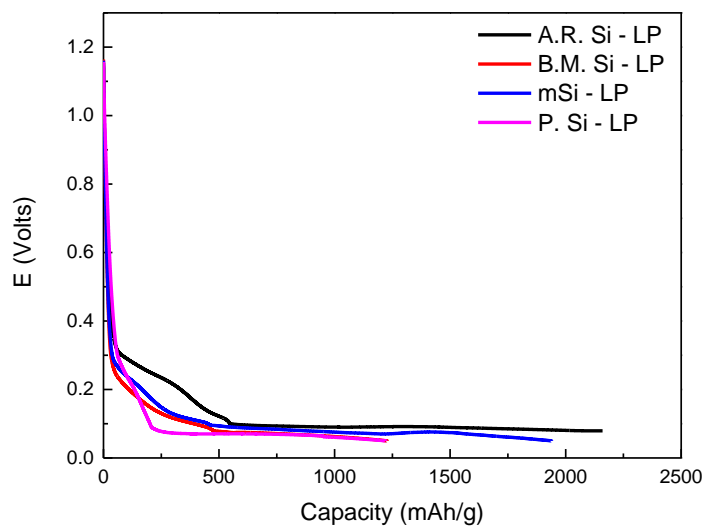


Figure 8.19 The first discharge curves of LP coated silicon powders.

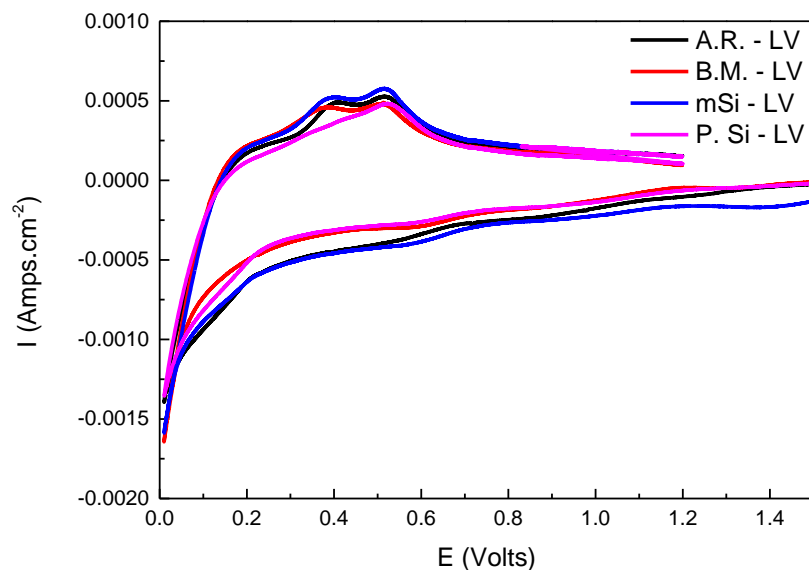


Figure 8.20 Cyclic voltammetry of LV coated powders.

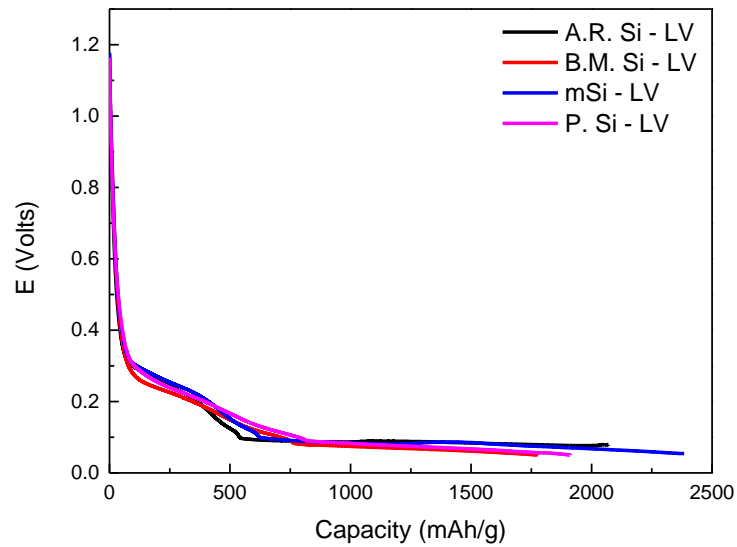


Figure 8.21 The first discharge curves of LV coated silicon powders.

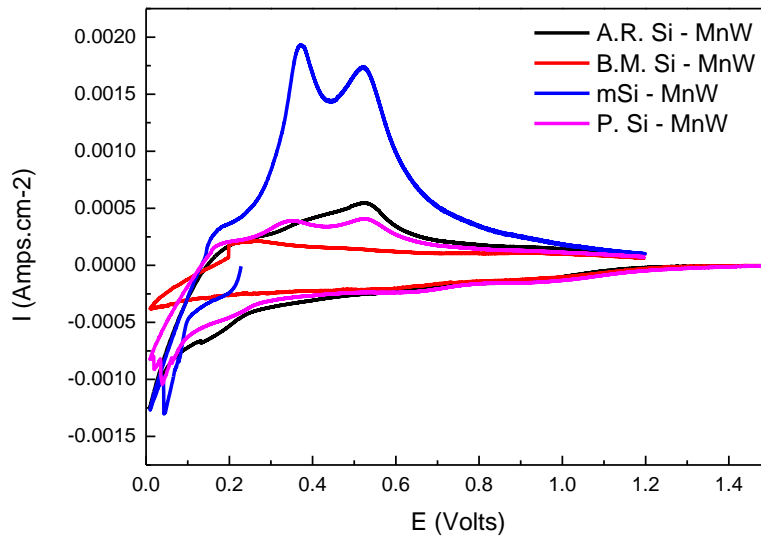


Figure 8.22 Cyclic voltammetry of MnW coated powders.

In the case of MnW, the situation is different. there is a dual drop at the tail part of the cathodic sweep for mSi and P. Si. A.R. Si powder had one sharp drop which looks like that of the LP and LV coatings however, there is a sharp undefined drop around 0.1 V. It can be said that MnW took part in the lithiation reactions. However, as mentioned earlier inserted lithium atoms do not return from the structure upon cycling which

probably resulted from the consumption of some of the lithium ions in the first discharge and this reduced the reversible capacities. When the voltammogram of ball-milled powder investigated, only the capacitive behavior was observed. It was so because of the high amount of MnW, which increased the impedance drastically. Figure 8.23 shows the discharge curves. B.M. Si did not give any capacity and P. Si has a poor capacity value compared to the other two. However, in terms of capacity retention it was not too bad. Although diffusion of lithium through MnW, SiO₂ and Si phases was very slow and difficult, they helped the silicon to stay stable during volume expansion.

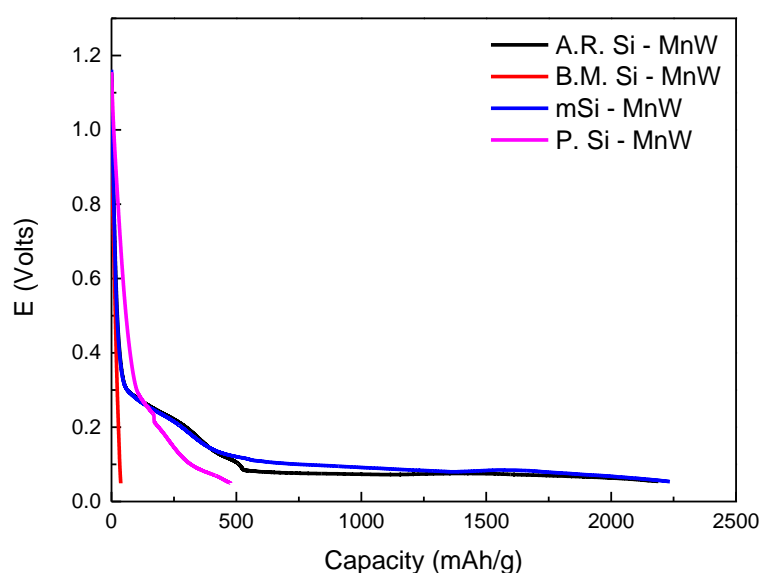


Figure 8.23 The first discharge curves of MnW coated silicon powders.

When CV graphs of ZrP coated powders were investigated, cathodic sides involved four different peaks for all the four systems. However the voltages of each peak shifted a little bit, which is related to the impedances of the electrodes. The voltage needed for the corporation of Li ions changes accordingly. Different from the other coated powders there is a third peak at the anodic part at around 0.9V which indicates a third oxidation reaction. According to this finding it can be said that ZrP contributes to electrochemical reaction. However, the CV tests were only measured for the first cycle

and reversibility of ZrP-Li reaction is not clear. On the other hand, it may be reversible but the ZrP amount on the produced powders was so small (4wt% for ball-milled powder is max.) its contribution to capacity was negligible. This may be the reason for the poor cycling performance. During lithiation, the structure of the ZrP probably was deformed and expected protection was not met resulting poor cycling of silicon powders.

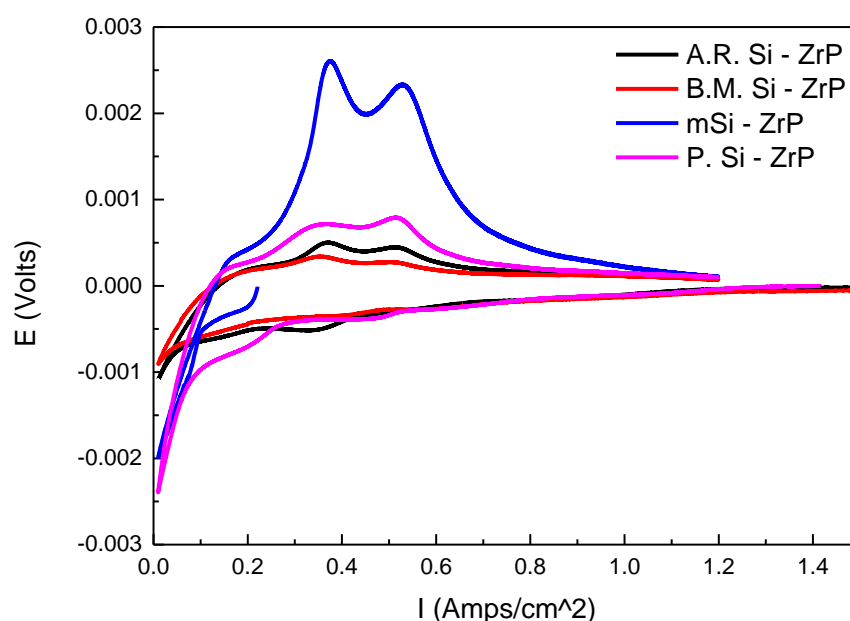


Figure 8.24 Cyclic voltammetry of ZrP coated powders.

Unfortunately, ZrV coating did not give a good confinement result as expected in the beginning. Capacity retention of the powders was poor and after seven cycling capacities dropped under 300 mAh.g^{-1} . CV of ZrV coated ball-milled powders showed capacitive behavior. Other three had standard lithiation/delithiation peaks of silicon with small voltage shifts. The peaks under 0.25 V corresponds to the formation of amorphous Li_xSi phase. (Figure 8.26) the discharge curves of all powders had similar shapes (Figure 8.27). The first discharge capacities of powders were above 2000 mAh.g^{-1} .

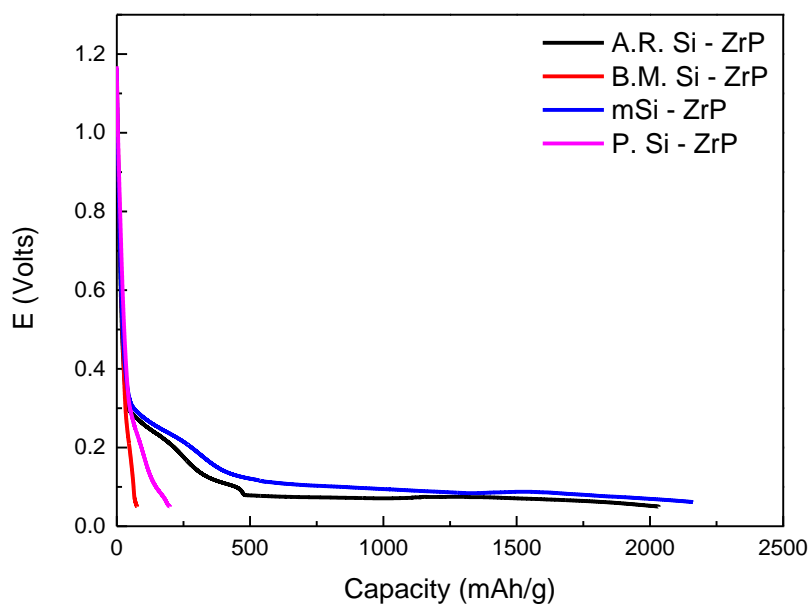


Figure 8.25 The first discharge curves of ZrP coated silicon powders.

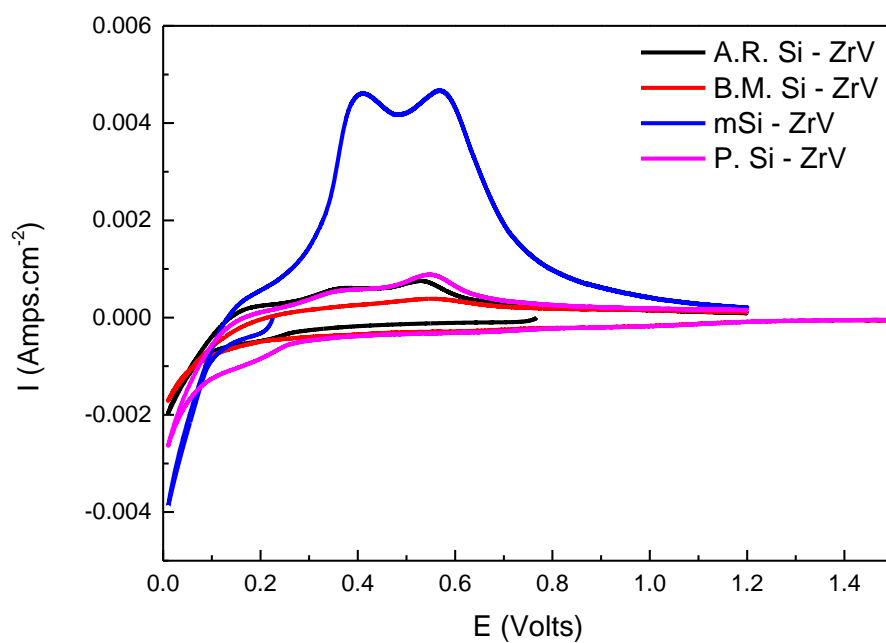


Figure 8.26 Cyclic voltammetry of ZrV coated powders.

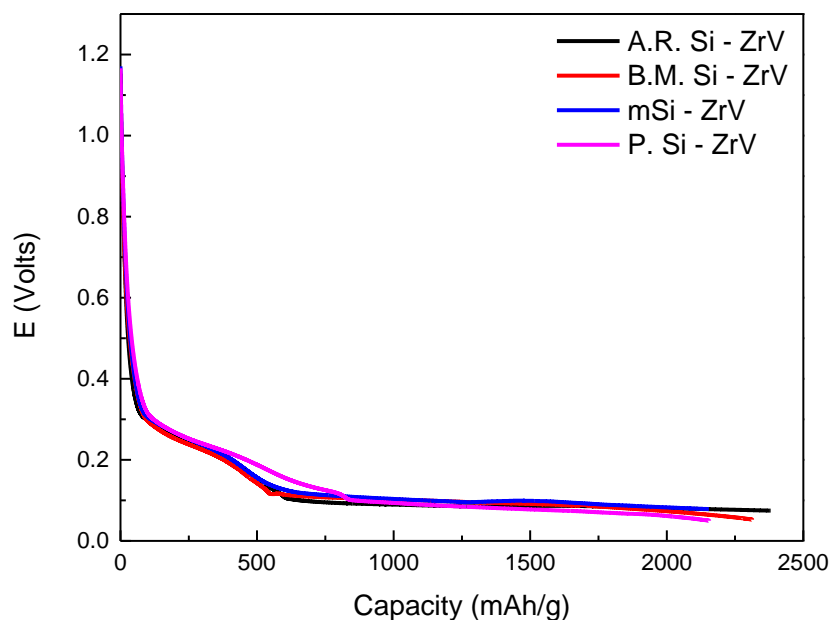


Figure 8.27 The first discharge curves of ZrV coated silicon powders.

Figure 8.28 shows the CV graphs of carbon coated powders. Comparisons showed that carbon coated samples had a peak at the cathodic side at around ~ 0.4 V for B.M. Si powder and at 0.6 V for P.Si powder. These peaks were attributed to the formation of SEI layer resulting from the decomposition of electrolyte. Carbon did not contribute to the lithiation process.

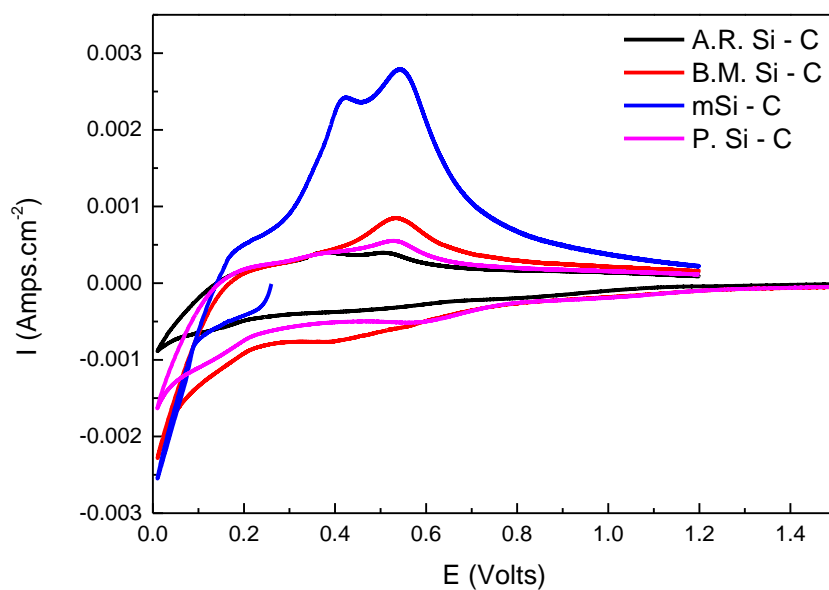


Figure 8.28 Cyclic voltammetry of carbon coated powders.

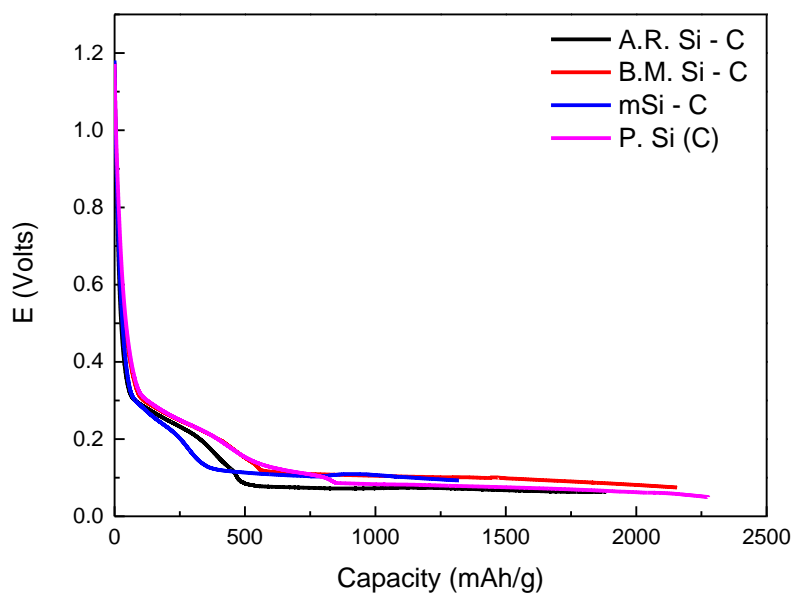


Figure 8.29 The first discharge curves of carbon coated silicon powders.

CHAPTER 9

CONCLUSIONS

To use readily available silicon powder as anode material for LIBs, particle size reduction and coating with inorganic material strategies were employed. For size reduction metal assisted chemical etching, ball-milling and induction plasma synthesis were applied. After production of various powders, they were coated with Li_3PO_4 , Li_3VO_4 , ZrP_2O_7 , ZrV_2O_7 , MnWO_4 and carbon to improve the electrochemical stability. Inorganic and carbon coating was achieved by sol-gel and pyrolysis techniques, respectively.

In ball-milling approach, optimum milling parameters were found to be the following 10 mm ball size, 15:1 weight ratios of ball to powder, 60% mill charge and 24 hours milling time. Average particle size is reduced from 17 μm to 0.2 μm and surface area increased from 2.4 to 3.6 $\text{m}^2\cdot\text{g}^{-1}$. Sub-micron particles were obtained but agglomeration and contamination problems have occurred. Ball-milled silicon powder did not show superior electrochemical results compared to the raw powder. The highest first discharge capacity has belong to zirconium vanadate coated powder with the value of 2313 $\text{mAh}\cdot\text{g}^{-1}$. On the other hand, in terms of capacity retention lithium vanadate coating has shown better cycle life. After 20 cycles lithium vanadate coated sample could maintain 200 $\text{mAh}\cdot\text{g}^{-1}$ capacity.

Metal assisted chemical etching is a successfully utilized method in order to produce nanowires on top of silicon wafers. Our studies confirmed the applicability of the method to powders as well. It produces a high surface to volume ratio structure. Surface area was increased to 7.1 $\text{m}^2\cdot\text{g}^{-1}$. Coating the etched structure with Li_3PO_4 , Li_3VO_4 , ZrP_2O_7 , ZrV_2O_7 , MnWO_4 and carbon had a negative effect on the

electrochemical properties because of ineffective coating on columnar structure. On the other hand, multi-dimensional silicon yielded the highest first discharge capacity with the value of 2900 mAh.g⁻¹ and even after 20 cycles, its capacity was around 200 mAh.g⁻¹ without any coating material. This method was the optimal solution studied during this study.

As a promising and high-tech powder processing method, induction plasma synthesis was applied to the as-received powder. The average particle size decreased to sub-micron range and the surface area increased to 7.7 m².g⁻¹. Carbon encapsulation was successful; however, an electrochemically inert SiC phase is formed around silicon particles up to approximately 30 wt. %. The highest first discharge capacity was belong to as-produced powder with 2277 mAh.g⁻¹ capacity. Among various coating materials lithium vanadate and carbon were the top contenders. But, carbon had a higher end capacity after 20 cycles. The reason may be the existence of double coating layer at lithium vanadate coated structure. Secondary coating layer may slow ion diffusion.

In general, sol-gel coating silicon powders with Li₃PO₄, Li₃VO₄, ZrP₂O₇, ZrV₂O₇, MnWO₄ and carbon did not produce the desired effect. As in induction plasma method, carbon and lithium vanadate coating gave the best results.

Combining structural improvement with coating did little good because of deterioration of the compounds' impedance leveled out the benefits. However, capacity fade during cycling was improved by synthesizing nano-structures because the mechanical wear of lithiation&delithiation was restricted.

REFERENCES

1. Winter, M. and R.J. Brodd, *What are batteries, fuel cells, and supercapacitors?* Chemical Reviews, 2004. **104**(10): p. 4245-4269.
2. Budde-Meiwes, H., J. Drillkens, B. Lunz, J. Muennix, S. Rothgang, J. Kowal and D.U. Sauer, *A review of current automotive battery technology and future prospects.* Proceedings of the Institution of Mechanical Engineers, Part D: Journal of Automobile Engineering, 2013. **227**(5): p. 761-776.
3. Opitz, A., P. Badami, L. Shen, K. Vignarooban and A.M. Kannan, *Can Li-Ion batteries be the panacea for automotive applications?* Renewable and Sustainable Energy Reviews, 2017. **68**: p. 685-692.
4. Reddy, T.B., *Linden's Handbook of Batteries, Fourth Edition* 2011: McGraw-Hill Education: New York, Chicago, San Francisco, Athens, London, Madrid, Mexico City, Milan, New Delhi, Singapore, Sydney, Toronto.
5. Tarascon, J.M. and M. Armand, *Issues and challenges facing rechargeable lithium batteries.* Nature, 2001. **414**(6861): p. 359-367.
6. James F. Rohan, M.H., Sanjay Patil, Declan P. Casey, Tomás Clancy, *Energy Storage: Battery Materials and Architectures at the Nanoscale.* 2014: ICT - Energy - Concepts Towards Zero - Power Information and Communication Technology, Dr. Giorgos Fagas (Ed.), InTech, DOI: 10.5772/57139. Available from: <http://www.intechopen.com/books/ict-energy-concepts-towards-zero-power-information-and-communication-technology/energy-storage-battery-materials-and-architectures-at-the-nanoscale>.
7. Jiang, F. and P. Peng, *Elucidating the Performance Limitations of Lithium-ion Batteries due to Species and Charge Transport through Five Characteristic Parameters.* Scientific Reports, 2016. **6**: p. 32639.
8. Jeong, G., Y.-U. Kim, H. Kim, Y.-J. Kim and H.-J. Sohn, *Prospective materials and applications for Li secondary batteries.* Energy & Environmental Science, 2011. **4**(6): p. 1986-2002.

9. Zuo, X., J. Zhu, P. Müller-Buschbaum and Y.-J. Cheng, *Silicon based lithium-ion battery anodes: A chronicle perspective review*. Nano Energy, 2017. **31**: p. 113-143.
10. Chen, R., T. Zhao, X. Zhang, L. Li and F. Wu, *Advanced cathode materials for lithium-ion batteries using nanoarchitectonics*. Nanoscale Horizons, 2016. **1**(6): p. 423-444.
11. Aifantis, K.E., *Next-Generation Anodes for Secondary Li-Ion Batteries*, in *High Energy Density Lithium Batteries*. 2010, Wiley-VCH Verlag GmbH & Co. KGaA. p. 129-164.
12. Spinner, N., L. Zhang and W.E. Mustain, *Investigation of metal oxide anode degradation in lithium-ion batteries via identical-location TEM*. Journal of Materials Chemistry A, 2014.
13. Armand, M. and J.M. Tarascon, *Building better batteries*. Nature, 2008. **451**(7179): p. 652-657.
14. Xu, W., J. Wang, F. Ding, X. Chen, E. Nasybulin, Y. Zhang and J.-G. Zhang, *Lithium metal anodes for rechargeable batteries*. Energy & Environmental Science, 2014. **7**(2): p. 513-537.
15. Winter, M., J.O. Besenhard, M.E. Spahr and P. Novák, *Insertion Electrode Materials for Rechargeable Lithium Batteries*. Advanced Materials, 1998. **10**(10): p. 725-763.
16. Vetter, J., P. Novák, M.R. Wagner, C. Veit, K.C. Möller, J.O. Besenhard, M. Winter, M. Wohlfahrt-Mehrens, C. Vogler and A. Hammouche, *Ageing mechanisms in lithium-ion batteries*. Journal of Power Sources, 2005. **147**(1-2): p. 269-281.
17. Zamfir, M.R., H.T. Nguyen, E. Moyen, Y.H. Lee and D. Pribat, *Silicon nanowires for Li-based battery anodes: a review*. Journal of Materials Chemistry A, 2013. **1**(34): p. 9566-9586.
18. Park, C.-M., J.-H. Kim, H. Kim and H.-J. Sohn, *Li-alloy based anode materials for Li secondary batteries*. Chemical Society Reviews, 2010. **39**(8): p. 3115-3141.
19. Zhang, W.-J., *Lithium insertion/extraction mechanism in alloy anodes for lithium-ion batteries*. Journal of Power Sources, 2011. **196**(3): p. 877-885.

20. Larcher, D., S. Beattie, M. Morcrette, K. Edstrom, J.-C. Jumas and J.-M. Tarascon, *Recent findings and prospects in the field of pure metals as negative electrodes for Li-ion batteries*. Journal of Materials Chemistry, 2007. **17**(36): p. 3759-3772.
21. Boukamp, B.A., G.C. Lesh and R.A. Huggins, *All- Solid Lithium Electrodes with Mixed- Conductor Matrix*. Journal of The Electrochemical Society, 1981. **128**(4): p. 725-729.
22. Xie, Z., Z. Ma, Y. Wang, Y. Zhou and C. Lu, *A kinetic model for diffusion and chemical reaction of silicon anode lithiation in lithium ion batteries*. RSC Advances, 2016. **6**(27): p. 22383-22388.
23. Choi, J.W. and D. Aurbach, *Promise and reality of post-lithium-ion batteries with high energy densities*. Nature Reviews Materials, 2016. **1**: p. 16013.
24. Xu, C., F. Lindgren, B. Philippe, M. Gorgoi, F. Björefors, K. Edström and T. Gustafsson, *Improved Performance of the Silicon Anode for Li-Ion Batteries: Understanding the Surface Modification Mechanism of Fluoroethylene Carbonate as an Effective Electrolyte Additive*. Chemistry of Materials, 2015. **27**(7): p. 2591-2599.
25. Ge, M., J. Rong, X. Fang, A. Zhang, Y. Lu and C. Zhou, *Scalable preparation of porous silicon nanoparticles and their application for lithium-ion battery anodes*. Nano Research, 2013. **6**(3): p. 174-181.
26. Kim, H., M. Seo, M.-H. Park and J. Cho, *A Critical Size of Silicon Nano-Anodes for Lithium Rechargeable Batteries*. Angewandte Chemie International Edition, 2010. **49**(12): p. 2146-2149.
27. Huang, H., G. Han, J. Xie and Q. Zhang, *The effect of commercialized binders on silicon oxide anode material for high capacity lithium ion batteries*. International Journal of Electrochemical Science, 2016. **11**(10): p. 8697-8708.
28. Bourderau, S., T. Brousse and D.M. Schleich, *Amorphous silicon as a possible anode material for Li-ion batteries*. Journal of Power Sources, 1999. **81-82**: p. 233-236.
29. Jung, H., M. Park, Y.-G. Yoon, G.-B. Kim and S.-K. Joo, *Amorphous silicon anode for lithium-ion rechargeable batteries*. Journal of Power Sources, 2003. **115**(2): p. 346-351.
30. Zhang, F.L., M. Zhu and C.Y. Wang, *Parameters optimization in the planetary ball milling of nanostructured tungsten carbide/cobalt powder*. International Journal of Refractory Metals and Hard Materials, 2008. **26**(4): p. 329-333.

31. Aktekin, B., G. Çakmak and T. Öztürk, *Induction thermal plasma synthesis of Mg₂Ni nanoparticles*. International Journal of Hydrogen Energy, 2014. **39**(18): p. 9859-9864.
32. Zhong, H., M. Sun, Y. Li, J. He, J. Yang and L. Zhang, *The polyacrylic latex: an efficient water-soluble binder for LiNi_{1/3}Co_{1/3}Mn_{1/3}O₂ cathode in li-ion batteries*. Journal of Solid State Electrochemistry, 2016. **20**(1): p. 1-8.
33. Baláž, P., *High-Energy Milling*, in *Mechanochemistry in Nanoscience and Minerals Engineering*. 2008, Springer Berlin Heidelberg: Berlin, Heidelberg. p. 103-132.
34. Suryanarayana, C., *Mechanical alloying and milling*. Progress in Materials Science, 2001. **46**(1-2): p. 1-184.
35. Dutta, H., P. Sahu, S.K. Pradhan and M. De, *Microstructure characterization of polymorphic transformed ball-milled anatase TiO₂ by Rietveld method*. Materials Chemistry and Physics, 2003. **77**(1): p. 153-164.
36. Yim, C.-H., F.M. Courtel and Y. Abu-Lebdeh, *A high capacity silicon-graphite composite as anode for lithium-ion batteries using low content amorphous silicon and compatible binders*. Journal of Materials Chemistry A, 2013. **1**(28): p. 8234-8243.
37. Li, X., *Metal assisted chemical etching for high aspect ratio nanostructures: A review of characteristics and applications in photovoltaics*. Current Opinion in Solid State and Materials Science, 2012. **16**(2): p. 71-81.
38. Smith, Z.R., R.L. Smith and S.D. Collins, *Mechanism of nanowire formation in metal assisted chemical etching*. Electrochimica Acta, 2013. **92**(0): p. 139-147.
39. Zhang, M.-L., K.-Q. Peng, X. Fan, J.-S. Jie, R.-Q. Zhang, S.-T. Lee and N.-B. Wong, *Preparation of Large-Area Uniform Silicon Nanowires Arrays through Metal-Assisted Chemical Etching*. The Journal of Physical Chemistry C, 2008. **112**(12): p. 4444-4450.
40. Bang, B.M., H. Kim, H.-K. Song, J. Cho and S. Park, *Scalable approach to multi-dimensional bulk Si anodes via metal-assisted chemical etching*. Energy & Environmental Science, 2011. **4**(12): p. 5013-5019.
41. Sim, S., P. Oh, S. Park and J. Cho, *Critical Thickness of SiO₂ Coating Layer on Core@Shell Bulk@Nanowire Si Anode Materials for Li-Ion Batteries*. Advanced Materials, 2013. **25**(32): p. 4498-4503.

42. McSweeney, W., H. Geaney and C. O'Dwyer, *Metal-assisted chemical etching of silicon and the behavior of nanoscale silicon materials as Li-ion battery anodes*. Nano Research, 2015. **8**(5): p. 1395-1442.
43. Spatschek, K.-H., *High temperature plasmas : theory and mathematical tools for laser and fusion plasmas* 2012: WILEY-VCH Verlag GmbH & Co. KGaA.
44. *APPLICATION 46 - SYNTHESIS OF NANOPARTICLES BY RF INDUCTION THERMAL PLASMA*, in *Nanoparticle Technology Handbook*, M. Hosokawa, K. Nogi, M. Naito, and T. Yokoyama, Editors. 2012, Elsevier: Spain p. 612-617.
45. Seo, J.-H.H., Bong-Guen, *THERMAL PLASMA SYNTHESIS OF NANO-SIZED POWDERS*. Nuclear Engineering and Technology, 2012. **44**(1): p. 9-20.
46. Bystrzejewski, M., A. Huczko, H. Lange, P. Baranowski, G. Cota-Sanchez, G. Soucy, J. Szczytko and A. Twardowski, *Large scale continuous synthesis of carbon-encapsulated magnetic nanoparticles*. Nanotechnology, 2007. **18**(14): p. 145608.
47. Borysiuk, J., A. Grabias, J. Szczytko, M. Bystrzejewski, A. Twardowski and H. Lange, *Structure and magnetic properties of carbon encapsulated Fe nanoparticles obtained by arc plasma and combustion synthesis*. Carbon, 2008. **46**(13): p. 1693-1701.
48. Athanassiou, E.K., R.N. Grass and W.J. Stark, *Large-scale production of carbon-coated copper nanoparticles for sensor applications*. Nanotechnology, 2006. **17**(6): p. 1668.
49. Lee, C.-H., P. Rai, S.-Y. Moon and Y.-T. Yu, *Thermal plasma synthesis of Si/SiC nanoparticles from silicon and activated carbon powders*. Ceramics International, 2016. **42**(15): p. 16469-16473.
50. Guo, J.Y., F. Gitzhofer and M.I. Boulos, *Induction plasma synthesis of ultrafine SiC powders from silicon and CH₄*. Journal of Materials Science, 1995. **30**(22): p. 5589-5599.
51. Zhong, L., J. Guo and L. Mangolini, *A stable silicon anode based on the uniform dispersion of quantum dots in a polymer matrix*. Journal of Power Sources, 2015. **273**: p. 638-644.
52. Mangolini, L., E. Thimsen and U. Kortshagen, *High-Yield Plasma Synthesis of Luminescent Silicon Nanocrystals*. Nano Letters, 2005. **5**(4): p. 655-659.

53. Chen, Z., Y. Cao, J. Qian, X. Ai and H. Yang, *Antimony-Coated SiC Nanoparticles as Stable and High-Capacity Anode Materials for Li-Ion Batteries*. The Journal of Physical Chemistry C, 2010. **114**(35): p. 15196-15201.
54. Foucher, F., G. Lopez-Reyes, N. Bost, F. Rull-Perez, P. Rößmann and F. Westall, *Effect of grain size distribution on Raman analyses and the consequences for in situ planetary missions*. Journal of Raman Spectroscopy, 2013. **44**(6): p. 916-925.
55. Meier, C., S. Lüttjohann, V.G. Kravets, H. Nienhaus, A. Lorke and H. Wiggers, *Raman properties of silicon nanoparticles*. Physica E: Low-Dimensional Systems and Nanostructures, 2006. **32**(1-2 SPEC. ISS.): p. 155-158.
56. Xi, G., S. Yu, R. Zhang, M. Zhang, D. Ma and Y. Qian, *Crystalline Silicon Carbide Nanoparticles Encapsulated in Branched Wavelike Carbon Nanotubes: Synthesis and Optical Properties*. The Journal of Physical Chemistry B, 2005. **109**(27): p. 13200-13204.
57. John D. Wright, N.A.J.M.S., *Sol-Gel Materials Chemistry and Applications*. Advanced Chemistry Texts, ed. P.O.B. David Phillips, Stan Roberts. Vol. 4. 2001, Great Britain: Taylor & Francis Books Ltd.
58. Lozano-Gorrín, A.D., *Structural Characterization of New Perovskites, Polycrystalline Materials - Theoretical and Practical Aspects*, P.Z. Zakhariiev, Editor. 2012, InTech: Available from: <http://www.intechopen.com/books/polycrystalline-materials-theoretical-and-practical-aspects/structural-characterization-of-new-perovskites>.
59. Rahaman, M.N., *Ceramic processing and sintering*. Second ed. Materials and Corrosion. 2003, New York, U.S.A.: Marcel Dekker, Inc.
60. Li, J., N.J. Dudney, J. Nanda and C. Liang, *Artificial Solid Electrolyte Interphase To Address the Electrochemical Degradation of Silicon Electrodes*. ACS Applied Materials & Interfaces, 2014. **6**(13): p. 10083-10088.
61. Lee, H.Y. and S.M. Lee, *Carbon-coated nano-Si dispersed oxides/graphite composites as anode material for lithium ion batteries*. Electrochemistry Communications, 2004. **6**(5): p. 465-469.
62. Terranova, M.L., S. Orlanducci, E. Tamburri, V. Guglielmotti and M. Rossi, *Si/C hybrid nanostructures for Li-ion anodes: An overview*. Journal of Power Sources, 2014. **246**(0): p. 167-177.

63. Liu, Y., K. Hanai, J. Yang, N. Imanishi, A. Hirano and Y. Takeda, *Silicon/carbon composites as anode materials for li-ion batteries*. *Electrochemical and Solid-State Letters*, 2004. **7**(10): p. A369-A372.
64. Wang, M.S. and L.Z. Fan, *Silicon/carbon nanocomposite pyrolyzed from phenolic resin as anode materials for lithium-ion batteries*. *Journal of Power Sources*, 2013.
65. Pietrzyk, B., S. Miszczak, H. Szymanowski and D. Kucharski, *Plasma enhanced aerosol-gel deposition of Al₂O₃ coatings*. *Journal of the European Ceramic Society*, 2013. **33**(12): p. 2341-2346.
66. Yang, Y., Y. Bai, S. Zhao, Q. Chang and W. Zhang, *Electrochemical performances of Si/TiO₂ composite synthesized by hydrothermal method*. *Journal of Alloys and Compounds*, 2013. **579**: p. 7-11.
67. Zeng, Z.Y., J.P. Tu, X.H. Huang, X.L. Wang, X.B. Zhao and K.F. Li, *Electrochemical properties of a mesoporous Si/TiO₂ nanocomposite film anode for lithium-ion batteries*. *Electrochemical and Solid-State Letters*, 2008. **11**(6): p. A105-A107.
68. Himpsel, F.J., F.R. McFeely, A. Taleb-Ibrahimi, J.A. Yarmoff and G. Hollinger, *Microscopic structure of the SiO₂/Si interface*. *Physical Review B*, 1988. **38**(9): p. 6084-6096.
69. Zhang, T., J. Gao, H.P. Zhang, L.C. Yang, Y.P. Wu and H.Q. Wu, *Preparation and electrochemical properties of core-shell Si/SiO nanocomposite as anode material for lithium ion batteries*. *Electrochemistry Communications*, 2007. **9**(5): p. 886-890.
70. Shi, D.Q., J.P. Tu, Y.F. Yuan, H.M. Wu, Y. Li and X.B. Zhao, *Preparation and electrochemical properties of mesoporous Si/ZrO₂ nanocomposite film as anode material for lithium ion battery*. *Electrochemistry Communications*, 2006. **8**(10): p. 1610-1614.
71. Kohandehghan, A., P. Kalisvaart, M. Kupsta, B. Zahiri, B.S. Amirkhiz, Z. Li, E.L. Memarzadeh, L.A. Bendersky and D. Mitlin, *Magnesium and magnesium-silicide coated silicon nanowire composite anodes for lithium-ion batteries*. *Journal of Materials Chemistry A*, 2013. **1**(5): p. 1600-1612.
72. Edfouf, Z., F. Cuevas, M. Latroche, C. Georges, C. Jordy, T. Hézèque, G. Caillon, J.C. Jumas and M.T. Sougrati, *Nanostructured Si/Sn-Ni/C composite as negative electrode for Li-ion batteries*. *Journal of Power Sources*, 2011. **196**(10): p. 4762-4768.

73. Zuo, P.J., G.P. Yin, Z.B. Wang, X.Q. Cheng, C.Y. Du, D.C. Jia and P.F. Shi, *Si/C/B₂O₃ composite anode for lithium ion batteries*. Gao Xiao Hua Xue Gong Cheng Xue Bao/Journal of Chemical Engineering of Chinese Universities, 2009. **23**(4): p. 705-708.
74. Konno, H., T. Morishita, C. Wan, T. Kasashima, H. Habazaki and M. Inagaki, *Si-C-O glass-like compound/exfoliated graphite composites for negative electrode of lithium ion battery*. Carbon, 2007. **45**(3): p. 477-483.
75. Song, H.G., J.Y. Kim, K.T. Kim and Y.J. Park, *Enhanced electrochemical properties of Li(Ni_{0.4}Co_{0.3}Mn_{0.3})O₂ cathode by surface modification using Li₃PO₄-based materials*. Journal of Power Sources, 2011. **196**(16): p. 6847-6855.
76. Li, X., R. Yang, B. Cheng, Q. Hao, H. Xu, J. Yang and Y. Qian, *Enhanced electrochemical properties of nano-Li₃PO₄ coated on the LiMn₂O₄ cathode material for lithium ion battery at 55 °C*. Materials Letters, 2012. **66**(1): p. 168-171.
77. Pu, X. and C. Yu, *Enhanced overcharge performance of nano-LiCoO₂ by novel Li₃VO₄ surface coatings*. Nanoscale, 2012. **4**(21): p. 6743-6747.
78. Li, H., X. Liu, T. Zhai, D. Li and H. Zhou, *Li₃VO₄: A Promising Insertion Anode Material for Lithium-Ion Batteries*. Advanced Energy Materials, 2013. **3**(4): p. 428-432.
79. Urcelay-Olabarria, I., J.M. Perez-Mato, J.L. Ribeiro, J.L. García-Muñoz, E. Ressouche, V. Skumryev and A.A. Mukhin, *Incommensurate magnetic structures of multiferroic MnWO₄ studied within the superspace formalism*. Physical Review B, 2013. **87**(1): p. 014419.
80. Heyer, O., N. Hollmann, I. Klassen, S. Jodlank, L. Bohatý, P. Becker, J.A. Mydosh, T. Lorenz and D. Khomskii, *A new multiferroic material: MnWO₄*. Journal of Physics: Condensed Matter, 2006. **18**(39): p. L471.
81. Montemayor, S.M. and A.F. Fuentes, *Electrochemical characteristics of lithium insertion in several 3D metal tungstates (MWO₄, M=Mn, Co, Ni and Cu) prepared by aqueous reactions*. Ceramics International, 2004. **30**(3): p. 393-400.
82. Kaygusuz, B., *DEVELOPMENT AND CHARACTERIZATION OF TUNGSTATES AND MOLYBDATES FOR LI-ION BATTERIES*, in *Metallurgical and Materials Engineering Department*. 2016, Middle East Technical University. p. 89.

83. Sahoo, P.P., S. Sumithra, G. Madras and T.N. Guru Row, *Synthesis, Structure, Negative Thermal Expansion, and Photocatalytic Property of Mo Doped ZrV₂O₇*. Inorganic Chemistry, 2011. **50**(18): p. 8774-8781.
84. Buchanan, R.C. and G.W. Wolter, *Properties of Hot- Pressed Zirconium Pyrovanadate Ceramics*. Journal of The Electrochemical Society, 1983. **130**(9): p. 1905-1910.
85. Sacks, R., Y. Avigal and E. Banks, *New Solid Electrolytes Based on Cubic ZrP₂O₇*. Journal of The Electrochemical Society, 1982. **129**(4): p. 726-729.
86. Wu, H.M., I. Belharouak, A. Abouimrane, Y.K. Sun and K. Amine, *Surface modification of LiNi_{0.5}Mn_{1.5}O₄ by ZrP₂O₇ and ZrO₂ for lithium-ion batteries*. Journal of Power Sources, 2010. **195**(9): p. 2909-2913.
87. Gu, P., R. Cai, Y. Zhou and Z. Shao, *Si/C composite lithium-ion battery anodes synthesized from coarse silicon and citric acid through combined ball milling and thermal pyrolysis*. Electrochimica Acta, 2010. **55**(12): p. 3876-3883.
88. Zuo, P., G. Yin, Z. Yang, Z. Wang, X. Cheng, D. Jia and C. Du, *Improvement of cycle performance for silicon/carbon composite used as anode for lithium ion batteries*. Materials Chemistry and Physics, 2009. **115**(2-3): p. 757-760.
89. Si, Q., K. Hanai, N. Imanishi, M. Kubo, A. Hirano, Y. Takeda and O. Yamamoto, *Highly reversible carbon-nano-silicon composite anodes for lithium rechargeable batteries*. Journal of Power Sources, 2009. **189**(1): p. 761-765.
90. Yang, X., Z. Wen, X. Zhu and S. Huang, *Preparation and Electrochemical Properties of Silicon/Carbon Composite Electrodes*. Electrochemical and Solid-State Letters, 2005. **8**(9): p. A481-A483.
91. Beaulieu, L.Y., T.D. Hatchard, A. Bonakdarpour, M.D. Fleischauer and J.R. Dahn, *Reaction of Li with Alloy Thin Films Studied by In Situ AFM*. Journal of The Electrochemical Society, 2003. **150**(11): p. A1457-A1464.
92. Khomenko, V.G. and V.Z. Barsukov, *Characterization of silicon- and carbon-based composite anodes for lithium-ion batteries*. Electrochimica Acta, 2007. **52**(8): p. 2829-2840.
93. Hansen, S., E. Quiroga-González, J. Carstensen and H. Föll, *Size-dependent cyclic voltammetry study of silicon microwire anodes for lithium ion batteries*. Electrochimica Acta, 2016. **217**: p. 283-291.

94. Wei, L., C. Chen, Z. Hou and H. Wei, *Poly (acrylic acid sodium) grafted carboxymethyl cellulose as a high performance polymer binder for silicon anode in lithium ion batteries*. Scientific Reports, 2016. **6**: p. 19583.

CURRICULUM VITAE

PERSONAL INFORMATION

Surname, Name: Miser, Burcu

Nationality: Turkish (TC)

Date and Place of Birth: 8 September 1982, Ankara

Marital Status: Married

Phone: +90 533 770 1511

email: burcumiser@gmail.com

EDUCATION

Degree	Institution	Year of Graduation
MS	Middle East Technical University	2010
BS	Marmara University	2006
High School	Ankara Ayrancı High School	2000

WORK EXPERIENCE

Year	Place	Enrollment
2010-2013	Yiğit Akü Malzemeleri Sanayi Ticaret A.Ş	R&D Engineer
2007-2010	Middle East Technical University – Metallurgical & Materials Engineering Department	Project Assistant of TUBİTAK 1001 project

FOREIGN LANGUAGES

Advanced English

HOBBIES

Swimming, Gourmet, Movies, Fitness